DISSERTATION

REMOTE CONTINENTAL AEROSOL CHARACTERISTICS IN THE ROCKY MOUNTAINS OF COLORADO AND WYOMING

Submitted by

Ezra JT Levin

Department of Atmospheric Science

In partial fulfillment of the requirements

For the Degree of Doctor of Philosophy

Colorado State University

Fort Collins, Colorado

Spring 2013

Doctoral Committee:

Advisor: Sonia M. Kreidenweis

Jeffrey L. Collett Jr.
Susan C. van den Heever
Jay Ham

ABSTRACT

REMOTE CONTINENTAL AEROSOL CHARACTERISTICS IN THE ROCKY MOUNTAINS OF COLORADO AND WYOMING

The Rocky Mountains of Colorado and Wyoming enjoy some of the cleanest air in the United States, with few local sources of particulate matter or its precursors apart from fire emissions, windblown dust, and biogenic emissions. However, anthropogenic influences are also present with sources as diverse as the populated Front Range, large isolated power plants, agricultural emissions, and more recently emissions from increased oil and gas exploration and production. While long-term data exist on the bulk composition of background fine particulate matter at remote sites in the region, few long-term observations exist of aerosol size distributions, number concentrations and size resolved composition, although these characteristics are closely tied to important water resource issues through the potential aerosol impacts on clouds and precipitation. Recent modeling work suggests sensitivity of precipitation-producing systems to the availability of aerosols capable of serving as cloud condensation nuclei (CCN); however, model inputs for these aerosols are not well constrained due to the scarcity of data. In this work I present aerosol number and volume concentrations, size distributions, chemical composition and hygroscopicity measurements from long-term field campaigns. I also explore the volatility of organic material from biomass burning and the potential impacts on aerosol loading.

Relevant aerosol observations were obtained in several long-term field studies: the Rocky Mountain Atmospheric Nitrogen and Sulfur study (RoMANS, Colorado), the Grand Tetons

Reactive Nitrogen Deposition Study (GrandTReNDS, Wyoming) and as part of the Bio-hydro-atmosphere interactions of Energy, Aerosols, Carbon, H_2O, Organics & Nitrogen project (BEACHON, Colorado). Average number concentrations ($0.04 < D_p < 20$ μm) measured during the field studies ranged between 1000 – 2000 cm^{-3} during the summer months and decreased to 200 – 500 cm^{-3} during the winter. These seasonal changes in aerosol number concentrations were correlated with the frequency of events typical of new particle formation. Measured sub-micron organic mass fractions were between 70 – 90% during the summer months, when new particle formation events were most frequent, suggesting the importance of organic species in the nucleation or growth process, or both. Aerosol composition derived from hygroscopicity measurements indicate organic mass fractions of 50 – 60% for particles with diameters larger than 0.15 μm during the winter. The composition of smaller diameter particles appeared to be organic dominated year-round.

High organic mass fractions led to low values of aerosol hygroscopicity, described using the κ parameter. Over the entire year-long BEACHON study, κ had an average value of 0.16 ± 0.08, similar to values determined during biologically active periods in tropical and boreal forests, and lower than the commonly assumed value of $\kappa_{continental} = 0.3$. There was also an observed increase in κ with size, due to external mixing of the fine mode aerosol. Incorrect representations of κ or its size dependence led to erroneous values of calculated CCN concentrations, especially for supersaturation values less than 0.3%. At higher supersaturations, most of the measured variability in CCN concentrations was captured by changes in total measured aerosol number concentrations.

While data from the three measurement sites were generally well correlated, indicating similarities in seasonal cycles and in total number concentrations, there were some variations

between measurements made at different sites and during different years that may be partly due to the effects of local emissions. The averaged data provide reasonable, observationally-based parameters for modeling of aerosol number size distributions and corresponding CCN concentrations.

Field observations clearly indicated the episodic influence of wildfire smoke on particle number concentrations and compositions. However, the semi-volatile nature of the organic carbon species emitted makes it difficult to predict how much of the emitted organic mass will remain in the condensed phase downwind. To better constrain the volatility of organic species in smoke, emissions from laboratory biomass combustion experiments were subjected to quantified dilution, resulting in reduction of aerosol mass concentrations over several orders of magnitude and a corresponding volatilization response of the organic particles that was fit to the commonly-applied Volatility Basis Set. Organic emissions from all burns with initial organic aerosol concentrations greater than 1000 $\mu g\ m^{-3}$ contained material with saturation concentration values ranging between 1 and 10,000 $\mu g\ m^{-3}$, with most of the organic mass falling at the two extremes of this range. For most burns, a single distribution was able to capture the volatility behavior of the organic material, within experimental uncertainty, despite the considerable variability in fuel and fire characteristics, suggesting that a simplified two-product model of gas-aerosol partitioning may be adequate to describe the evolution of biomass burning organic aerosol in models.

ACKNOWLEDGEMENTS

Sonia Kreidenweis, my advisor, has been a constant source of education, motivation and inspiration throughout my time at CSU. I appreciate her willingness and availability to answer questions and give advice, her enthusiasm for her students and their work and her scientific insights. I have learned a great deal from working with Sonia, and am extremely thankful that she offered me the opportunity to do my graduate research with her.

I would also like to thank my committee members, Jeff Collett, Sue van den Heever and Jay Ham who all provided great advice and feedback as I completed this work.

As is the nature of all field measurement campaigns, many people were involved in the RoMANS, GrandTReNDS, BEACHON and FLAME studies. Thus, while there can only be one name listed as author for this dissertation, the data and results presented here represent a collaborative effort from a great number of participants, and many thanks and acknowledgments are due. During RoMANS and GrandTReNDS, Amy Sullivan, Derek Day, Florian Schwandner, Katie Benedict, Kip Carrico, Misha Schurman, Taehyoung Lee, Tony Prenni, Yi Li and Yury Desyaterik all operated instruments and performed data analysis. I would specifically like to thank Misha and Taehyoung for supplying the AMS data used in this work and Sam Atwood for running the HYSPLIT model for me. Sonia, Jeff, Kip, Tony, Bill Malm and Bret Schichtel all helped with planning and logistics for these studies.

During BEACHON, Christina McCluskey, Elvin Garcia, John Ortega, Tony and Yutaka Tobo all assisted with the CCN measurements. Brett Palm operated the AMS and performed initial quality control and data analysis. Paul DeMott, Jim Smith, Tony and Sonia were all involved in planning and organization for BEACHON.

During FLAME 3, Taehyoung Lee operated the AMS and performed data analysis. I would also like to thank Taehyoung for his willingness to answer all my AMS questions over the last few years, although that instrument remains a mystery to me. Kip Carrico built and operated the dilution system used during FLAME 3, Andy May ran the CMU thermodenuder, Dan Welsh-Bon provided VOC data, Gavin McMeeking performed SP2 measurements and the AERODYNE gas instruments were operated by Tim Onasch. Kyle Wold assisted with the burns and ran the FSL gas instrumentation and Jose Jiminez, Wei Min Hoa, Allen Robinson, Jeff and Sonia were all involved in the planning and successful completion of this study.

Parts of this work were funded by the National Park Service, the National Science Foundation the Environmental Protection Agency and the Joint Fire Sciences Program.

Finally, I must thank Jenny for putting up with being married to a student for so long. I am truly fortunate to be married to such a patient and wonderful woman. Thank you!

DEDICATION

For my parents, who taught me to read and write and, through great patience, perseverance and personal pain, instilled in their delinquent son a lifelong love of learning.

TABLE OF CONTENTS

LIST OF TABLES

LIST OF FIGURES

1. Introduction

1.1. Purpose

In this dissertation, I present measurements of aerosol physical and chemical properties from a number of long-term field campaigns located in mountainous areas of the western United States. These data provide a unique look at aerosol concentrations, size distributions, chemical composition and hygroscopicity in remote, mid-latitude, continental regions. Because of the generally clean conditions in the study areas, changes to aerosol properties due to natural or anthropogenic causes could have large impacts, motivating the need to understand current conditions in these areas. As well as data from field campaigns, I present data from a laboratory study focused on determining the volatility of organic material emitted from biomass burning. Smoke from prescribed and wildfires is a major contributor to aerosol loadings in the western US and these data complement the field data in helping to better understand the nature and behavior of aerosols in the mountains of the western US. The goal of this work is to present aerosol characteristics and identify relationships that can be used to improve or validate model representations of aerosols and their impacts in this region.

1.2. Aerosols, models and the need for measurements

By now, it is well known, and well documented, that aerosols play an important role in many, if not all, atmospheric processes through direct impacts or feedbacks. Aerosols are necessary for cloud and precipitation formation, they scatter and absorb solar and terrestrial radiation and participate in atmospheric chemistry, among other processes, all of which have

potential further feedbacks on such important issues as local weather and global climate. Because of the important role aerosols play in these processes, they must be included in models, and many parameterizations, with many levels of complexity have been developed in order to do so. Aerosols are intrinsically difficult to model, however, due to their varied sources and short lifetimes, leading to large spatial variability, complex composition, large size range and variability in interactions with water and radiation [*Ghan et al.*, 2012; *Liu et al.*, 2012]. Because of this large variability, aerosol effects and feedbacks are often considered to represent the largest uncertainty in predictions of future climate change, leading to increased efforts to model atmospheric aerosol [*Fuzzi et al.*, 2006; *Kanakidou et al.*, 2005; *Kinne et al.*, 2006; *Textor et al.*, 2006; *Y Zhang*, 2008; *Y Zhang et al.*, 2010]. Due to the focus on improving predictions of future climate change, global climate models (GCM) have come a long way in their ability to represent aerosol properties from the models used for the first Intergovernmental Panel on Climate Change (IPCC) assessment report which did not include any aerosol processes in their calculations [e.g. *Schlesinger and Jiang*, 1991]. However, even the highly sophisticated GCMs currently in use cannot capture the full complexity of aerosol properties and their feedbacks due to the prohibitively large computing power this would require [*Fuzzi et al.*, 2006]. Representative aerosol parameters are therefore needed. Measurements of aerosol properties and relationships between them are helpful in determining the most important parameters to include in models to minimize computing time while still capturing the processes important for global climate simulation [*Fuzzi et al.*, 2006; *Roesler and Penner*, 2010].

In order to properly represent aerosol effects and feedbacks in GCMs, we must first understand how aerosols affect clouds and precipitation on much smaller scales. Numerous modeling studies have been conducted to determine the effects of changing aerosol size,

composition and concentrations on the development of clouds and precipitation in many different environments [*Khain and Lynn*, 2009; *Khain et al.*, 2005; *S S Lee*, 2012; *Lerach and Cotton*, 2012; *Lerach et al.*, 2008; *Romakkaniemi et al.*, 2012; *Storer et al.*, 2010; *van den Heever et al.*, 2006; *Van Den Heever and Cotton*, 2007; *van den Heever et al.*, 2011; *Zhao et al.*, 2012]. In general, these and other cloud and aerosol modeling studies have shown that for the same liquid water contents, enhancements in idealized aerosol concentrations result in more numerous, but smaller, modeled cloud droplets with resulting decreases in precipitation formation, leading to more water being transported to higher levels in the cloud, increasing latent heat release and thereby invigorating convection. These and other processes change not only the location, duration and amount of precipitation, but also alter the optical properties and lifetimes of clouds which have further effects on radiative transfer and global climate. In order to take the results of these idealized cases and apply them to actual conditions, or use them as forecasting tools to predict changes in local, regional or global weather or climate, high quality measurements of aerosol size, concentration and chemical properties are needed in the regions of cloud and precipitation formation.

Chemical transport models (CTM) such as the Goddard Earth Observing System Chemical transport model (GEOS-Chem) [*Ford and Heald*, 2012; *Lapina et al.*, 2011; *Leibensperger et al.*, 2012; *Ridley et al.*, 2012], the Particulate Matter Comprehensive Air-quality Model with extensions (PMCAMx) [*Fountoukis et al.*, 2011; *Jung et al.*, 2010] and the Multiscale Air Quality Simulation Platform (MAQSIP) [*Mathur et al.*, 2005] as well as coupled chemical transport and meteorology models such as the Weather Research and Forecasting model coupled with Chemistry (WRF-Chem) [*Luo and Yu*, 2011; *Saide et al.*, 2012; *Ward and Cotton*, 2011a; *Y Zhang et al.*, 2010; *Zhao et al.*, 2012], can provide regional to global maps of

modeled aerosol composition, concentration, size distribution, mixing state and other parameters based on modeled emission, transport, chemical transformation and removal mechanisms. The resulting model outputs are helpful for determining the role of aerosol particles in scales ranging from local air quality to global climate and are useful in filling in gaps in aerosol data from in-situ measurements and satellite retrievals. These models are also critical in assessing the current contribution of aerosols to cloud and radiative processes, with subsequent climatic effects, and for predicting changes in aerosol properties and processes due to changes in climate and emissions [*Heald et al.*, 2012; *Leibensperger et al.*, 2012]. However, modeled aerosol concentrations and properties need to be tested against some kind of ground truth measurements to determine the utility and veracity of the model and to determine what modeled processes need to be improved upon or included in future model versions [*Heald et al.*, 2011; *Heald et al.*, 2012; *Jung et al.*, 2010]. Organic aerosols are particularly difficult to correctly represent in CTMs due to their many sources, highly complex composition and variability in properties such as hygroscopicity and volatility. Historically, modeled organic aerosol mass has been severely underrepresented in chemical models [*Heald et al.*, 2005; *Volkamer et al.*, 2006]. Although more recent model developments have strived to better represent organic aerosol formation and volatility characteristics [*Fountoukis et al.*, 2011; *Fuzzi et al.*, 2006], correctly modeling organic aerosol concentrations and properties remains a problem in chemical models [*Ward and Cotton*, 2011a]. The data presented in this dissertation should be specifically useful in contributing to the continued improvement of organic aerosol representation in models. Both the field and laboratory data shown here focus on predominantly organic aerosol and should help to constrain and validate the modeled regional concentrations, size distributions, hygroscopicity and volatility of these particles.

1.3. Why the mountains of Colorado and Wyoming?

The field measurements presented in this work were all made in remote, high altitude locations in Colorado and Wyoming. These areas represent a unique and interesting environment, and given the typically clean conditions, may be particularly sensitive to changes in aerosol concentrations and properties. While the examples above motivate the general need for high-quality, in-situ measurements of aerosol concentration and properties for model development and validation, aerosol measurements in the mountain areas of the Western US are also important and useful for several specific reasons. First, studies have shown that the Eastern slope of the Rocky Mountains is a particularly favorable location for the formation of Mesoscale Convective Systems (MCS) [*Augustine and Caracena*, 1994; *Fritsch et al.*, 1986; *Maddox*, 1980; *Tucker and Crook*, 1999]. These large, organized systems are important for providing precipitation to areas of the central US, east of the Rocky Mountains. Rain from MCSs can account for up to 70% of warm season precipitation in this region [*Fritsch et al.*, 1986] and years with particularly high or low MCS activity have been linked to flooding and drought in the central US [*Ashley et al.*, 2003]. Recent model studies have shown that changes in aerosol concentrations affect modeled microphysical properties, such as cloud and rain droplet size and concentrations, in MCSs [*S S Lee*, 2012; *Xie and Liu*, 2011]. Correctly modeling MCSs, and their downwind impacts on local precipitation requires a good understanding of the conditions under which they form and develop. Measurements of aerosol properties in the typical formation regions, therefore, should be useful.

As well as affecting precipitation downwind, aerosol loading in the mountain regions may be important for local precipitation [*Jirak and Cotton*, 2006; *Ward and Cotton*, 2011b]. Orographic clouds, created by topographically forced upward motion, have been shown to be an

important contributor to winter snow in the mountains of Colorado, a main source of water year-round in this region [*Saleeby and Cotton*, 2005; *Saleeby et al.*, 2011]. Increased concentrations of cloud nucleating aerosol are expected, based on model results, to decrease the precipitation efficiency of orographic clouds, due to decreased riming of ice crystals passing through the super cooled liquid water layer, resulting in shifts in precipitation from windward to leeward slopes, and potentially into different watersheds [*Borys et al.*, 2000; *Cotton et al.*, 2009; *Saleeby and Cotton*, 2005; *Saleeby et al.*, 2011; *Saleeby et al.*, 2009; *Ward and Cotton*, 2011b]. However, the models used in these studies had to be initialized with assumed or modeled aerosol compositions and size distributions, in the absence of measured data. Measured aerosol properties in these mountain regions would be useful in realistically representing the effects of aerosols on precipitation in this area.

Finally, many regions in the Western US fall under the jurisdiction of the Regional Haze Rule, part of the Clean Air Act, mandating assessment and improvement of visibility in federally protected Class I areas such as national parks and wilderness areas [*Malm et al.*, 2004; *Watson*, 2002]. In 1988 the Interagency Monitoring of Protected Visual Environments (IMPROVE) network was established to measure the aerosols responsible for visibility reduction in Class I areas. A large number of these sites are located in the mountains of the western US, highlighting the importance of this area [*Malm et al.*, 2004; *Malm et al.*, 1994]. As well as continuous monitoring from the IMPROVE network, many intensive field campaigns have focused on measuring visibility impairing aerosols in the western US [*Carrico et al.*, 2005; *Hand and Kreidenweis*, 2002; *Hand et al.*, 2002; *Levin et al.*, 2009; *Malm and Day*, 2000; *McMeeking et al.*, 2005a; *McMeeking et al.*, 2005b; *McMeeking et al.*, 2006]. The Rocky Mountain Atmospheric Nitrogen and Sulfur (RoMANS) studies, discussed in Chapter 2, were part of this

effort to determine the concentration, composition and characteristics of aerosols which could be impacting visibility in Rocky Mountain National Park (RMNP). Data from some of these intensive measurement campaigns have been used in back-trajectory and receptor models to determine the sources most responsible for increased aerosol concentrations in these protected areas [*Gebhart et al.*, 2001; *Gebhart et al.*, 2006; *Gebhart et al.*, 2011; *Pitchford et al.*, 2005; *Schichtel et al.*, 2005]. The data I present in this work could also be useful for this purpose.

1.4. IMPROVE measurements

Data from the IMPROVE network provides a useful picture of typical aerosol conditions in the regions focused on in this work. Figure 1.1, from *Malm et al.* [2004], shows annually averaged maps of $PM_{2.5}$ organic and sulfate aerosol mass concentrations. The mountainous areas of the central US are distinct from other regions in Figure 1.1 as they have some of the lowest measured mass concentrations, although some regions of the northwest US also have similarly low sulfate concentrations. The generally clean conditions in these areas are due, partly, to low population density and large areas of uninhabited and uncultivated land. Assessing current conditions in these remote areas is very important if population increases lead to increased levels of anthropogenic pollution in the future.

Seasonal cycles of $PM_{2.5}$ mass composition in three mountainous regions of the western US are shown in Figure 1.2 [*Malm et al.*, 2004]. The Central Rockies region is most representative of the measurement sites discussed here, but the other regions are included for comparison. In all three regions, there is an increase in aerosol $PM_{2.5}$ organic and sulfate mass from a winter minimum to a maximum in summer, or early fall. In the Northern Rockies region

there are actually two peaks in organic mass, in May and August/September, corresponding to periods of prescribed burning and wildfires in the northwestern US. In the Colorado Plateau and Central Rockies regions there is an increase in soil concentrations in the spring, likely due to long range Asian dust transport [*Malm et al.*, 2004].

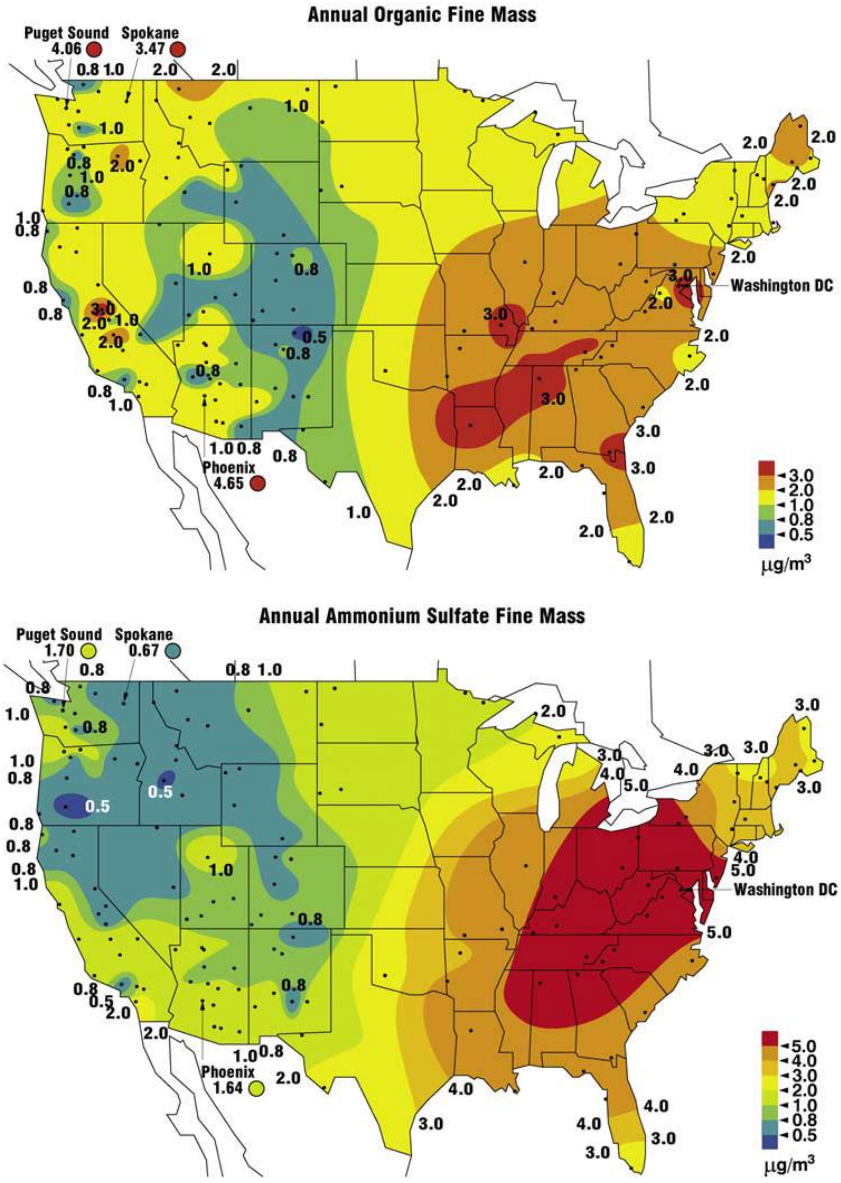

Figure 1.1 Maps of $PM_{2.5}$ organic and sulfate aerosol mass concentrations from IMPROVE network measurements. Taken from *Malm et al.* [2004].

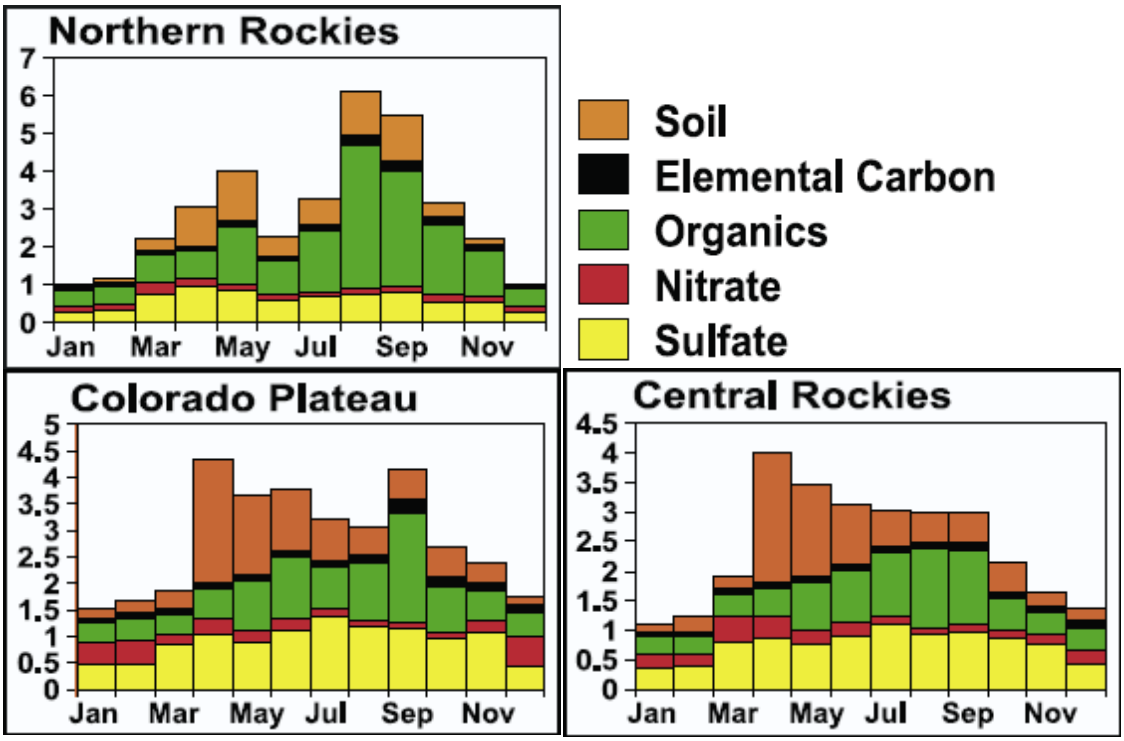

Figure 1.2 Seasonal cycles of aerosol $PM_{2.5}$ mass compositions averaged over three regions. Data are from IMPROVE network measurements; y-axis units are [μg m^{-3}]; figure from *Malm et al.* [2004].

To further examine the organic fraction of the Rocky Mountain regional aerosol, *Schichtel et al.* [2008] analyzed filters from the IMPROVE network for ^{14}C. Their objective was to develop a better understanding of the relative contributions of fossil (anthropogenic) and modern (largely biogenic) carbon to total carbonaceous aerosol. Total carbon (TC) aerosol includes both organic (OC) and elemental carbon (EC), although as shown in their paper the ratio of EC to TC at Rocky Mountain National Park was on the order of 0.1 – 0.2. Based on their findings, in the Rocky Mountain region it is likely that over 90% of the total carbon aerosol was from contemporary sources during the summer (Figure 1.3). While *Schichtel et al.* [2008] observed an increased importance of anthropogenic sources to TC in the winter, contemporary sources were still dominant (>75% of the carbon aerosol). Based on these previous findings

biogenically-derived organic carbon is likely a major contributor year-round to the aerosol measured during the studies presented here, but with its relative contribution to aerosol mass concentrations increasing in the summertime.

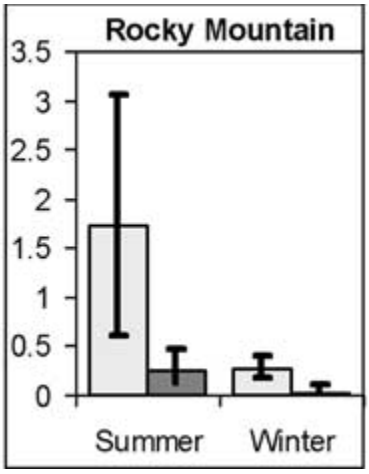

Figure 1.3 Modern (light bars) and fossil (dark bars) carbon averaged over the summer and winter months in Rocky Mountain National Park. Data are from IMPROVE network measurements; y-axis units are [μg m^{-3}]; figure from *Schichtel et al.* [2008].

1.5. Dissertation layout

In this dissertation I present data collected during three field campaigns located in the mountains of Colorado and Wyoming as well as data from a laboratory biomass burning experiment. The field campaigns were: the Rocky Mountain Atmospheric Nitrogen and Sulfur (RoMANS) studies, the Grand Teton Reactive Nitrogen Deposition Study (GrandTReNDS) and the Bio-hydro-atmosphere interactions of Energy, Aerosols, Carbon, H_2O, Organics & Nitrogen (BEACHON) project. The laboratory study was the third Fire Laboratory at Missoula Experiment (FLAME 3). While all four studies were related to aerosol properties, the specific focus of each was different, and the data collected were targeted at the specific project goals. In

Chapter 2 I present aerosol size distributions and concentrations. Chapter 3 focuses on aerosol hygroscopicity and chemical composition. Chapter 4 discusses the volatility distribution of organic material from biomass combustion. Each chapter presents specific motivation for the projects discussed therein as well as descriptions of measurement locations and methodology (instrument descriptions are in Appendix 1). Specific conclusions are also given in each chapter. I present general conclusions and recommendations for future work in Chapter 5.

The goal of this work is to develop a better understanding of aerosol properties in the mountains of Colorado and Wyoming. Specifically I seek to:

1. Present typical aerosol number and volume concentrations and size distributions as well as seasonal cycles and the factors that influence these properties
2. Determine aerosol chemical composition and hygroscopicity and their importance to CCN concentrations
3. Determine the volatility distribution for organic material from biomass combustion

A good understanding of these properties is necessary to constrain the aerosol assumptions used for model initialization, for testing model results and for realistically describing aerosol behavior in models. These data and results should help to improve our understanding of aerosol properties in the Mountains of Colorado and Wyoming and allow for more realistic modeling of these aerosols and their effects on precipitation, visibility and climate.

2. Aerosol size distributions and concentration

2.1. Introduction and background

Of all factors influencing the impacts of atmospheric aerosols on air quality, clouds, global radiative balance, human and environmental health and visibility, the number and size of particles are likely the most important [*Luo and Yu,* 2011, and references therein]. Mass concentrations of particulate matter (PM) smaller in aerodynamic diameter than 2.5 μm ($PM_{2.5}$) and 10 μm (PM_{10}) are regulated under the Clean Air Act, as part of the National Ambient Air Quality Standards (NAAQS), since increased exposure to PM has been linked with increased respiratory and cardiac illness and other health problems as well as higher mortality rates [*Colburn and Johnson*, 2003; *Kunzli et al.*, 2000; *Mehta et al.*, 2012; *Perez et al.*, 2010]. These health impacts have been observed at all aerosol concentrations, highlighting the importance of knowing aerosol concentrations even in relatively clean environments.

Aerosols scatter and absorb light and can alter the amount of solar radiation absorbed and reflected by the atmosphere and reaching the surface, leading to changes in global albedo, atmospheric lapse rates and surface heating [*Andreae et al.*, 2004; *Charlson et al.*, 1992; *Hansen et al.*, 1997; *Pilinis et al.*, 1995; *Ramanathan et al.*, 2001; *Trenberth and Fasullo*, 2009]. Aerosol optical properties also impact visible range with increased aerosol concentrations contributing to visibility degradation [*Cabada et al.*, 2004; *Hand and Malm*, 2007; *Malm et al.*, 2004; *Pitchford et al.*, 2007; *Watson*, 2002]. Under the Regional Haze Rule, also part of the Clean Air Act, all federal Class 1 areas, such as national parks and wilderness areas, are required to return visibility to natural levels by 2060 [*Malm and Hand*, 2007]. Both aerosol size and number contribute to visibility degradation [*Levin et al.*, 2009; *Malm et al.*, 2009].

The number of aerosol particles available to serve as cloud condensation nuclei plays a large role in the development, characteristics and lifetimes of clouds and precipitation [*Albrecht*, 1989; *Lerach and Cotton*, 2012; *Lerach et al.*, 2008; *Ramanathan et al.*, 2001; *Twomey*, 1974; *van den Heever et al.*, 2011; *Ward et al.*, 2010]. Clouds play an important role in governing global radiative balance and changes in cloud properties, lifetimes and distributions affect both incoming and outgoing radiation, and will thus have impacts on global surface temperature and climate [*Clement et al.*, 2009; *Trenberth and Fasullo*, 2009; *Trenberth et al.*, 2009]. The effects of aerosols on clouds will be discussed further in the next chapter.

Finally, aerosol transport and deposition can transfer bio-available nitrogen, and other key nutrients such as iron, to various nutrient limited environments [*Beem et al.*, 2010; *Fenn et al.*, 2003]. Many remote, high altitude environments are nitrogen limited and any increase in nitrogen inputs, which are primarily from anthropogenic sources, could cause changes in biodiversity and ecosystem health in these areas [*Baron et al.*, 2000]. Since wet deposition is an important route for deposition of aerosol species to the earth's surface, it is important to develop a good understand of the incorporation of particulate matter into precipitation, including via cloud nucleus scavenging.

The above examples motivate the need for measurements and modeling of aerosol number concentrations, size distributions, and cloud nucleation activity on local to global scales. However, due to the non-routine nature of the associated measurements, automated network observations are not available, particularly in remote ecosystems where atmospheric processes may be especially sensitive to variations in aerosol properties. The approach taken in this work is to conduct longer-term (months to year) observations at remote sites, to characterize variability

on seasonal and annual scales, and to develop relationships that can be used to drive or validate models.

In this chapter I present aerosol size distribution and concentration data from two Rocky Mountain Atmospheric Nitrogen and Sulfur studies (RoMANS 2, Nov 2008 – Nov 2009 and RoMANS 2010, May – Sep 2010) and from the Grand Teton Reactive Nitrogen Deposition Study (GrandTReNDS, July – Sep 2011). The main goal of these studies was to investigate nitrogen deposition in Rocky Mountain and Grand Teton National Parks. These highly sensitive ecosystems could potentially be impacted by anthropogenic pollution, especially from urban emissions and agricultural practices upwind. Both of these study areas fall under the mandate of the Regional Haze Rule, and, thus visibility degradation is also a concern. As part of these studies I operated an aerosol sizing system which measured size dependent aerosol number concentrations of particles with diameters between 0.04 and 20 μm. These data are helpful in determining the role of aerosols in nitrogen deposition [*Beem et al.,* 2010, *Benedict et al.*, 2012 (in review)] and visibility reduction [*Levin et al.*, 2009; *Malm et al.*, 2009] and also provide estimates of typical aerosol size distribution parameters for high altitude, continental conditions, key inputs to modeling studies which are focused on aerosol impacts in the mountain regions of Colorado and Wyoming [e.g. *Ward and Cotton*, 2011b, *Saleeby and Cotton*, 2005; *Saleeby et al.,* 2011; *Saleeby et al.,* 2009].

2.2. Measurement site locations and wind characteristics

Figure 2.1 shows the location of the main RoMANS (lat 40.28˚ N, lon 105.55˚ W) and GrandTReNDS (lat 43.78˚ N, lon 110.94˚ W) measurement sites as well as the BEACHON (lat

39.10˚ N, lon 105.10˚ W) site which is the focus of the next chapter. During both the RoMANS and GrandTReNDS studies, aerosol and gas species were also measured at a number of ancillary sites around the main site which are not shown on the map. The main measurement site for the two RoMANS studies, where the aerosol sizing instruments were located, was on the eastern side of Rocky Mountain National Park (RMNP) at an elevation of 2750 m. This site was previously used during RoMANS 1 [*Beem et al.*, 2010; *Levin et al.*, 2009; *Malm et al.*, 2009] which occurred during two phases in the spring (23 March – 30 April) and summer (6 July – 12 August) of 2006. The RoMANS main site was collocated with an Interagency Monitoring of Protected Visual Environments (IMPROVE) site which has been in operation since 1988 as well as a Clean Air Status and Trends Network (CASTNet) site. The RoMANS site was located roughly 8 km south of Estes Park CO, a popular summer tourist location. The site bordered a summer camp and was a few hundred meters from CO HW 7, so some local emissions could have impacted the measurements at this location. Because I am interested in regional aerosol characteristics, time periods with obvious impacts from local emissions, specifically campfires, were removed. These time periods were identified as described in Appendix 1.

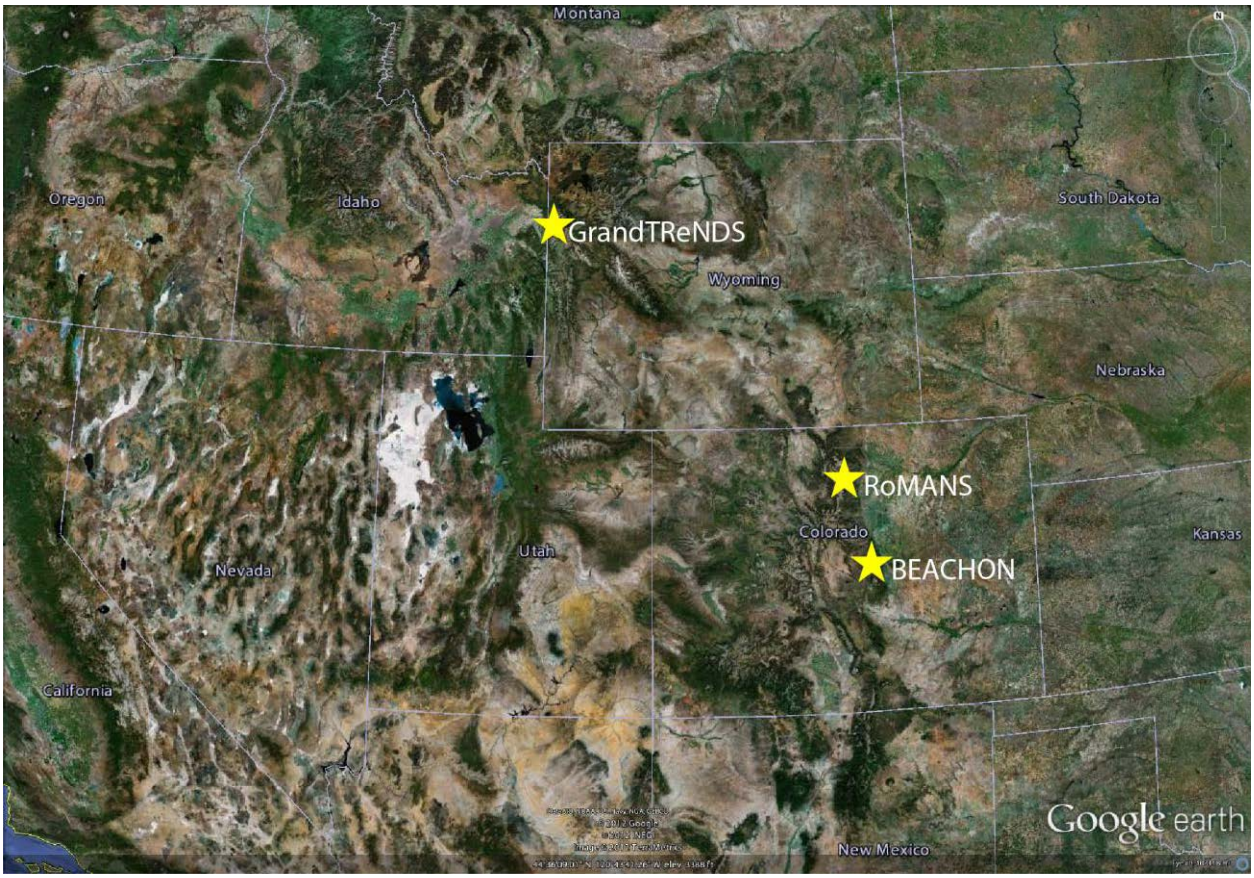

Figure 2.1 Map showing the locations of the RoMANS, GrandTReNDS and BEACHON measurement sites.

Seasonally averaged (2008 – 2011) 500 mb winds over the continental US from the North American Regional Reanalysis (NARR) are shown in Figure 2.2. During all seasons, upper air, synoptic scale flow over Colorado and Wyoming was predominately westerly with a shift towards the southwest in the summer. This shift is due to the monsoonal circulation in the southwestern US and Mexico [*Douglas et al.*, 1993]. There was also a seasonal shift in upper air wind speed with generally weaker flow during the summer (note the different color bar scales). Because of this decreased synoptic scale forcing, local thermally driven circulations, such as mountain valley winds, are more important in the summer [*Abbs and Pielke*, 1986].

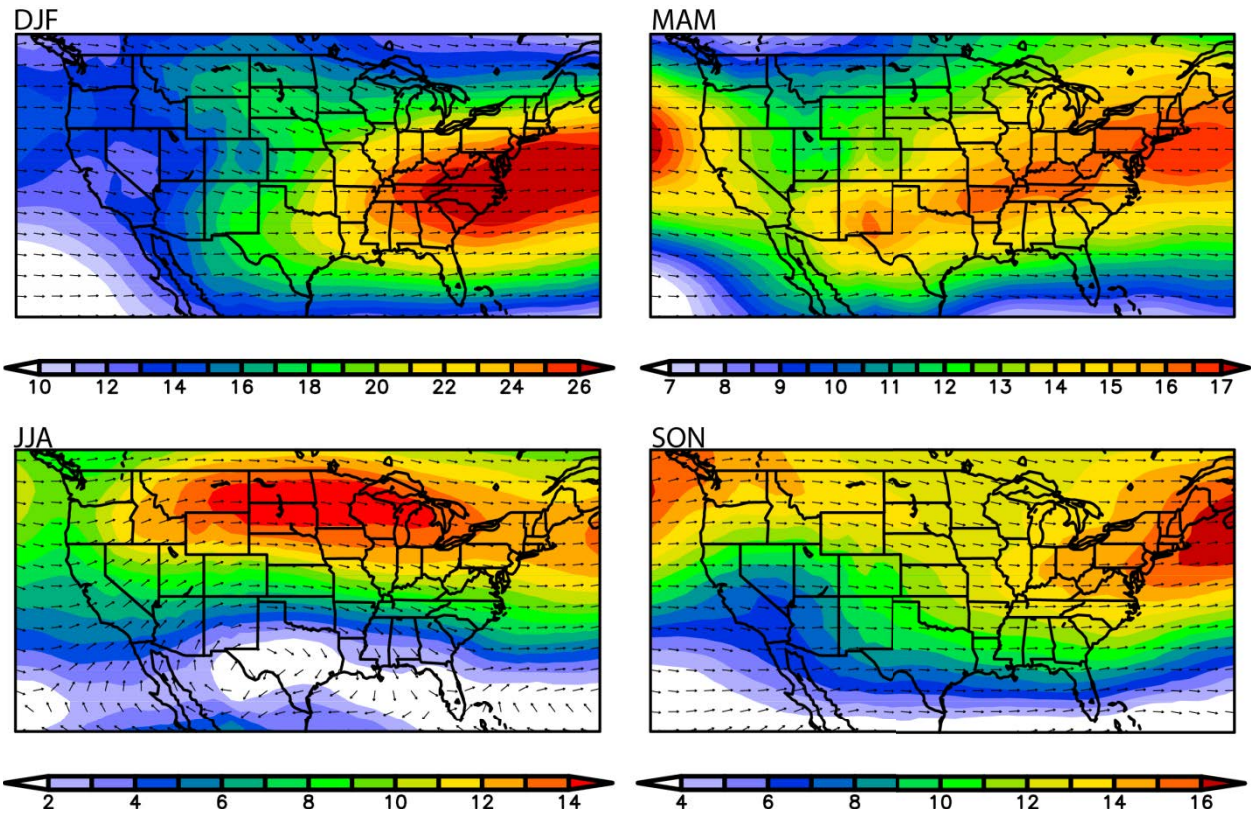

Figure 2.2 Seasonally averaged 500 mb wind speed and direction over the continental US. Data are from the NARR (www.esrl.noaa.gov/psd/data/gridded/reanalysis/). Color bar units are m/s.

Although surface winds are influenced and channeled by topography, they are also influenced by the synoptic scale flows shown above [*Abbs and Pielke*, 1986]. Surface winds at the RoMANS site came predominantly from the west to northwest, although a diurnal shift due to a mountain valley circulation was often observed with upslope winds coming from the southeast in the afternoon. There was also some seasonality to both surface wind speed and direction, shown by the wind roses in Figure 2.3. The fastest winds were measured during the winter months and were always from the west, consistent with the stronger westerly flows at 500 mb (Figure 2.2). During the other seasons, there was less variability in wind speed. Surface winds, however, can be strongly influenced by topography, especially in mountainous areas with

complex terrain. Therefore, these data may not represent larger scale circulation, and the origins of air masses impacting the site. To better understand large scale flow in the area, I examined National Weather Service sounding data from the Denver CO station (station number 72469). This site is located ~80 km southeast of the RoMANS site, but is the closest location with regular sounding data. Soundings are taken at this site daily at 0z and 1200z. Figure 2.4 shows seasonal wind roses for 700 mb winds at the Denver station. Similar to the surface winds at the RoMANS site, these upper air data also show a strong westerly component of the wind in the winter, and more variability in wind direction in the summer. The greater variability seen in the upper air data versus surface measurements could be the result of topographical forcing of the surface winds into certain flow channels. Thus, while some of the wind, and transport, characteristic determined from surface wind data may be influenced by larger scale flow, it is highly likely that local topography is also impacting these measurements.

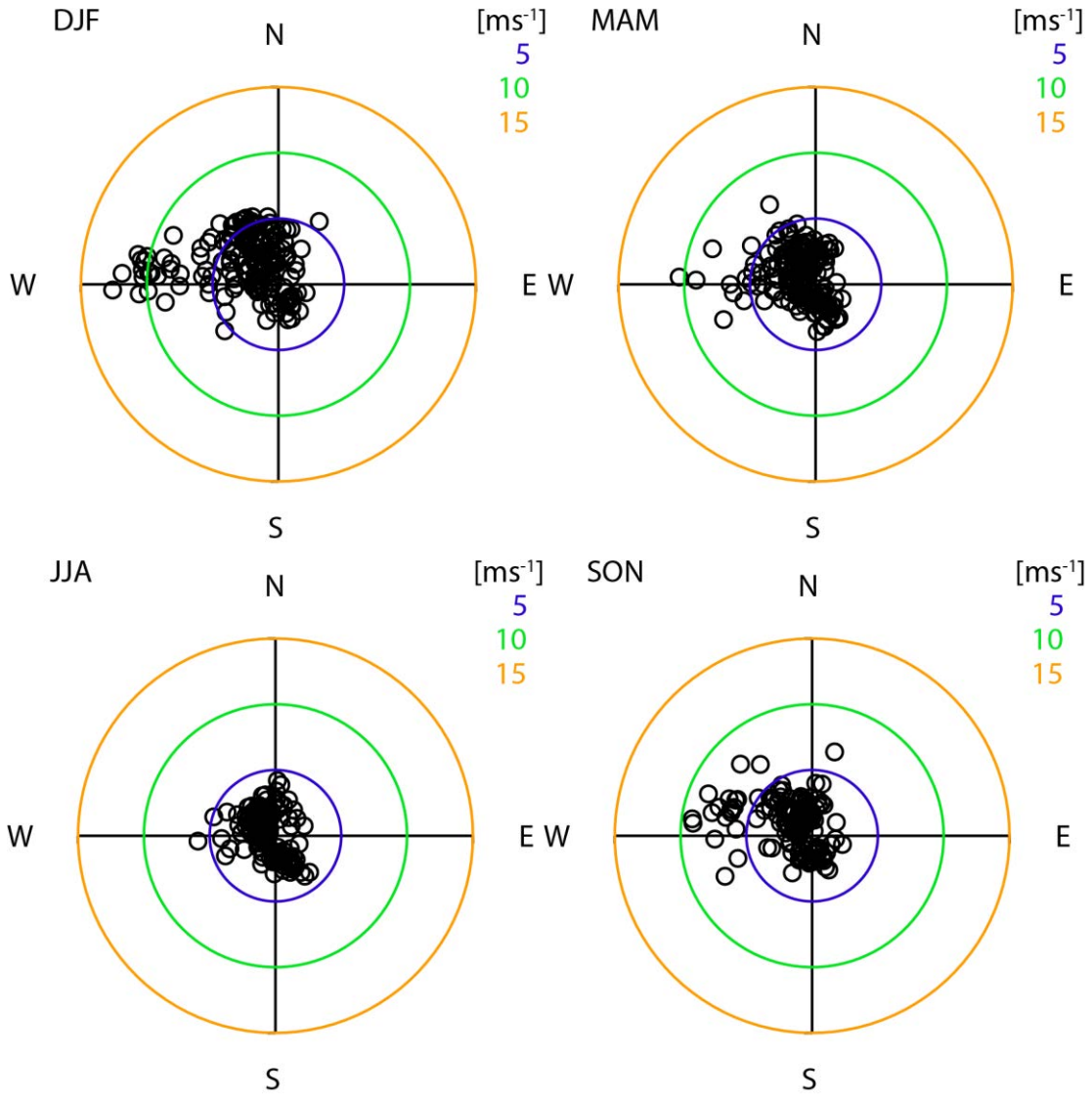

Figure 2.3 Hourly averaged, seasonal surface winds at the RoMANS site during the yearlong RoMANS 2 time period. Distance from the origin indicates wind speed.

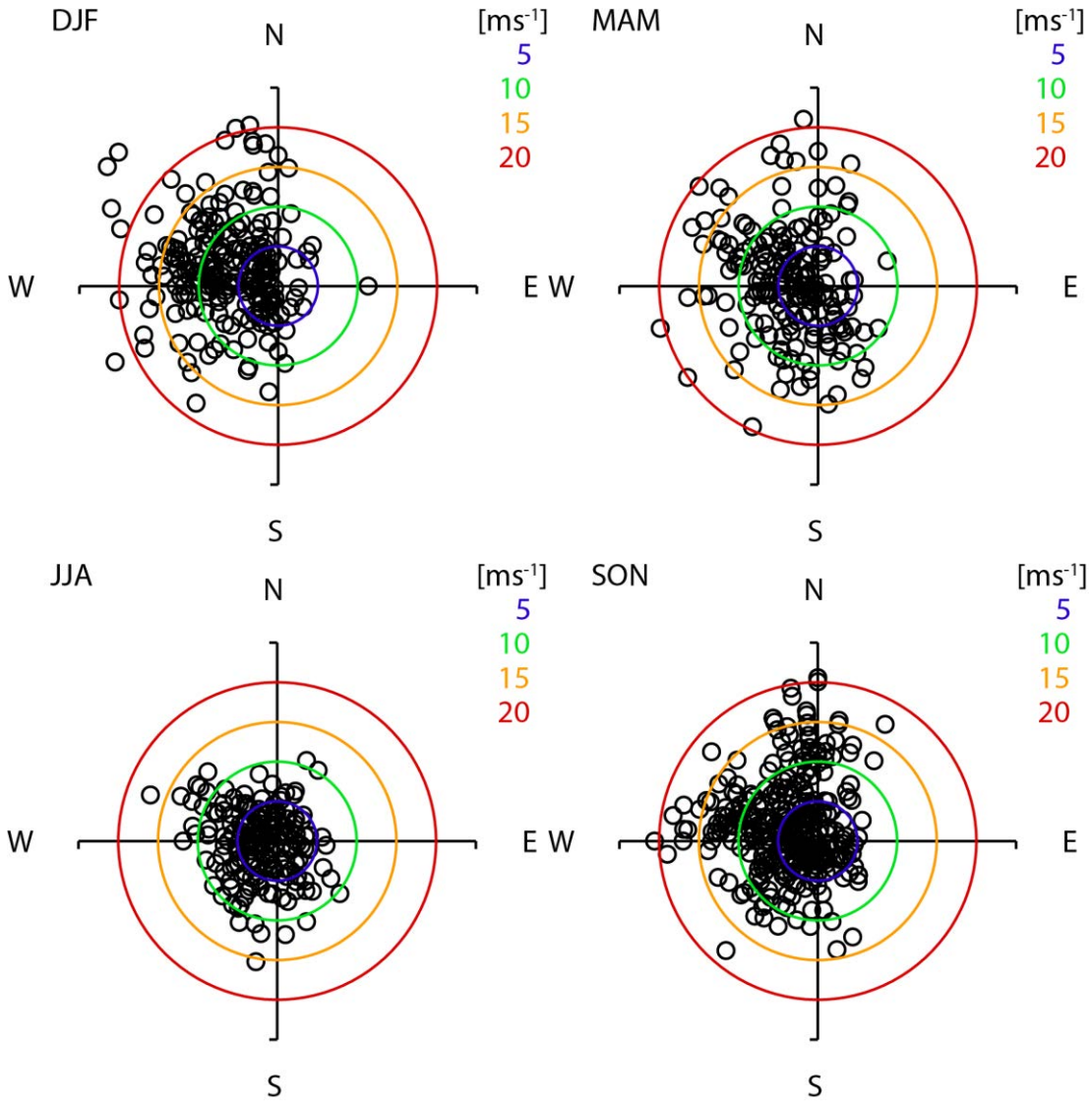

Figure 2.4 Seasonal 700 mb winds at Denver, CO during the yearlong RoMANS 2 time period. Distance from the origin indicates wind speed. Soundings were taken daily at 0z and 1200z.

The potential influence of pollution sources on the measurements made at the RoMANS site as a function of wind speed and direction is illustrated by Figure 2.5 which shows NO_x concentrations measured during the year-long RoMANS 2 study plotted versus wind speed and colored by wind direction. There appears to be two main modes of surface winds at the site, corresponding to the mountain and valley winds. Westerly and northerly winds were generally

associated with much cleaner air masses (lower NO_x), as these air masses came from, or passed over, the remote regions of RMNP. Southerly and easterly winds generally had higher NO_x concentrations, likely due to pollution from the much more populated Front Range region. Figure 2.6 shows a wind rose of the lowest (blue) and highest (red) 5% of NO_x concentrations measured during RoMANS 2. The highest NO_x concentrations were clearly associated with southeasterly winds, while low NO_x was generally associated with westerly and northerly winds, further highlighting the impact of local winds on potential pollution concentrations at the RoMANS site.

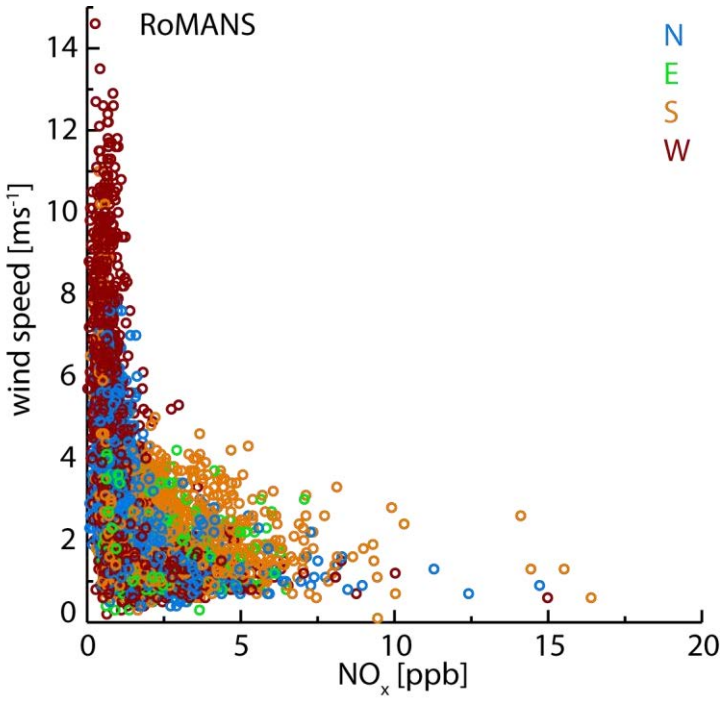

Figure 2.5 NO_x concentrations measured during RoMANS 2 versus wind speed and colored by wind direction.

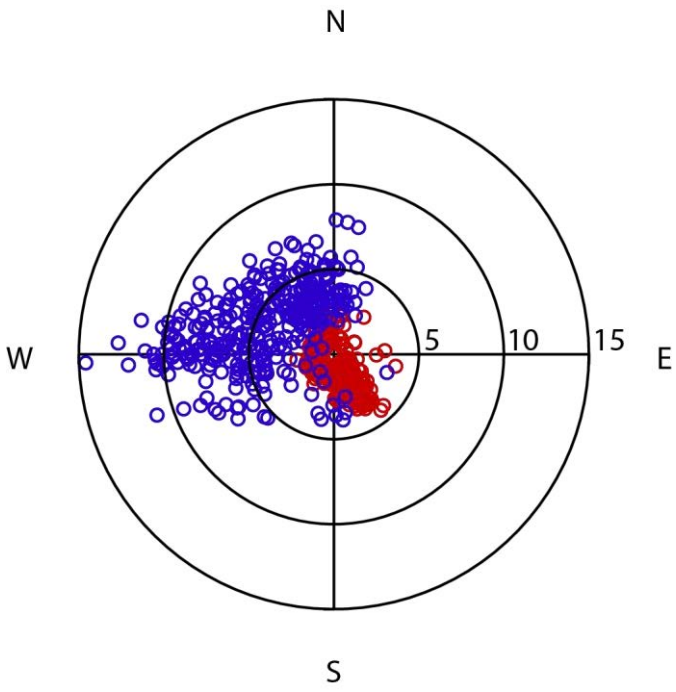

Figure 2.6 Wind rose of 5th (blue) and 95th (red) percentile NO_x concentrations during RoMANS2. Distance from the origin is wind speed [m s^{-1}].

The main GrandTReNDS site was located on the western side of Grand Teton National Park (GTNP) at the top of Grand Targhee ski resort (elevation = 2711 m). To the west of the site was the Snake River Valley, ID, a large agricultural area (Figure 2.8). The GrandTReNDS site was roughly two miles from the closest public road or inhabited building. Aside from a few weekend festivals, the ski resort was only lightly used by hikers and mountain bikers during the GrandTReNDS study period.

Surface winds at the GrandTReNDS site (Figure 2.7) ranged from southeasterly to southwesterly, with winds rarely coming from any northerly direction. This lack of surface winds from the north was probably due to the local topography. A low topographical ridge loacted a few hundred meters north of the measurement site likely acted as a wind break for any surface winds coming from that direction. Figure 2.8 shows the locations of the two closest

National Weather Service sites with regular sounding data: Boise, ID (BOI, station number 72681) and Riverton, WY (RIW, station number 72672). While the Riverton site is closer, about 220 km from the GrandTReNDS site, it is located on the eastern side of the Wind River mountain range which likely influences local winds. The Boise station is located 430 km west of the GrandTReNDS site at the western end of the Snake River Valley. Figure 2.9 shows wind roses of 700 mb winds measured at at the BOI and RIW sites. Both of these wind roses show a predominantly westerly flow, as expected from 500 mb analysis (Figure 2.2), with more variability in the Boise data. Neither of these locations show as strong of an easterly or southeasterly component of the wind, as was observed in the GrandTReNDS surface data. Therefore, perhaps the easterly winds measured at the GrandTReNDS site were more influenced by local circulations than by the larger scale flow.

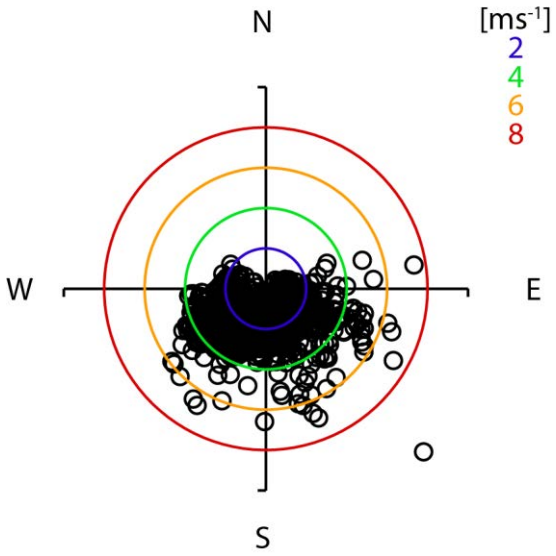

Figure 2.7 Surface winds at the GrandTReNDS site. Distance from the origin indicates wind speed.

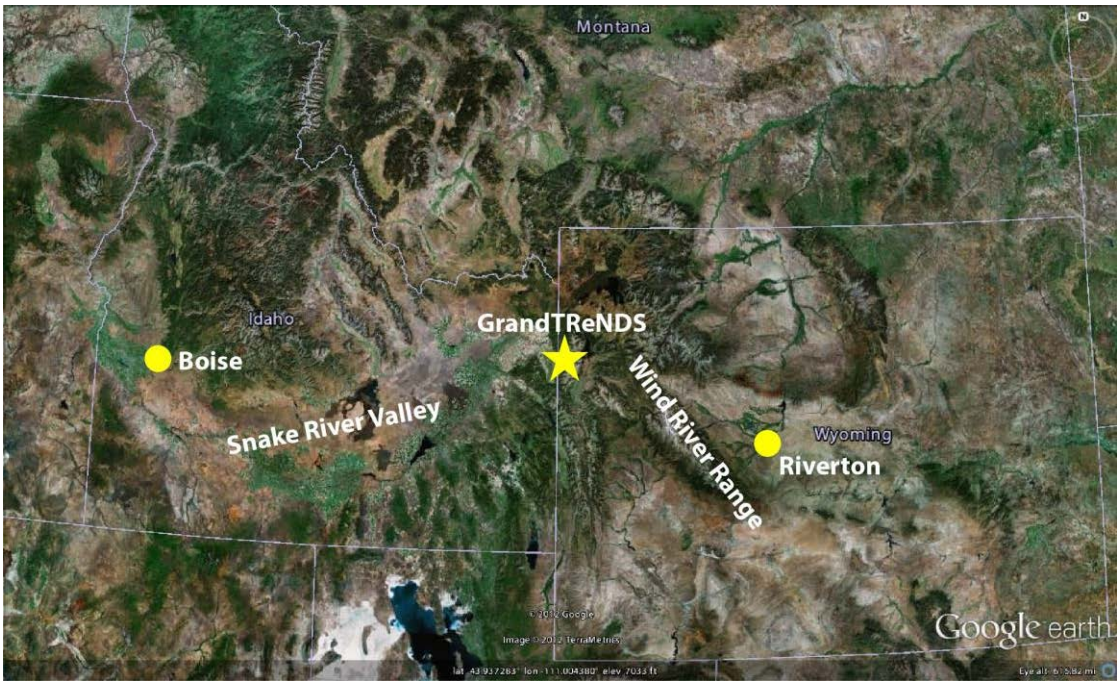

Figure 2.8 Locations of the two NWS sounding sites closest to the GrandTReNDS site.

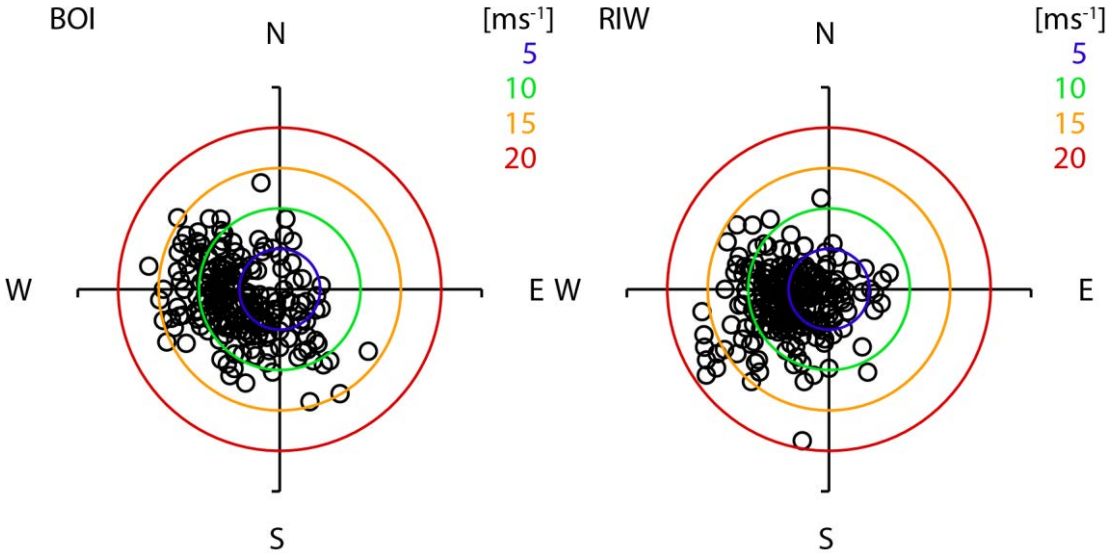

Figure 2.9 700 mb winds at Boise, ID and Riverton, WY measured during the GrandTReNDS time period. Distance from the origin indicates wind speed. Soundings were taken at 0z and 1200z.

Figure 2.10 shows NO_x concentrations measured during GrandTReNDS versus wind speed and colored by wind direction. During this study, westerly and southerly winds were generally associated with slightly higher NO_x than those from the east, although these values were very low and variable during GrandTReNDS (Figure 2.10). Winds from the east generally came from GTNP, and other uninhabited mountainous and wilderness areas, and thus are expected to have low impact from anthropogenic pollution. However, unlike the RoMANS study location, there is no clear relationship between wind direction and speed and NO_x concentration. The wind rose of the highest and lowest 5% of NO_x concentrations shown in Figure 2.11 also shows little relationship between wind direction and potential pollution impacts.

To better examine the origins of air masses impacting the GrandTrends site, Figure 2.12 shows three day back-trajectory residence time analysis using the Hybrid Single Particle Lagrangian Integrated Trajectory (HYSPLIT) model [*Draxler*, 1999; *Draxler and Hess*, 1997; 1998] and the Global Data Assimilation System (GDAS) one degree meteorological data set. This analysis shows that air masses impacting the GrandTReNDS site during the study period came predominantly from the west and southwest (consistent with upper air wind data). There was a seasonal shift in air mass back trajectory with a larger fraction of air masses originating to the south, in Utah, towards the later part of the study. This shift in back-trajectory origin is also consistent with the seasonal shift in monsoonal flow [*Douglas et al.*, 1993].

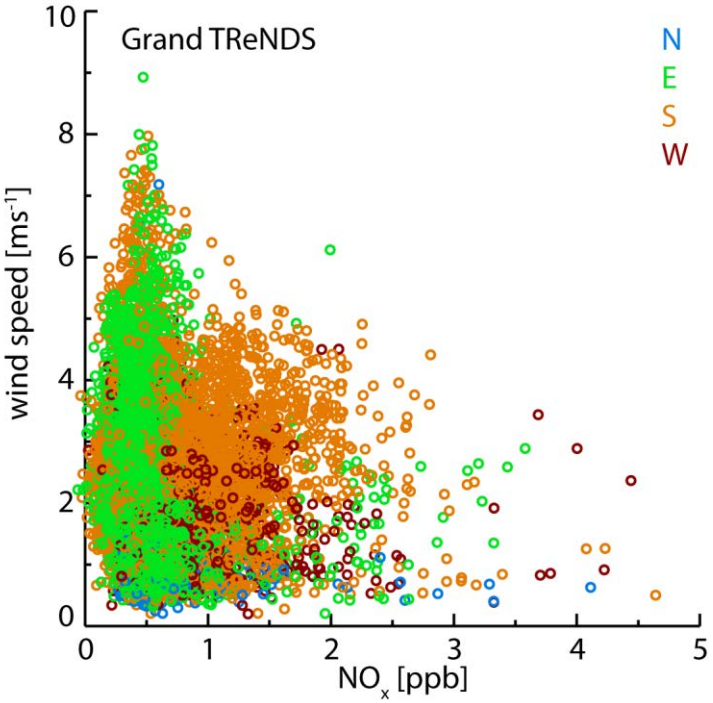

Figure 2.10 NO_x concentrations measured during GrandTReNDS versus wind speed and colored by wind direction.

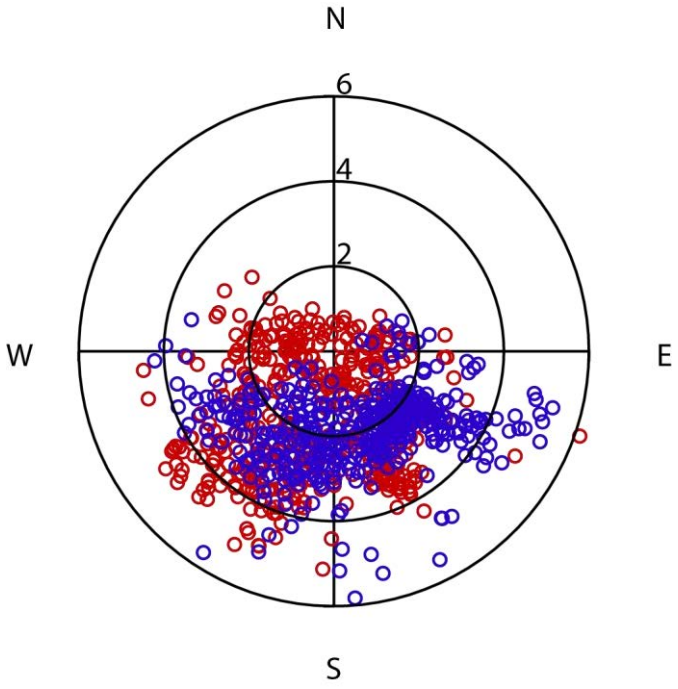

Figure 2.11 Wind rose of 5th (blue) and 95th (red) percentile NO_x concentrations during GrandTReNDS. Distance from the origin is wind speed [m s^{-1}].

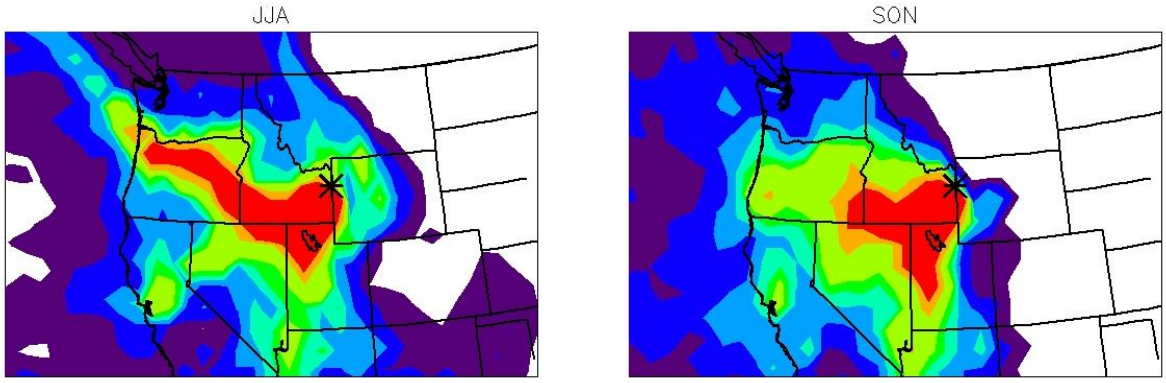

Figure 2.12 Seasonal Residence Time Analysis (RTA) for the GrandTReNDS receptor site based on 2010 HYSPLIT back-trajectories. Contours of 1° x 1° grid boxes indicate the relative average residence time of an air parcel in each grid box.

2.3. Results

2.3.1. Aerosol concentration

Figure 2.13 shows example aerosol number and volume distributions measured during RoMANS 2. By integrating across the entire measured size range (0.04 – 20 μm) I calculated total aerosol number and volume concentrations in this range during the three studies (Appendix 1 presents a description of the instruments, measurement strategy, data quality control and analyses methods used in this work). All measurements were made on dry aerosol, thus removing effects of relative humidity on the aerosol size distribution parameters. As seen in Figure 2.13, volume distributions were generally bi-modal with local minima in concentration between the two modes occurring, on average, at a diameter of 0.68 μm during RoMANS 2 and 0.72 μm during both RoMANS 2010 and GrandTReNDS. Therefore, as well as total volume concentrations I also calculated the volume concentrations in the fine and coarse modes using the measured minimum to compute the split for each measured distribution. Timelines of total

aerosol number and volume concentration are shown in Figure 2.14 and Figure 2.15. Figure 2.14 also includes published data from the first RoMANS study [*Levin et al.*, 2009] as well as the year-long BEACHON study [*Levin et al.*, 2012]. During BEACHON, aerosol concentrations and size distributions were measured across the diameter range 0.015 – 0.35 μm, extending to smaller sizes than the RoMANS and GrandTReNDS data but not measuring any of the coarse mode aerosol. To compare volume concentrations measured during BEACHON I plotted fine mode only volume concentrations for all studies in Figure 2.16. Median and standard deviation values, as well as the median fraction of total volume accounted for by the fine mode are summarized in Table 2.1. For RoMANS 2 and 2010 I also calculated median aerosol concentration values from July 27 – Sep 21, corresponding to the GrandTReNDS measurement period. These time periods are denoted GT in Table 2.1 and allow for more direct comparison among the studies, although of course the locations and years are different.

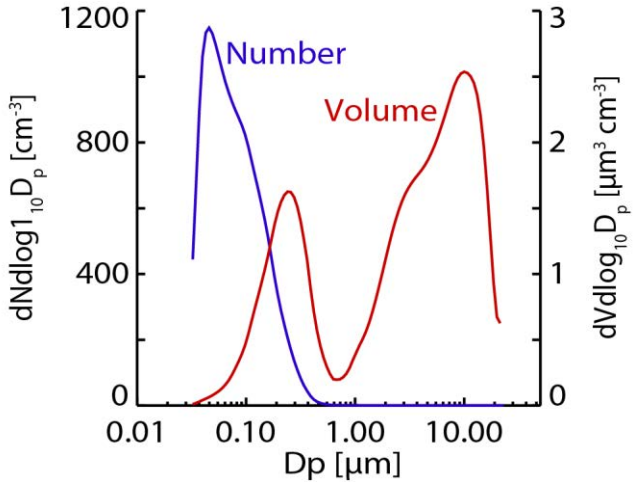

Figure 2.13 Example number (blue) and volume (red) distributions measured during RoMANS 2**.**

In all three figures of aerosol concentration (Figure 2.14 - Figure 2.16) there appears to be considerable coherence among measurements with data from all studies falling within a similar range and displaying similar seasonality, despite the spatial and temporal study differences. However, during the overlapping time periods, aerosol number, total volume and fine volume concentrations from each study were all statistically significantly different from each other using a two tailed T-test at a confidence level of, at least, 90%. The T-test determines whether the mean values from two samples could be representative of the same larger population. The statistically significant differences between each pair of measurements indicate that these data cannot be assumed to represent some regionally, and inter-annually, homogenous aerosol population, but that spatial and yearly variability exists. Therefore, while these data do provide useful constraints on typical aerosol concentrations in remote mountain areas, they should not be viewed as necessarily representative of the entire region during any given year. As noted in the introduction, the many sources and short lifetimes of aerosols lead to large temporal and spatial variability, making them difficult to model. The data presented here help to fill in some unknowns in aerosol characteristics, but, as always, more data would be useful in further constraining aerosol concentrations and properties. In the following sections I examine some of the spatial, annual and inter-annual variability in aerosol number and volume concentrations.

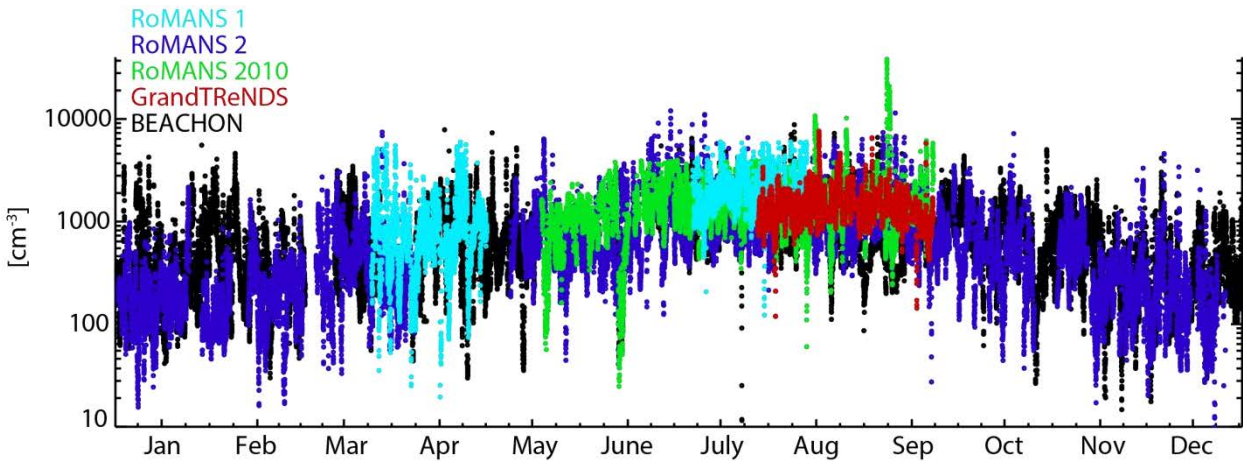

Figure 2.14 Total aerosol number concentration ($0.04 < D_p < 20$ µm) during RoMANS 1 (light blue), RoMANS 2 (blue), RoMANS 2010 (green), GrandTReNDS (red) and BEACHON (black). BEACHON data are for the size range ($0.015 < D_p < 0.35$ µm). Data points are every 15 min. Note that all studies occurred in different years but are plotted versus month of year.

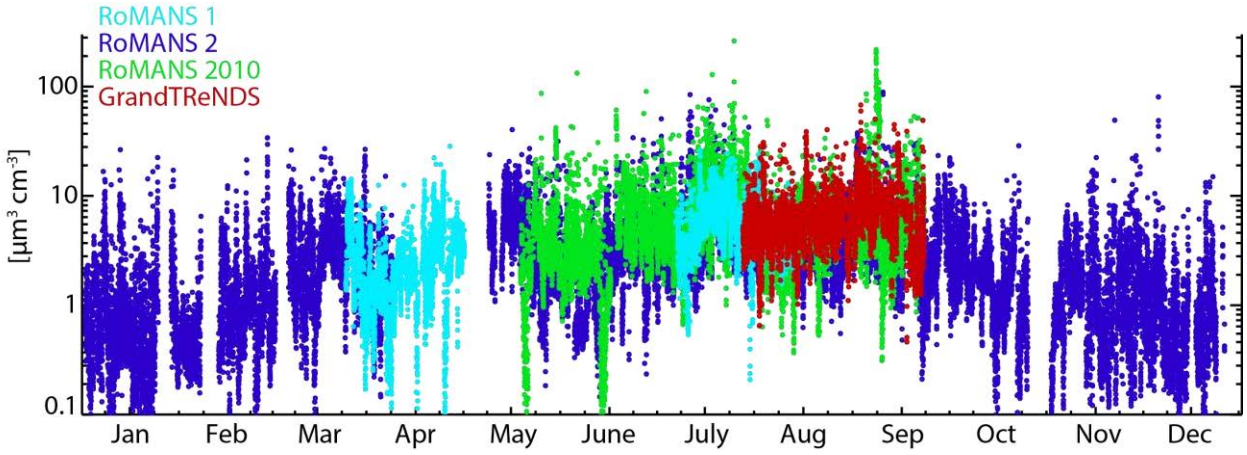

Figure 2.15 Total aerosol volume concentration ($0.04 < D_p < 20$ µm) during RoMANS 1 (light blue), RoMANS 2 (blue), RoMANS 2010 (green) and GrandTReNDS (red).

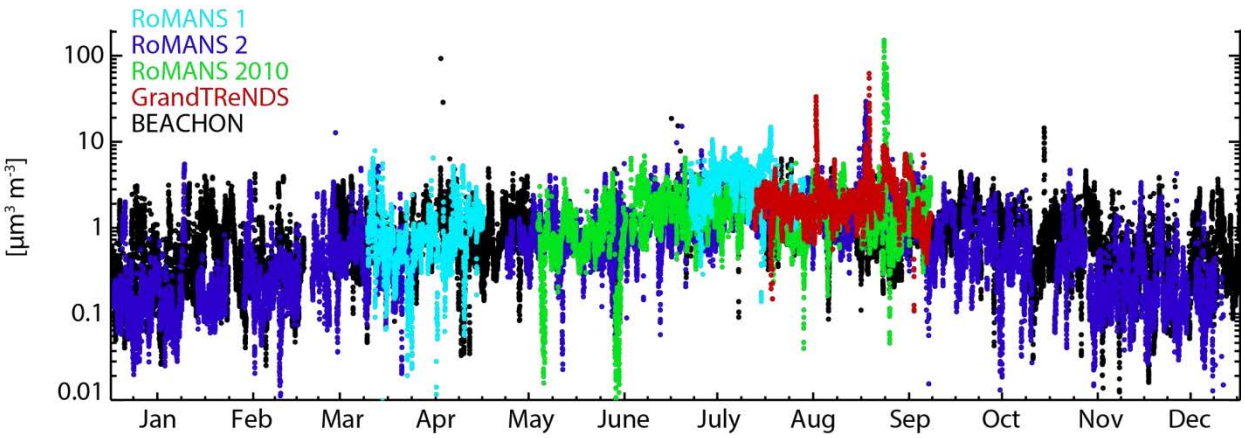

Figure 2.16 Fine mode aerosol volume concentration ($0.04 < D_p < \sim 0.7$ μm) during RoMANS 1 (light blue), RoMANS 2 (blue), RoMANS 2010 (green), GrandTReNDS (red) and BEACHON (black). BEACHON data are for the size range ($0.015 < D_p < 0.35$ μm).

Table 2.1 Median (± 1 standard deviation) number and volume concentrations and fine mode volume fraction during RoMANS 2, RoMANS 2010 and GrandTReNDS as well as published data from RoMANS 1 [*Levin et al.*, 2009]. Values are also shown for RoMANS 2 and 2010 during the time period corresponding to GrandTReNDS.

	N [cm^{-3}]	V [$\mu m^3\ cm^{-3}$]	Fine mode V fraction
RoMANS 2 (full study)	737 ± 772	3.30 ± 4.01	0.33 ± 0.20
RoMANS 2 (GT time)	1242 ± 857	5.03 ± 4.59	0.42 ± 0.15
RoMANS 2010 (full study)	1527 ± 1713	6.81 ± 10.4	0.31 ± 0.17
RoMANS 2010 (GT time)	1778 ± 2382	7.02 ± 12.3	0.32 ± 0.15
GrandTReNDS	1417 ± 605	6.70 ± 4.73	0.37 ± 0.15
RoMANS 1 (Spring)	880 ± 770	2.2 ± 2.6	-
RoMANS 1 (Summer)	2080 ± 940	6.5 ± 3.9	-

2.3.1.1. Spatial variability

To examine the spatial variability in aerosol concentrations more closely, I plotted histograms of aerosol number (Figure 2.17) and volume (Figure 2.18) concentrations for the RoMANS 2 and 2010 and GrandTReNDS studies over the GT time period (July 27 – Sep 21). As can be seen in Figure 2.17 measured aerosol number concentrations fell within a similar range at the GrandTReNDS and RoMANS locations, although, again the means were statistically different. The peak in GrandTReNDS number concentration frequency was close to that of the RoMANS 2010 studies, while the peak frequency in number concentration measured during ROMANS 2, during the GT time period, was slightly lower. Also, variability in number concentrations measured during GrandTReNDS was lower than during either of the RoMANS studies, indicated by the narrower histogram in Figure 2.17.

The peak frequency in aerosol volume concentrations measured during GrandTReNDS was higher than both RoMANS studies (Figure 2.18). The median volume concentration measured during GrandTReNDS (Table 2.1) was 5.7 $\mu m^3\ cm^{-3}$, while those for RoMANS 2 and RoMANS 2010 during the GT time period were 3.9 and 4.6 $\mu m^3\ cm^{-3}$ respectively. Higher volume concentrations during GrandTReNDS were observed in both the fine and coarse modes (Figure 2.19).

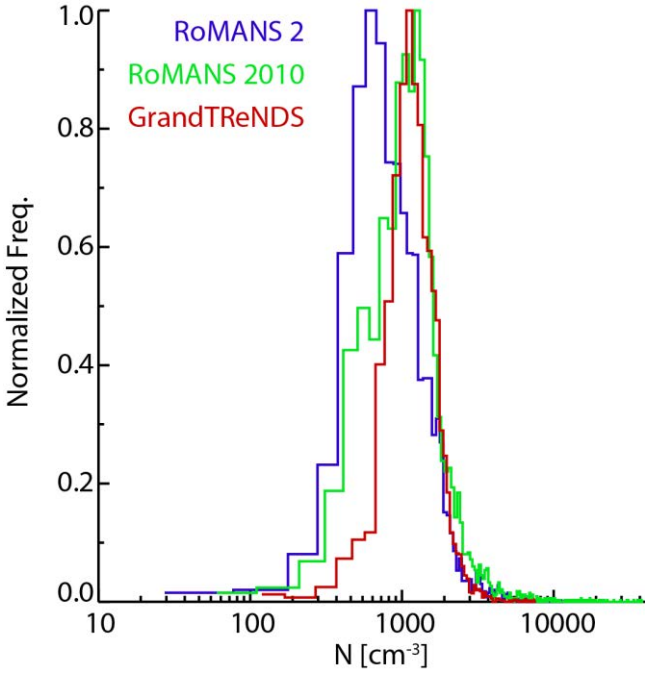

Figure 2.17 Normalized frequency of aerosol number concentrations ($0.04 < D_p < 20$ µm) during RoMANS 2 (blue), RoMANS 2010 (green) and GrandTReNDS (red).

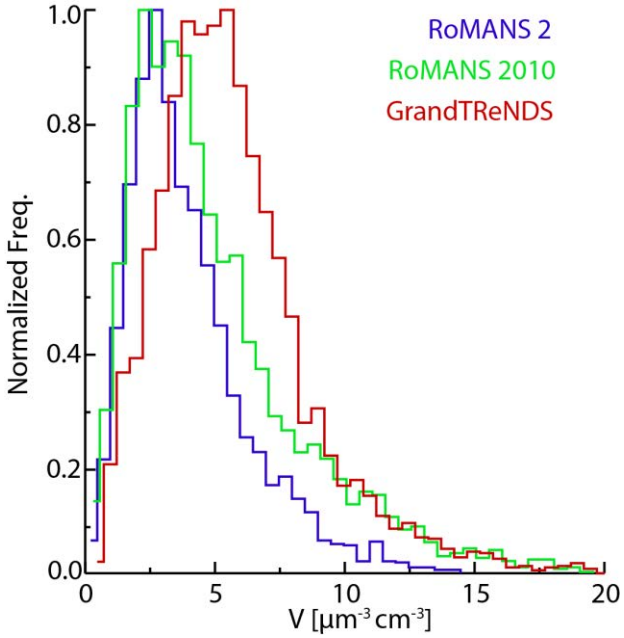

Figure 2.18 Normalized frequency of aerosol volume concentrations ($0.04 < D_p < 20$ µm) during RoMANS 2 (blue), RoMANS 2010 (green) and GrandTReNDS (red).

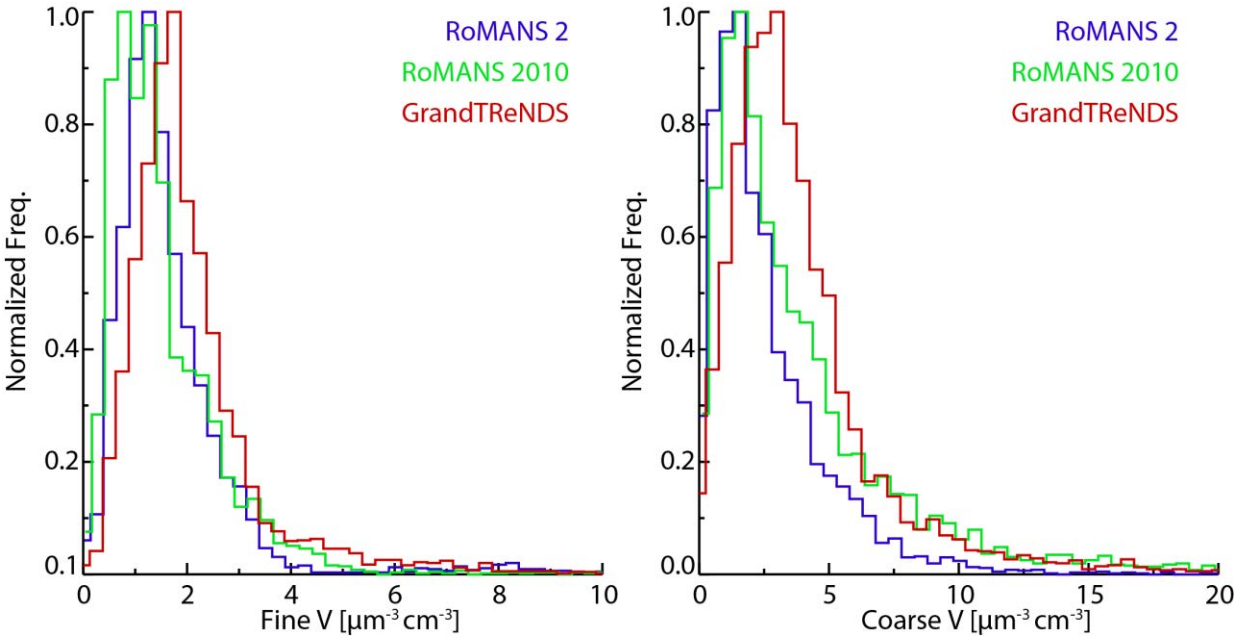

Figure 2.19 Normalized frequency of aerosol fine mode (left) and coarse mode (right) volume concentrations during RoMANS 2 (blue), RoMANS 2010 (green) and GrandTReNDS (red).

2.3.1.2. Inter-annual variability

Comparing the summer data (GT time) collected in RMNP during the two RoMANS campaigns there is some year to year variability. During RoMANS 2010, aerosol number and volume concentrations were higher, on average, and more variable. From Figure 2.17 it can be seen that during RoMANS 2010 the peak frequency in aerosol number concentration occurred at higher values than during RoMANS 2. The peak volume concentration frequencies were more similar during the two studies (Figure 2.18), but higher concentration events were more frequent during RoMANS 2010. Because impacts from local campfire smoke were removed from the RoMANS data set, these differences should indicate changes in regional-scale aerosol concentrations, not just changes in local activity. Table 2.1 also shows data from RoMANS 1 [*Levin et al.*, 2009]. Number and volume concentrations measured during the RoMANS 1

summer time period, July 6 through August 12, were even higher than those measured during RoMANS 2010, indicating the large inter-annual variability in aerosol concentrations at this site.

2.3.1.3. Annual variability

Seasonal variability in aerosol concentrations was observed during the year-long RoMANS 2 study as well as the year-long BEACHON study (Figure 2.20). The BEACHON data shown in Figure 2.20 have been limited to particles larger in diameter than 0.04 μm to better compare with RoMANS 2 data. During both studies, aerosol number concentrations increased from a minimum in the winter months to a maximum during the summer. The observed seasonal cycle during both BEACHON and RoMANS 2 is statistically significant with mean January and July values differing at the 99% confidence level. Again, however, monthly means between the two data sets are also statistically different, showing the spatial variability in aerosol concentrations. The seasonal cycle was consistent with, but slightly lower than, the results from RoMANS 1 where average spring number concentrations were 880 ± 770 cm^{-3} and increased to 2080 ± 940 cm^{-3} in the summer (Table 2.1). Some of the seasonal increase in aerosol number concentration at the RoMANS site could be attributable to increased local traffic and other anthropogenic emissions, since RMNP is a popular summer vacation destination. However, as shown by *Schichtel et al*. [2008] and discussed in Chapter 1, fossil carbon, indicative of anthropogenic pollution, was a minor component of total carbon in RMNP, particularly in the summer. The BEACHON study took place in a much less visited area of Colorado and is expected to be even less directly impacted by anthropogenic emissions than the RoMANS site. During BEACHON, number concentrations were highly correlated with the frequency of events

typical of new particle formation (NPF) and it seems that these events were a controlling factor in determining number concentration at this location. While the measurements made during RoMANS and GrandTReNDS do not allow for the unambiguous confirmation of NPF events (measurements need to extend to smaller diameters than 40 nm to detect the onset of nucleation) it is possible that NPF also played an important role in the seasonal cycle observed during RoMANS 2. Besides the measurements made during BEACHON, NPF has been observed in several other high elevation locations in Colorado [*Boy et al.*, 2008; *Hallar et al.*, 2011; *Weber et al.*, 1997]. *Hallar et al.* found a strong correlation between UV irradiance, which is higher in the summer, and new particle formation.

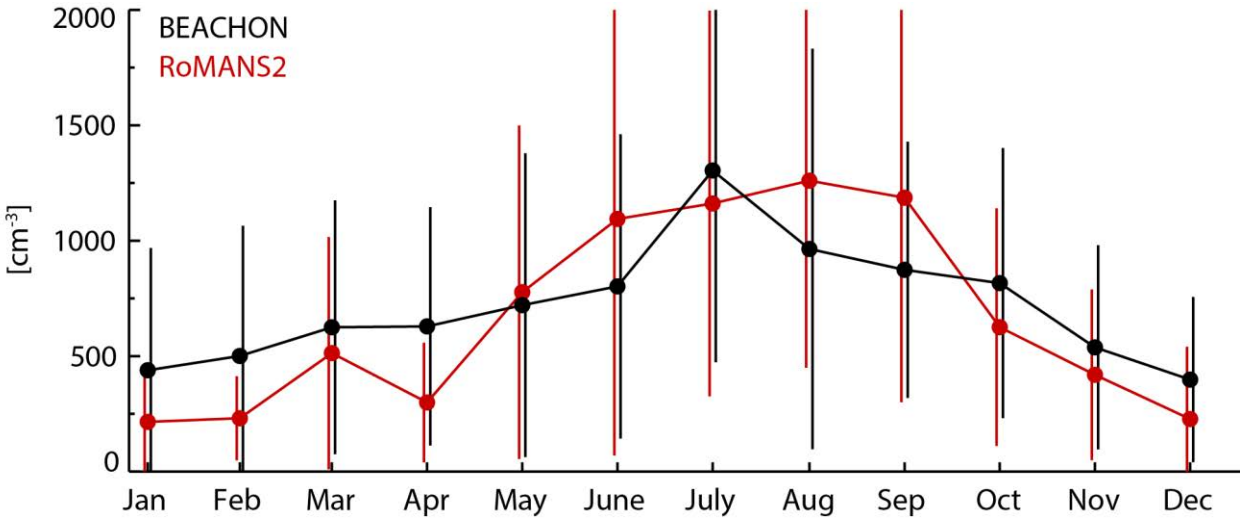

Figure 2.20 Month averaged aerosol number concentration during RoMANS 2 and BEACHON. BEACHON data have been limited to $D_p > 0.04$ µm to match the lower limit of the RoMANS 2 measurements. Error bars show monthly standard deviations.

Monthly averaged fine mode volume concentrations during BEACHON and RoMANS 2 are shown in Figure 2.21. As with number concentrations, there was an increase in aerosol fine mode volume concentrations from winter to summer during both studies. During RoMANS 2, however, the peak in fine mode volume concentration occurred later, in September and October. The RoMANS 2 data are actually more similar to the seasonal cycle of $PM_{2.5}$ from IMPROVE data in the Central Rockies region (Figure 1.2), assuming that the dust component is in the coarse mode [*Malm et al.*, 2009]. Examining just the sulfate, nitrate and organic components in Figure 1.2, $PM_{2.5}$ mass varied between ~ 0.5 and 2.5 μg m^{-3} from January to September in the Central Rockies. For a reasonable assumption of average aerosol density = 1.5 g cm^{-3}, fine mode mass measured during RoMANS 2 varied between 0.3 and 2.6 μg m^{-3}.

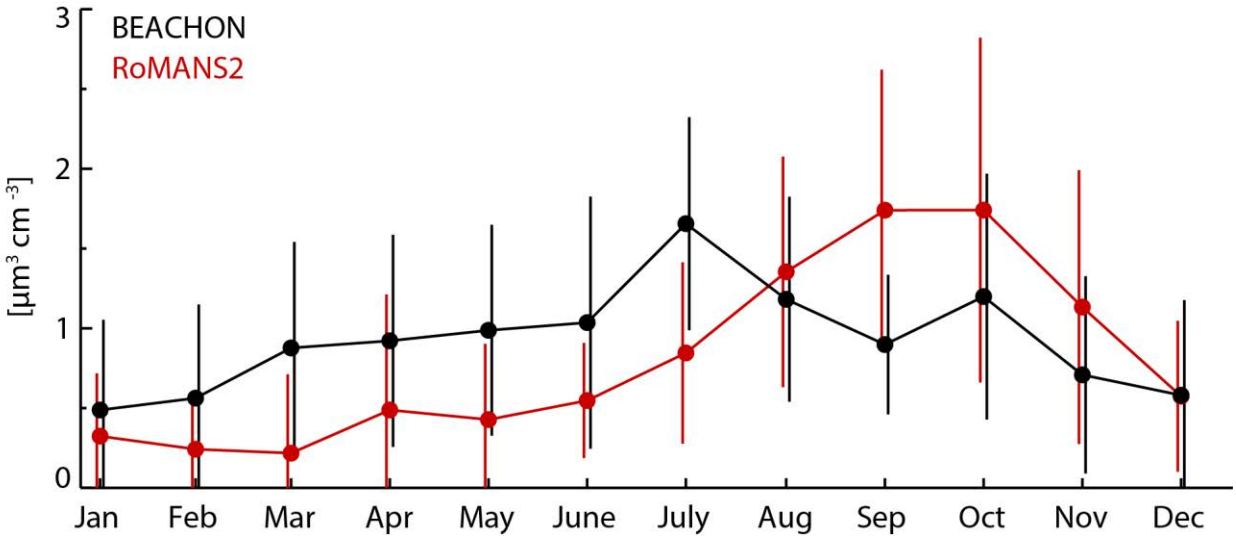

Figure 2.21 Month averaged fine mode volume concentration during RoMANS 2 and BEACHON. BEACHON data have been limited to $D_p > 0.04$ μm to match the lower limit of the RoMANS 2 measurements. Error bars show monthly standard deviations.

2.3.2. Aerosol size distribution

Cumulative number and volume size distributions averaged over the three studies and normalized are shown in Figure 2.22. Note that the x-axis for the number distribution plot is truncated to better show the data. The distributions shown in Figure 2.22 clearly show the mono-modal nature of the number distributions, while the volume distributions were distinctly bi-modal. Also, average distributions from the three studies show a remarkable similarity with little spatial (comparing RoMANS and GrandTReNDS) or temporal (comparing the two RoMANS studies) variability.

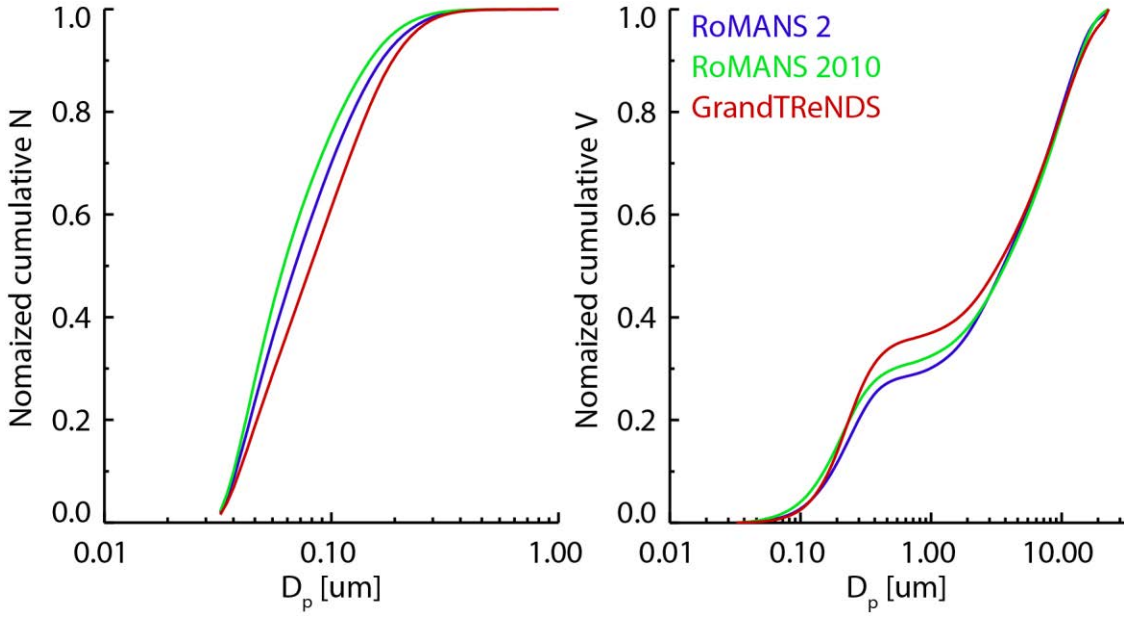

Figure 2.22 Study averaged normalized cumulative number and volume distributions during RoMANS 2 (blue), RoMANS 2010 (green) and GrandTReNDS (red).

For each 15-minute number distribution I calculated geometric mean diameters (D_g) and geometric standard deviations (σ_g). I also calculated these parameters for the fine and coarse modes of the corresponding volume distributions for each study. Volume distributions were separated into coarse and fine modes based on the local minima between the two modes. Number distributions only showed one distinct mode and I thus calculated just one parameter for the entire distribution.

Table 2.1 lists median D_{gn} and D_{gv} values for each study period as well as the GT time periods for the two RoMANS studies while Table 2.3 lists the corresponding σ_g values for these distributions. Also shown in Table 2.2 and 2.3 are published values from RoMANS 1 as well as those from the Yosemite Aerosol Characterization Study (YACS) which occurred in the summer of 2002 [*McMeeking et al.*, 2005b], and the 1999 Big Bend Regional Aerosol and Visibility Observational (BRAVO) study [*Hand et al.*, 2002]. During both YACS and BRAVO aerosol size distributions were measured with the same aerosol sizing system used here. Normalized frequency histograms of D_{gn} and D_{gv} for both coarse and fine modes are shown in Figure 2.23 and Figure 2.24 and σ_{gn} and σ_{gv} values are shown in Figure 2.25 and Figure 2.26 for GrandTReNDS and the GT time periods of RoMANS 2 and 2010. Again, number distributions and both modes of the volume distributions appear very similar across all three studies, but, saving the ROMANS 2 (GT time period) and GrandTReNDS D_{gn} values, were statistically different from one another at the 90% confidence level.

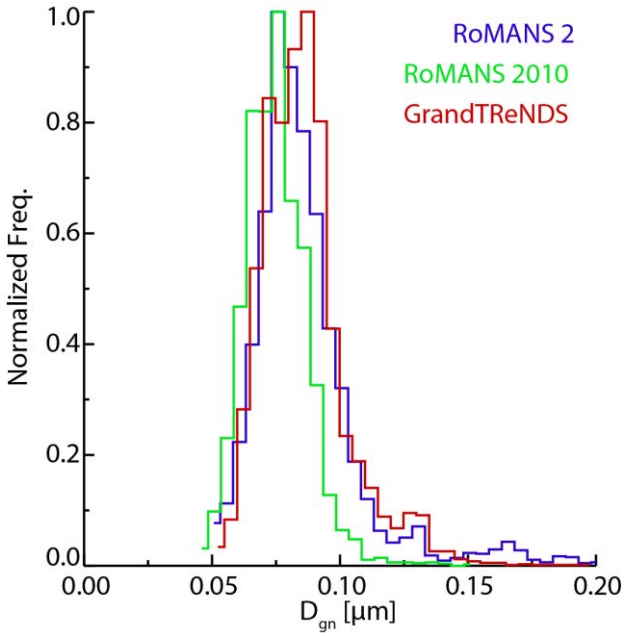

Figure 2.23 Normalized frequency of aerosol number distribution geometric mean diameters during RoMANS 2 (blue), RoMANS 2010 (green) and GrandTReNDS (red).

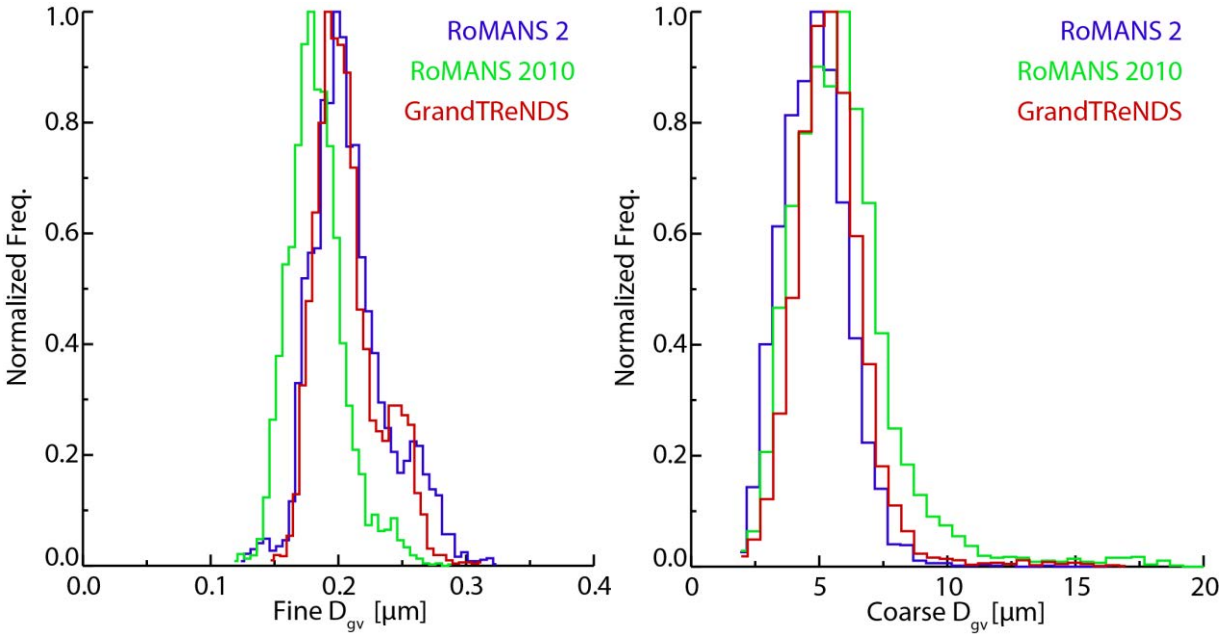

Figure 2.24 Normalized frequency of aerosol fine mode (left) and coarse mode (right) volume distribution geometric mean diameters during RoMANS 2 (blue), RoMANS 2010 (green) and GrandTReNDS (red).

Table 2.2 Median (± 1 standard deviation) geometric means for the number and volume volume distributions during the three studies as well as published data from the RoMANS 1 [*Levin et al.*, 2009], YACS [*McMeeking et al.*, 2005b] and BRAVO [*Hand et al.*, 2002] campaigns. Volume distribution parameters are divided into fine and coarse modes.

	D_{gn} [µm]	Fine D_{gv} [µm]	Coarse D_{gv} [µm]
RoMANS 2 (full study)	0.080 ± 0.015	0.19 ± 0.03	4.73 ± 2.04
RoMANS 2 (GT time)	0.085 ± 0.023	0.21 ± 0.03	5.06 ± 1.30
RoMANS 2010 (full study)	0.076 ± 0.013	0.18 ± 0.02	5.80 ± 2.57
RoMANS 2010 (GT time)	0.077 ± 0.012	0.18 ± 0.02	5.93 ± 2.16
GrandTReNDS	0.087 ± 0.017	0.21 ± 0.03	5.59 ± 1.50
RoMANS1 (Spring)	0.08 ± 0.01	0.20 ± 0.03	3.40 ± 1.30
RoMANS1 (Summer)	0.09 ± 0.02	0.21 ± 0.03	4.70 ± 0.89
YACS	-	0.28 ± 0.05	-
BRAVO	-	0.26 ± 0.04	3.4 ± 0.8

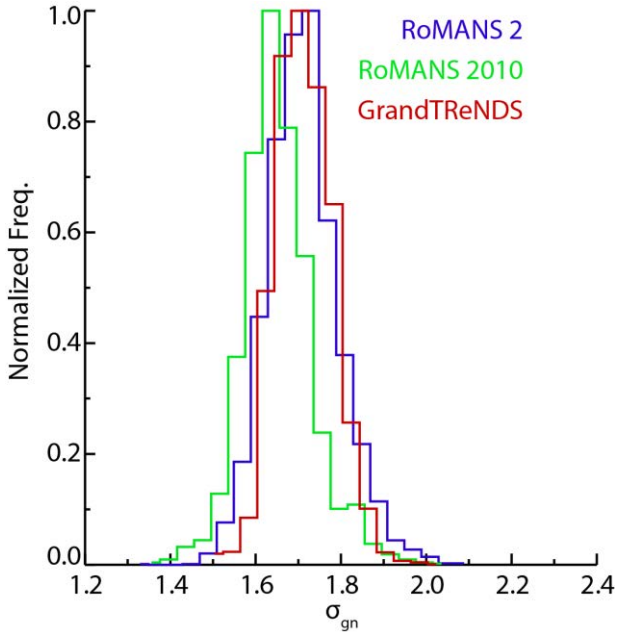

Figure 2.25 Normalized frequency of aerosol number distribution geometric standard deviations during RoMANS 2 (blue), RoMANS 2010 (green) and GrandTReNDS (red).

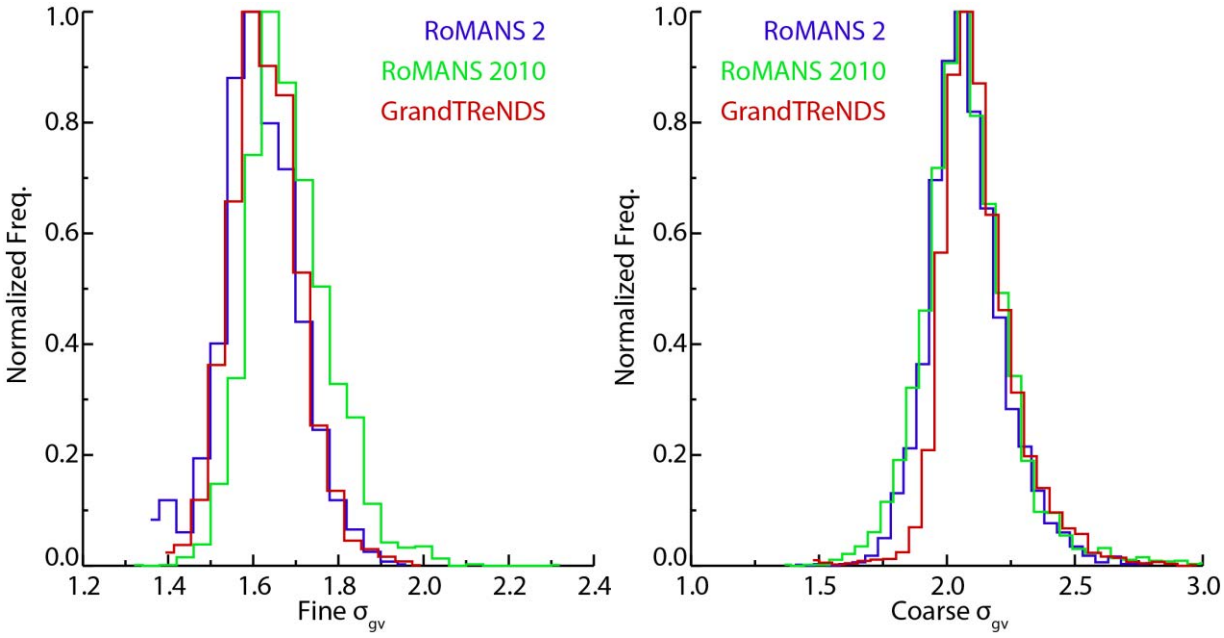

Figure 2.26 Normalized frequency of aerosol fine mode (left) and coarse mode (right) volume distribution geometric standard deviations during RoMANS 2 (blue), RoMANS 2010 (green) and GrandTReNDS (red).

Table 2.3 Median (± 1 standard deviaition) geometric standard deviations for the number and volume volume distributions during the three studies as well as published data from the RoMANS 1 [*Levin et al.*, 2009], YACS [*McMeeking et al.*, 2005b] and BRAVO [*Hand et al.*, 2002] campaigns. Volume distribution parameters are divided into fine and coarse modes.

	σ_{gn} [µm]	Fine σ_{gv} [µm]	Coarse σ_{gv} [µm]
RoMANS 2 (full study)	1.71 ± 0.10	1.67 ± 0.10	2.06 ± 0.22
RoMANS 2 (GT time)	1.72 ± 0.08	1.63 ± 0.09	2.09 ± 0.15
RoMANS 2010 (full study)	1.67 ± 0.09	1.69 ± 0.11	2.10 ± 0.19
RoMANS 2010 (GT time)	1.67 ± 0.08	1.69 ± 0.10	2.09 ± 0.19
GrandTReNDS	1.73 ± 0.07	1.65 ± 0.08	2.13 ± 0.15
RoMANS1 (Spring)	1.70 ± 0.10	1.80 ± 0.12	2.0 ± 0.19
RoMANS1 (Summer)	1.8 ± 0.08	1.6 ± 0.07	1.9 ± 0.11
YACS	-	1.67 ± 0.11	-
BRAVO	-	1.58 ± 0.08	1.82 ± 0.14

2.3.3. Factors influencing aerosol size and concentration

2.3.3.1. Wind speed and direction

So far in this chapter I have presented measured aerosol concentrations and size distributions from the RoMANS and GrandTReNDS studies. In this section I will examine some potential influences on these concentration and size distribution values. Wind direction could be an important factor as air masses originating in different regions could be influenced by different sources, thus resulting in differing aerosol characteristics. At the RoMANS site there were two main wind modes, westerly and southeasterly, which showed distinct characteristics in NO_x concentration. It would be reasonable, therefore, to assume that aerosol concentrations were similarly affected by wind speed and direction at this site. Figure 2.27 shows aerosol number concentration as a function of wind speed, colored by wind direction. As with NO_x, the highest speed winds were associated with lower aerosol number concentrations, and, again, came typically from the west. However, some of the highest aerosol number concentrations were measured when surface winds at the site were from the west, but with low wind speeds. Figure 2.28 shows a wind rose plot of aerosol number concentration during RoMANS 2. This figure further highlights the fact that during the year-long ROMANS 2 study there was no strong relationship between aerosol concentrations and surface wind direction at the site. However, winds from the south and east did have, on average, slightly higher number concentrations. These winds were also associated with higher NO_x. Therefore, it is reasonable to assume that transport of emissions from more populated areas east of RMNP did impact air quality during the RoMANS studies, but are not necessarily responsible for the highest measured concentrations.

Figure 2.29 and Figure 2.30 are the same as Figure 2.27 and Figure 2.28 but for aerosol volume concentrations. These Figures show a similar picture. There were a few high volume concentration events associated with north and westerly winds at the site, again with low wind speeds. However, these points are clear outliers. In general, there is little relationship between wind direction and aerosol volume concentrations at this site. Over both year and seasonal timeframes, there was no correlation between wind speed or wind direction and aerosol number or volume concentrations.

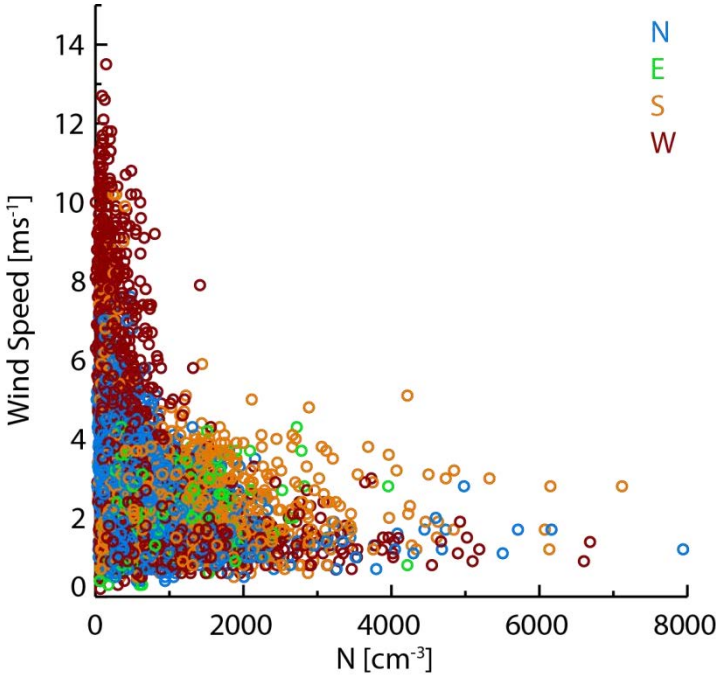

Figure 2.27 Aerosol number concentrations measured during RoMANS 2 versus wind speed and colored by wind direction.

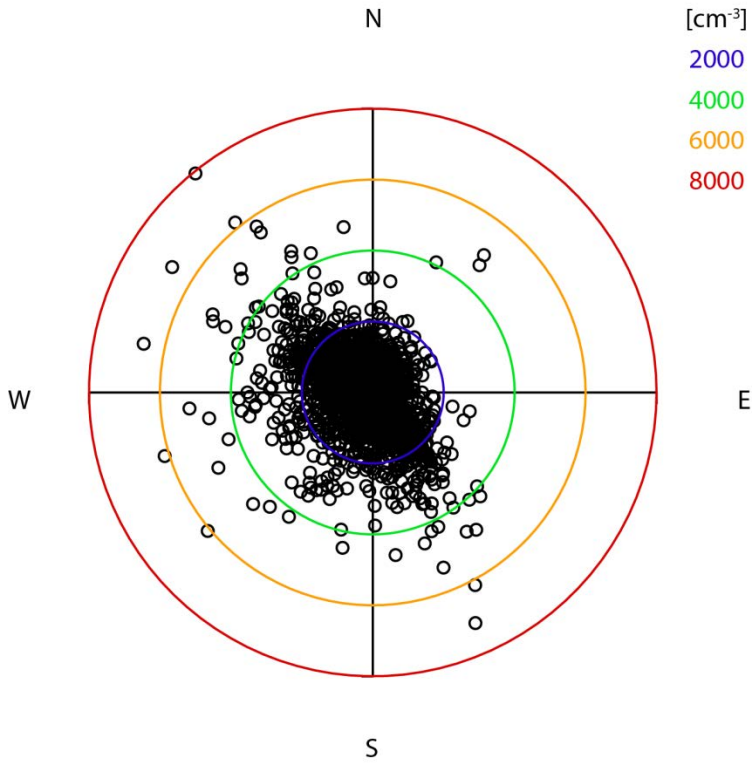

Figure 2.28 Wind rose showing aerosol number concentration as a function of wind direction during RoMANS 2. Colored circles are isopleths of number concentration.

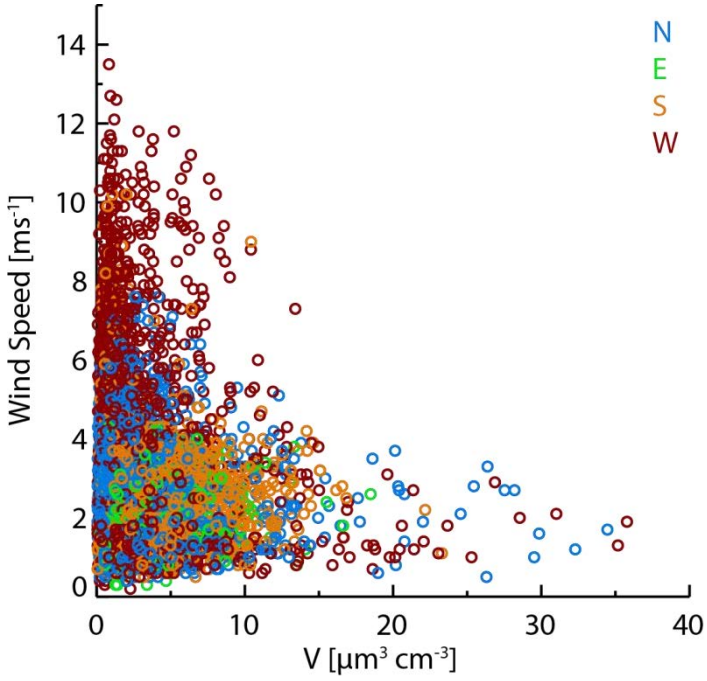

Figure 2.29 Aerosol volume concentrations measured during RoMANS 2 versus wind speed and colored by wind direction.

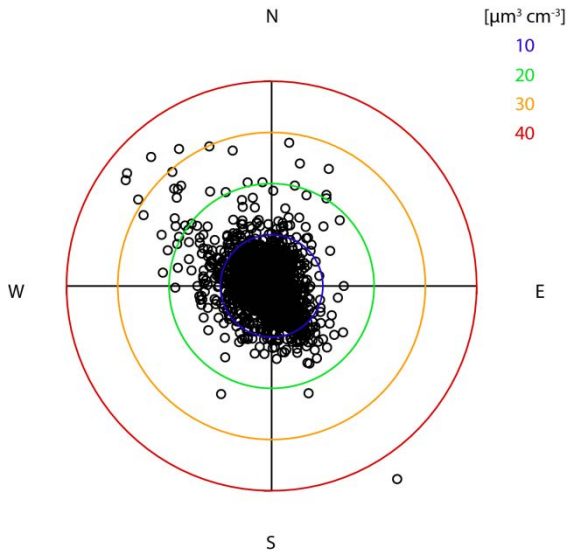

Figure 2.30 Wind rose showing aerosol volume concentration as a function of wind direction during RoMANS 2. Colored circles are isopleths of volume concentration.

The GrandTReNDS site did not have the same bi-modal wind characteristics seen at the the RoMANS site, and, as with NO_x (Figure 2.11), aerosol concentrations showed no trends with wind direction. Wind roses of aerosol number (Figure 2.31) and volume (Figure 2.32) concentrations are shown below. Hour averaged winds at the site never came from the north, perhaps due to local terrain effects, but aerosol concentrations were very similar from all other directions. The only high number concentration event was due to smoke impacts at the site, and will be discussed below.

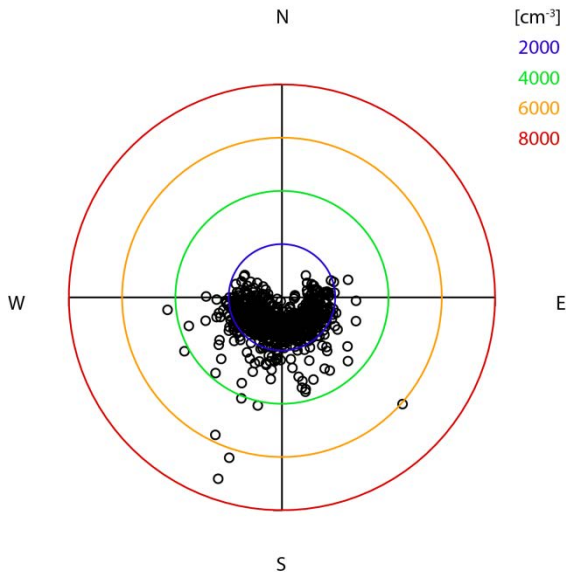

Figure 2.31 Wind rose showing aerosol number concentration as a function of wind direction during GrandTReNDS. Colored circles are isopleths of number concentration.

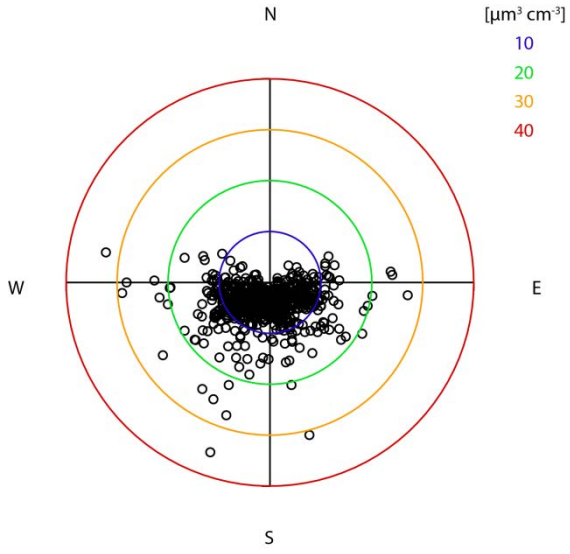

Figure 2.32 Wind rose showing aerosol volume concentration as a function of wind direction during GrandTReNDS. Colored circles are isopleths of volume concentration.

2.3.3.2. Meteorological events

While there was little systematic relationship between aerosol concentration and local wind direction, there were episodic meteorological effects on aerosol concentrations observed during RoMANS and GrandTReNDS. Figure 2.33 shows a contour plot of aerosol volume distributions from July 20 – 30, during the RoMANS 2010 study, a time period in which fine and coarse mode volume were elevated. The coarse mode mean size was also much larger during this time period (greater than 15 μm) than the study average (5.8 μm). This large mode size could indicate that these particles are of local origin as larger particles tend to deposit faster and have shorter lifetimes. Fine mode mass concentrations were also measured by the CSU aerosol mass spectrometer (AMS) during this period (Figure 2.34). The AMS data were provided by Taehyoung Lee and Misha Schurman who operated the instrument and performed all data analysis and quality controls. The AMS data also show an increased aerosol fine mode concentration followed by a rapid decrease on July 28, when there were unfortunately no aerosol sizing data available.

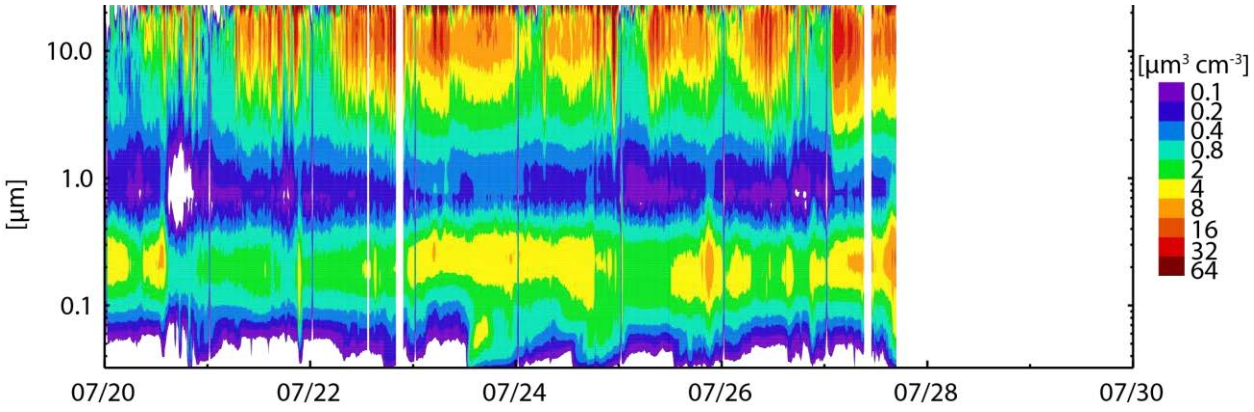

Figure 2.33 Aerosol volume distributions measured during a period of RoMANS 2010 with high coarse mode concentrations.

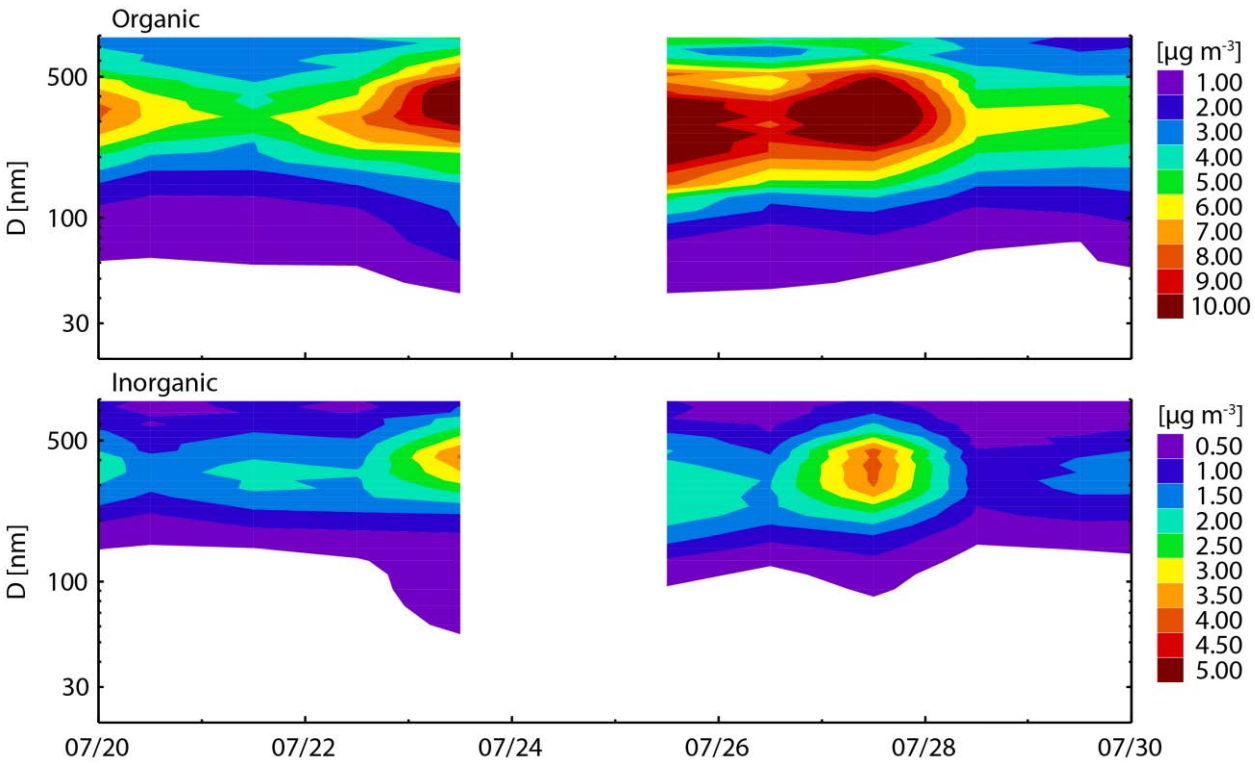

Figure 2.34 Aerosol mass composition measured by an AMS during the same RoMANS 2010 period shown in Figure 2.33 (data provided by Taehyoung Lee and Misha Schurman).

This increase in aerosol concentrations appears to be related to a high pressure system which was over the western US during this time period (Figure 2.35), persisting for several days. This stagnation episode likely allowed local pollution to build up at the RoMANS site. On July 28th a cold front swept across the US (Figure 2.36), leading to a large rain event at the RoMANS site, rapidly cleaning out the elevated aerosol concentrations.

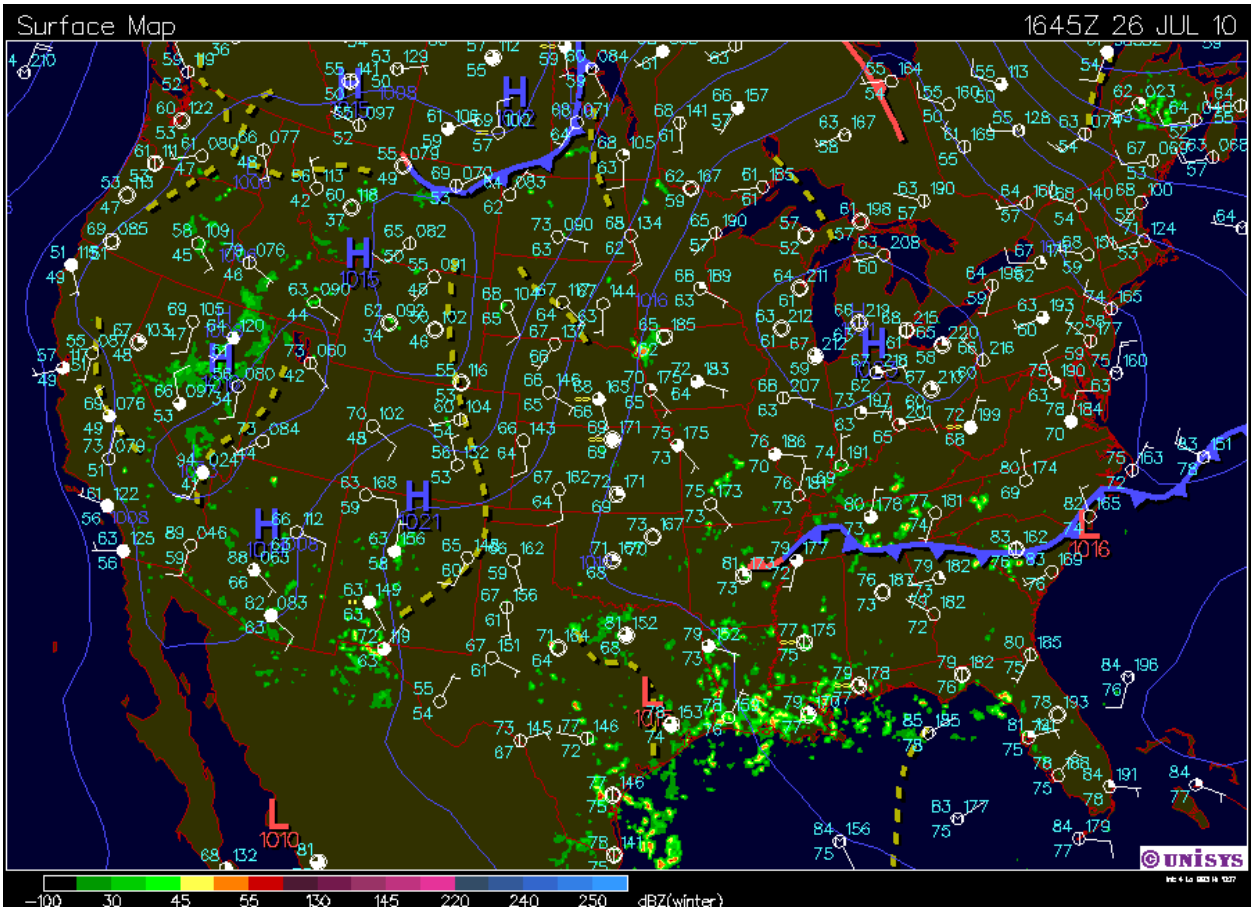

Figure 2.35 North American surface meteorological analysis for July 26, 2010 showing high pressure over Colorado. Data and analysis are from Unisys (http://weather.unisys.com/archive/sfc_map/).

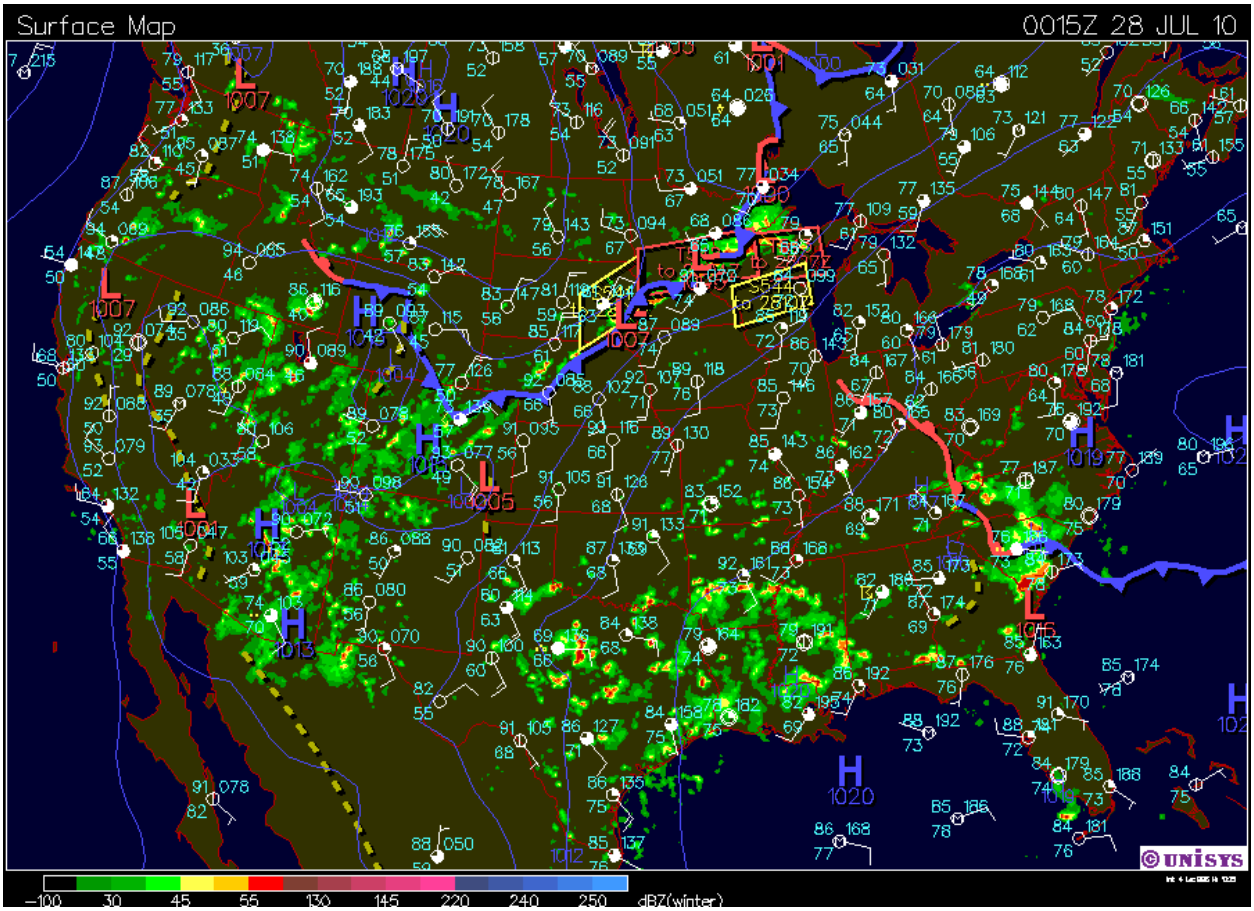

Figure 2.36 North American surface meteorological analysis for July 27, 2010 showing a frontal system approaching the RoMANS site. Data and analysis are from Unisys (http://weather.unisys.com/archive/sfc_map/).

A similar event occurred during GrandTReNDS from August 19th through the 31st. During the beginning of this time period there was an increase in surface pressure measured at the site (Figure 2.37). During this high pressure influenced time period, there were increases in aerosol number (Figure 2.38) and volume (Figure 2.39), in both coarse and fine modes. The increase in aerosol concentration was most obvious in the AMS data (Figure 2.40). During this time period the aerosol mass spectrometer (AMS) measured the second highest fine mass concentrations of the study. The only higher aerosol mass concentrations were measured when

the site was impacted by a wildfire smoke plume (discussed below). Also similar to the RoMANS 2010 stagnation event, the higher aerosol concentrations were cleaned out by a large rain event at the site (circles in Figure 2.37).

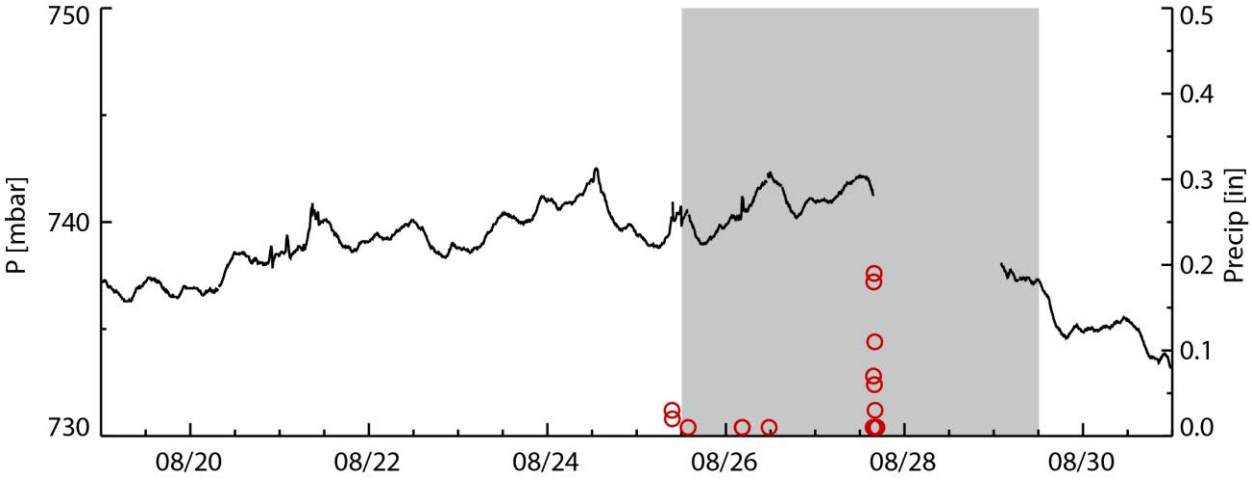

Figure 2.37 Surface pressure (black line) and precipitation amount (red circles) from August 19th through the 31st at the main GrandTReNDS measurement site. The shaded area corresponds to the time periods shown in Figures 2.36 and 2.37 and highlighted in Figure 2.38.

While surface meteorology may help to explain why aerosol concentrations increased during these events it does not provide any information on the source of these aerosols. Because of the very large coarse mode size measured during the RoMANS 2010 event, it appears that local dust was an important source. There was a small increase in coarse mode D_{gv} during the GrandTReNDS event, but not nearly as large as that seen during the RoMANS 2010 event. Volume distributions measured during the GrandTReNDS event are indicative of new particle formation, with an increase at the smallest measured size and subsequent growth, but the measured size range does not go to small enough size to capture new particle nucleation.

However, as discussed above, NPF events could certainly have influenced concentrations at this site. Also, from the AMS data measured during the GrandTReNDS event it can be seen that inorganic concentrations, which were almost entirely sulfate during this study, were at their highest. This suggests that some anthropogenic pollution may have also been building up at the site during the higher pressure time period.

While these episodic events appear to be related to local surface pressure, with aerosol concentrations increasing during times of stagnation, there was no general correlation between aerosol concentration and pressure. During GrandTReNDS, surface pressure was measured at the main site using an AIO-210 weather station (Climatronics Corp. Bohemia, NY). Over the entire study period, the correlation coefficient between aerosol number concentration and surface pressure was 0.02, indicating no systematic relationship between these variables. However, surface pressure alone is an inadequate indicator of stagnation conditions, and thus the role of stagnation in influencing particle number and mass concentrations should be further explored using additional meteorological characterization.

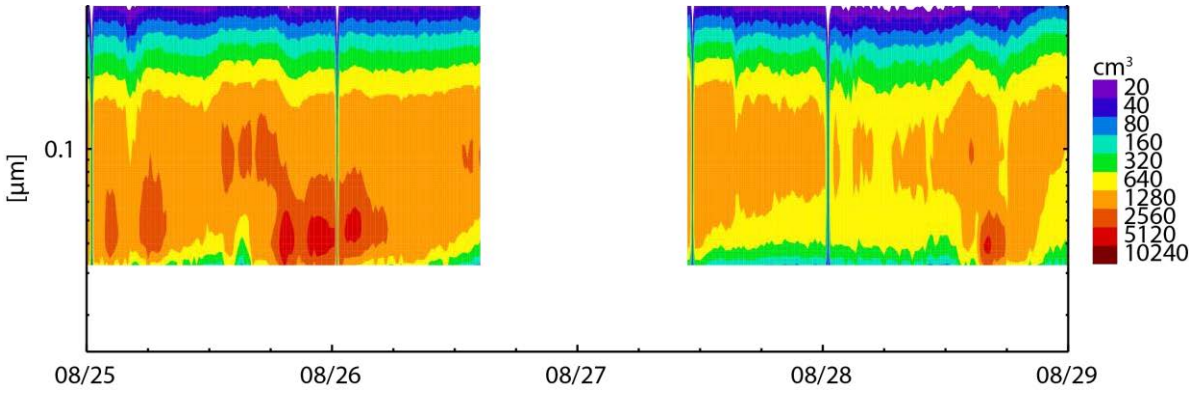

Figure 2.38 Aerosol number distributions during a GrandTReNDS stagnation event.

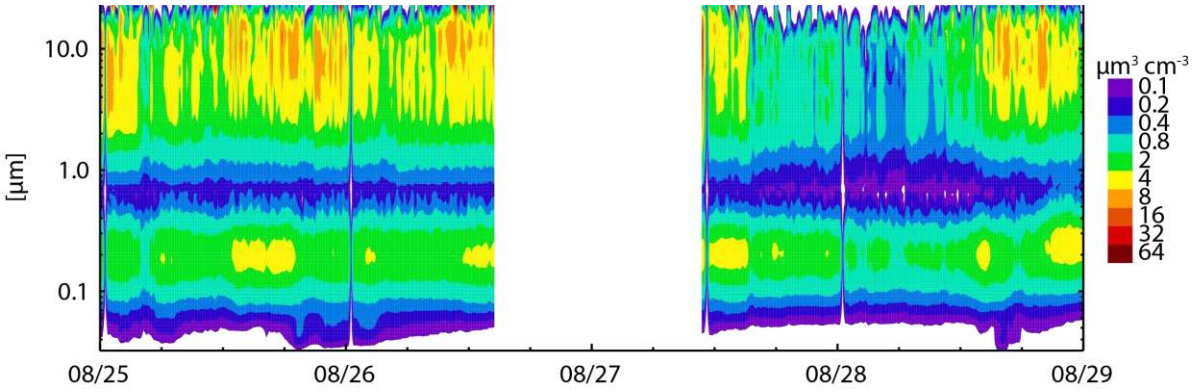

Figure 2.39 Aerosol volume distributions during a GrandTReNDS stagnation event.

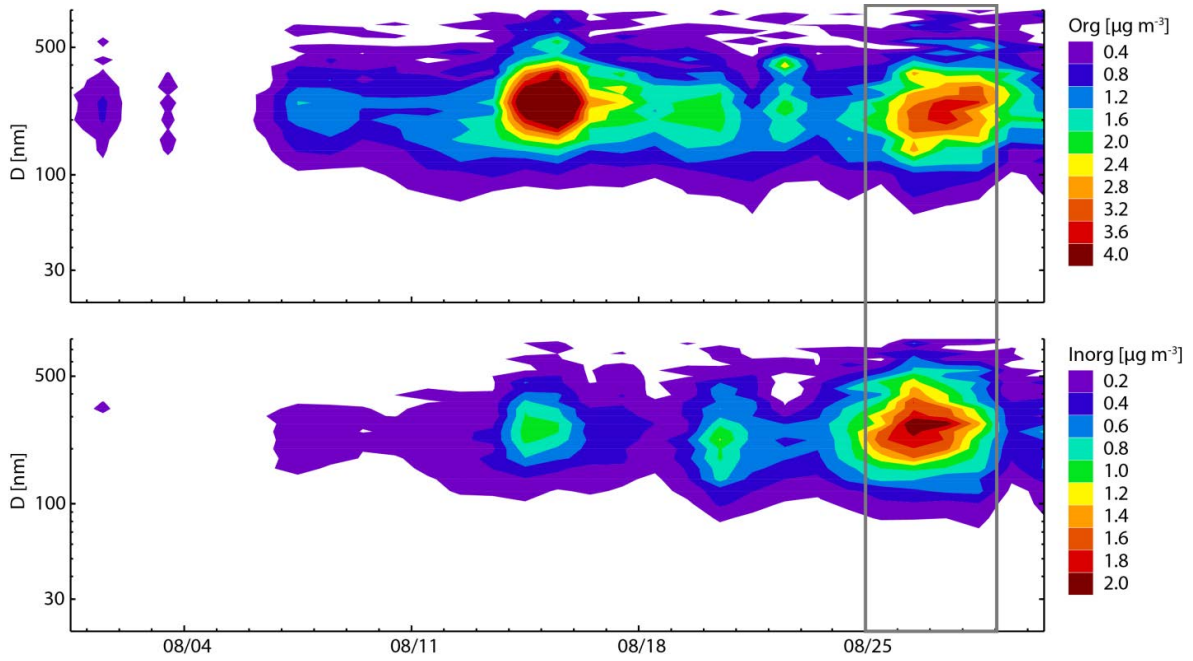

Figure 2.40 Aerosol mass composition measured by an AMS during GrandTReNDS. The boxed area is the same time period shown in Figure 2.38 and 2.38 (data provided by Taehyoung Lee and Misha Schurman).

2.3.3.3. High concentration events

While average aerosol number and volume concentrations were generally low during the three studies there were some high impact, low frequency events which strongly affected these parameters. For example, in the spring of 2009, during RoMANS 2, there was an increase in coarse mode aerosol which appeared to be due to transported dust. The Navy Aerosol Analysis and Prediction System (NAAPS) model showed high concentrations of surface dust at the RoMANS site during this time (Figure 2.41). This model, developed by the Naval Research Lab (NRL) is a global, three dimensional aerosol model described by *Witek et al* [2007] and based on the model described by *Christensen* [1997]. As well as the model indications of dust impact, there was also an increase in the fraction of fine mass attributed to soil in the IMPROVE data collected at the RoMANS site during the months of April and May 2009. This is not unusual for this site as *Levin et al.* [2009] showed a similar increase in dust mass fractions during the spring RoMANS 1 study. The effect of this dust impact on aerosol size distributions was a large increase in coarse mode concentrations, typical of dust transport events [*Hand et al.*, 2002].

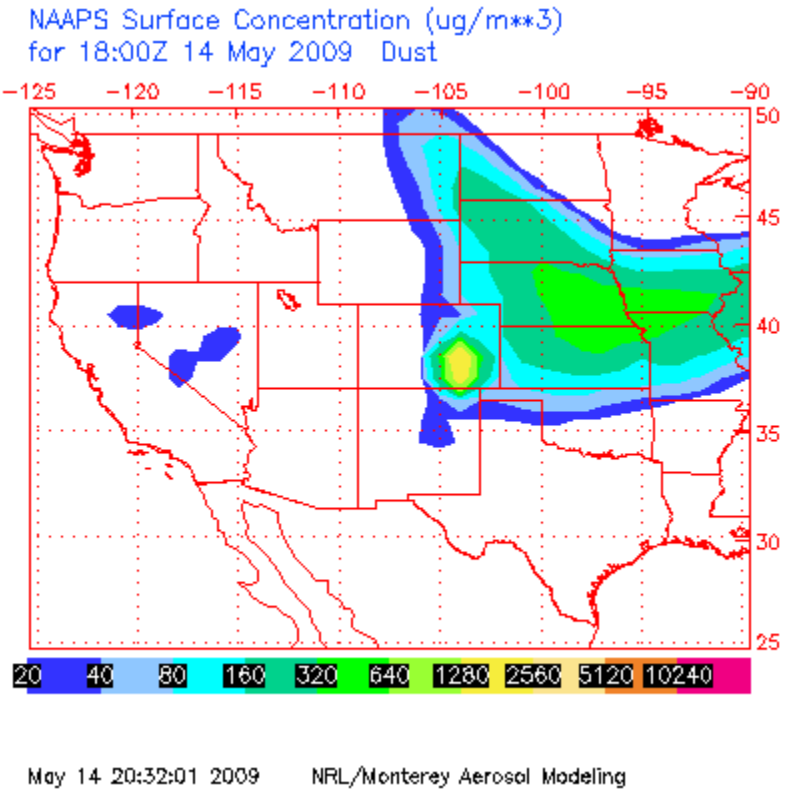

Figure 2.41 Modeled aerosol surface dust concentration from NAAPS on May 14, 2009.

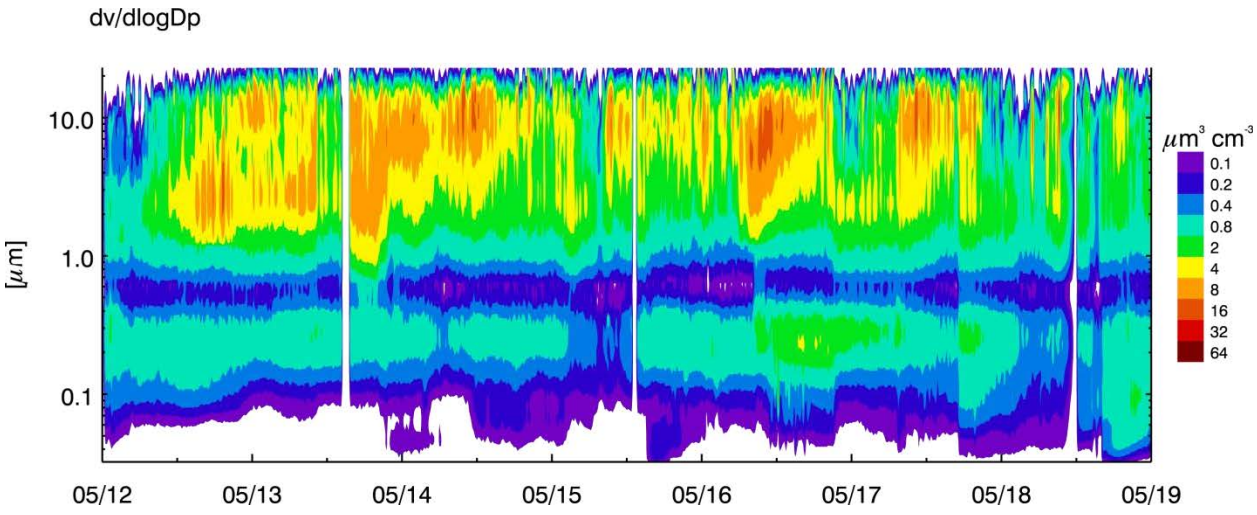

Figure 2.42 Contour of aerosol volume distribution during a RoMANS 2 dust event.

During all three studies, the measurement sites were impacted by smoke from wildfires. The fires ranged in size and distance from the measurement sites and the resulting impacts on aerosol characteristics also showed large variability. This observation is not at all surprising since fire emissions are highly variable depending on fuel type, fuel moisture and fire intensity. Adding variations in transport and meteorology further increases the variability of these emissions downwind of the fires. Biomass burning emissions and their potential influence on aerosols in the western US will be discussed in more detail in Chapter 4. Here I will present the ambient data collected during clearly fire-impacted times at the RoMANS and GrandTReNDS sites.

The Station Fire burned 160,577 acres in southern California during late August and early September 2009. This fire was roughly 1300 km from the RoMANS measurement site, but as indicated by the NAAPS model (Figure 2.43), smoke from this fire was transported directly over RMNP. The RoMANS site was clearly impacted by transported smoke from Aug 30 – Sep 1. The following year, during RoMANS 2010, the site was impacted by emissions from a much closer and smaller fire. The Four Mile Canyon fire burned just 6,181 acres, but was located only 30 km from the measurement site. The site was hit briefly by the smoke plume on Sep 6 and 7. A number of fires collectively called the August Lighting Fires burned 137,000 acres about 160 km southwest of the GrandTReNDS site. The GrandTReNDS site was clearly impacted by the smoke only briefly on Aug 15.

All of these fires had large impacts on the measured aerosol concentrations with increases in number (Figure 2.44) and volume (Figure 2.45) concentrations during all three studies. Also, during all three fire events volume concentrations were shifted towards the fine mode with this mode accounting for roughly 80% of total volume concentrations (Figure 2.46), much higher

than the study average values (Table 2.2). *Levin et al.* [2010] showed that volume distributions from fresh biomass burning emissions are dominated by fine mode aerosol. These ambient measurements show that this mode was still dominant even after some transport and aging, in the case of the RoMANS 2 fire event. Despite the similarity in fine mode fraction, the effects of the fires on number and volume concentrations were not consistent, except in that they all led to increased concentrations. For number concentrations, the magnitude of increase was related to distance from the fire, with the Fourmile Fire (RoMANS 2010) emissions resulting in the highest concentration increase followed by the August Lightning Fires (GrandTReNDS) and then the Station Fire (RoMANS 1).

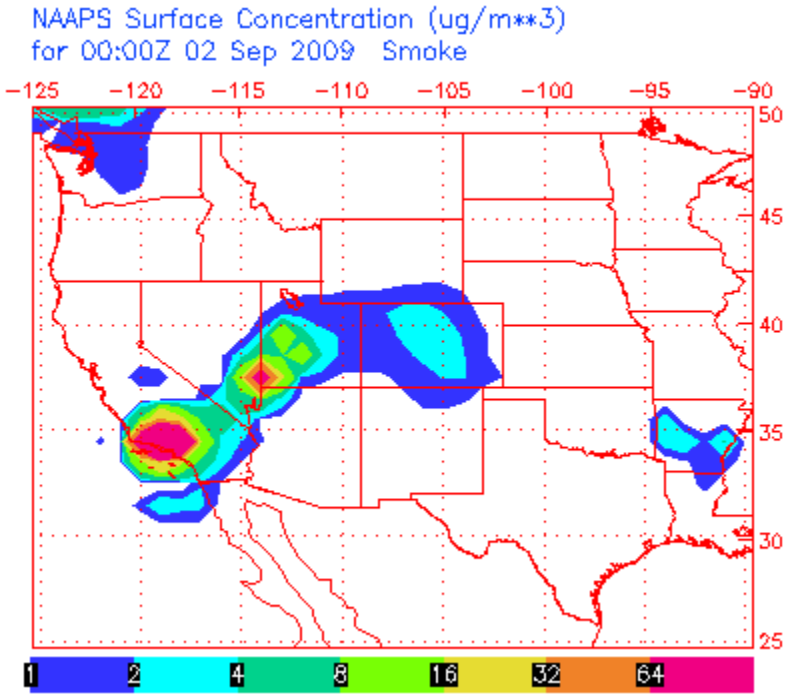

Figure 2.43 Modeled aerosol surface smoke concentration from NAAPS on Sep 2, 2009.

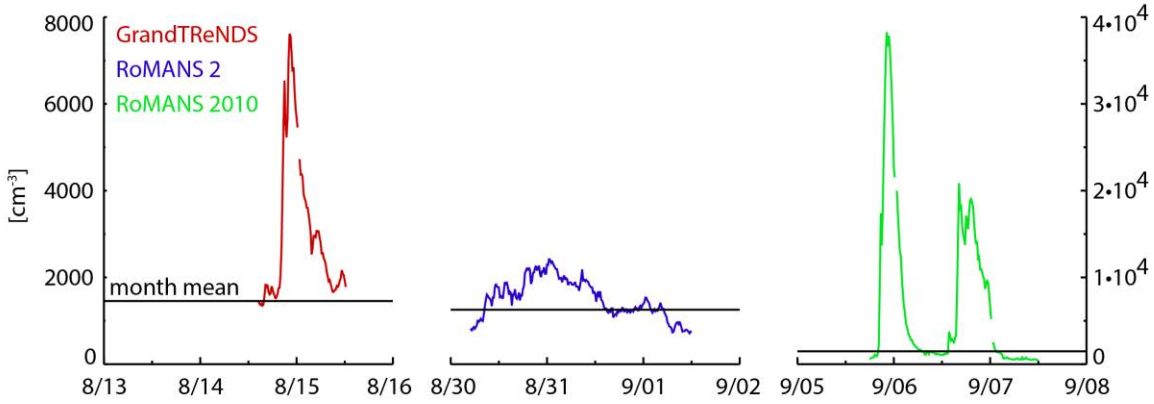

Figure 2.44 Aerosol number concentration during three different fire events. Note the different y-axis for the RoMANS 2010 event.

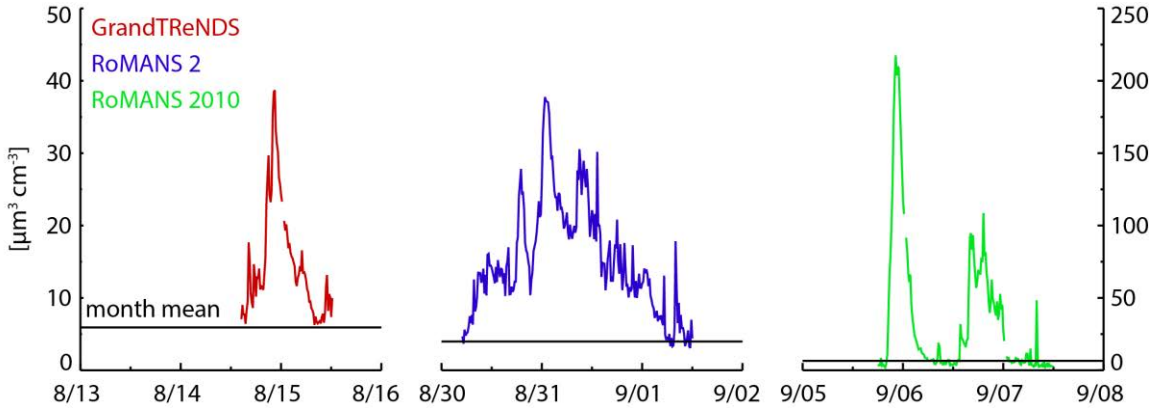

Figure 2.45 Aerosol volume concentration during three different fire events. Note the different y-axis for the RoMANS 2010 event.

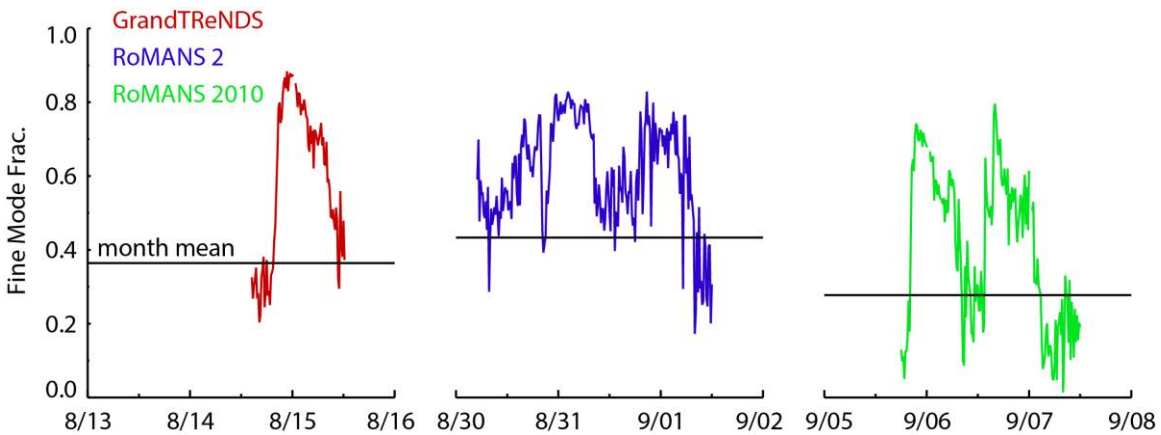

Figure 2.46 Aerosol fine volume mode fraction during three different fire events.

2.3.4. Comparison between concentration and size

In this section I present comparisons between aerosol concentration and size distribution mean diameters. Any relationship between these properties would be potentially useful in constraining and verifying modeled aerosol properties. Figure 2.47 shows the relationship between D_{gn} and aerosol number concentrations during the three studies, divided by season. At higher concentrations there was a general trend of decreasing aerosol mean diameter with increasing number concentrations, especially during the spring and summer months. The decrease in D_{gn} with increasing number concentration could be due to new particle formation impacts at the measurement sites, as these events are typified by large number increases at very small particle sizes. During the winter, aerosol concentrations were very low (note the log x-axis) and there was no apparent relationship between aerosol number concentration and size.

There are a few periods of obvious deviation from the typical behavior in Figure 2.47. These periods all correspond to times when the measurement sites were impacted by smoke, indicated by black symbols. During all these smoke events there was a strong increase in D_{gn} with increasing number concentrations, and these distributions represent the highest measured D_{gn} values during each study. The rate of increase in D_{gn} with increasing N was different during each smoke event and appears to be related to the distance from the fire, and, thus perhaps the age of the smoke. During RoMANS 2010, the site was impacted by smoke from a fire ~30 km away, while the smoke measured during RoMANS 2 was from a fire in Southern California. Smoke sampled during GrandTReNDS fell between these two and the trend shown in Figure 2.47 also falls between those of the two RoMANS studies. *Levin et al.* [2010] measured the evolution of biomass burning aerosol number distributions over several hours during laboratory studies. They observed an increase in D_{gn} values over a few hours of aging, due likely to

coagulation of the smallest aerosol particles and condensation of semi-volatile gasses onto the aerosol. The same processes could be occurring here with these ambient smoke measurements, leading to the observed increase in D_{gn} for the, potentially, most aged emissions. The large deviations due to smoke events measured during the RoMANS and GrandTReNDS studies also helps to highlight the general uniformity of the typical ambient conditions at these sites.

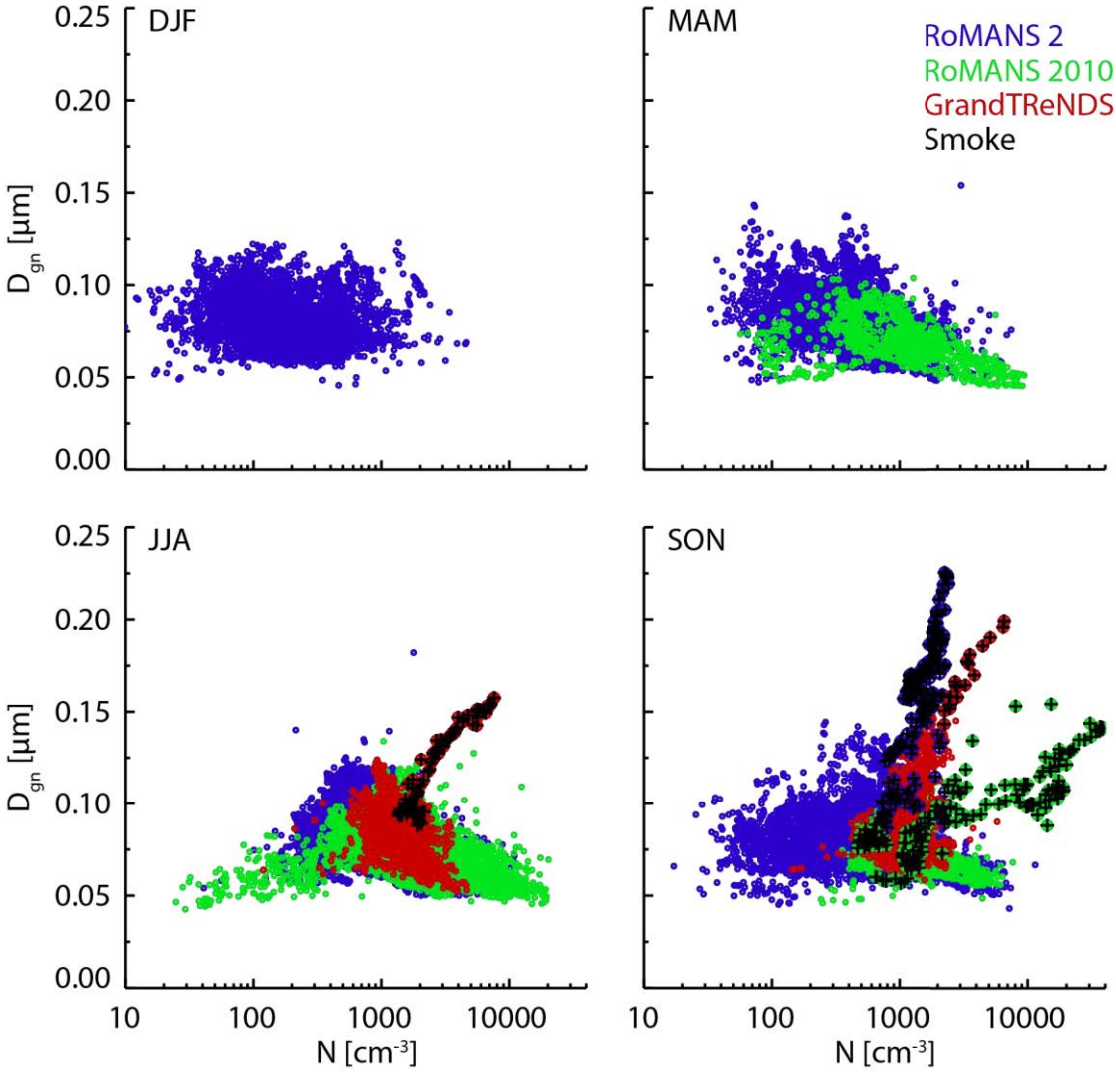

Figure 2.47 Seasonal number distribution geometric mean diameters (D_{gn}) versus number concentration. Black symbols indicate times when the measurement sites were impacted by smoke.

While there was some increase in volume distribution mean diameters (D_{gv}) with increasing concentrations for both the fine (Figure 2.48) and coarse (Figure 2.49) modes, there was considerable scatter in these data. Smoke impacted fine mode aerosol was remarkable only in volume concentrations, with the D_{gv} values falling within the range observed during typical ambient conditions. Smoke events were even less notable for coarse mode volume distributions; however, recall that smoke primarily impacted fine mode concentrations. Coarse mode D_{gv} was also much more variable as coarse mode volume concentrations increased (Figure 2.49). This is mainly due to the fact that there were very few aerosol counts in the coarse mode, especially at the largest sizes. Therefore, just a few particles in a large size bin would be sufficient to shift the mean diameter, as well as increase volume loading. The time periods with very high coarse mode D_{gv}, higher than 15 μm measured during the RoMANS 2010 summer period correspond to the stagnation event shown in Figure 2.33.

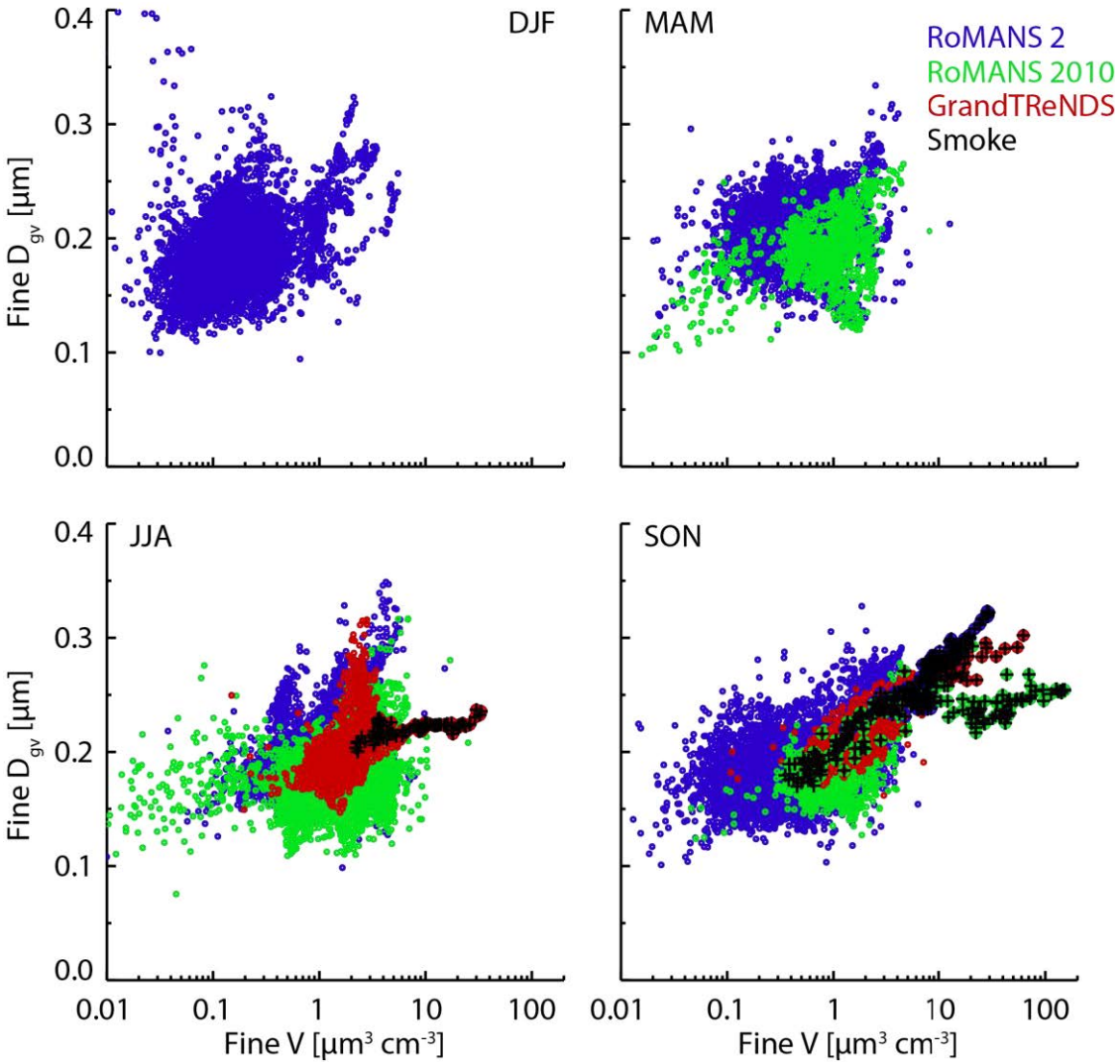

Figure 2.48 Seasonal fine mode volume distribution geometric mean diameter (D_{gv}) versus fine mode volume concentration. Black symbols indicate times when the measurement sites were impacted by smoke.

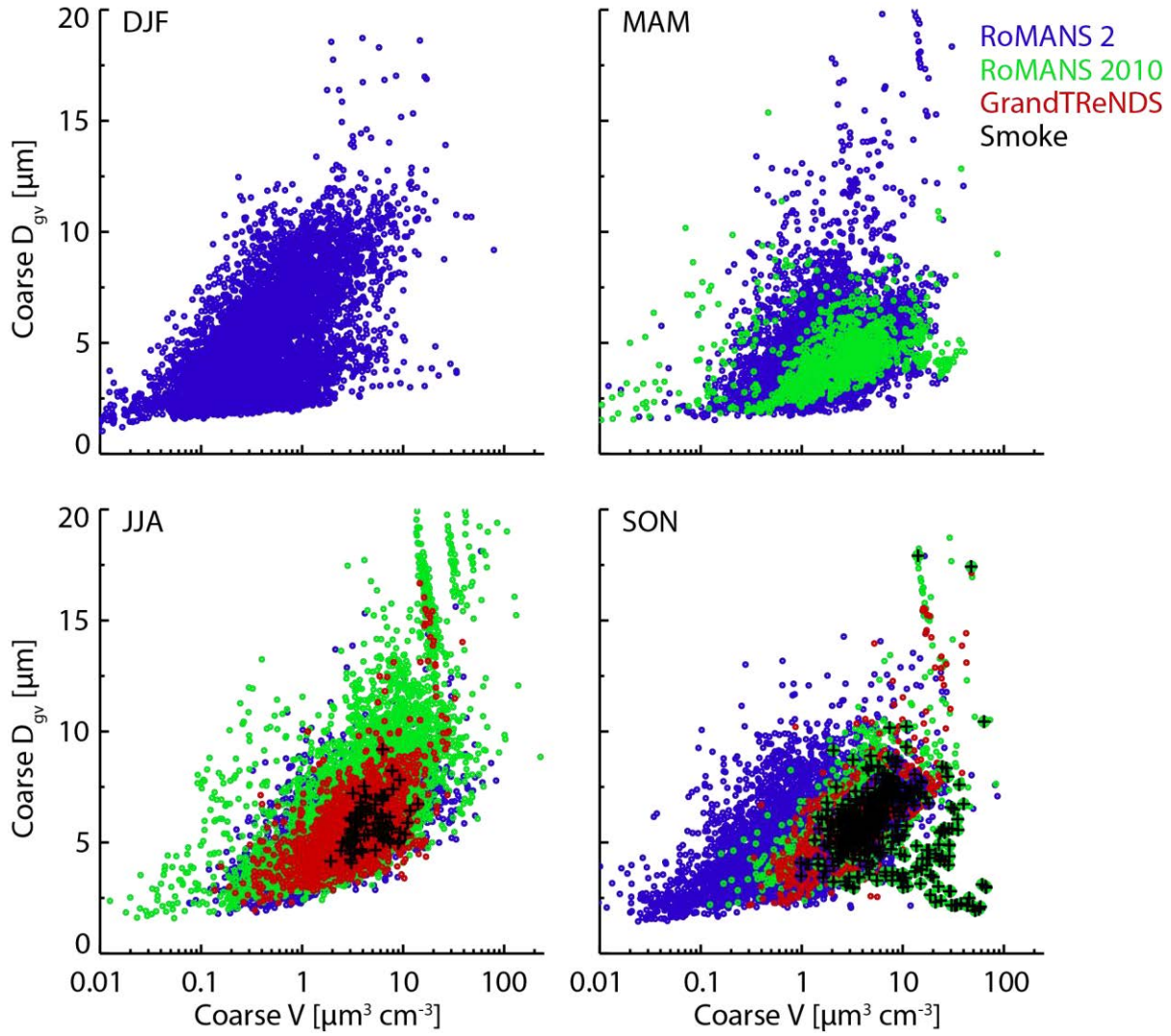

Figure 2.49 Seasonal coarse mode volume distribution geometric mean diameter (D_{gv}) versus coarse mode volume concentration. Black symbols indicate times when the measurement sites were impacted by smoke.

2.4. Summary and Conclusions

Aerosol number and volume concentrations and size distributions were measured during three different studies at two locations in the Rocky Mountain region over a three year period. While aerosol number and volume concentrations and mode statistics from all studies fell within similar ranges, these values were all statistically different between all studies, highlighting the

temporal and spatial variability in aerosol concentrations and parameters and the need for continued aerosol measurement campaigns.

Where the measurements among the three studies differed the most was when the measurement sites were clearly impacted by a specific aerosol or meteorological event. Dust events, only detected during RoMANS 2, were characterized by an increase in coarse mode aerosol volume concentration. During both RoMANS and GrandTReNDS, increases in aerosol concentration were associated with high pressure systems leading to several-day stagnation events. In both cases these elevated concentrations were cleaned out by large rain events.

During all three studies, the measurement sites were impacted by smoke from wildfires. These fires ranged, in orders of magnitude, in both distance from the measurement sites and burned area resulting in large event to event variation in measured number and volume concentrations. However, during all three studies, smoke impacted time periods were clear outliers in aerosol concentrations, highlighting the importance of these events and the role of smoke on regional aerosol concentrations and characteristics. While there was large variability in aerosol concentrations measured during the three smoke events, volume distributions during all the smoke events were characterized by a dominant fine mode, with the fine mode accounting for 70 – 80% of aerosol volume instead of the typical 30 – 40%. Smoke impacted aerosol also tended to have increased D_{gn} values, especially for cases with smoke from more distant fires, i.e. the RoMANS 2 event.

As well as spatial and inter-annual variability measured over the different studies, seasonal variability in aerosol properties was also observed during the year-long RoMANS 2 study. Aerosol number concentrations measured during this study were lowest during the winter

months, increasing to a maximum in August, similar to previous studies at this site [*Levin et al.*, 2009] as well as the BEACHON site [*Levin et al.*, 2012]. The seasonality in aerosol number concentrations observed during BEACHON was likely impacted by new particle formation (discussed more in Chapter 3), which could also have contributed to aerosol concentrations and properties during the studies discussed here. The general trend of decreasing number distribution geometric mean diameter with increasing number concentrations could also be due to new particle formation events. However, because aerosol size measurements only went down to 0.04 μm, new particle nucleation could not be directly measured during the RoMANS or GrandTReNDS studies.

3. Aerosol hygroscopicity in the Rocky Mountains

3.1. Importance of aerosol hygroscopicity

Cloud droplets in the atmosphere cannot form without a condensation nucleus provided by an aerosol particle. In a particle free air mass, water vapor concentrations would have to reach relative humidities far above water saturation before water vapor could homogeneously nucleate and form droplets. As described by the Kelvin equation, the vapor pressure over a curved surface is inversely, exponentially related to the radius of curvature of the surface [*Seinfeld and Pandis*, 2006]. A homogeneously nucleated water droplet would have a very small initial radius, and thus require a very high relative humidity to remain in the liquid phase, instead of quickly evaporating. These high RH conditions are never achieved in the ambient atmosphere. Cloud condensation nuclei allow water vapor to condense at atmospherically relevant RH values by increasing the initial size of the droplet, and thus decreasing the radius of curvature, and by changing the water activity of the droplet. This second effect, the solute or Raoult effect, decreases the vapor pressure over the droplet by effectively reducing the number of water molecules at the surface of the droplet [*Seinfeld and Pandis*, 2006]. Both the curvature and solute effects are described by Köhler theory which gives the equilibrium saturation ratio over a solution droplet of specified composition and size [*Kohler*, 1936]. Application of this theory will be discussed below.

The number of aerosol particles that can take up water and activate as cloud condensation nuclei (CCN) under given environmental conditions can have large effects on cloud and precipitation formation. More CCN will result in more abundant, but smaller, cloud droplets as the available water vapor is spread out among more droplets. Higher droplet number

concentrations are expected to cause changes in both cloud structure and lifetime, leading to enhancements in cloud reflectivity [*Twomey*, 1974], suppression of drizzle [*Albrecht*, 1989], changes in intensity and distribution of precipitation [*Khain and Lynn*, 2009; *Khain et al.*, 2005; *Rosenfeld et al.*, 2008; *Storer et al.*, 2010; *van den Heever et al.*, 2006; *Van Den Heever and Cotton*, 2007; *van den Heever et al.*, 2011] and even changes in updraft and storm intensity [*Lerach and Cotton*, 2012]. These changes to clouds and precipitation may have further impacts ranging from localized weather to global climate. In order to correctly model these important processes, therefore, it is necessary to correctly represent the number and characteristics of CCN in the model.

Whether or not a particle will act as a CCN under certain environmental conditions, that is a given supersaturation, depends on the particle's size and hygroscopicity, the latter referring to how readily the particle takes up water. Larger particles, ~5 μm in diameter and larger, are often termed giant CCN [*Feingold et al.*, 1999] and will take up water at low supersaturation even if the particle has a low hygroscopicity. There are, however, generally few particles in this size range. For particles in the accumulation mode, where the majority of atmospheric aerosols are typically found, aerosol hygroscopicity can have large impacts on the number of available CCN at a given supersaturation [*Petters and Kreidenweis*, 2007]. As will be shown in this chapter, at these sizes small changes in hygroscopicity can modify by a factor of 2 the number of available CCN. Thus, correctly representing aerosol hygroscopicity in models is very important to correctly determine the number of available CCN as a function of cloud supersaturation, which in turn is necessary to correctly model cloud and precipitation properties.

In this portion of the work, I seek answers to two questions about CCN in the mountains of Colorado and Wyoming: (1) Over an annual cycle, what are the ground-level number

concentrations of CCN active at typical atmospheric supersaturations? And (2) what are the compositions and likely sources of these CCN? The approach is to analyze relevant data on aerosol hygroscopic properties and size distributions determined from surface measurements taken during several field campaigns in the eastern Rocky Mountain region. The chapter is divided into two main sections. In the first section (3.2) I discuss CCN and hygroscopicity measurements made as part of the BEACHON project. In the second section (3.3 and 3.4) I present chemical composition data from the RoMANS 2010 and GrandTReNDS projects and use these data to derive aerosol hygroscopicity, and ultimately to obtain estimates of CCN concentrations in those regions and time periods. Parts of this chapter were previously published in in JGR [*Levin et al.*, 2012] and have been included here by permission of the publisher.

3.2. BEACHON

The Bio-hydro-atmosphere interactions of Energy, Aerosols, Carbon, H_2O, Organics & Nitrogen (BEACHON) project is a large, multi-investigator, interdisciplinary project which seeks to better understand the interactions and feedbacks among the atmosphere, biosphere and hydrosphere through the carbon and water cycles. As part of this much larger project, measurements of size resolved aerosol hygroscopicity were made at the Manitou Experimental Forest in Colorado during two time periods: March 2010 - March 2011 and July - August 2011. This second time period was during the intensive BEACHON-RoMBAS (Rocky Mountain Biogenic Aerosol Study). These measurements provide a unique look at a full seasonal cycle of CCN concentration and aerosol hygroscopicity at a forested, mountainous site. In addition, in line with the primary goals of BEACHON, these measurements help to better understand the role

of biogenic aerosol in linking the biosphere, hydrosphere and atmosphere through the carbon and water cycles.

The biosphere, hydrosphere and atmosphere interact in complex ways through numerous linkages and feedbacks across a large range of spatial and temporal scales. Many of these linkages are understood, at least conceptually [*Andreae et al.*, 2002; *Barth et al.*, 2005; *Kulmala et al.*, 2004a]; however, much work remains to quantitatively understand these processes. The water and carbon cycles are particularly important in linking these systems. For example, soil moisture, relative humidity and precipitation all affect biological activity and emissions of biogenic volatile organic compounds [*Barth et al.*, 2005; *Duhl et al.*, 2008; *Sharkey et al.*, 2008; *Telford et al.*, 2010], while these biogenic emissions can impact the number and characteristics of cloud droplet nucleating particles [*Andreae and Rosenfeld*, 2008; *Fuzzi et al.*, 2006]. As discussed above, changes in CCN, in turn, can lead to large changes in cloud characteristics with resulting changes in precipitation and incoming solar radiation. These changes in available water and sunlight complete the loop by further impacting the biosphere, although the strengths and even directions of potential feedbacks are largely unknown.

Biogenic secondary organic aerosol (BSOA) is a key component in this feedback loop. One pathway for formation of BSOA involves oxidation of volatile organic compounds emitted from vegetation, leading to the formation of lower vapor pressure reaction products which can partition into the particle phase. Biogenic compounds can condense onto existing particles and are also an important contributor to new particle formation and growth events [*Dusek et al.*, 2010; *Kulmala et al.*, 2004a; *Kulmala et al.*, 2004b]. Organic particles compose a large fraction of the global submicron aerosol mass [*Jimenez et al.*, 2009; *Q Zhang et al.*, 2007], and biogenic precursors are a major source of these particles [*Kanakidou et al.*, 2005; *N H Robinson et al.*,

2011]. There are numerous species that contribute to this biogenic aerosol component, making it highly impractical to determine the cloud condensation nuclei (CCN) activity of these particles by considering the contribution of individual species to the overall hygroscopicity. Instead, laboratory studies [*Asa-Awuku et al.*, 2010; *Engelhart et al.*, 2011; *King et al.*, 2010; *Massoli et al.*, 2010; *Petters et al.*, 2009c; *Prenni et al.*, 2007] have been conducted to constrain the hygroscopic properties of model BSOA particles and link variations in these to precursor species and oxidation conditions. Field studies have also been conducted exploring ambient aerosol hygroscopicity in areas dominated by biogenic organic species such as tropical [*Gunthe et al.*, 2009] and boreal forests [*Cerully et al.*, 2011; *Sihto et al.*, 2010]. In addition, field studies have examined the seasonal variability in CCN concentrations and aerosol hygroscopicity [*Fors et al.*, 2011; *Kammermann et al.*, 2010] and the effects of organic dominated new particle formation on aerosol hygroscopicity [*Dusek et al.*, 2010]. The measurements made as part of the BEACHON project add to these field studies by examining aerosol hygroscopicity over multiple seasons at a semi-arid, continental, mountainous location.

3.2.1. Biogenic aerosol at the BEACHON site

A goal of the BEACHON project is to assess the impact of biogenic emissions of volatile organic gasses and their oxidation products on the population of CCN. Because of the location of the measurement site, such impacts are likely primarily through the formation of BSOA which can modify CCN populations in one of three ways: by increasing total particle number concentrations through their participation in new particle formation; by shifting aerosol size distributions to larger sizes by condensing onto existing particles; and by altering the

hygroscopicity of particles onto which they condense. Although there are no complete observations of BSOA precursors for the entire annual cycle covered in this study, *Kim et al.* [2010] recently reported PTR-MS observations of biogenic volatile organic compounds (BVOC) and their oxidation products from an intensive campaign during the summer of 2008 at the BEACHON field site. In addition, some measurements during the 2010 and 2011campaigns at this location confirmed the presence of expected biogenic compounds, particularly, 2-methyl-3-butene-2-ol (MBO) and various monoterpenes.

3.2.2. Site location and characteristics

The measurement site for both the year-long BEACHON study and BEACHON-RoMBAS was situated in the Manitou Experimental Forest located in Pike National Forest, Colorado (lat. 39.10˚ N, lon. 105.10˚ W). The site is at an elevation of 2300 m and is ~72 km southwest of Denver and ~40 km northwest of Colorado Springs. The Experimental Forest covers roughly 67 km^2 and is representative of the Central Rocky Mountains montane zone [*Kim et al.*, 2010]. In the vicinity of the measurement site, the vegetation is almost entirely open-canopy ponderosa pine. However, the Experimental Forest also contains large areas of Douglas fir, aspen and open grassy areas, and upwind ecosystems may include these species as well as oak and spruce forests, and riparian willow zones [*Kim et al.*, 2010]. The BEACHON site was specifically chosen to have minimal impact from nearby anthropogenic gas and particle emissions and to be in a region with significant BVOC emissions.

Back-trajectory residence time analysis using the Hybrid Single Particle Lagrangian Integrated Trajectory (HYSPLIT) model [*Draxler*, 1999; *Draxler and Hess*, 1997; 1998] and the

Global Data Assimilation System (GDAS) one degree meteorological data set shows that air masses impacting the BEACHON site during the study period came predominantly from southwest Colorado (Figure 3.1), a sparsely populated mountainous region. Back-trajectories were rarely clearly impacted by air masses from the Front Range of Colorado, consistent with findings from the prior study at this location by *Kim et al.* [2010]. While some seasonal variability exists (Figure 3.1), southwest Colorado remained the dominant source region for air masses impacting the site in all seasons. Thus, the measurements discussed here are considered to be representative of remote aerosol characteristics in this region.

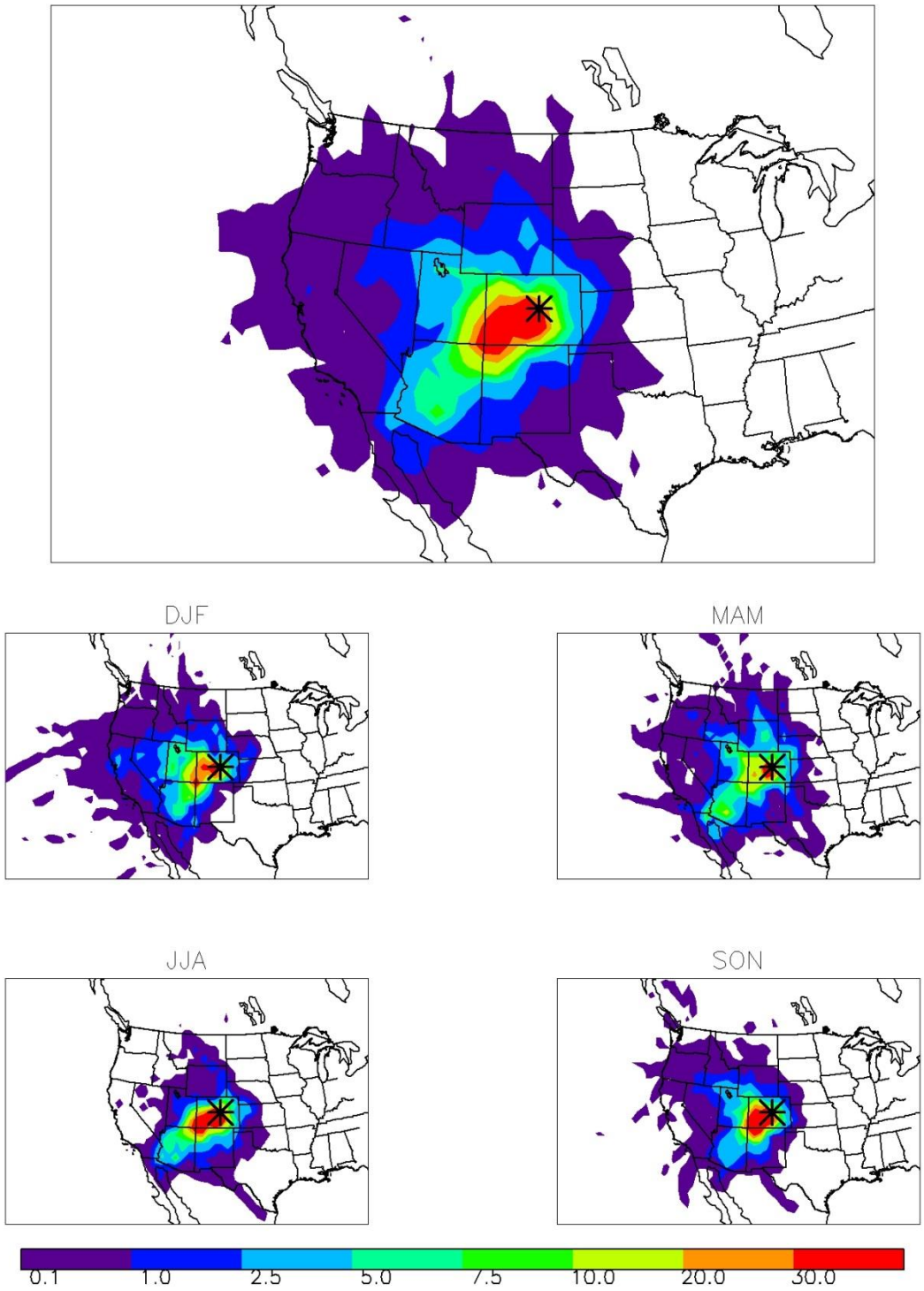

Figure 3.1 Annual (top) and seasonal (bottom) Residence Time Analysis (RTA) for the BEACHON receptor site based on 2010 HYSPLIT back-trajectories. Contours of 1° x 1° grid boxes indicate the relative average residence time of an air parcel in each grid box.

3.2.3. Instrumentation and measurement technique

During the BEACHON field campaigns, instrumentation was housed in a climate controlled, modified shipping container which was maintained at ~18 – 20 ºC. Sample was drawn at a rate of 1.5 LPM through a stainless steel inlet which extended to ~3 m above ground level (AGL). Sample residence time in the inlet tubing was approximately 6 s.

Total aerosol and CCN size distributions were measured using a CPC (TSI 3010 or 3760) and a cloud condensation nucleus counter (CCNC; Droplet Measurement Technologies, Boulder, CO) downstream of a DMA (TSI 3071) following the setup described by *Petters et al.* [2009b; 2007] and shown in Figure 3.2. The DMA had a sheath to sample flow ratio of 10:1.5. After being drawn into the container housing the instruments, sample flow first passed through a diffusion drier and a bipolar charge neutralizer (Aerosol Dynamics Inc, Berkeley, CA.), containing four ^{210}Po strips (NRD Staticmaster 2U500, Amstat Industries Inc., Glenview, IL). The charging strips were replaced twice during the study so the strips were never older than 6 months. Particles were then size selected using the DMA and the quasi-monodisperse sample flow was split and sent to the CPC (1 LPM) and CCNC. The CCNC had a total flow of 0.5 LPM with a sheath to sample flow rate ratio of 10:1. The DMA stepped through 20 different dry particle diameter settings between 14 and 350 nm and measurements were made at each size for 30 s. The DMA midpoint diameters were chosen such that $d\log_{10}D_p$ was approximately constant. After stepping through all sizes, the CCNC supersaturation was changed and the DMA size steps were repeated.

Supersaturation (s = RH – 100%) inside the CCNC is controlled by the temperature gradient (ΔT) along the growth column and flow rate through the column. The temperature of

the column wall is controlled and increases in the direction of air flow. The walls of the flow column are also wetted, leading to RH = 100% along the interior surface of the column. Because water vapor diffuses faster than heat, a particle at the centerline of the flow column will experience water vapor concentration originating from a warmer region of the column wall than the temperature at the centerline [*Roberts and Nenes*, 2005]. Thus, supersaturation is achieved inside the CCNC growth column. For a given flow rate and temperature gradient, the *s* value along the center of the column is approximately constant. The *s* value at the centerline can be altered by changing the flow rate through the column or by changing ΔT, with higher values resulting in higher *s* [*Roberts and Nenes*, 2005]. The latter method was used during BEACHON with five different ΔT settings: 4, 8, 12, 16 and 19 °C.

A full cycle, stepping through all 20 DMA size bins at each of the 5 CCNC ΔT settings, took about 75 min after which there was a five minute delay to allow the CCNC column to return to the lowest ΔT setting. All DMA and CCNC settings were controlled automatically by a LabVIEW program (National Instruments, Austin, TX).

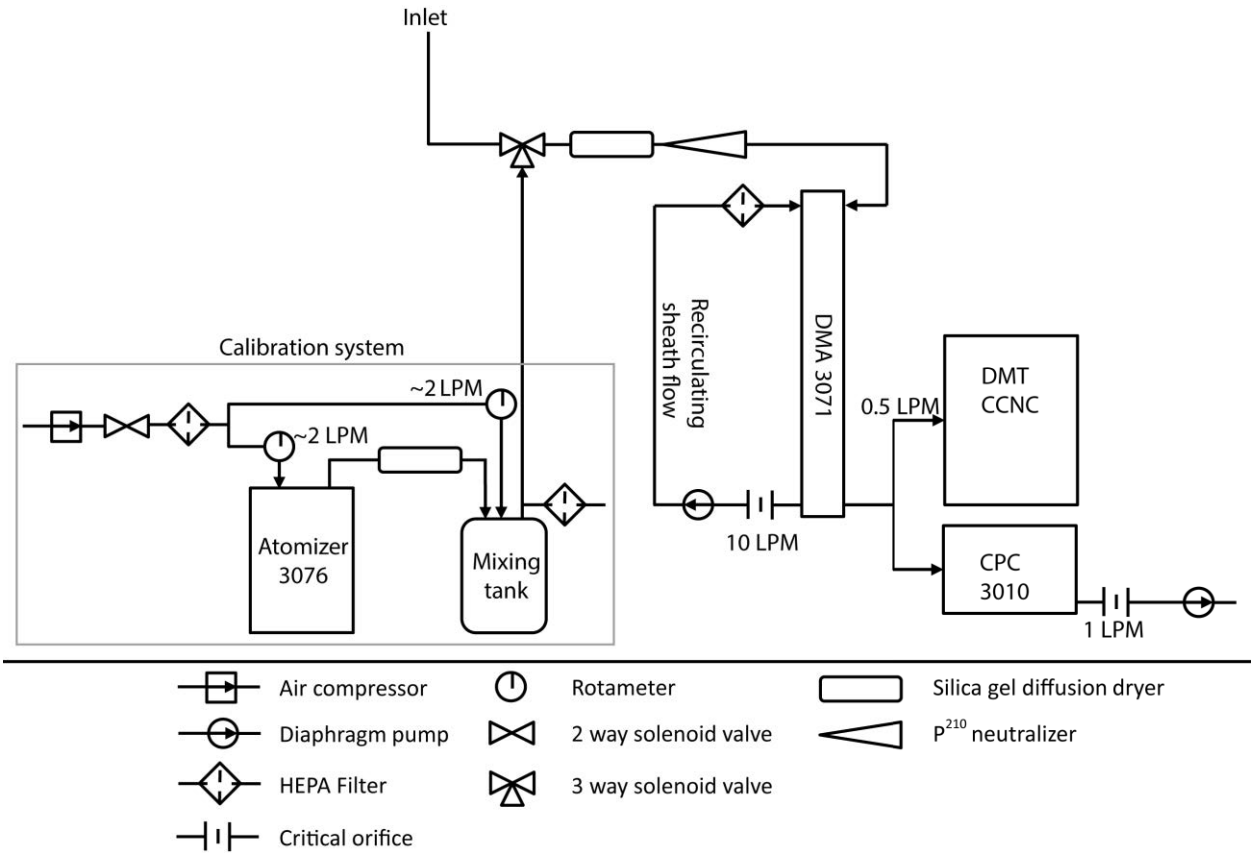

Figure 3.2 Diagram of size selected CCN measurement system.

The *s* inside the CCNC flow column was determined for each ΔT setting by calibrations performed with ammonium sulfate aerosol generated using a TSI 3076 atomizer [*Petters et al.*, 2009b; *Rose et al.*, 2008]. For each calibration scan, data from the CCNC and CPC were used to generate CCN activation curves (the fraction of particles that activate as CCN at the set ΔT as a function of dry particle diameter). The activated fraction was fit with a Gaussian cumulative distribution function weighted by the Poisson counting statistics in each size bin, and the midpoint of these curves, the diameter corresponding to 50% activation, was taken as the critical activation diameter (D_c). The critical supersaturation (s_c), the supersaturation at which the particle activates into a droplet, corresponding to this dry diameter was then determined using

Köhler theory and the thermodynamic properties of ammonium sulfate aqueous solutions as prescribed by the Aerosol Inorganics Model [*Clegg et al.*, 1998]. Calibrations were performed automatically at each of the five CCNC ΔT settings slightly less than once per day (time between repeat calibrations at the same ΔT was about 27 hr). All CCNC data were interpreted using the most recent calibration point at the same ΔT setting. Table 3.1 shows the average and one standard deviation *s* value for each ΔT setting for the entire year-long study period as well as the associated range in the hygroscopicity parameter, κ [*Petters and Kreidenweis*, 2007], calculated from the standard deviation in *s*. Table 3.1 also lists D_c values for a particle with a κ of 0.2 at the average *s* values.

Table 3.1 Study average (± 1 standard deviation) supersaturation (*s*) values determined from ammonium sulfate calibrations at each CCNC ΔT setting and corresponding critical activation diameters (D_c) for a particle with $\kappa = 0.2$ as well as the range of κ, from the range in *s* at the D_c.

ΔT [°C]	*s* [%]	D_c (κ = 0.2) [nm]	± in κ (from ± in *s*)
4	0.14 ± 0.01	152 ± 14	0.06
8	0.36 ± 0.01	81 ± 3	0.02
12	0.56 ± 0.01	60 ± 2	0.01
16	0.78 ± 0.06	47 ± 5	0.07
19	0.97 ± 0.06	42 ± 3	0.05

Because of differences between ambient and trailer temperature, as well as heating inside the CCNC column, some volatile organic species may have been lost (see chapter 4 for theoretical discussion of aerosol volatility), thus introducing a bias into the measurements [*Asa-Awuku et al.*, 2009; *Poulain et al.*, 2010]. Any loss of organic material, which has generally low

hygroscopicity, would enhance the importance of more hygroscopic species such as ammonium sulfate in the aerosol. Ammonium nitrate is also volatile and could evaporate at the trailer temperatures. Unlike organic components, however, ammonium nitrate is highly hygroscopic and any loss should lead to a decrease in κ [Petters and Kreidenweis, 2007]. Large changes in either volatile organics or ammonium nitrate should be detectable through a correlation between temperature and κ. I observed no such correlations; however, because the trailer temperature remained roughly constant, I cannot fully test this hypothesis. Further studies, using an experimental configuration specifically designed to look for such effects, are needed in order to better understand the role of volatilization in influencing CCN measurements of ambient aerosol.

There were no significant instrument problems with the CCNC throughout the year-long or RoMBAS study periods. There were, however, several failures of the CPC, and several different CPC's were used during the studies. A TSI 3010 was used from March 12 – June 6, a TSI 3760 from June 10 – June 18, a different TSI 3010 from June 24 – July 8, and finally a third TSI 3010 from July 8 through the end of the year-long study and during BEACHON-RoMBAS. When changing CPCs, no changes were observed in measured aerosol concentration due to differences in CPC counting efficiency.

3.2.4. Hygroscopicity parameter: κ

I use the hygroscopicity parameter, κ, presented by *Petters and Kreidenweis* [2007] to describe the hygroscopicity of the aerosol measured during BEACHON. Köhler theory, which defines the saturation ratio, S, over a droplet can be written in terms of κ as follows:

$$S(D) = \frac{D^3 - D_d^3}{D^3 - D_d^3(1-\kappa)} \exp\left(\frac{4\sigma_{s/a} M_w}{RT\rho_w D}\right) \qquad \textbf{Eq 3.1}$$

where D and D_d are wet diameter and dry diameter, $\sigma_{s/a}$ is surface tension of the air-water interface, assumed to be equal to the surface tension of water, $\sigma_w = 0.072$ J m^{-2}, R is the universal gas constant, T is temperature and M_w and ρ_w are the molecular weight and density of water. The maximum of Eq 3.1 is the critical saturation ratio, S_c, from which critical supersaturation ($s_c = (S_c - 1) \times 100$) can be calculated. For a given particle size a higher κ will result in a lower s_c. That is, the particle requires a lower supersaturation to activate as a CCN.

I followed the procedure presented by *Petters et al.* [2009b] to calculate κ values from the CCNC and CPC data. First, both the number distributions measured by the CCNC and CPC (example distributions shown in Figure 3.3) were corrected for multiply charged particles. Because the measurements only went up to 350 nm and there was no impactor on the DMA inlet, there could be some unconstrained contribution from multiply charged particles with diameters larger than the upper end of the measured distribution. However, at the s values used during this study I am concerned with particles with critical activation diameters of about 150 nm and smaller (see Table 3.1). At the DMA flow settings used here, a particle larger than 350 nm would need to carry an electrical charge of four to have sufficient mobility to be sized smaller than 150 nm. However, it should be noted that for particles larger than ~350 nm, the fraction of singly-charged particles decreases while the fraction of multiply charged particles increases. Thus, it is possible that the particles sent to and activated in the CCNC, particularly at the lowest supersaturation, may reflect the composition and hygroscopic properties of particles larger than 350 nm.

After inverting the CPC and CCNC data I calculated CCN activated fraction (open circles in Figure 3.3), fit these with a Gaussian cumulative distribution function (dashed line in Figure 3.3) and found critical activation diameters (solid circle in Figure 3.3) as described above for the ammonium sulfate calibrations. The curve fitting routine not only returned the 50% activation diameter, assumed to be the critical activation diameter, but also the uncertainty in this parameter weighted by the Poisson counting statistics. The critical activation diameter for each scan was then used along with the s inside the CCNC to determine κ using Eq 3.1 as follows. For a specified κ and D_d, wet diameter was varied iteratively until the maximum of Eq 3.1 was found. This maximum supersaturation is the critical supersaturation. This process was repeated for a 2D matrix of geometrically spaced D_d and κ values to construct a lookup table that relates s_c, D_d, and κ. Kappa of the sampled aerosol was then found from a set of measured D_d and s_c by performing a four point nearest neighbor interpolation in the lookup table.

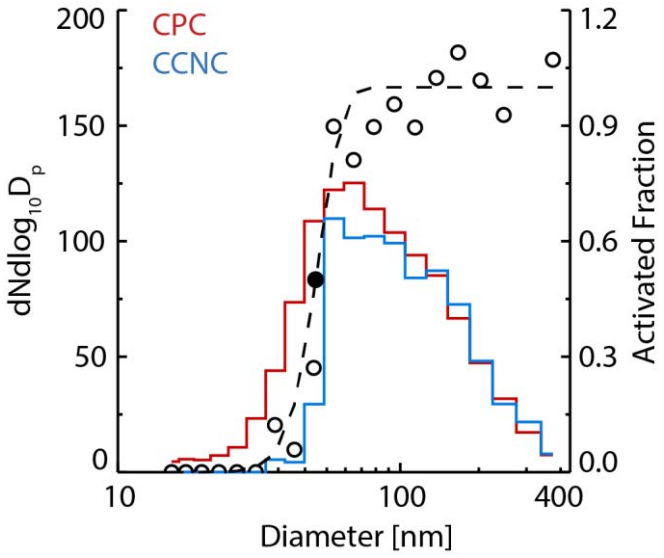

Figure 3.3 Measured aerosol (red) and ccn (blue) distributions and calculated activated fractions (black). The dashed line is the activated fraction curve fit and the solid black circle is taken as the critical activation diameter.

3.2.5. BEACHON Results

3.2.5.1. Seasonal cycle of kappa and CCN

Figure 3.4 shows daily averaged κ values determined at the five CCNC *s* settings for the entire year-long study period. Gray lines show daily standard deviation (note that this is showing the daily variability in κ, not the Poisson-counting uncertainty in κ). Breaks in the timeline are due to the instrument malfunctions mentioned above. Figure 3.4 also shows the corresponding changes in critical activation diameter at each *s* setting. Daily-averaged κ for sub-100 nm particles (s = 0.36 – 0.97%) showed only small seasonal changes with values remaining ~0.15 for much of the study. To place these results in context, typical values of κ determined from laboratory measurements are 0.5 - 1.4 for hygroscopic salts such as ammonium sulfate and ammonium nitrate, ~0.1 for fresh secondary organic aerosol and ~0 for nonhygroscopic, wettable components [*Petters and Kreidenweis*, 2007; *Prenni et al.*, 2007]. Studies have also been performed to determine κ values of ambient aerosol in locations dominated by BSOA. For example, *Gunthe et al.* [2009] report an average κ value of 0.15 for measurements during the organic-aerosol-dominated wet season in the Amazon rainforest, while *Sihto et al.* [2010] and *Cerully et al.* [2011] found average κ values of 0.18 and 0.20, respectively, at a forested, boreal site in Hyytiälä, Finland.

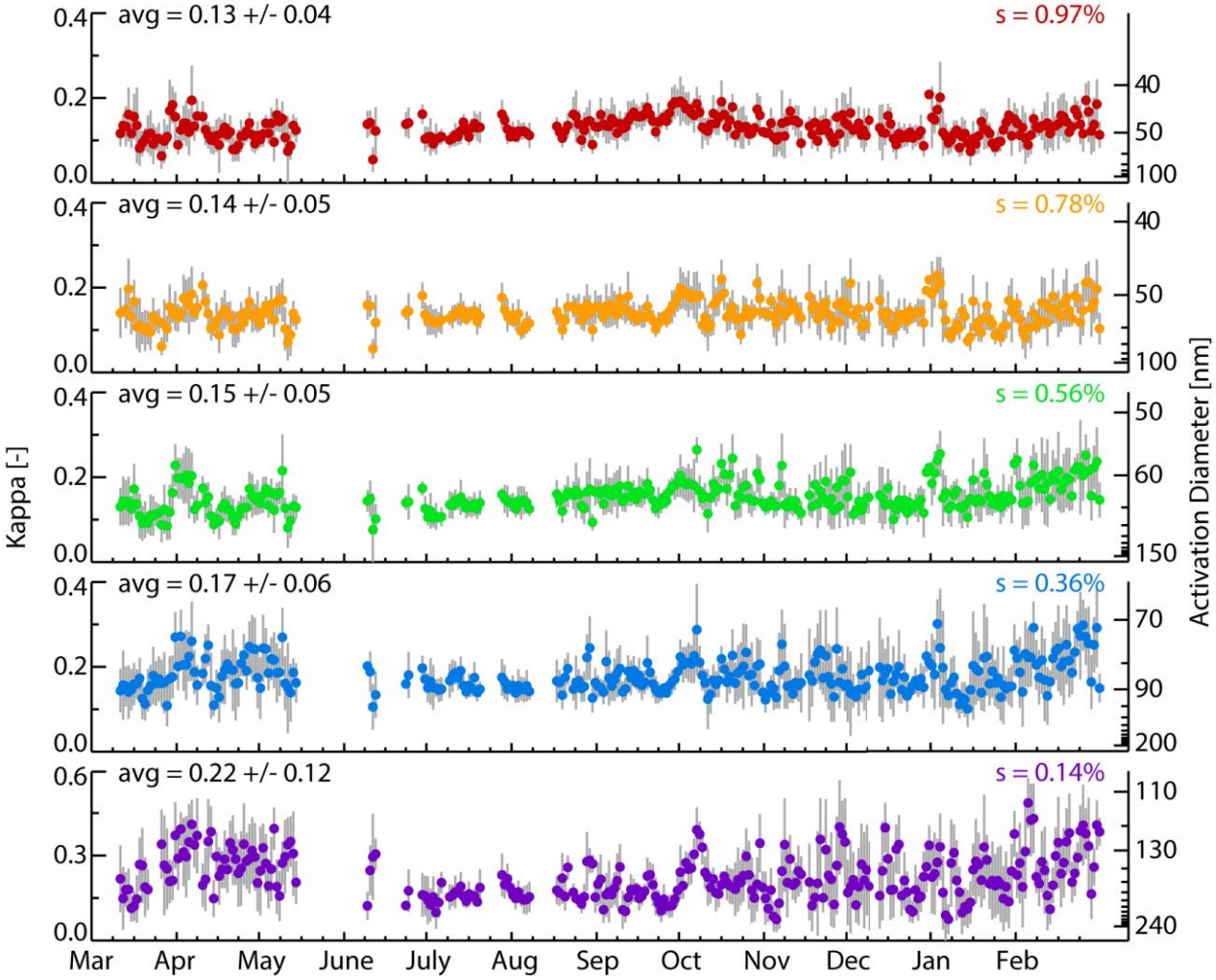

Figure 3.4 Daily averaged κ values at each supersaturation setting for the year-long study period. Bars indicate daily standard deviation in κ.

While there was little change in κ values at the higher s settings, at s = 0.14% there was a noticeable decrease in daily averaged κ during the summer. Since κ is tied to the chemistry of the aerosol, this indicates some shift in chemical composition in the particles that activated at the lowest s setting; i.e. particles with diameters of ~150 nm and larger. During the summer there was also much less variability in κ for the s = 0.14% measurements than during the other seasons. Much of the higher variability in κ was due to the low CCN number concentrations during the winter months, especially at the lower s settings where fewer particles activate as

CCN. However, even with this large variability, the decrease in κ at s = 0.14% from spring to summer, and the subsequent increase in κ in the fall, was statistically significant at the 99% confidence level using a two-tailed t-test.

Study average (± 1 standard deviation) κ values, determined at each s setting, are also given in Figure 3.4. At higher s settings, κ values were similar to those determined in laboratory SOA studies [e.g. *Prenni et al.*, 2007, *Duplissy et al.*, 2008, *King et al.*, 2010]. There was a slight increase in average κ with decreasing s, from 0.13 ± 0.04 at s = 0.97% to 0.22 ± 0.12 at s = 0.14%. These means are statistically different, with 99% confidence intervals, determined using the t-statistic, of ± 0.002 and 0.004 respectively. This shift in κ indicates a size dependent chemical composition with the largest particles, characterized in the s = 0.14% scans, having slightly higher hygroscopicity. This increased hygroscopicity of the largest particles may be due to the fact that larger particles are likely more aged and may have been cloud processed, and thus may have a larger inorganic component [*Fors et al.*, 2011].

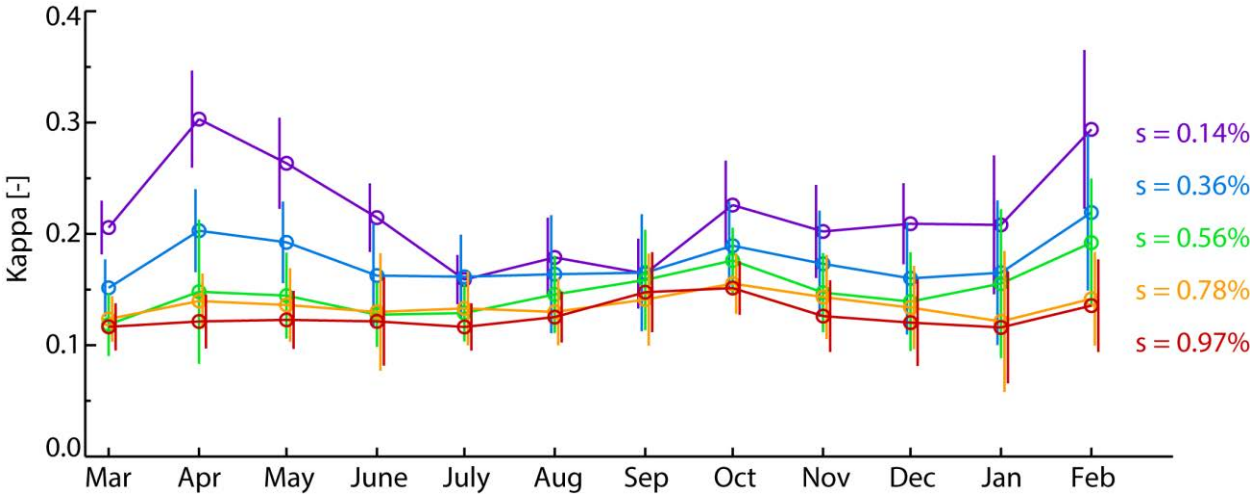

Figure 3.5 Monthly averaged κ at the five supersaturation settings. Bars represent monthly averaged uncertainty in κ from curve fitting.

Seasonal differences in κ as a function of s become more apparent when examining monthly averaged κ values (Figure 3.5). Error bars in Figure 3.5 show the monthly averaged uncertainty in κ calculated from the uncertainty in activation diameter reported by the curve fitting routine. During July-September, there was essentially no difference in κ at the different CCNC measurement settings. For example, during the month of September the range in κ from the lowest to highest s setting was only 0.16 – 0.15, with uncertainties in κ of ~0.03 at both settings. The range in κ increased later in the fall and winter months and had a maximum during the spring ($\Delta\kappa$ = 0.18 in April). These differences in April monthly averaged κ values at the highest and lowest s are also statistically significant at the 99% confidence level using a two tailed t-test. At s = 0.14%, κ showed the largest seasonal variability with a peak value of 0.3 in April, steadily decreasing to a minimum value of 0.16 in July and September, and then increasing back to 0.3 in February. Kappa at higher s showed some similar features; however, there was decreased seasonal variability with increasing s. The seasonal changes in κ indicate that, on average, the aerosol population during the summer months was less hygroscopic than in the spring and fall, especially at the larger diameters. This observation would be consistent with an increase in aerosol organic fraction during this time period, as organic species are less hygroscopic than soluble inorganic salts. However, other aerosol constituents, such as black carbon and dust species, also have a low hygroscopicity and increases in their relative contributions to the submicron aerosol mass concentrations can also reduce the observed κ.

In addition to changes in aerosol hygroscopicity during the study, there were also large changes in CCN number concentration. Figure 3.6 shows monthly averaged CCN number concentrations as well as the total aerosol number concentration (in the range of D_p = 14 – 350 nm) determined from CPC measurements. Total aerosol concentrations were highest in July and

dropped to their lowest value in December. There was a similar seasonal variability in aerosol volume concentrations calculated from number concentration measurements (Figure 3.7). The January median value was 0.31 μm^3 cm^{-3}, whereas the July value was 1.6 μm^3 cm^{-3}. For reasonable aerosol densities in the range 1-2 g cm^{-3}, these estimates of seasonal variations in total submicron mass concentrations are consistent with those in the limited data set of *Schichtel et al.* [2008], who reported aerosol carbon-only concentrations in the Rocky Mountain region of ~2 µg m^{-3} during the summer, and ~0.5 µg m^{-3} during the winter. Note that these values must be multiplied by an appropriate factor to account for the molecular form of C (~1.8 if organic dominated [*Turpin and Lim*, 2001], ~1 for elemental carbon).

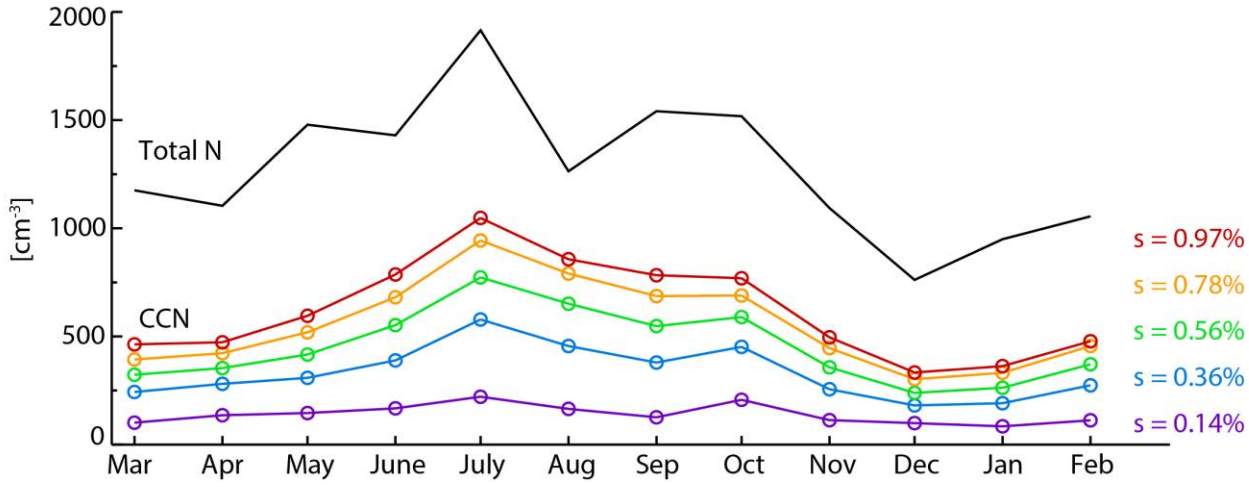

Figure 3.6 Monthly averaged total aerosol (black) and CCN (colored) concentrations.

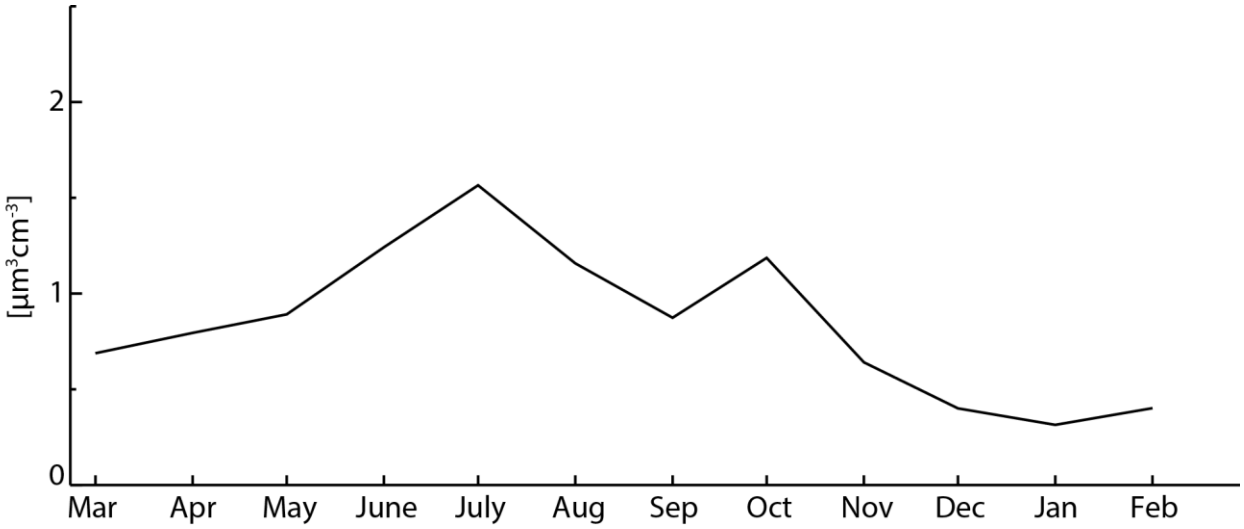

Figure 3.7 Monthly median aerosol volume concentrations, $14 < D_p < 350$ nm.

Concentrations of CCN followed a similar trend and were three times higher in July than December for all but the $s = 0.14\%$ measurements, for which they were roughly double. The monthly averaged activated fraction (the fraction of total particle number concentration measured by the CPC that activated as CCN) showed a slightly different trend than that of CCN concentration (Figure 3.8). Instead of peaking in July, the maximum activated fraction (again excluding $s = 0.14\%$ measurements) occurred in August, with a value of 0.68 at $s = 0.97\%$. At the $s = 0.14\%$ setting, activated fraction showed essentially no seasonal change, remaining around 0.1 for the entire study. Since aerosol size measurements only went up to 350 nm, the contributions of larger particles to the total number concentrations, and hence activated fraction, are not included. However, even in the presence of an event having a large-diameter mode (e.g., a dust event), the contributions to the total number concentrations at a particular s are expected to be negligible, except perhaps for the $s = 0.14\%$ mode.

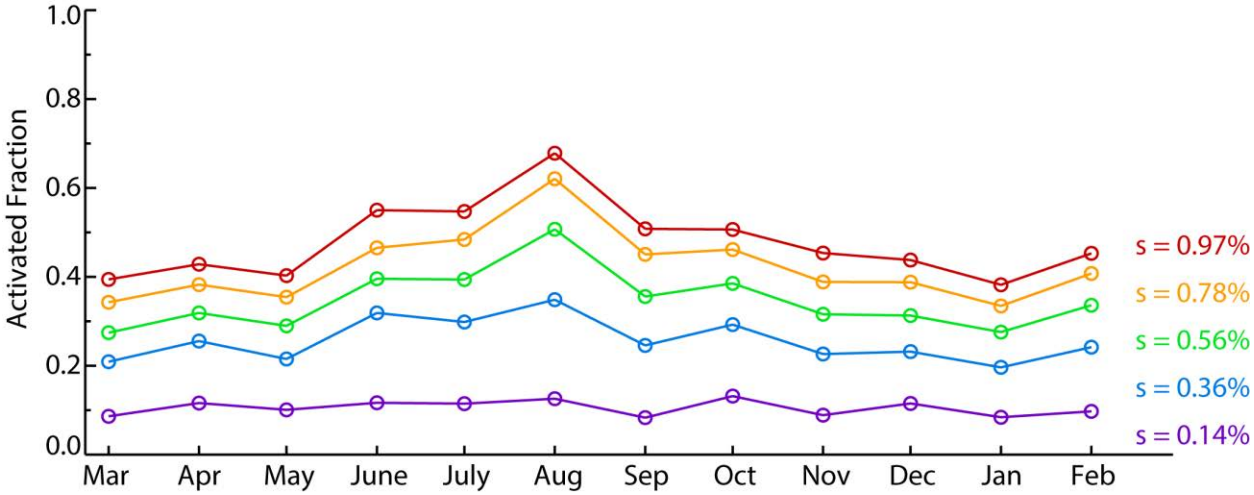

Figure 3.8 Monthly averaged activated fractions.

Number concentrations of CCN should be strongly correlated with total aerosol number concentrations if κ and the size distribution remain the same. Therefore, given that average κ values were lower in summer, it might seem surprising that there is a maximum in the fraction of particles that activate as CCN during this time. This apparent discrepancy can be reconciled by examining the changes in aerosol size distribution during the study. Figure 3.9 shows the monthly averaged geometric mean diameter (D_{gn}) and geometric standard deviation (σ_{gn}) for the aerosol number distributions. There was a clear increase in D_{gn} during the summer, peaking in August. Since CCN activation is a function of both hygroscopicity and particle size, this increase in D_{gn} was sufficient to increase the activated fraction to a maximum during the summer, even with the decrease in κ.

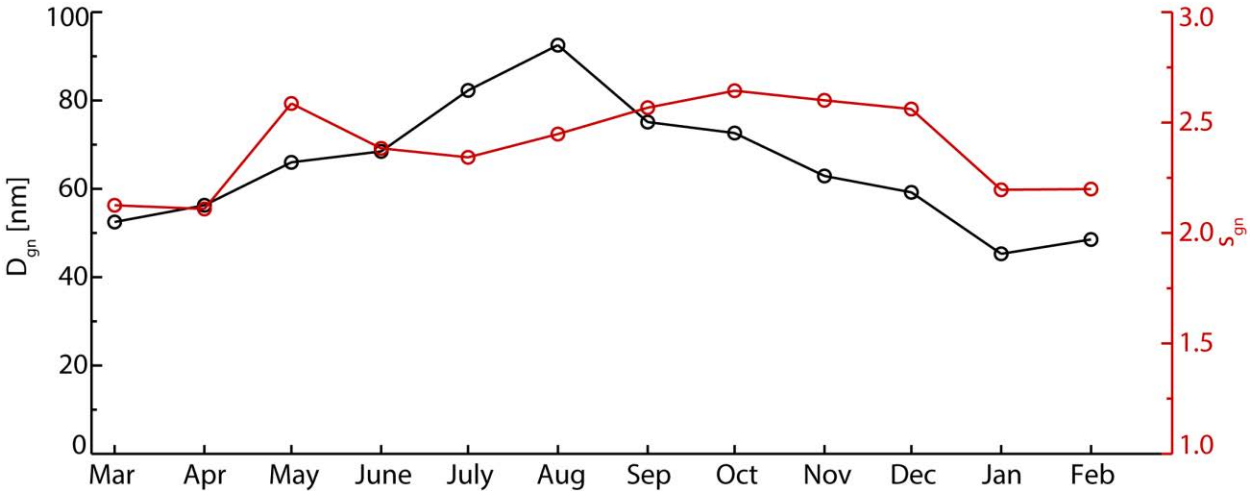

Figure 3.9 Geometric mean diameters (black) and geometric standard deviations (red) for the monthly averaged aerosol number distributions, $14 < D_p < 350$ nm.

3.2.5.2. Aerosol composition and hygroscopicity

Aerosol hygroscopicity is a function of aerosol chemical composition and the κ values for many individual compounds, both inorganic salts and secondary organic species, have been determined from laboratory studies. Thus, while there are no aerosol composition data from the year-long BEACHON study, κ values can be used as an indicator of bulk aerosol composition during this study.

Petters and Kreidenweis [2007] showed that the κ of a mixture follows a simple mixing rule:

$$\kappa = \sum_i \varepsilon_i \kappa_i \qquad \textbf{Eq 3.2}$$

where ε_i and κ_i are the volume fraction and hygroscopicity parameter of each individual component in the aerosol. This mixing rule has been shown to apply to mixed organic and

sulfate particles [*King et al.*, 2007; *King et al.*, 2010] to determine κ of the resulting aerosol. *Gunthe et al.* [2009] used this approach to calculate κ based on measurements of aerosol composition from an AMS in the Amazon rainforest. They found good agreement between κ calculated from a two component (organic and sulfate) composition assumption and that calculated from size-resolved CCN measurements, with submicron organic mass fractions of 0.65 - 0.95 during the Amazonian wet season.

I followed this same approach, assuming a two component aerosol containing organic species ($\kappa_{organic} = 0.1$) and inorganic salts ($\kappa_{inorganic} = 0.6$, for predominantly ammonium sulfate aerosol). Sulfate aerosol from anthropogenic sources has been shown to be present year round in the Rocky Mountain area [*Levin et al.*, 2009; *Malm et al.*, 2004; *Malm et al.*, 1994], likely as a component of the regional background aerosol. As shown by *Levin et al.* [2009] organic and sulfate species generally represent the dominant mass fractions of the $PM_{2.5}$ aerosol in the region.

The low κ values found during this study indicate that organic species dominate the submicron aerosol mass in Manitou Forest throughout the year. The slightly higher, and more variable, κ values at larger sizes (lower *s*) suggest some size and seasonal dependent changes in aerosol hygroscopicity; still, average κ values indicate that organic mass fraction ($X_{organic}$) was ~0.8 or greater for sub-350 nm aerosol throughout the study. While there is some uncertainty in the value assumed for $\kappa_{organic}$ [*Petters et al.*, 2009c], the range in this value is low, generally $0.05 < \kappa_{organic} < 0.2$. Thus, even if the organic aerosol makeup varies considerably over the year, changes in measured κ would be small for organic dominated aerosol, consistent with the observations. Even for the extreme case of $\kappa_{organic} = 0$, monthly averaged κ values from the BEACHON study indicate that organic species were still the dominant component with $X_{organic} >$

0.5 for all diameters and > 0.75 for the sub-100 nm aerosol (determined from $s > 0.14\%$ measurements).

3.2.5.3. Hygroscopicity and chemistry closure during BEACHON-RoMBAS

While there are no chemical data for the year-long BEACHON study, aerosol chemical composition was measured during the BEACHON-RoMBAS intensive campaign. Measurements were made with the University of Colorado (CU) AMS which measures non-refractory aerosol mass between ~30 and 700 nm in aerodynamic diameter. The AMS data for BEACHON-RoMBAS study were provided by Brett Palm who operated the instrument and performed all data analysis and quality controls. Because both aerosol composition and size resolved CCN concentrations, from which κ can be calculated, were measured during BEACHON-RoMBAS, these data can be used to validate the assumption that aerosol hygroscopicity can be modeled using a two component (organic/inorganic) system, at least in this location. In this section I present aerosol composition derived from CCNC measurements and measured directly by the AMS.

Figure 3.10 shows daily average (± 1 standard deviation) κ values during BEACHON-RoMBAS at the five different CCNC s_c settings. This plot is similar to Figure 3.4, but for the RoMBAS time period. Similar to the summer months of the year-long study, aerosol hygroscopicity during BEACHON-RoMBAS showed little variability with consistently low κ values. Also similar to the year-long results, at all s_c settings κ values were more similar to those reported for secondary organic species [*Prenni et al.*, 2007] than hygroscopic inorganic species such as ammonium sulfate [*Petters and Kreidenweis*, 2007]. While κ was low at all settings,

there was a small increase in κ with decreasing s_c, which corresponds to a larger activation diameter. That is, there appears to be some change in aerosol composition with size, with larger particles containing a larger fraction of more hygroscopic material.

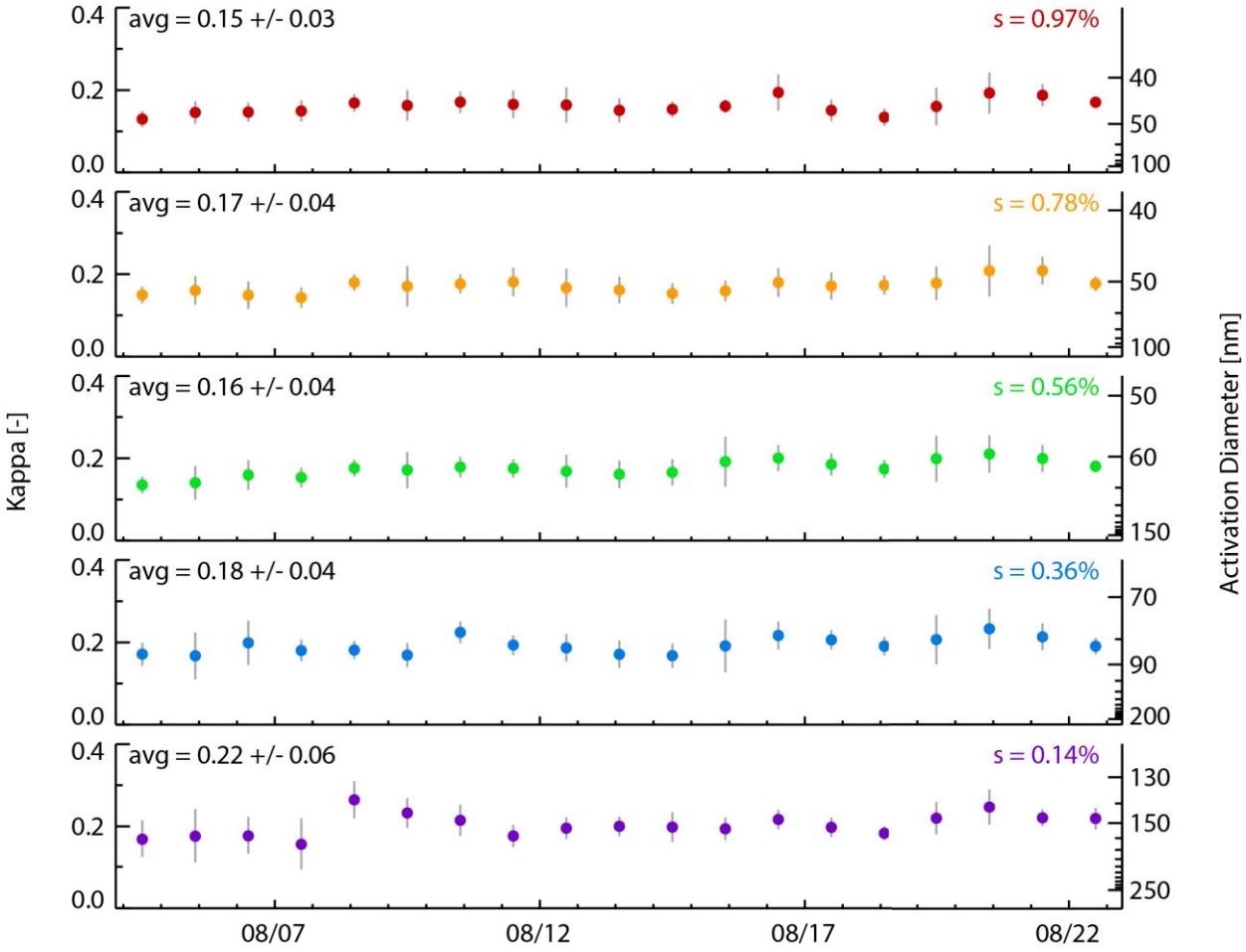

Figure 3.10 Daily averaged κ values at each supersaturation setting during BEACHON-RoMBAS. Bars indicate daily standard deviation in κ.

Using the assumptions discussed above I calculated aerosol composition from BEACHON-RoMBAS study averaged κ values listed in Figure 3.10. Figure 3.11 shows the study averaged organic mass fraction ($X_{organic}$) as a function of study averaged critical activation diameter. Aerosol mass was calculated from aerosol volume assuming densities of 1.4 [*Bahreini et al.*, 2005; *Kroll and Seinfeld*, 2005; *Poulain et al.*, 2010] and 1.8 g cm^{-3} [*Tang*, 1996] for the organic and inorganic fractions respectively. As can be seen, the organic mass fraction decreased slightly with increasing activation diameter as expected. The gray shading shows the range in organic mass fraction with different assumptions about organic aerosol hygroscopicity. I allowed $\kappa_{organic}$ to vary between 0, completely non-hygroscopic, and 0.15. A $\kappa_{organic}$ value of 0 provides a lower bound for $X_{organic}$. Studies have shown that κ of more oxidized secondary organic species can be as high as 0.22 [*Chang et al.*, 2010]. However, the lowest average κ value determined during BEACHON-RoMBAS was only 0.15. Assuming that $\kappa_{organic}$ does not change over the course of the study, or as a function of size, this limits the maximum assumed $\kappa_{organic}$ value to 0.15. Assuming a value higher than this would lead to a physically meaningless negative inorganic fraction for some time periods. However, regardless of the assumption made about the hygroscopicity of the organic material during this study, Figure 3.11 shows that this fraction dominated the aerosol at all measured sizes. Further, given the steadiness of κ during BEACHON-RoMBAS (Figure 3.10) it appears that organics were the dominant aerosol component throughout the study period.

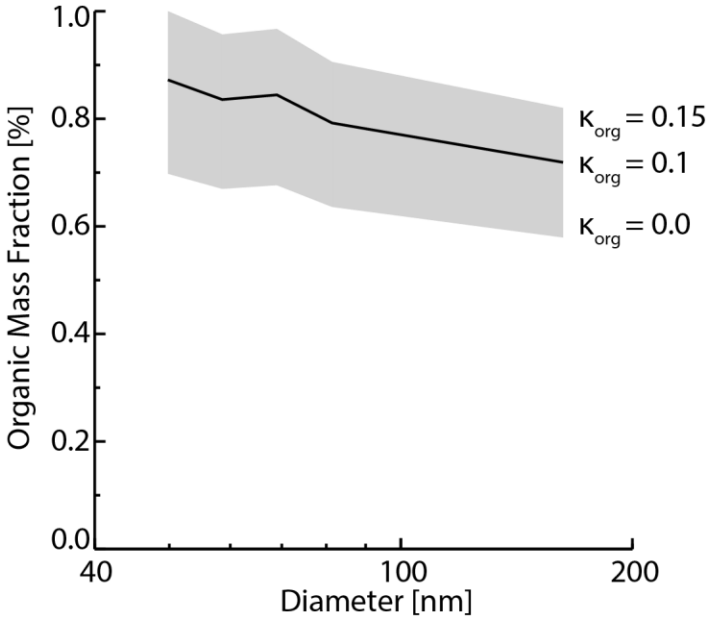

Figure 3.11 Aerosol organic mass fraction calculated from κ during BEACHON-RoMBAS. Grey shading shows range in this value do to the possibly range in $\kappa_{organic}$.

Study averaged aerosol composition data measured by an AMS are shown in Figure 3.12. The AMS data were averaged over the same time period as the CNNC data above. While the AMS can speciate a number of organic and inorganic compounds I have lumped the data into two components to compare to the two component composition estimated from size resolved CCNC measurements. The inorganic component consists of the measured SO_4^{2-} multiplied by 1.37. This assumes that all the SO_4^{2-} is present as ammonium sulfate, an assumption justified by the fact that bulk AMS measurements indicated the presence of enough NH_4^+ to fully neutralize the measured SO_4^{2-} (plots of measured NH_4^+ versus the amount need to fully neutralize the aerosol are shown in Appendix 2). Nitrate mass was extremely low, often below the detection limit. When present it appeared to be in the form of organic nitrate [*Palm*, personal communication], and was thus added to the organic mass. All other species were negligible and were not included. As expected from aerosol hygroscopicity measurements, the AMS data

shown in Figure 3.12 indicate that the aerosol was predominantly organic during BEACHON-RoMBAS, especially at smaller sizes. At larger diameters the inorganic component did increase, but the measured aerosol mass was still mostly organic. Figure 3.12 also shows κ values calculated from the AMS data.

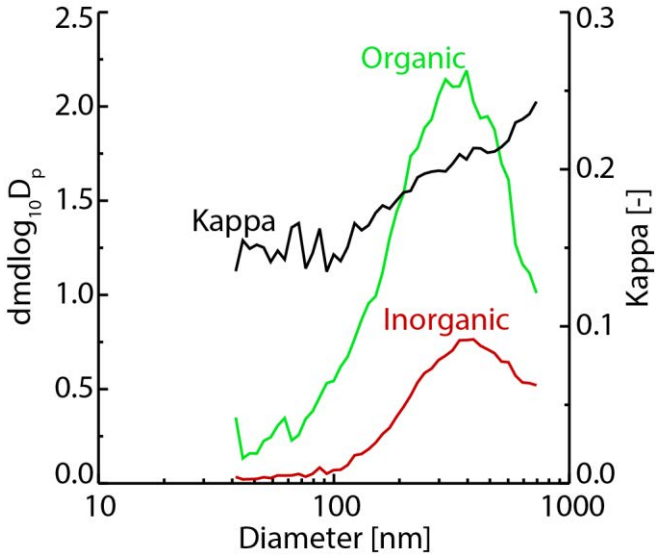

Figure 3.12 Study averaged organic (green) and inorganic (red) mass distributions measured by an AMS as well as κ (black) calculated from these data (data provided by Brett Palm).

To directly compare aerosol composition measured by the AMS and calculated from κ values, Figure 3.13 shows study averaged organic mass fractions determined from the two methods. The black line and gray shaded region are the same data shown in Figure 3.11. In the overlap region between the two measurements, $43 < D_p < 150$ nm, the agreement in organic mass fraction is good, with AMS derived $X_{organic}$ falling generally within the gray shaded area, but nearer the $\kappa_{organic} = 0.15$ values, indicated by the top edge of the gray shading. The offset between AMS and CCNC derived $X_{organic}$ values could indicate that the organic fraction had a κ

value closer to 0.15 than 0.1 during this study. However, there are also considerable uncertainties in the AMS measurements. *Bahreini et al.* [2009] reported uncertainties of 20% for AMS mass measurements. Applying this value to the RoMBAS data gives the range shaded in orange in Figure 3.13. Also note that the AMS calculated $X_{organic}$ is very variable at smaller sizes due to the low mass loadings. Given these uncertainties, these data cannot be used to precisely define $\kappa_{organic}$ during this study. However, even with the uncertainties in the AMS data and assumptions about $\kappa_{organic}$, the trend of decreasing $X_{organic}$ with increasing size is very similar between the two measurements. While the AMS has some limitations in measuring aerosol, including that it can only detect non-refractory particles between ~30 and 700 nm, it appears to capture the important species for determining aerosol hygroscopicity in this size range at this location. It is important to determine aerosol hygroscopicity for particles in this range as this is where the majority of particle number are located. As shown in Chapter 2 (Figure 2.22) almost 100% of the particle number measured during the RoMANS and GrandTReNDS studies were smaller than ~0.4 μm in diameter. These are the particles that are most important in determining the number of available CCN, and thus it is important to know their hygroscopicity.

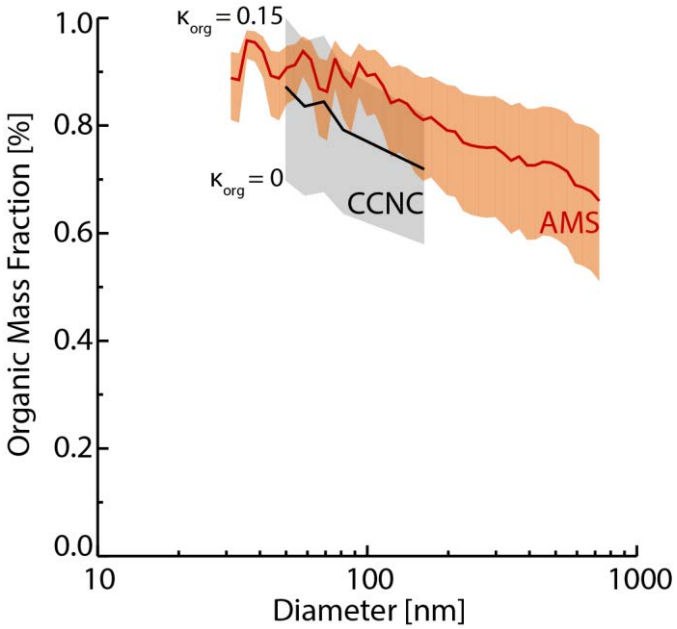

Figure 3.13 Aerosol organic mass fraction measured by an AMS (red) during BEACHON-RoMBAS as well as organic mass fraction (black) calculated from κ. Gray shading is the same as in Figure 3.11. Orange shading indicates the range in AMS derived κ resulting from the ±20% uncertainty in the size resolved AMS mass measurements.

Figure 3.14 shows daily averaged organic and inorganic distributions measured by the AMS. Similar to the study averaged values shown in Figure 3.13, organics were the dominant component of the aerosol throughout the BEACHON-RoMBAS measurement period. I used these data to calculate aerosol hygroscopicity, using the same assumptions for $\kappa_{organic}$ and $\kappa_{inorganic}$ used above, and the resulting κ values are shown in Figure 3.15. While κ values were low at all diameters and throughout the study, there was a small increase in κ with increasing size, similar to that seen with the size resolved CCNC measurements.

To more directly compare κ values calculated from CCNC and AMS measurements I plotted the κ values determined from each CCNC ΔT setting with those calculated from AMS composition at the D_c corresponding to each CCNC setting. These values are shown in Figure

3.16. While these values are within a similar range, the CCNC κ values are generally slightly higher than those calculated from AMS measurements. This again could be due to an incorrect assumption for κ_{org} or the uncertainty in the AMS measurements. An arrow in Figure 3.16 shows the average increase in AMS calculated κ values for an increase in $\kappa_{organic}$ to 0.15, from the assumed value of 0.1. The best agreement, smallest χ^2 value, between AMS and CCNC derived κ was for an assumed $\kappa_{organic}$ value of 0.13. The assumed value for organic aerosol density will also affect the κ values calculated from AMS data, and this is also indicated by an arrow in Figure 3.16. Decreasing the assumed density of the organic component to 1.0 g cm^{-3} decreased AMS κ by 0.015 on average, much smaller than the change due to $\kappa_{organic}$ uncertainty. The assumption that sulfate is present as fully neutralized $(NH_4)_2SO_4$ could also impact the calculated AMS κ values. Acidic sulfate aerosol have much higher hygroscopicities [*Petters and Kreidenweis*, 2007], as well as differences in density. However, unlike the assumptions about the organic aerosol component, the assumption that the inorganic aerosol mass is fully neutralized is supported by direct AMS measurements (Appendix 2).

The error bars for AMS calculated κ in Figure 3.16 represent the range in κ due to the 20% uncertainty in AMS mass measurements. The CCN κ error bars are from the uncertainty in curve fitting discussed above. Together, these uncertainties account for much of the scatter in Figure 3.16. The one outlier point in Figure 3.16 was from August 23rd, when organic aerosol concentrations measured by the AMS were at their lowest, resulting in the larger error bars.

From Figure 3.14 it can be seen that the AMS κ values shown in Figure 3.16 were calculated at diameters where mass loadings were very low, leading to highly variable κ values (Figure 3.15). At larger diameters, above the measureable range for the CCNC system, the AMS values are likely more certain, due to the higher mass concentrations. The CCNC measurement

is a number measurement, and is thus most reliable at highest number concentrations. The AMS, however, is most reliable at the highest mass concentrations. Therefore, comparing results from these two systems is challenging. However, the general agreement between organic fraction and κ determined from these two measurement systems justifies use of the AMS data to calculate hygroscopicity and the size resolved CCNC data to calculate two component aerosol composition.

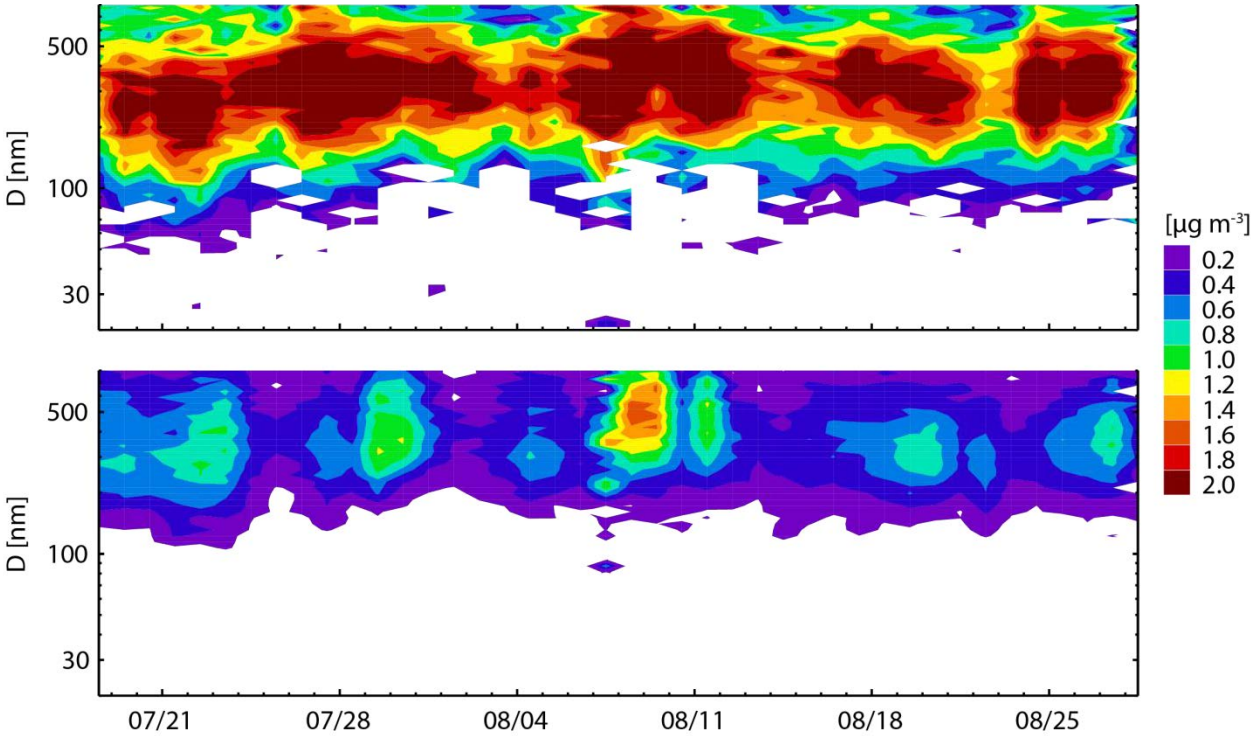

Figure 3.14 Daily organic (top) and inorganic (bottom) mass distributions measured by an AMS (data provided by Brett Palm).

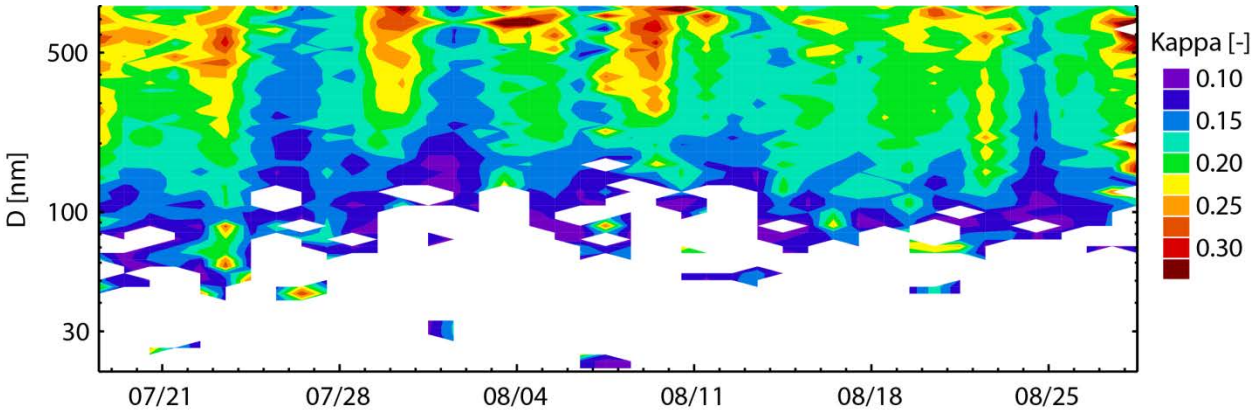

Figure 3.15 Daily κ distributions calculated from measured aerosol composition.

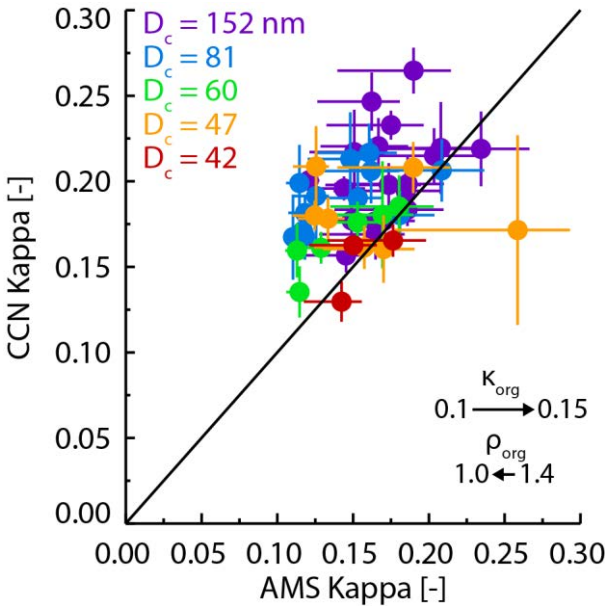

Figure 3.16 Kappa values calculated from size resolved CCNC measurements versus κ calculated from AMS measurements. The black line is the 1:1 line. Arrows indicate the change in AMS calculated kappa for the indicated changes in assumed κ_{org} and ρ_{org} values.

3.2.5.4. Seasonal cycle of aerosol composition from CCN measurements

I used the year-long CCNC data and the same method applied to the BEACHON-RoMBAS data to calculate monthly average aerosol composition distributions. These distributions are shown in Figure 3.17 with the green and blue bars showing the organic and inorganic fractions, respectively. As above, the gray shaded region shows the range in calculated organic mass fraction for variable assumed $\kappa_{organic}$ values. There was a very similar trend throughout the year-long study period as seen during the intensive BEACHON-RoMBAS campaign, with aerosol organic fraction decreasing slightly with increasing diameter. There were, however, some seasonal changes in this pattern. During July-September there was much less change in chemical composition with size. During this time period the entire size distribution was dominated by organic species with $X_{organic} > 0.8$ at all sizes. In the fall, winter and spring months, when VOC emissions, and thus BSOA production, is expected to be lower than during the summer [*Saarikoski et al.*, 2008], $X_{organic}$ decreased with size with a minimum in April. However, the smaller particles remained almost entirely organic throughout the entire study period. These results are in good agreement with the findings of *Gunthe et al.* [2009] who report submicron organic mass fractions of 0.65 - 0.95 during the Amazonian wet season. They also found a $X_{organic}$ size dependence similar to that shown here with campaign averaged $X_{organic}$ decreasing from ~0.95 at 60 nm to 0.75 at 600 nm.

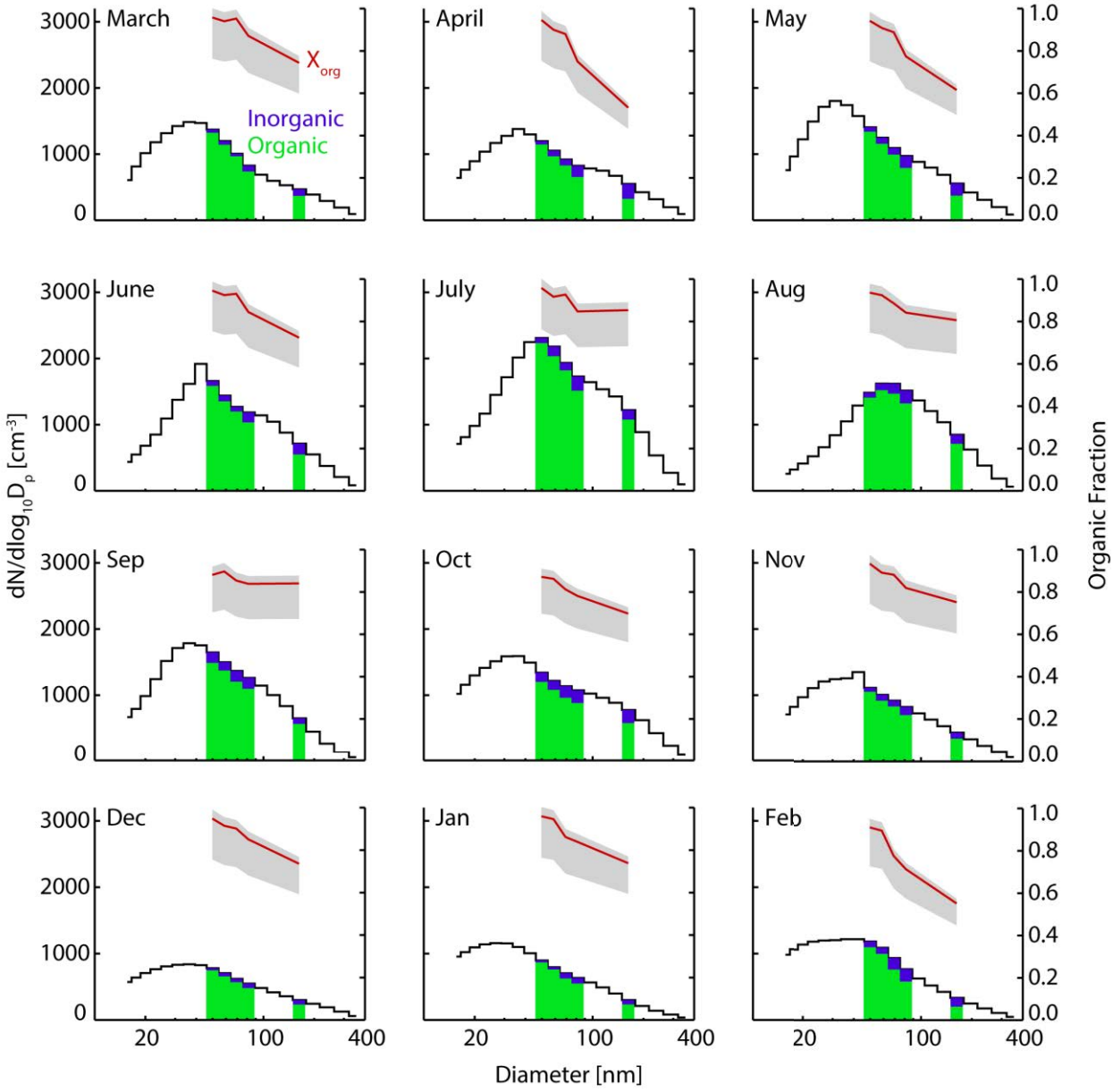

Figure 3.17 Monthly averaged aerosol size distributions (black) and two component chemical composition (green = organic, blue = inorganic) calculated from hygroscopicity measurements during the year-long study. Red lines show organic mass fraction ($X_{organic}$) and gray shading shows the range in this value due to uncertainty in $\kappa_{organic}$.

3.2.5.5. Small Particle Events

During the BEACHON measurement campaigns, seasonal cycles were observed in total particle number and CCN concentration, size distributions, hygroscopicity and calculated chemical composition. One potential contributor to all of these aerosol properties, and possible cause of the observed seasonal cycles, is new particle formation.

Throughout both BEACHON studies there were numerous examples of increases in number concentrations of the smallest measured particles, with subsequent evolution of the aerosol size distribution. In character, these occurrences were similar to new particle formation (NPF) events documented in the literature in a variety of locations worldwide [*Hallar et al.*, 2011; *Kulmala et al.*, 2004b]. *Boy et al.* [2008] presented analysis of NPF events observed at the University of Colorado Mountain Research Station, located about 100 km northwest of the Manitou Experimental Forest at an elevation of 2900 m. They divided days which showed clear NPF into two categories, A and B, both of which showed nucleation and growth of the new particles. For A-events, nucleation mode particles (3 – 20 nm) were clearly observed at the initiation of the event. For B-events, particles smaller than 6 nm were not present, but particles > 6 nm were observed. They hypothesized that for B-events nucleation began upwind with subsequent particle growth as the aerosol population was transported to the site. Finally, cases characterized by a sharp increase in particle concentration but little or no detectable growth were labeled as C, or undefined, events. Cases similar to A-, B- and C-events were observed during BEACHON. However, the BEACHON measurement setup did not extend to small enough particle sizes to clearly identify new particle nucleation, and thus A- and B-events cannot be distinguished. Because the measurements were not set up to detect new particle nucleation, and thus clearly classify the events, I will use the term "small particle event" (SPE) to discuss these

observations. *Boy et al.* [2008] also observed higher concentrations of mono- and sesquiterpenes during times of NPF and hypothesized that these organic compounds were important for particle growth. Although these compounds were not measured during the year-long study, these BVOCs previously were shown to be emitted at or upwind of the BEACHON site by *Kim et al.* [2010]. *Riipinen et al.* [2011] also showed that organic species were important in growing new particles to CCN sizes and noted the importance of biogenic organic species in this process during the summer months, when biologic and photochemical processes are most active.

Figure 3.18 shows aerosol number concentrations measured during a SPE in April 2010. In this example, typical of these events, there was a burst in particle number concentration at the smallest measured diameters in the late morning of April 14, and these particles then grew, within ~12 hr, into the accumulation mode. The sharp dip in aerosol concentration seen in Figure 3.18 just prior to the event may represent a change in air mass at the site, or rapid dilution of the ambient air by mixing from aloft; however, there was not a clear change in wind speed or wind direction just prior to the SPE. Because it is unclear whether conditions before and during the event represent the continuous evolution of the same aerosol, in the following I will examine changes in aerosol hygroscopicity and CCN concentration only during the SPE itself.

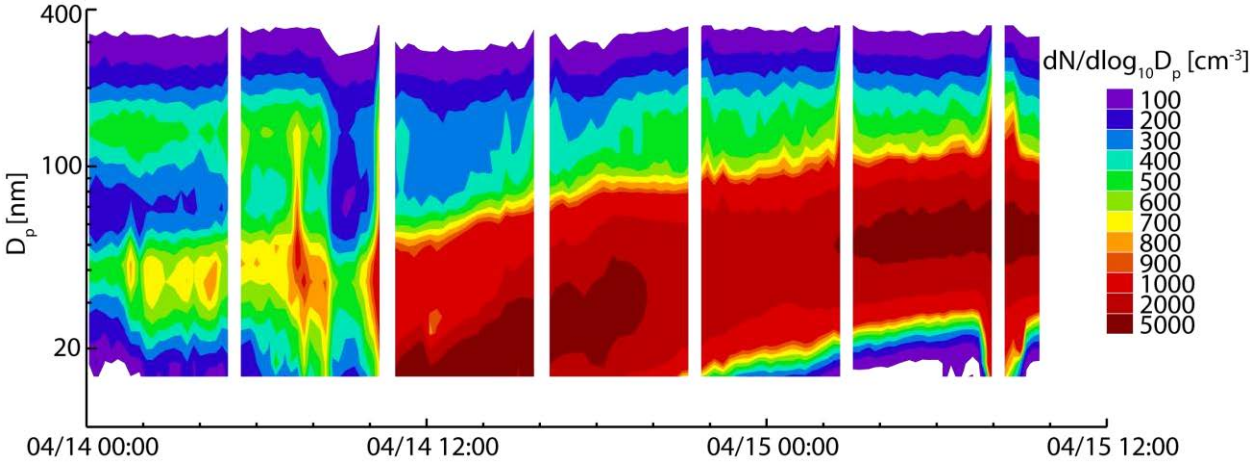

Figure 3.18 Aerosol number distribution evolution during a small particle event.

Figure 3.19 shows the total number concentration ($14 < D_p < 350$ nm) during this same time period, determined from CPC measurements, as well as CCN concentrations at each s setting. As expected, there was a large increase in total aerosol concentration during the event, increasing from less than 500 to 4500 cm^{-3}. The concentration of CCN also increased, although there was a time lag in the increase of CCN concentrations, compared to total number concentrations, as the small particles grew large enough to activate (see Table 3.1 for typical activation diameters). At $s = 0.14\%$ there was little increase in CCN concentration during this event.

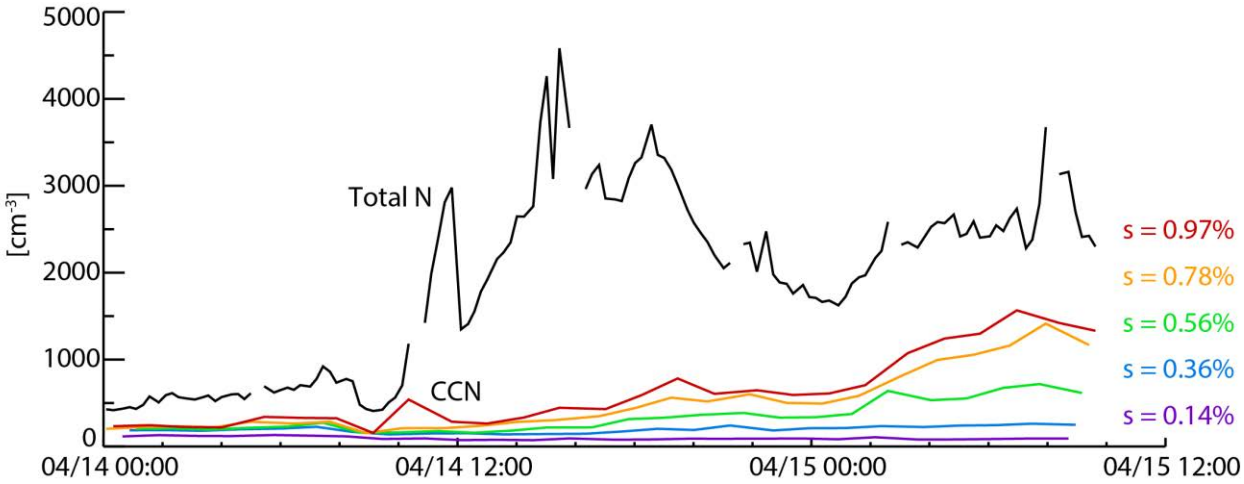

Figure 3.19 Total aerosol, $14 < D_p < 350$ nm, (black) and CCN (colored) concentrations during a small particle event.

While this event led to increases in total particle and CCN concentrations, it had only a small effect on κ. Figure 3.31 shows κ at each s during this same time period. At the three highest s settings, κ remained consistently low throughout the event, suggesting that the event did not measurably alter the chemical composition at these sizes. Kappa values at these sizes were also similar to those measured before the event. Therefore, even if there was an air mass change prior to the SPE, this shift did not correspond to a chemical change in the aerosol at the smaller sizes. Given the low κ values, it is likely that the smallest sampled particles were dominated by SOA both before and after the SPE. However, at the lowest supersaturations there was a decrease in κ as the new particles grew to sizes large enough to activate (Table 3.1), suggesting an important compositional effect for these larger particles.

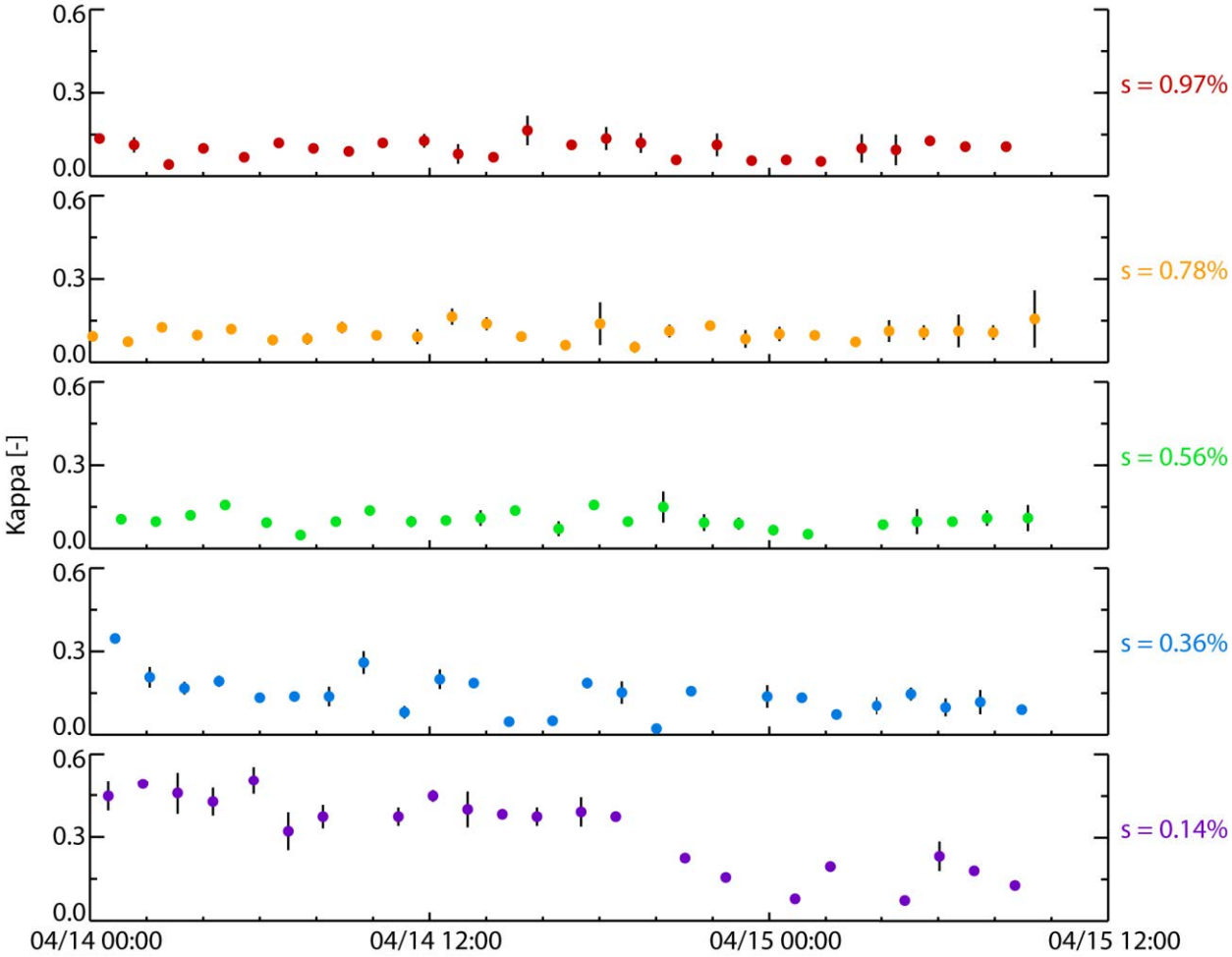

Figure 3.20 Kappa values at each supersaturation setting during a small particle event. Bars (smaller than symbols for most points) represent uncertainty in κ from curve fitting.

Small particle events were observed throughout the year-long study but occurred most frequently in the summer. From July through September, SPEs occurred on 64% of the days for which data are available. During February, this number dropped to 11%. These more frequent SPEs in the summer are likely a main cause for the increased aerosol number concentrations during this time. Figure 3.21 shows monthly averaged total number and CCN concentrations plotted against the percentage of days with SPEs in that month. There is a clear positive trend in total number concentration as would be expected if these events were due to new particle

formation. This increase in aerosol concentration also led, eventually, to an increase in mean diameter (Figure 3.22), likely resulting either from particle coagulation or condensation of volatile vapors onto new particles, or both. Since SPEs are correlated with both increases in aerosol number concentration and mean diameter, CCN concentrations also increased as the percentage of days with SPEs increased (Figure 3.21). At $s = 0.14\%$, however, there was only a small increase in the number of CCN. As seen in the example case above, SPEs led to minimal increases in CCN concentrations at low s.

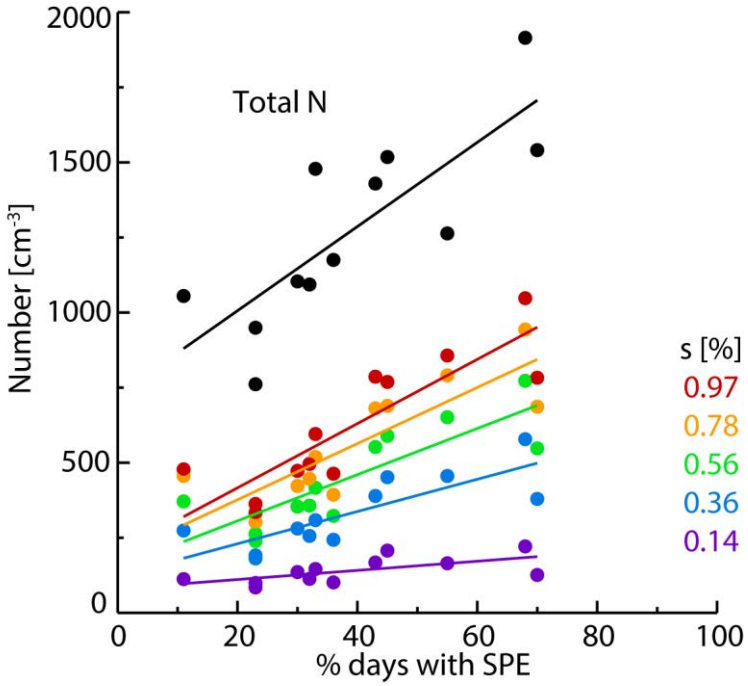

Figure 3.21 Monthly averaged aerosol number, $14 < D_p < 350$ nm, (black) and CCN (colored) concentrations plotted against the percent of days with small particle events in each month.

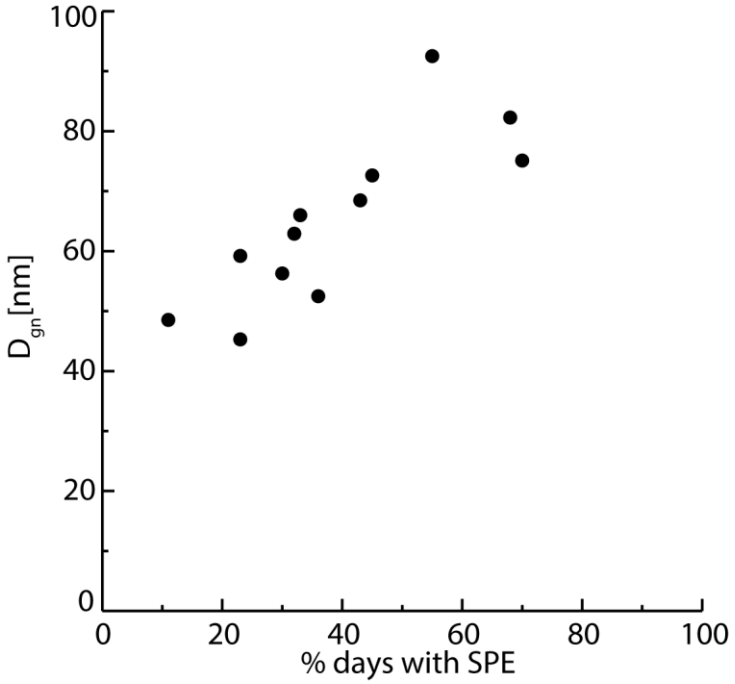

Figure 3.22 Monthly averaged aerosol number distribution geometric mean diameter plotted against the percent of days with small particle events in each month.

In addition to affecting aerosol number concentrations and mean diameters, SPEs also appeared to impact aerosol hygroscopicity at larger activation diameters. Figure 3.23 shows monthly averaged κ values plotted against the monthly percentage of days with SPEs. There was a clear decrease in κ at low s settings as the number of SPEs increased. For the higher s settings, there was no change in κ. Again, this finding is consistent with the event shown above in which there was no change in κ, and thus chemical composition, at the smaller sizes during an SPE. At the larger sizes, however, SPEs seem to increase the fraction of the aerosol population composed of lower κ species, likely organics. These particles' low hygroscopicity values led to the decreased κ values during times of high SPE. It must be noted that condensation of organic vapors onto pre-existing particles may lower κ; however, it will also increase the particle diameter. If κ of the condensing material is > 0 this increase in size will lead to an increase in CCN concentration at a given s even if the overall hygroscopicity of the particle decreases. For

condensing material with $\kappa = 0$, the decrease in particle hygroscopicity will be offset by the increase in size and lead to no change in CCN activity (see Appendix 3 for proof).

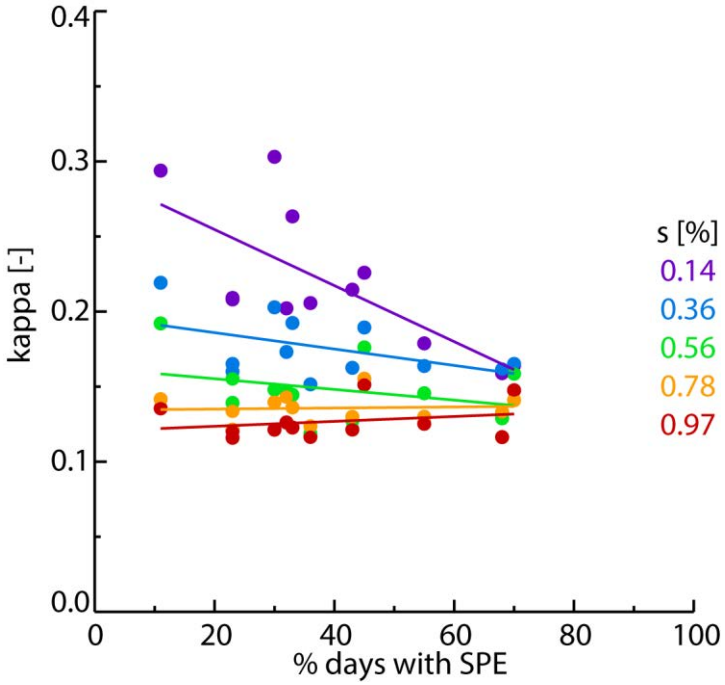

Figure 3.23 Monthly averaged κ values plotted against the percent of days with small particle events in each month.

3.2.6. Aerosol hygroscopicity during RoMANS 2010

As shown by Eq 3.2, κ of an aerosol can be calculated from the volume fractions of its constituent species, if the κ values of these fractions are known. In the above discussion I used this equation in reverse to calculate aerosol composition from κ, assuming a two component aerosol. I also showed the validity of this method for the case of the BEACHON-RoMBAS data where the organic mass fraction calculated from κ matched well with that determined from AMS measurements. *Gunthe et al.* [2009] performed a similar analysis for data from the Amazon during the wet season, finding good agreement between aerosol hygroscopicities calculated from

CCN measurements and those computed from AMS data. On the basis of these previous results, in the next two sections I use composition data collected during RoMANS 2010 and GrandTReNDS to derive aerosol hygroscopicity during these studies.

I used size resolved aerosol composition data from the CSU AMS operated during RoMANS 2010 (July – August, 2010) to calculate aerosol hygroscopicity distributions, assuming the same values for $\kappa_{organic}$ (0.1) and $\kappa_{inorganic}$ (0.6) as well as $\rho_{organic}$ (1.4) and $\rho_{inorganic}$ (1.8) used above. I used these values and the total organic and inorganic mass concentration (again assuming all of the inorganic mass was present as ammonium sulfate, Appendix 2) at each aerodynamic diameter reported by the AMS to calculate κ as a function of aerosol size. Figure 3.24 shows the study averaged aerosol composition and κ distributions. Very similar to aerosol composition during BEACHON, there was a small increase in κ at larger aerosol sizes due to a higher fraction of inorganic species at these sizes. Given the similar composition, the κ values for ROMANS 2010 are also very similar to those measured during both BEACHON studies. This is perhaps not surprising due to the similar mountainous, forested locations of the two sites.

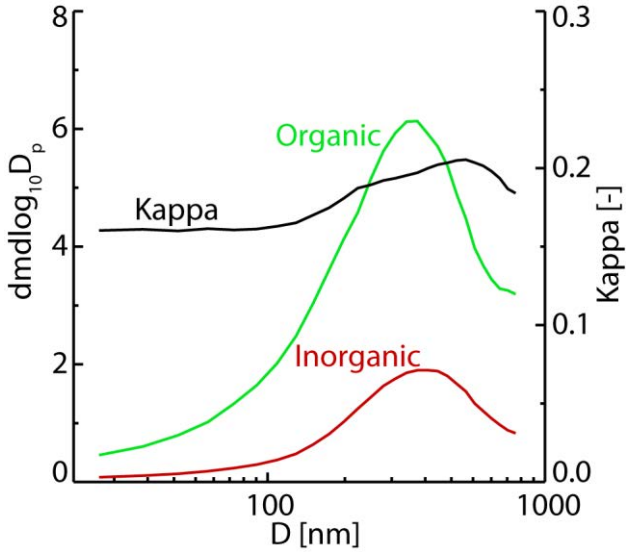

Figure 3.24 Study average aerosol composition distributions and calculated κ distribution during RoMANS 2010 (data provided by Taehyoung Lee and Misha Schurman).

After calculating κ as a function of aerodynamic diameter (as determined by the AMS), I used these values to calculate critical activation diameters (D_c). Petters and Kreidenweis [2007] present an analytical approximation for κ which can be rearranged to solve for D_c as a function of s and κ.

$$D_c = \left(\frac{4A^3}{27\ln(S)^2\kappa}\right)^{\frac{1}{3}} \qquad \textbf{Eq 3.3}$$

$$A = \frac{4\sigma_{s/a}M_w}{RT\rho_w}$$

A is evaluated at $T = 298.15$ K and a surface tension ($\sigma_{s/a}$) of pure water, 0.072 J m^{-2}. By performing this calculation for a range of s values at each aerosol size I created an array of critical activation diameters for the κ values calculated in each AMS size bin. I then found the

lowest s value at which the critical diameter was larger than, or equal to, the midpoint diameter of each AMS bin and took this as the critical supersaturation. This is the supersaturation necessary for the particles at that size (with a given κ) to activate as CCN. Equivalently, this also gives the diameter necessary for a particle in a size bin to activate given a supersaturation.

Figure 3.25 shows the aerosol number distribution (Chapter 2) averaged over the whole RoMANS 2010 study with the critical activation diameters for ten s values plotted as colored bars. By integrating under the curve at all sizes larger than each critical activation diameter, I used these values to calculate the cumulative number concentrations of CCN (N_{ccn}) as a function of s (Figure 3.26). Not surprisingly, as s increases more particles are able to activate as CCN and thus N_{ccn} increases. The rate of increase, for a given aerosol number distribution, is controlled by κ. To illustrate this, Figure 3.26 shows CCN concentrations calculated assuming two constant, representative values of κ: 0.05 (blue) and 0.3 (red) and the same aerosol number distribution. As can be seen, increasing κ from 0.05 to 0.3 more than doubles the number of available CCN in this case.

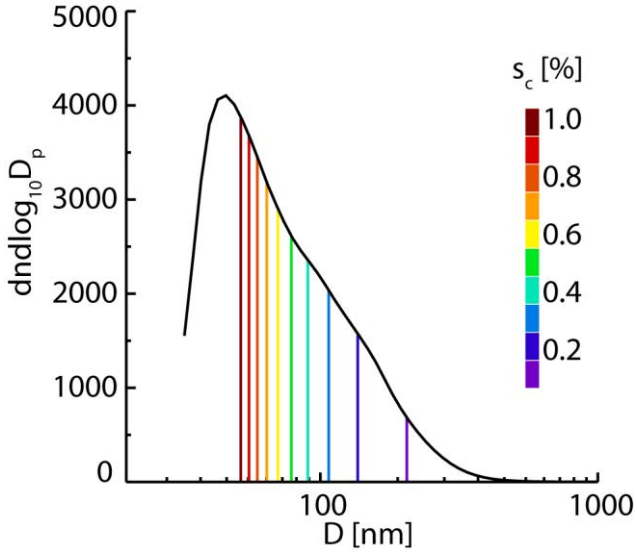

Figure 3.25 Study average aerosol number distribution during RoMANS 2010. Colored bars show critical activation diameters at 10 different supersaturations.

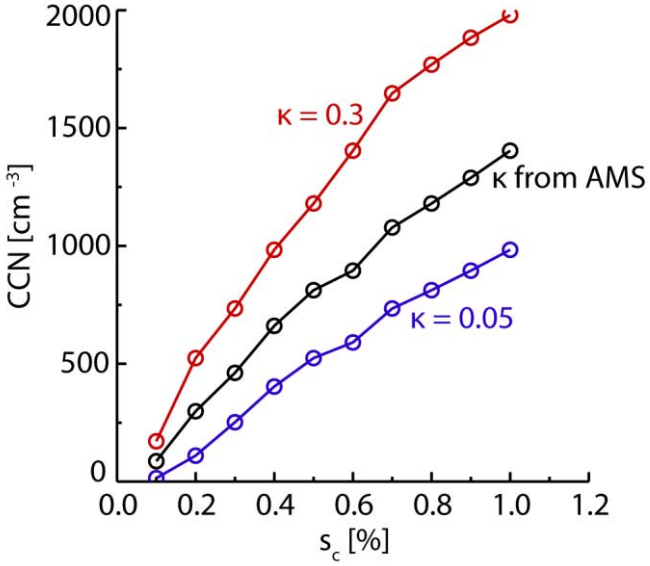

Figure 3.26 CCN number concentration as a function of supersaturation averaged over the RoMANS 2010 study period calculated using κ from AMS data (black) and two constant values (red and blue).

Figure 3.27 shows timelines of daily averaged organic and inorganic mass distributions measured by the AMS during RoMANS 2010. As with the study averaged values shown above, organic species dominated the aerosol during almost the entire study (note that the color scales are different by a factor of 2 for the two contour plots in Figure 3.27). Fractionally, organic species were especially dominant at sizes below ~100 nm, where there was very little measured inorganic mass.

As with the study averaged data above, I used the daily aerosol composition data to calculate distributions of κ during RoMANS 2010 (Figure 3.28). As expected, these values are low throughout the study especially at small sizes. Only at the end of the study, when aerosol mass concentrations were very low, does κ reach 0.3, a commonly assumed value for continental aerosol [*Andreae and Rosenfeld*, 2008; *Poschl et al.*, 2009; *Pringle et al.*, 2010].

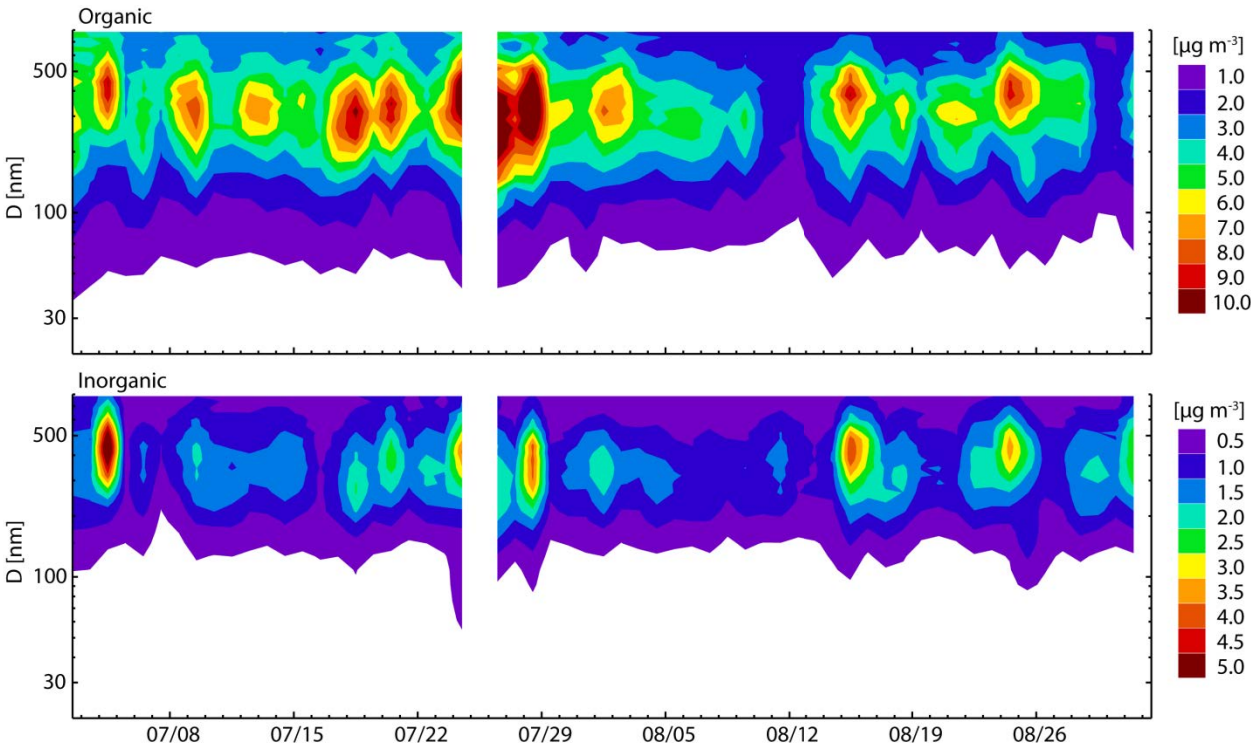

Figure 3.27 Contour plots of organic (top) and inorganic (bottom) mass distributions measured by the AMS during RoMANS 2010 (data provided by Taehyoung Lee and Misha Schurman). Note the different scales for the plots.

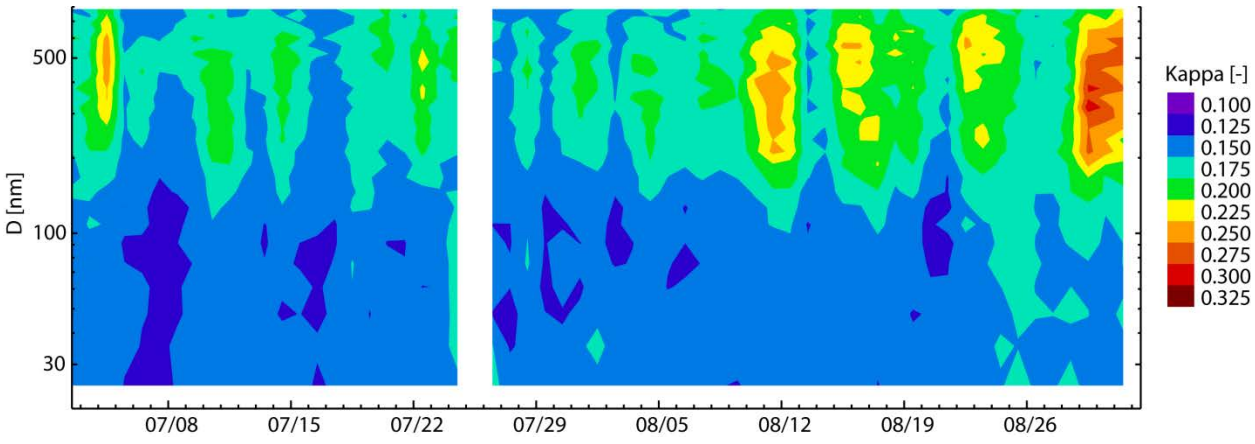

Figure 3.28 Kappa distributions calculated from size resolved AMS data during RoMNAS 2010 (data provided by Taehyoung Lee and Misha Schurman).

Figure 3.29 shows daily N_{ccn} as a function of s_c calculated as described above. There is considerably more daily variability in these numbers than in the aerosol composition or hygroscopicity values shown above, due mainly to the changes in aerosol number concentrations, since the number of particles available to activate as CCN is obviously the most important factor controlling N_{ccn}, especially at higher s_c. Figure 3.30 shows daily averaged total CCN concentrations calculated at each s_c value versus daily averaged total measured N concentrations. As s_c increases, more of the number distribution is able to activate as CCN, and the ratio of CCN to N approaches 1. Therefore, at these higher s_c values, CCN concentration is much more sensitive to changes in total N concentrations. At the highest s_c value shown in Figure 3.30, the correlation coefficient (r^2) between total N and CCN is 0.99, while it is only 0.17 for the lowest s_c values. However, as shown in Figure 3.26 the aerosol hygroscopicity still strongly influences the number of particles which can activate as CCN at a given s_c value and cannot be ignored.

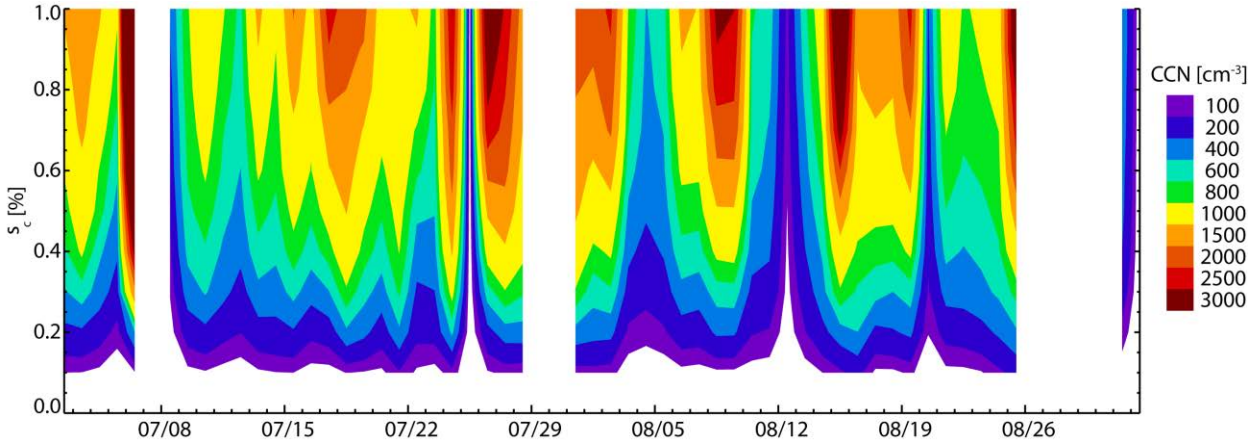

Figure 3.29 CCN number concentrations as a function of critical supersaturation during RoMANS 2010.

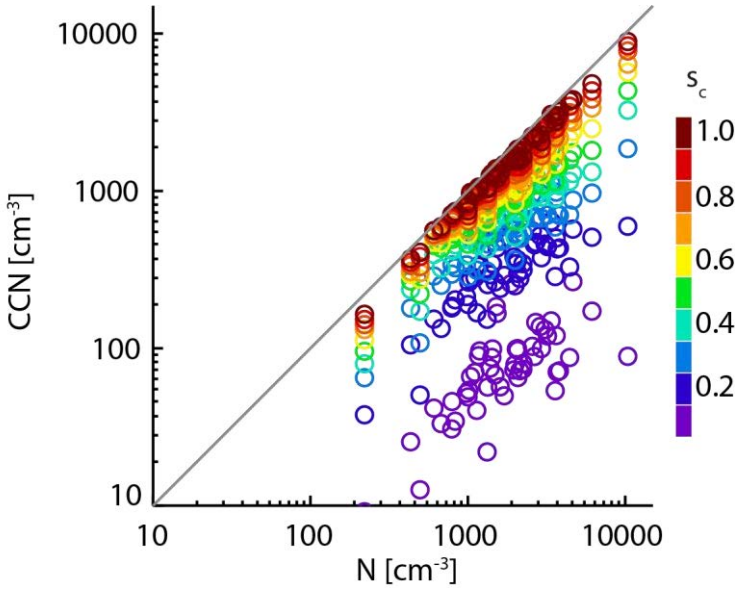

Figure 3.30 Daily averaged CCN versus N at 10 different supersaturations during RoMANS 2010.

Aerosol chemical composition data were also available from the IMPROVE site co-located with the RoMANS site. The IMPROVE samplers collect aerosols for 24 hours onto Teflon, nylon and quartz filters which are subsequently analyzed for aerosol mass, inorganic ions (SO_4^{2-}, NO_3^-), common soil elementals (Al, Si, Ca, K, Fe, Ti, Mg and Na) and carbon (in both organic and elemental form). Sample is collected onto two Teflon filters with respective $PM_{2.5}$ and PM_{10} inlets which are used to determine total aerosol mass concentrations in these size ranges. All other measurements are for $PM_{2.5}$ only [*Pitchford et al.*, 2007]. I used these bulk chemical composition data to determine aerosol hygroscopicity using Eq 3.2. As well as the organic and inorganic components I included the elemental carbon and dust mass measured by the IMPROVE samplers in the κ calculation with an assumed κ value of 0 [*Koehler et al.*, 2009; *Yamashita et al.*, 2011].

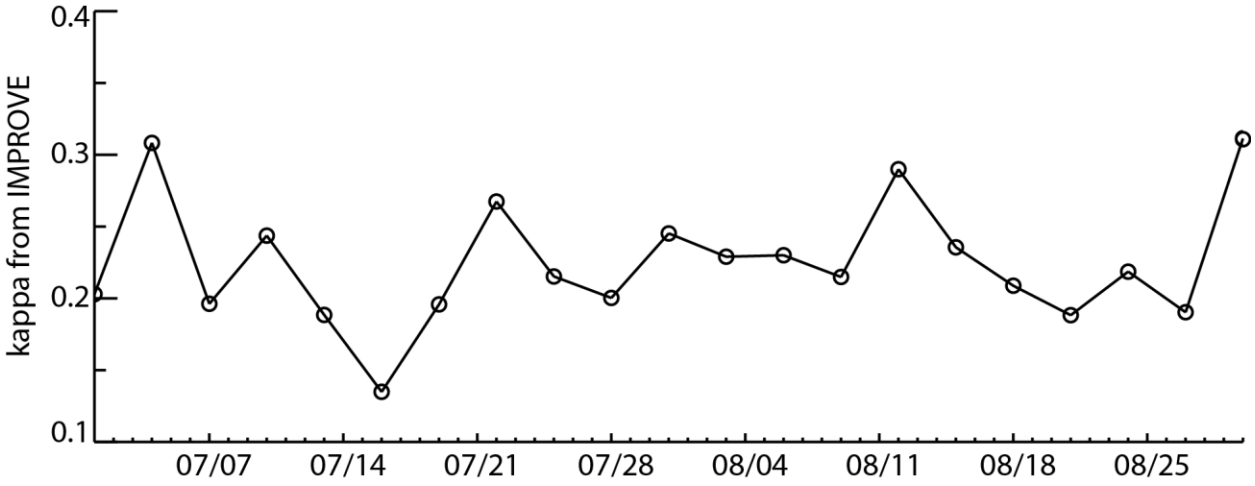

Figure 3.31 Kappa calculated from IMPROVE composition measurements.

Figure 3.31 shows the timeline of κ calculated from bulk chemical data measured by the IMPROVE sampler. Even with the inclusion of nonhygroscopic dust and EC which the AMS cannot measure, these values are higher than most of those shown in Figure 3.28. This is likely due to the fact that bulk $PM_{2.5}$ measurements are far more influenced by the composition of larger particles which contain most of the aerosol mass. As shown by both BEACHON and RoMANS AMS data, the aerosol in these regions tends to be dominated by organic material, with low κ, at small sizes with an increase in more hygroscopic inorganic salts at larger sizes. Therefore, $PM_{2.5}$ mass measurements will be more influenced by the higher κ larger particles. However, the peak in aerosol number during these studies was around or below 100 nm (see Figure 3.25 and Chapter 2) and these smaller particles are generally more organic dominated and thus have lower hygroscopicity than the bulk $PM_{2.5}$ (Figure 3.28). Thus, the increase in κ when using bulk measurements from filter samplers should lead to an increase in calculated N_{ccn} as well. This was in fact the case. When using κ derived from IMPROVE data there was an increase in N_{ccn} at all s_c with larger increases at lower s_c. Figure 3.32 shows the percent increase

in N_{ccn} when using κ calculated from IMPROVE versus size resolved AMS data. To calculate N_{ccn} from IMPROVE measurements I simply assumed the entire aerosol size distribution had the κ value determined from the bulk composition measurements and followed the same procedure as described above.

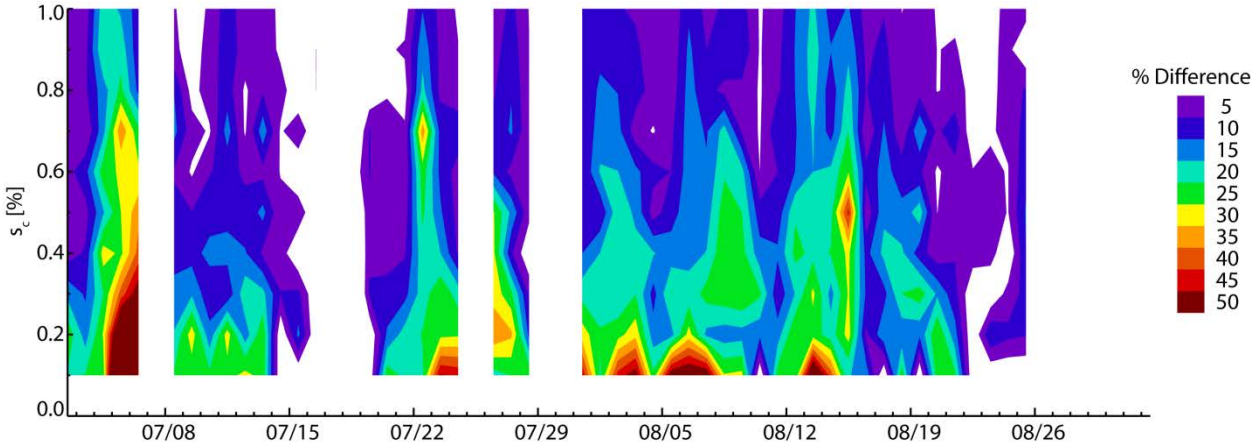

Figure 3.32 Percent difference in the number of CCN when calculating aerosol hygroscopicity from bulk IMPROVE measurements instead of size resolved AMS measurements.

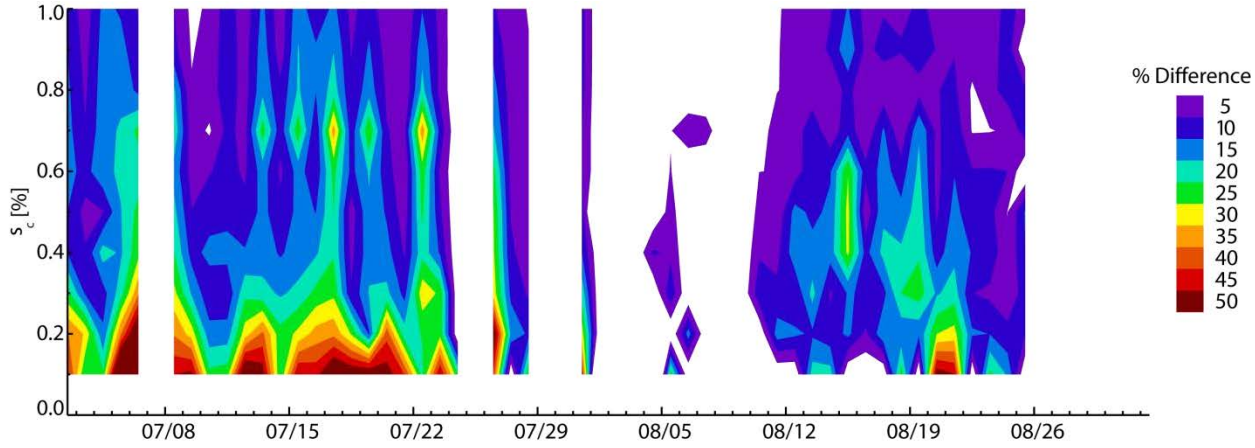

Figure 3.33 Percent difference in the number of CCN when calculating aerosol hygroscopicity from bulk AMS measurements instead of size resolved AMS measurements.

The IMPROVE samplers measure up to 2.5 μm, much higher than the ~0.7 μm size cut of the AMS. Therefore, a number of particles are included in the IMPROVE measurement which cannot be detected by the AMS. The discrepancy between aerosol composition, and resulting N_{ccn} between the two measurements could, therefore, be due to this difference in measurement range. Another factor is that the IMPROVE sampler can only determine bulk aerosol composition, while the AMS can measure size resolved composition. If the aerosol was internally mixed this should lead to no differences in calculated N_{ccn} as composition, and κ, would be the same at all sizes. As was already shown above, however, during both RoMANS 2010 and BEACHON there were some changes in κ with size. To investigate the effects of size resolved versus bulk composition measurements further, I calculated N_{ccn} from bulk AMS composition measurements and compared these values to those calculated from size resolved AMS measurements (Figure 3.33). Very similar to the results shown above for IMPROVE data, using bulk AMS data to calculate κ, and using this κ to calculate N_{ccn}, leads to an increase in N_{ccn}, especially at low s_c.

Moore et al. [2012] found that using size averaged versus size resolved aerosol data from the same AMS during the CalNex campaign resulted in an over prediction of κ resulting in a 30 – 75% over prediction of N_{ccn}. Because both the bulk and size resolved measurements were over the same size range, unlike AMS and IMPROVE data, their findings indicate that the aerosol was not completely internally mixed in the accumulation mode. *Cubison et al.* [2008] also found that they had to assume an externally mixed aerosol to achieve CCN closure for measurements in a polluted location in Riverside, CA. Both of these examples are for more polluted air masses which tend to have more complex aerosol characteristics due to the more numerous sources and fresher emissions than for the locations discussed here. However, even in the remote areas of the

BEACHON and RoMANS studies it appears that the aerosol was, at least somewhat, externally mixed with aerosol composition changing as a function of particle size. Thus, using bulk aerosol composition or assuming an internally mixed aerosol may lead to errors in modeling CCN in these regions as well. Because aerosol hygroscopicity tended to increase with size during both campaigns, assuming an internal mixture leads to an over prediction of CCN number concentrations at any supersaturation, but especially at low and moderate supersaturations.

3.2.7. Aerosol hygroscopicity during GrandTReNDS

Sub-micron aerosol composition was measured by the CSU AMS during GrandTReNDS. These measurements were made during August 2011 at the main GrandTReNDS measurement site at the top of Grand Targhee ski resort. While aerosol mass concentrations in the AMS measurement size range were generally low during the study, organic species were still dominant (Figure 3.34), consistent with the BEACHON and RoMANS study findings.

Two time periods of increased mass loadings stand out in Figure 3.34. These two events are the August Lightning Fire event and the high pressure event discussed in Chapter 2. During the first event, August 15 – 16, organic mass increased much more than inorganic mass, as would be expected for biomass burning emissions [*Levin et al.*, 2010]. During the second event, August 26 – 29, both organic and inorganic mass increased, but organics were still dominant. Figure 3.35 shows the aerosol composition and κ distributions averaged over these two time periods. As is expected, there were differences in the calculated κ size distributions during these two events as well. During the first event, dominated by organic species, κ was consistently low, ~0.15, at all sizes. Also, the aerosol appeared to be internally mixed as there was no clear

change in κ with size. During the second event, κ increased with size, similar to what was observed during BEACHON and RoMANS 2010. However, even with the large increase in the contribution of inorganic mass concentrations during this event, κ was still less than the commonly assumed value for continental aerosol of 0.3 across most of the size range. This means that using this value would overestimate aerosol hygroscopicity, and thus N_{ccn}, at this site.

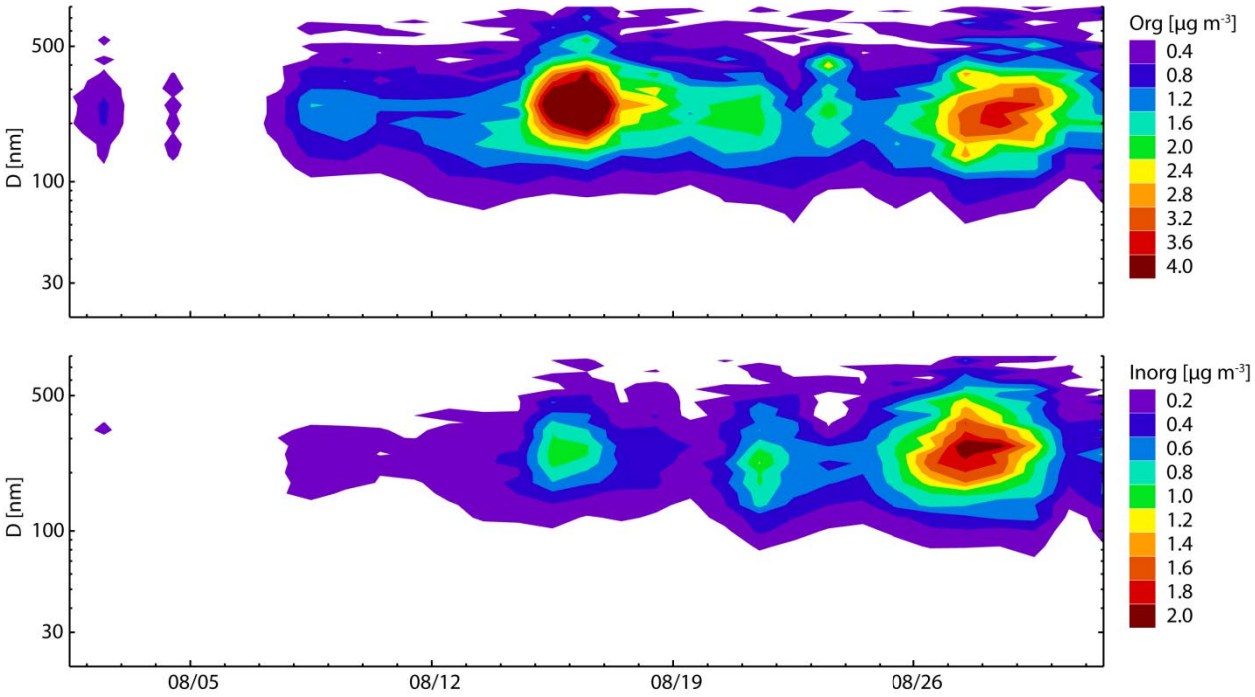

Figure 3.34 Contour plots of organic (top) and inorganic (bottom) mass distributions measured by the AMS during GrandTReNDS (data provided by Taehyoung Lee and Misha Schurman. Note the different scales for the plots.

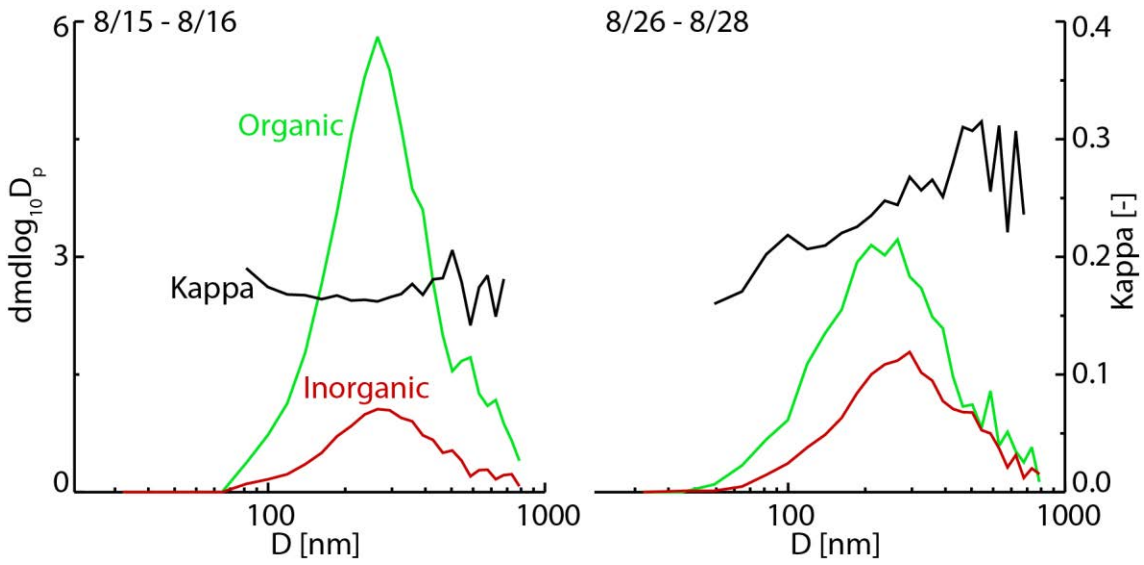

Figure 3.35 Aerosol composition and κ distributions during two time periods during GrandTReNDS.

3.2.8. Relevance of ground based measurements

All of the data reported thus far from the two BEACHON studies, RoMANS 2010 and GrandTReNDS were from measurements made ~3 m AGL. After the conclusion of the year-long BEACHON study measurements were also made from an inlet ~25 m AGL from May 12 through June 5, 2011 to determine whether measurements made near the ground were representative of particles above the canopy. The tower to which this inlet was attached was located ~20 m from the container housing the instrumentation. Air was drawn down through copper tubing (12.5 mm ID) by a 1/4 hp carbon-vane pump at ~10 LPM (resulting in a residence time of ~15 s) and sample flow was then drawn off of this larger flow immediately ahead of the instrumentation. While this inlet height was still well below typical inversion and cloud base heights, it was above the forest canopy and may better represent the characteristics of the aerosol

being entrained into clouds, and thus affecting cloud and precipitation formation and development.

Data coverage was poor during May – June 2010 and thus the time periods between the tower and low inlet measurements do not match perfectly. Nevertheless, very little difference was observed between measurements taken from the two inlets. Averaged over the entire tower measurement period and all *s* settings, $\kappa = 0.18 \pm 0.11$, while the average κ from the 3 m inlet from May – June 2010 was 0.19 ± 0.09. Comparisons between average κ values at each *s* setting are shown in Table 3.2. Mean κ values were statically different for three of the *s* settings (indicated in bold in Table 3.2), but the differences in these values were small. These similar hygroscopic properties measured above and below the forest canopy give validity to determining CCN hygroscopicity at ground level, at least for this site.

Table 3.2 Average (± 1 standard deviation) kappa values measured from the ground (3 m) and tower (25 m) inlets. Ground based measurements are for May – June 2010 while tower measurements were made May – June 2011.

ΔT [°C]	κ at 3 m	κ at 25 m
4	0.25 ± 0.1	0.25 ± 0.1
8	**0.19 ± 0.07**	**0.20 ± 0.07**
12	**0.14 ± 0.05**	**0.18 ± 0.06**
16	0.14 ± 0.05	0.14 ± 0.05
19	**0.13 ± 0.04**	**0.15 ± 0.04**

3.3. Summary and conclusions

Atmospheric particles, particularly those that act as CCN, are important in controlling cloud and precipitation formation and lifetime, and can have considerable effects on local ecosystems and global climate. High quality measurements of CCN concentration and aerosol hygroscopicity are needed in order to constrain and verify modeled cloud and precipitation processes, and their subsequent impacts on water cycles and radiative transfer. In this chapter I presented aerosol composition and hygroscopicity data as well as CCN concentrations from three study locations, BEACHON, RoMANS and GrandTReNDS, located along the eastern Rocky Mountains (Figure 2.1). During the two BEACHON studies I used size resolved CCN measurements to determine CCN concentration and aerosol hygroscopicity, represented with the κ parameter. During BEACHON-RoMBAS, RoMANS 2010 and GrandTReNDS aerosol chemical composition was measured with an Aerosol Mass Spectrometer (AMS). Because hygroscopicity is a function of aerosol chemical composition, I was able to use these data to calculate κ during these studies. During the BEACHON-RoMBAS study, when both size resolved CCN and AMS data were available, I found good agreement between κ values calculated from size resolved AMS data and those from the CCN measurements. As well, I used CCN derived κ values to calculate two component aerosol composition, which agreed well with direct AMS measurements. Below I present the main findings from these studies.

Aerosol chemical composition measured by an AMS as well as hygroscopicity derived from size resolved CCN measurements indicates that the aerosol measured during all three studies was predominantly organic, and thus had low κ values. In fact, averaged over the entire BEACHON study, and all *s* settings, κ had an average value of 0.16 ± 0.08, similar to values determined in organic dominated locations such as a tropical forest in the Amazon [*Gunthe et al.*,

2009; *Poschl et al.*, 2010] and a boreal forest in Finland [*Sihto et al.*, 2010], and much lower than the commonly assumed value of $\kappa_{continental} = 0.3$. The relatively low κ values measured at these locations suggest a predominance and potential importance of organic species, which generally have low hygroscopicity [*King et al.*, 2010; *Petters et al.*, 2009c; *Prenni et al.*, 2007]. It is known that highly biologically active areas such as boreal and tropical forests will have large contributions from organic aerosol leading to low κ values. However, results from the three studies presented here all indicate that the aerosol in these semi-arid, high altitude locations are also dominated by organic species, and therefore also have low hygroscopicity.

While organic species were dominant at all sizes, there were some changes in aerosol composition with size, with the organic fraction typically decreasing slightly at larger diameters. This trend was seen at all three study locations in both AMS and size resolved CCN data. Therefore, even in these remote locations, far from major sources, the aerosol appears to be, at least somewhat, externally mixed. The major conclusion from this result is that because of the size dependence of aerosol chemical composition, bulk chemical measurements will misrepresent the aerosol hygroscopicity. Because the organic fraction tended to decrease with size, bulk measurements will underrepresent this fraction, leading to erroneously high κ values and calculated CCN concentrations.

While the trend of decreasing organic fraction with larger diameters was observed year round, there was some seasonality to this trend observed during the year-long BEACHON study. During the winter months there was a sharper decrease in calculated organic mass fraction with size, although even at the largest diameter (~150 nm) the aerosol was still predominantly organic. During the summer months, there was very little change with size. It is postulated that the increased organic fraction at larger diameters during the summer is due to increased

biological activity during this time period, resulting in increased emissions of BVOCs, precursors of organic aerosol.

Because of the seasonal changes in aerosol chemistry, there was also some seasonality in κ, especially at larger activation diameters. At s = 0.14%, κ decreased from 0.3 in April to 0.16 in July and September. The hygroscopic properties of smaller particles, determined from higher s measurements, showed very little seasonal change with values changing only between 0.12 and 0.16 at s = 0.97%. These consistently low values suggest that there was little change in the aerosol composition at these sizes throughout the year. For the particles with diameters ~150 nm and larger, however, there was an increase in the less hygroscopic fraction during the summer months.

While some seasonal changes were observed in κ, much larger changes were seen in CCN concentrations. In general, increases in CCN concentrations followed those of total measured aerosol concentrations, peaking in July. There was, however, an interesting seasonal change in the fraction of total aerosol that activated as CCN. Activated fraction increased during the summer, increasing from 38% in March to 68% in August at the highest s. This increase appears counterintuitive since aerosol hygroscopicity actually decreased during the summer. However, average aerosol number distributions shifted toward larger sizes during the summer, allowing more particles to activate as CCN despite their slightly depressed hygroscopic properties. This further highlights the importance of both aerosol concentration and size, such as the data shown in Chapter 2, in controlling the potential number of CCN.

Small particle events, indicative of new particle formation, were observed throughout the BEACHON study and appeared to affect both aerosol chemical and physical properties, and thus

CCN concentrations, and are likely a controlling factor in the observed seasonal variability. These events occurred year round, but with higher frequency during the summer, resulting in large increases in aerosol number concentrations and, after the particles had grown large enough, increases in CCN concentrations. As well as these physical impacts, small particle events were associated with some chemical changes in the aerosol. For the largest particle sizes measured, κ decreased as the frequency of SPEs increased. Because of the remote, forested location of the measurement site, it is likely that the new particles were predominantly biogenic secondary organic species [*Dusek et al.*, 2010; *Kim et al.*, 2010]. For the smaller particles, determined from higher *s* measurements, however, there was no change in κ with increasing new particle formation. Aerosol composition at these sizes appeared to be persistently dominated by organics and, therefore, the new particles led to no hygroscopicity changes.

The above discussion emphasizes the important role that organic aerosol, likely of biogenic origin given the remote locations of these studies, plays in controlling aerosol chemical composition and hygroscopicity even in high altitude semi-arid locations.

4. Volatility of primary organic emissions from biomass burning

4.1. Introduction

Complete combustion of carbonaceous material fully oxidizes the carbon in the fuel, breaking all carbon-carbon bonds and forming, primarily, CO_2 and H_2O, whereas incomplete combustion leaves some of these bonds intact. Together with other reactions occurring in the active flame front, the result of incomplete combustion is a huge array of carbonaceous emission products. Unlike fossil fuel which is engineered for high efficiency combustion, biomass burning, such as occurs in prescribed fires, wildfires, agricultural waste burning and domestic heating with wood stoves, is less efficient. Further, these different types of burning display a large range in efficiencies, even within a single event, depending on the time in the phase of the burn (ignition through smoldering and extinction), fuel type, fuel moisture content, availability of oxygen in various regions of the burn, meteorology, and terrain. This variability results in emission of minerals, metals, salts [*Levin et al.*, 2010], and elemental carbon from these fires, with a range in graphitic character and physical and chemical properties [*Bond and Bergstrom*, 2006]. Most of the fuel C is emitted as CO_2 and CO [*Reid et al.*, 2005a; *Reid et al.*, 2005b], with the remainder emitted as organic species with widely varying volatilities, spanning many orders of magnitude of saturation concentrations from highly volatile species which exist in the gas phase to compounds that readily condense and form organic aerosol [*Grieshop et al.*, 2009; *Lipsky and Robinson*, 2006]. Emitted carbonaceous compounds that co-exist in both gas and condensed phases in the atmosphere have been classified as semi-volatile organic compounds (SVOC) and as intermediate volatility organic compounds (IVOC) that could undergo oxidation reactions and form SVOCs [*Cubison et al.*, 2011; *Donahue et al.*, 2006]. Carbonaceous emissions from biomass burning represent a continuum in volatility space and the phase

partitioning will adjust dynamically between gas and aerosol mass fractions according to changing atmospheric conditions [*Lipsky and Robinson*, 2006; *Shrivastava et al.*, 2006]. In order to correctly model these emissions, therefore, we need to know not only how much total organic material is emitted, but also descriptions of the volatility behavior of these species in the atmosphere.

In the US, biomass burning emissions are especially important in the western states where large wildfires and prescribed burns are regular occurrences [*Park et al.*, 2007]. This was seen during both RoMANS studies as well as the GrandTReNDS study when the measurement sites were impacted by smoke plumes, leading to some of the highest measured aerosol concentrations (Chapter 2). Also, in the western US, including the Rocky Mountain region, wildfires are highly correlated with both temperature and precipitation [*Marlon et al.*, 2012]. Due to changes in climate in this region, as well as decades of fire suppression policies which allowed fuel to accumulate, wildfire size and intensity have been increasing in the western US [*Marlon et al.*, 2012]. Further, due to forecasted climate changes, these fires are predicted to increase in the future [*Litschert et al.*, 2012; *Yue et al.*, 2012]. Wildfires already account for an estimated 20% of the observed total annual carbon aerosol mass concentration in the western US [*Park et al.*, 2007] and further increases in fires will lead to even more emissions and a greater importance of these emissions to local, regional and global air quality and climate.

To understand and model the full impact of biomass burning emissions it is necessary to know what is emitted and how these emissions change in the atmosphere. Many authors such as *McMeeking et al.* [2009], *Janhall et al.* [2010] and *Akagi et al.* [2011] present emission factors for a wide range of gas and particulate emissions from a variety of biomass fuels and combustion conditions. While these data are useful in predicting emissions given an amount of consumed

fuel, they only represent aerosol concentrations at the measurement conditions, specifically temperature and total organic aerosol concentration. The full volatility distribution is required to model how the measured emission factors will adjust to changing environmental conditions, and thus what effect smoke emissions will have on aerosol concentrations and the host of related processes described in previous chapters. In this chapter I present data from an experiment in which we examined the volatilization of organic emissions from open biomass burning, and use these data to construct a volatility distribution for these emissions. The findings can be used to correct prior estimates of biomass burning emission factors, and to improve models of smoke aerosol impacts on regional air quality.

4.2. Background

4.2.1. Volatility basis set

There are thousands of organic compounds present in the atmosphere, exhibiting a wide range of volatilities [*Donahue et al.*, 2006]. As with aerosol hygroscopicity, discussed in Chapter 3, it is impractical to try to measure the volatility of each compound and include these values explicitly in models. Instead, some representative value, or set of values, is needed. *Donahue et al.* [2006] proposed lumping of organic species into a set of order of magnitude spaced saturation concentration (C^*) bins, referred to as the Volatility Basis Set (VBS). Figure 4.1, from *Donahue et al.* [2006], shows an example distribution of what ambient organic species might look like under this formulation. Note that this figure does not show measured data. The bars in this Figure 4.1 represent the total concentration (in any phase) of organic species in a given saturation concentration bin (plotted as $\log_{10}C^*$). Green shading in Figure 4.1 represents

the fraction of aerosol mass in each bin and the green arrow shows the ambient organic aerosol concentration (C_{OA}) for this example case. Figure 4.1 shows the organic mass at equilibrium with ambient conditions. Species with C^* values close to the C_{OA} value are split between the two phases, while more volatile material, larger C^* values, is all in the gas phase and lower volatility material is all condensed. Changes in either C_{OA} or the volatility of the organic material will push the system out of equilibrium, resulting in a repartitioning between gas and condensed phases. I will discuss these processes more below.

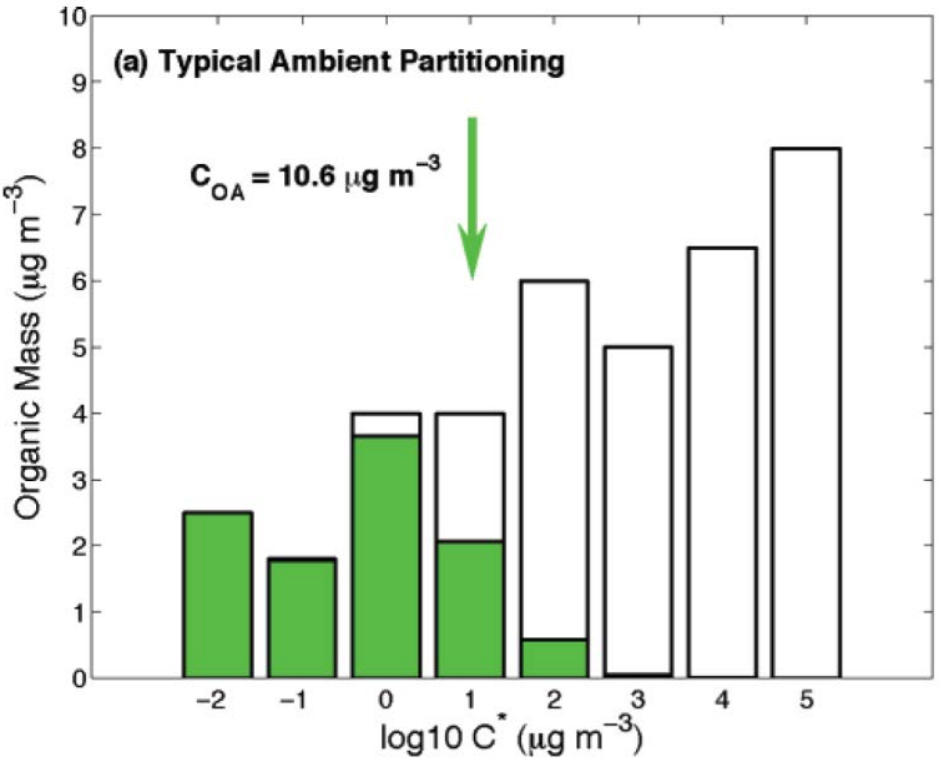

Figure 4.1 Example ambient volatility distribution fit to the volatility basis set. Bars represent total organic mass in each volatility bin while green shading shows aerosol mass. Figure taken from [*Donahue et al.*, 2006].

The VBS can be described mathematically via the equation presented by *Presto and Donahue* [2006]

$$\xi = \sum_{i=1}^{N} \left(1 + \frac{C_i^*}{C_{OA}}\right)^{-1} \times C_i \qquad \textbf{Eq 4.1}$$

where N is the number of volatility, or C^*, bins and C_i is the total mass in bin i. I use this equation to model the dilution data presented in this chapter.

4.2.2. Semi-volatile species and gas/particle partitioning

By representing volatility of the atmospheric organic mass with the VBS, changes in organic aerosol with changing atmospheric conditions can be easily modeled. To do so, however, the behavior of semi-volatile material must first be understood.

A species is semi-volatile if it can exist in both gas and condensed phases under typical ambient conditions [*Donahue et al.*, 2006; *A L Robinson et al.*, 2007]. Therefore, any species with a saturation concentration of the same order of magnitude as typical ambient concentrations should be considered semi-volatile. Organic aerosol mass concentrations are typically in the range of 0.1 – 100 μg m^{-3} [*Donahue et al.*, 2006], but can be much higher in smoke plumes.

Semi-volatile species partition between the gas and condensed phase either by adsorbing onto solid surfaces, such as mineral dust or elemental carbon, or by absorbing into liquid particles [*Odum et al.*, 1996; *Pankow*, 1987; 1988; 1994]. The ratio of adsorption to absorption is controlled by the concentration and type of the pre-existing aerosol. For biomass burning emissions in cases where the ratio of organic to elemental carbon is 2 or greater, it is thought that

absorption is the dominant process [*Shrivastava et al.*, 2006]. This is the case for emissions from most of the fuels I will discuss here [*Levin et al.*, 2010; *McMeeking et al.*, 2009].

In an unperturbed environment, semi-volatile species will be in equilibrium between the gas and condensed phases. The system can be pushed out of equilibrium by changing either the ambient aerosol concentration or by changing the saturation concentrations of the semi-volatile material, either by chemical processes or changes in temperature [*Donahue et al.*, 2006]. In terms of the VBS, changing ambient concentrations will move the green arrow in Figure 4.1, while changing saturation concentration will shift the entire volatility distribution either to higher or lower C^* values. In both cases the aerosol will re-equilibrate by adjusting gas/particle partitioning and, hence, the concentration of semi-volatile species in aerosol form. As shown by the green shading in Figure 4.1, at equilibrium a species with a saturation concentration similar to the ambient concentration of absorbing aerosol will be equally divided between the gas and condensed phases. If the ambient aerosol concentration decreases, shifting the green arrow to the left, partitioning will shift towards the gas phase, while the opposite is true for an increase in ambient concentrations [*Donahue et al.*, 2006].

Changes in temperature shift the saturation concentration of a species (C_i^*) as described by the Clausious-Clayperon equation [*Shrivastava et al.*, 2006]

$$C_i^*(T_2) = C_i^*(T_1)\exp\left(\frac{\Delta H_v}{R}\left(\frac{1}{T_1} - \frac{1}{T_2}\right)\right) \qquad \textbf{Eq 4.2}$$

where T_1 and T_2 are the initial and final temperatures, R is the universal gas constant and ΔH_v is the enthalpy of vaporization. An increase in temperature will lead to an increased saturation concentration, shifting the volatility distribution to the right. If this shift in volatility raises a

species' saturation concentration above the ambient absorbing aerosol concentration, the species will begin to evaporate. Naturally, the converse is true for a decrease in temperature. The sensitivity of saturation concentration, how much the volatility distribution shifts, to temperature change is dependent on a species' ΔH_v [*Donahue et al.*, 2006; *Shrivastava et al.*, 2006]. Measurements of ΔH_v for individual organic species in smog chamber experiments are in the range of 40 - 110 kJ mole^{-1}, although measurements of mixtures of species, more relevant for ambient conditions, tend to be at the lower end of this range [*Donahue et al.*, 2006; *Grieshop et al.*, 2009; *Shrivastava et al.*, 2006]. A lower ΔH_v will result in a lower sensitivity of C_i^* to changes in T.

Chemical processing can also affect the volatility of organic species by shifting some amount of mass across the distribution, e.g., from a higher to a lower volatility bin. Changes in volatility due to chemical processing have been examined in the case of new particle formation, where more volatile gas species are oxidized to produce less volatile species which can condense at typical ambient concentrations [*Hallquist et al.*, 2009; *Presto and Donahue*, 2006].

If a system at equilibrium is perturbed via one of the processes described above, the phase partitioning of semi-volatile material will adjust by either condensation or evaporation in order to achieve a new equilibrium state. The time-dependent approach to equilibrium can be described by the flux of material either to or away from a particle by the following equation [*Seinfeld and Pandis*, 2006]

$$J = 4\pi R_p D_A f(Kn, \alpha)(c_\infty - c_{eq}) \qquad \textbf{Eq 4.3}$$

where R_p is the radius of the particle, D is the diffusivity of the species, $f(Kn,\alpha)$ is a correction due to non-continuum effects and the uptake coefficient (α) and c_∞ and c_{eq} are concentrations of

the species far from the particle and at the surface. The surface concentration is assumed to be at equilibrium and is equal to the saturation concentration at a given temperature. As can be seen from the above equation, the flux of mass to or from a particle is directly proportional to the particle's size and the concentration gradient from the particle's surface to the surrounding environment. This flux is modified by the correction factor *f(Kn,α)* for which a number of different expressions have been proposed [*Seinfeld and Pandis*, 2006]. One formulation used by *Lee et al.* [2011], is that proposed by *Dahneke et al.* [1983]:

$$f(Kn,\alpha) = \frac{1+Kn}{1+2Kn(1+kn)/\alpha} \qquad \textbf{Eq 4.4}$$

where *Kn* is the Knudsen number, which is the ratio of the mean free path to a particle's radius [*Seinfeld and Pandis*, 2006].

The uptake coefficient (α) in Eq 4.4 corrects for the fact that a molecule does not always "stick" to a particle when it encounters it. That is, there is some resistance to uptake (or loss) of mass. Although this coefficient is commonly assumed to be 1, several studies have shown that it should be much smaller; estimates from organic aerosol evaporation and condensation studies range from 0.1 to 0.001 [*Grieshop et al.*, 2009; *Lipsky and Robinson*, 2005]. The implications of this will be discussed below.

The flux of mass to or from a particle will act to restore equilibrium. The characteristic timescale for an aerosol population to come into equilibrium with its gas phase concentration is [*Seinfeld and Pandis*, 2006]

$$\tau_S = \frac{1}{4\pi D_A \int_0^\infty n(R_p) R_p f(Kn,\alpha) dR_p} \qquad \textbf{Eq 4.5}$$

where $n(R_p)$ is the number of particles at a given radius and all other parameters are described above. This equilibration time also depends on α with smaller α values resulting in a longer equilibration time. The changes in α discussed above, 1 – 0.001, can change equilibration times from seconds to hours [*Grieshop et al.*, 2009]. *Wexler and Seinfeld* [1992] determined a τ_s of ~ 10 to 15 minutes for ambient aerosol in southern CA.

4.2.3. Determining organic aerosol volatility

Many studies have probed the volatility of organic material from various sources by pushing the system out of equilibrium via heating or dilution and measuring the resulting changes in organic aerosol mass concentration. One way this has been done is by heating the sample to high temperatures (~100 - 200 °C) with a thermodenuder, a temperature controlled, heated flow tube [*An et al.*, 2007; *Cappa and Jimenez*, 2010; *Grieshop et al.*, 2009; *B H Lee et al.*, 2011; *Ranjan et al.*, 2012; *Saleh et al.*, 2012]. As described above, heating an aerosol raises the saturation concentrations, shifting partitioning towards the gas phase and leading to particle evaporation as the system tries to re-equilibrate. By measuring the reduction in aerosol mass as a function of temperature, the volatility distribution of the aerosol can be determined [*Riipinen et al.*, 2010]. While the thermodenuder method can be effective in determining volatility distributions there are several caveats. First, to determine volatility from thermally driven evaporation requires an estimate of the enthalpy of evaporation [*Cappa and Jimenez*, 2010], which is not always known for complex mixtures of organic species. Second, residence times in the thermodenuder are typically only a few seconds [*Riipinen et al.*, 2010], although systems with longer residence times have been developed [*An et al.*, 2007], and the aerosol may not reach

equilibrium in the heated section. If the system is not in equilibrium, an evaporation kinetics model, such as Eq 4.3, must be employed to determine volatility from the measured change in aerosol concentration. However, evaporation kinetics models introduce another unknown parameter, α, which must be assumed. Variation in both ΔH_v and α can, therefore, lead to a large number of potential solutions for the volatility distribution of a given set of thermodenuder measurements.

Volatility distributions of organic material can also be determined via dilution. Like heating, dilution drives the system out of equilibrium as concentrations drop below the saturation concentrations of various semi-volatile compounds [*Donahue et al.*, 2012]. To balance this, some material will volatilize, thus decreasing the overall aerosol concentration. This process occurs in the atmosphere when highly concentrated plumes mix with ambient air and dilute as they move downwind, leading to decreased aerosol concentrations and repartitioning of semi-volatile material. Dilution samplers have long been used to study emissions from combustion sources such as engines, wood stoves and open biomass burning [*Grieshop et al.*, 2009; *Hildemann et al.*, 1989; *Hossain et al.*, 2012; *Lipsky and Robinson*, 2005; 2006]. These dilution systems take hot emissions and mix them with dilution air, decreasing both the aerosol concentration and temperature. This decrease in temperature actually causes more semi-volatile material to condense, thus offsetting some of the effects of dilution and increasing the aerosol concentrations [*Donahue et al.*, 2009]. Isothermal dilution avoids the complication of additional condensation and leads to much lower measured emission factors [*Lipsky and Robinson*, 2006]. Dilution samplers also tend to have very short residence times, 2 – 40 seconds for the system designed by Lipsky and Robinson [2005]. This may not be long enough for particles to reach equilibrium, as discussed above. However, samples from the dilution systems are often collected

on filters with collection times of tens of minutes. Aerosols on the filters will continue to evaporate (or condense) to come into equilibrium with the ambient conditions. Therefore, even if the particles do not reach equilibrium in the dilution system, they likely achieve equilibrium on the filters [*Lipsky and Robinson*, 2005]. Real time measurements downstream of dilution samplers, however, may not represent equilibrium conditions if residence times are not long enough. If measurements are made over a large range of concentrations, dilution systems can be used to construct volatility distributions by fitting the data with Eq. 4.1, assuming the system has reached equilibrium. This is the method used here.

4.3. Methods

The goal of this work is to develop representative volatility distributions for semi-volatile organic species emitted from biomass burning. To do this, a series of burns were conducted as part of the third Fire Laboratory at Missoula Experiment (FLAME 3) at the Fire Sciences Laboratory (FSL), operated by the United States Department of Agriculture Forest Service in Missoula, MT. FLAME 3 took place in October and November, 2009. During this experiment, fire emissions were allowed to fill a large room, the combustion laboratory, where they were naturally diluted over time by infiltration of outside air. The smoke was also actively diluted using a two barrel dilution system operating at dilution ratios of ~10:1 and ~100:1. By comparing the ratio of measured organic aerosol mass to the potential aerosol mass (taken as the consumed fuel adjusted for dilution) we can examine how much mass was lost due to volatilization as a function of total organic aerosol concentration. From this we can create a volatility distribution for the emitted organic species.

4.3.1. Description of burns, sampling and dilution setup

Controlled burns were conducted in the combustion lab at the FSL (Figure 4.2) which measured 12.4 x 12.4 x 19.6 m with a total volume of 3013.7 m^3 [*McMeeking et al.*, 2009]. For each experiment, between 150 and 1000 g of fuel were placed on a ceramic fuel bed and ignited with an electrical heating coil. The fuel bed was placed to the side of the combustion lab and the stack in the center of the lab was closed off, allowing smoke to fill the room. Large fans helped mix the smoke rapidly through the room. Fires typically lasted ~5 – 15 minutes, but smoke was held in the combustion lab for about 4 hours for each experiment. At the end of each experiment the combustion lab was vented with outside air.

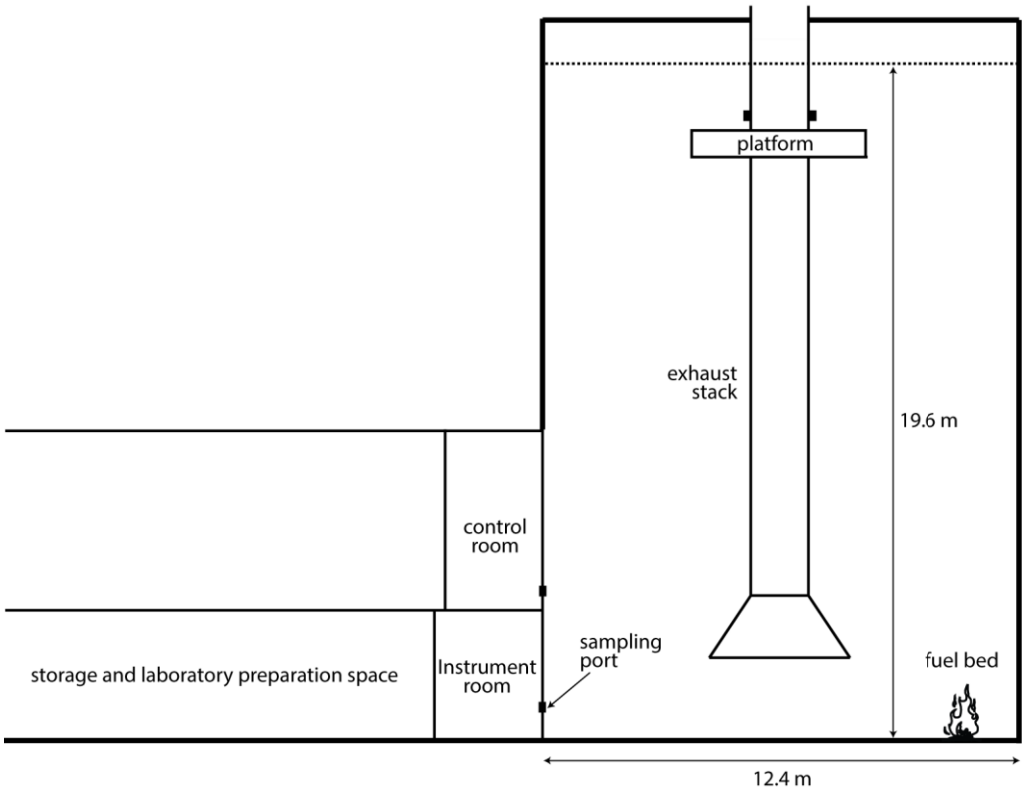

Figure 4.2 Set up of the combustion lab during FLAME 3 (modified with permission from *McMeeking et al* [2009]).

Table 4.1 List of fuels burned as well as initial fuel weight, remaining ash, fuel moisture content, combustion efficiency (CE) and modified combustion efficiency (MCE).

Burn #	Fuel	Fuel Weight [g]	Ash [g]	Moisture [%]	CE	MCE
38	Lodgepole pine	250.0	23.2	45.5	0.748	0.921
40	Ponderosa pine	250.0	37.4	74.2	0.529	0.889
42	Wire Grass	600.0	13.3	29.4	0.921	0.969
43	Saw Grass	350.0	11.0	10.8	0.904	0.958
44	Gallberry	500.0	21.6	39.3	0.899	0.954
45	Turkey oak	400.0	9.3	11.4	0.901	0.947
46	Wheat Straw	500.0	45.5	9.0	0.885	0.913
49	Sage	300.0	29.9	15.5	0.864	0.925
52	Turkey oak	401.0	13.4	42.8	0.773	0.900
53	Sage	300.0	26.4	15.6	0.875	0.924
54	Manzanita	500.0	31.0	11.1	0.925	0.956
56	Wire grass	500.0	17.5	12.1	0.880	0.959
57	Ponderosa pine	201.0	23.2	77.6	0.593	0.892
58	Saw grass	525.0	27.1	8.0	0.867	0.939
59	Chamise	500.0	46.0	10.0	0.906	0.943
60	Manzanita	501.9	18.1	8.4	0.926	0.956
61	Lodgepole pine	202.7	34.4	60.7	0.648	0.883
62	Ceanothus	1002.0	73.3	9.9	0.926	0.942
63	Pocosin	799.0	22.5	8.4	0.924	0.950

The fuels burned during FLAME 3 (Table 4.1) were typical of commonly burned species in the west and southeastern areas of the US, areas frequently impacted by smoke from both prescribed burns and wildfires. The combustion lab setup, ignition system and fuels used were similar to previous FLAME studies described in detail in several papers [*Carrico et al.*, 2010; *Hand et al.*, 2010; *Levin et al.*, 2009; *Mack et al.*, 2010; *McMeeking et al.*, 2009; *Petters et al.*, 2009a; *Petters et al.*, 2009d]. The FLAME 3 study and fuels burned are also described by

Hennigan et al. [2011]. Instrumentation, including the CSU AMS, was housed in a lab adjacent to the combustion lab. Sample was drawn into this room and then either sent directly to the instrumentation or through the dilution system.

Because we wish to understand the behavior of organic partitioning over a wide range of aerosol concentration, we actively diluted the sample by ratios of ~10:1 and ~100:1 using a two barrel dilution system (Figure 4.3). This system consisted of two 20 gallon (75.7 l) stainless steel barrels (Model ST2004, Skolnik Industries Inc., Chicago, IL). In each barrel about 1 LPM of sample flow was mixed with 10 LPM of dilution air, which was filtered, dried and scrubbed of gas phase organic species using activated charcoal. Based on measured flows, average residence time in each barrel was ~1.3 min. For the higher dilution barrel, the sample flow was drawn off of the lower dilution barrel, thus increasing the dilution ratio by a multiplicative factor. Sample flows were measured continuously using laminar flow elements (LFE) and pressure sensors; the flow rates were calibrated twice during the study and linearly interpolated between calibrations (Appendix 3). Dilution flow into the barrels was measured using mass flow meters (TSI 4140). To achieve a steady state concentration in each dilution barrel, sample was continuously drawn through the entire system and was then either sent to the instrumentation or dumped into a bypass flow similar to that of the combined instrumentation flows. However, the bypass flow and instrument flow were not perfectly matched, and thus the dilution ratios changed after each switch between the sample and bypass lines. To allow time for the system to re-equilibrate, we did not include the first 5 min of data after each sampling line switch from our final analyzed datasets. The bypass and excess flows coming out of the barrels were also continuously measured with flow meters. Temperature and humidity (Hygroclip S, Rotronic, Inc., Hauppauge

NY), and pressure (Model 760S, Teledyne Inc., San Diego, CA) were measured at the locations indicated in Figure 4.3.

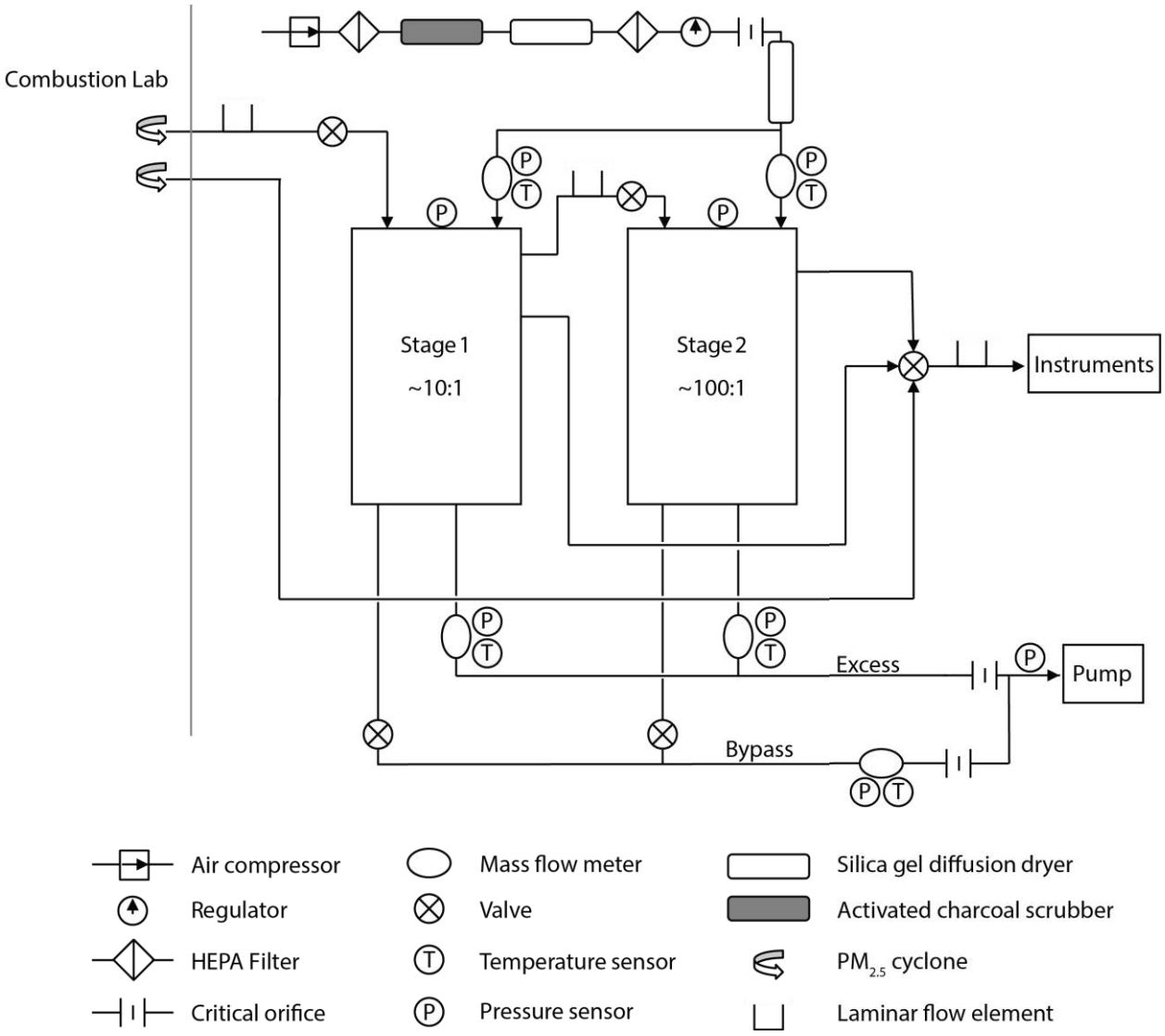

Figure 4.3 Diagram of the dilution system used during FLAME 3.

For each burn, sample was sequentially drawn directly from the combustion lab and from each of the two dilution barrels, although the sampling sequence varied for different burns. Samples were also passed through a thermodenuder, but these data are the subject of other work and will not be discussed here. Here I will focus on data from the isothermal dilution system.

A group from Carnegie Mellon University (CMU) also performed measurements during this study [*Hennigan et al.*, 2011]. They filled a 7 m^3 Teflon smog chamber with a sample from the smoke held in the combustion chamber, mixing it with clean dilution air. Although the primary goal of their study was to photochemically oxidize the smoke sample and examine production and destruction of organic species, they characterized the volatility of the smoke emissions before oxidation, as seen by their isothermal dilution process and by a thermodenuder. These data and analyses are the subject of separate publications [*May et al.*, in preparation], but I will present some of their volatility characterization results below for comparison with my results.

Descriptions of the instrumentation used during FLAME 3 are included in Appendix 1.

4.3.2. Calculating emission factors

As discussed above, organic aerosol volatility can be determined by perturbing the system, either by dilution or changes to saturation concentrations, and measuring the resulting adjustments in aerosol concentration. Both methods were used during FLAME 3, but I will focus mainly on the former method, isothermal dilution. Determining the organic aerosol response to dilution requires measurements of the fraction of total semi-volatile organic mass (in all phases) that is in aerosol form at a given aerosol concentration. Previous studies have done

this by measuring both organic aerosol mass and adsorbed organic vapors using quartz and Teflon filters downstream of a dilution system [*Lipsky and Robinson*, 2006; *Shrivastava et al.*, 2006]. Using this method, the ratio of organic aerosol mass (from the Teflon filter) to total gas + condensed phase semi-volatile organic mass (from the quartz filter) can be calculated. For the FLAME 3 study, I have measurements from the CSU AMS of particulate organic mass; however, I do not have measurements of total semi-volatile organic vapors in the combustion lab and dilution barrels for all burns (filter-based total semivolatile emissions were attempted, but the concentrations and substrate quality were too low to permit confident analyses). Some gas-phase VOC measurements were made for some burns but these measurements only account for a small fraction of total VOC mass. Further, for modeling purposes, relating emission to the dry fuel burned is usually more convenient. Thus, I used the dry consumed total mass for each burn as the maximum potential organic mass, although a large fraction of these emissions will be CO or CO_2, and thus not available for organic aerosol formation. Dividing the total mass of some component of biomass burning emissions by the consumed dry fuel mass is the same as calculating an emission factor [*McMeeking et al.*, 2009]. Thus, from the measurements in FLAME 3, I compute organic aerosol emission factors as a function of total organic aerosol loading at a range of concentrations.

Dry mass burned (DMB), was calculated by subtracting fuel moisture content and unconsumed ash from the original fuel mass for each burn (Table 4.1). Fuel moisture content was determined by placing a sample of each fuel in a room kept at 35 - 40 °C for 48 hours. The fuel sample was weighed before and after drying and the difference was taken as the water content. Carbon fraction in both the fuel and remaining ash were determined by laboratory analysis performed at the FSL. By multiplying DMB by the fuel's carbon fraction I calculated

the amount of combusted C for each burn. The amount of C emitted by the fire can be calculated by summing the measured C in the form of CO_2, CO, measured hydrocarbons, and particulate carbon emitted by each burn. To calculate burn emissions, measurement concentrations of all species were corrected for background concentrations in the combustion lab taken as measured values averaged over the 5 min before ignition. I multiplied background corrected concentrations of measured carbonaceous emissions by the volume of the combustion lab (adjusted for dilution as described below) to calculate total emitted carbon mass. To ensure emissions were well mixed in the combustion lab I waited 15 min after measured peak concentration and then averaged emitted C over a 5 min period. Figure 4.4 shows consumed C calculated from consumed fuel and from the total of measured C in gas and particle form. Overall, combusted carbon agreed well with measured carbon (r^2 = 0.93), indicating that emissions were well mixed in the combustion lab when the measurement time periods started and that the majority of emitted C mass is being measured in some form. For all burns except 40, 57 and 61 (the three lowest points in Figure 4.4), percent differences between measured and combusted C ranged between 1 and 36%. For the three lowest burns, percent differences were 84 – 141%. The fuels for these three burns were unique in that they were very fresh and their measured water content was much higher than that of any other fuel (greater than 60% instead of less than 40% for all other fuels). In cases of very high fuel moisture, the assumption that no moisture remains in the unconsumed ash may be false. Therefore, when calculating DMB, this mass would be subtracted twice, once as fuel moisture and once as unburned ash, leading to an incorrectly low combusted C mass. Because of this potential error, I used measured C, and the reported fuel carbon fraction, to calculate the mass of consumed fuel used in all subsequent calculations.

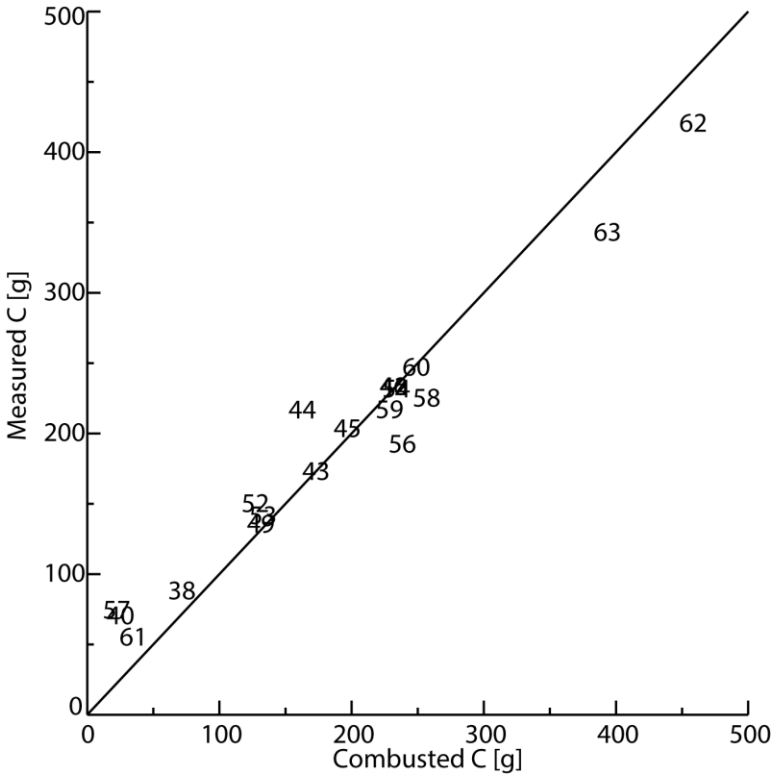

Figure 4.4 Carbon closure for the FLAME 3. Numbers indicate burn number.

To examine carbon closure in more detail, Figure 4.5 shows the mass of carbonaceous species, in gas and particle form, emitted by each burn. The crosses indicate the consumed C determined from gravimetric analysis. The right side of Figure 4.5 shows the percentage contribution of each component. As expected [*Andreae and Merlet*, 2001; *McMeeking et al.*, 2009], CO_2 accounted for the largest component of the emitted C, making up 80 – 90% in most cases. The only outliers were the three burns with high moisture content, which had much lower fractional CO_2 emissions. Complete combustion results in all of the carbon in the fuel being fully oxidized and converted to CO_2. Less efficient combustion, which would be expected for wetter fuels, will not fully oxidize the carbon in the fuel resulting in other carbonaceous emissions. Therefore, combustion efficiency (CE) can be quantified using the ratio of emitted

CO_2 to total carbon emissions, with higher CE values indicating more complete and efficient combustion. While total carbonaceous emissions were measured during FLAME 3, this is not typically the case and a modified combustion efficiency (MCE) is typically used instead [*McMeeking et al.*, 2009; *Yokelson et al.*, 2008]

$$MCE = \frac{\Delta[\boldsymbol{CO_2}]}{\Delta[\boldsymbol{CO}] + \Delta[\boldsymbol{CO_2}]} \qquad \textbf{Eq 4.6}$$

where Δ[CO] and $\Delta[CO_2]$ are CO and CO_2 emitted by the fire, corrected for background conditions as described above. Lower values of MCE indicate higher fractional CO emissions and are typical of smoldering combustion. Values below 0.9 are considered smoldering while MCE > 0.9 indicates flaming dominated combustion [*Reid et al.*, 2005b]. Combustion efficiency, as well as MCE values, for the FLAME 3 burns discussed here are shown in Table 4.1. Although CE values are a better way to determine combustion efficiency, I include MCE values to aid in comparison with other studies. As can be seen, the burns with very wet fuels were dominated by smoldering conditions (low CE and MCE), resulting in incomplete combustion, low emission of CO_2 and very high emission of hydrocarbons and organic aerosol. It must be noted that because of the large fractions of carbon emitted as hydrocarbons or organic aerosol, the MCE values for these burns is actually much higher than the combustion efficiency, although still in the range of smoldering combustion. For these burns, organic carbon aerosol accounted for almost 20% of the emitted carbon. This is much higher than typical OC emission factors reported in the literature [*Andreae and Merlet*, 2001; *McMeeking et al.*, 2009]. However, *Chen et al.* [2010] also observed enhanced OC emission factors for very wet fuels, and the values reported here fall within their reported range.

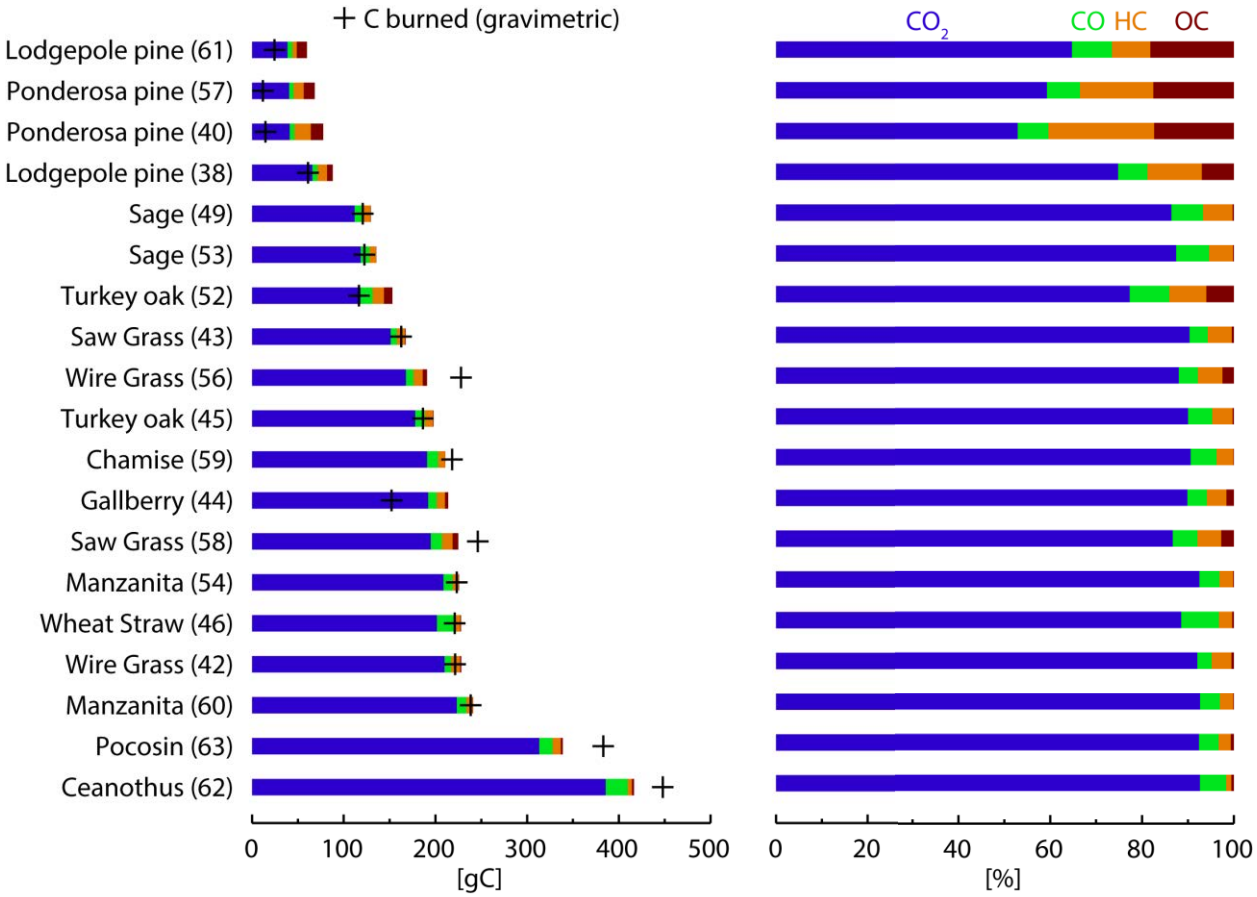

Figure 4.5 Mass of measured carbonaceous species (left) and fractional contribution to total measured carbon (right) for each burn.

4.3.3. Dilution in the combustion lab

All of the reported volatility distributions depend critically on accurate estimates of the dilution to which the emissions were exposed. Thus, I spent considerable effort computing this dilution in multiple ways in order to obtain a best estimate and also an uncertainty that should be applied to all derived volatility estimates. This section details the various calculations and summarizes the final, best-estimate dilution ratios.

Figure 4.5 shows the initial emissions (measured at the point of complete mixing through the chamber, which was generally ~15 min after ignition) of carbonaceous species for each burn, and can be used to calculate initial emission factors. To examine how the initial emission factor of organic aerosol changes with dilution, however, the dilution factors in both the combustion lab and dilution barrels have to be accounted for. Therefore, after calculating consumed fuel mass for each experiment (calculated from measured C as described above), I divided this mass by the volume of the combustion lab to get the initial mass concentration of all fire emissions in the room. This initial concentration was then decreased over time by infiltration of outside air into the combustion lab and active dilution in the two barrel dilution system. While dilution in the two barrel system was controlled and measured, I do not have any direct measurements of how much outside air entered the combustion lab during an experiment. I do, however, have evidence that the combustion lab was not airtight and air exchange was occurring. During all experiments, the concentrations of non-reactive gasses, such as CO and CO_2 decreased with time. Since these gasses will not react or dry deposit, this decrease can only be due to dilution by outside air, with lower concentrations of these gasses, leaking into the combustion lab. The decreases in non-reactive gasses can be used to calculate the rate at which outside air infiltrated into the combustion lab using the following equation:

$$V_{in}(t) = \frac{(C(t-1)\times V_0)-(C(t)\times V_0)}{(C(t)\times C_b)} \qquad \textbf{Eq 4.7}$$

where $V_{in}(t)$ is the volume coming in at time t and V_0 is the volume of the combustion lab, $C(t)$ is the measured gas concentration and C_b is the background concentration. Equation 4.7 gives the volume of air entering the combustion lab at every time step (in this case every minute). The dilution ratio for air in the lab can then be calculated as the combustion lab volume + infiltration

volume divided by the initial volume of the combustion lab. If the decrease in a non-reactive gas concentration is due only to infiltration of outside air, the concentration of this gas in the combustion lab at time *t* will be:

$$C(t) = \frac{C_0 \times V_0 + C_b \times V_{in}(t)}{V_0 + V_{in}(t)} \qquad \textbf{Eq 4.8}$$

During FLAME 3, measurements of NO, NO_2, CO and CO_2 were made inside the combustion lab (Appendix 1) and I can use any of these to calculate infiltration using Eq 4.7. Of these gasses, CO and CO_2 had the highest concentrations and least noise in the measurements. Also, these species should be the most chemically stable, although there was likely minimal chemistry occurring in the windowless combustion lab and thus NO and NO_2 should also be somewhat stable. Carbon monoxide is the best candidate tracer gas for estimation of the combustion lab leak rate. Further, background CO concentrations in Missoula can be obtained from an EPA monitoring site. Although data were not available during all burn days, I can use reported values as limits on my assumptions of CO_b.

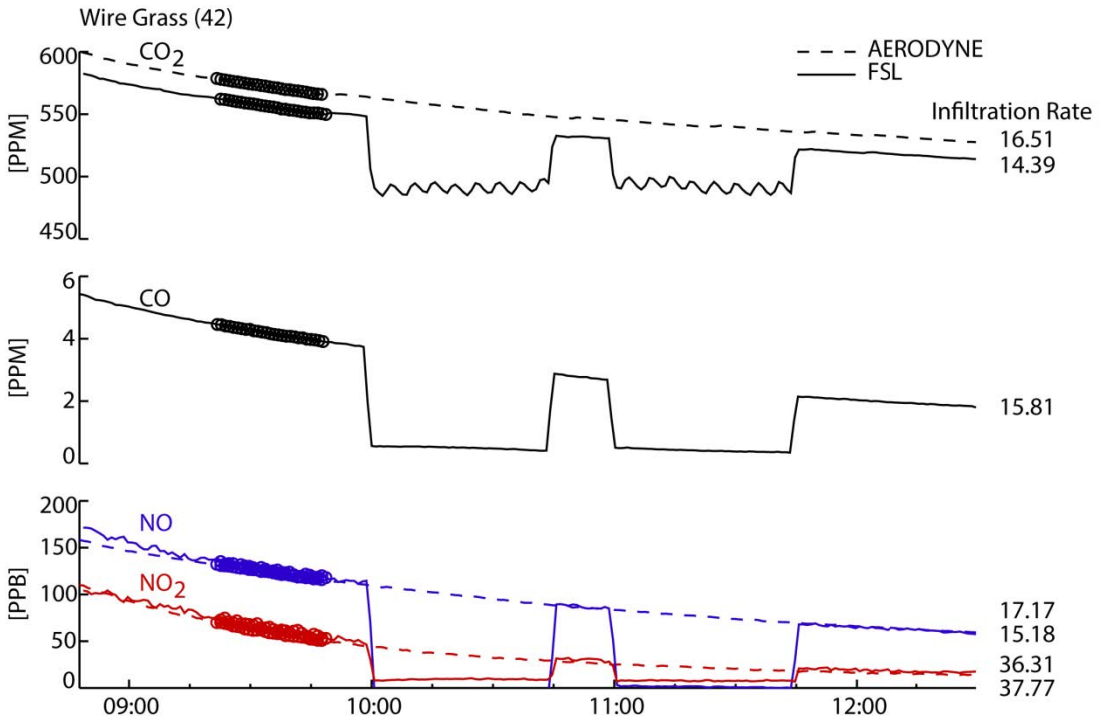

Figure 4.6 Measured gas concentrations in the combustion lab and dilution system during a wire grass burn. Infiltration of outside air into the combustion lab in m^3min^{-1} (listed on right) was calculated using the decrease in concentrations during the highlighted time period.

Figure 4.6 shows all the gas measurements for burn 42 (wire grass). The decrease in all gases is obvious, clearly indicating that these emissions were being diluted in the combustion lab during the course of the experiment. Measurements of NO and NO_2 by the FSL (solid lines) and Aerodyne (dashed lines) operated instruments agree very well in the combustion lab. There is an offset between the two CO_2 instruments due to calibrations. Also, uncompensated pressure effects on the CO_2 measurements can be seen in the data. Average infiltration rates (LPM) are shown by the numbers listed on the right in Figure 4.6. These rates are calculated using the decrease in gas concentrations during the highlighted time period. Infiltration rates agreed within 18% for values calculated from CO, CO_2 and NO. The values calculated from NO_2 measurements are much higher, however, although they agree with each other. This pattern was

seen throughout the study, perhaps indicating an unaccounted for loss of NO_2. A table listing calculated infiltration rates for all burns is shown in Appendix 5.

For the reasons stated above, and illustrated in Figure 4.6, I chose to use CO as the best indicator of the rate of outside air leaking into the combustion lab. For each burn I chose a ~20 minute time period to calculate average infiltration from CO, shown in Figure 4.6. This time period varied slightly from burn to burn so as to avoid any sharp dips or jumps in CO measurements and due to changes in sampling strategy, during some burns sample was drawn from the dilution barrels more frequently and thus there are less combustion lab data available. Also, for all burns I waited at least 15 minutes after peak CO concentrations to begin the infiltration calculation to ensure that all emissions were well mixed throughout the combustion lab and any changes in concentration were, in fact, due to infiltration only. Over all burns the average (± 1 standard deviation) infiltration rate calculated from CO was 17.7 ± 5.9 m^3 min^{-1}.

To check the assumption that gas concentrations in the combustion lab were only decreasing due to infiltration, I used the average CO infiltration rate and Eq 4.8 to calculate the decrease in CO for each burn. These calculated values for burn 42 are shown by the red line in Figure 4.7. As can be seen, the measured and calculated values agree quite well ($r^2 = 0.99$ for combustion lab points), thus lending validity to the assumptions that outside air entering the combustion lab led to the observed decrease in concentration and that a single average infiltration rate can be assumed for each burn.

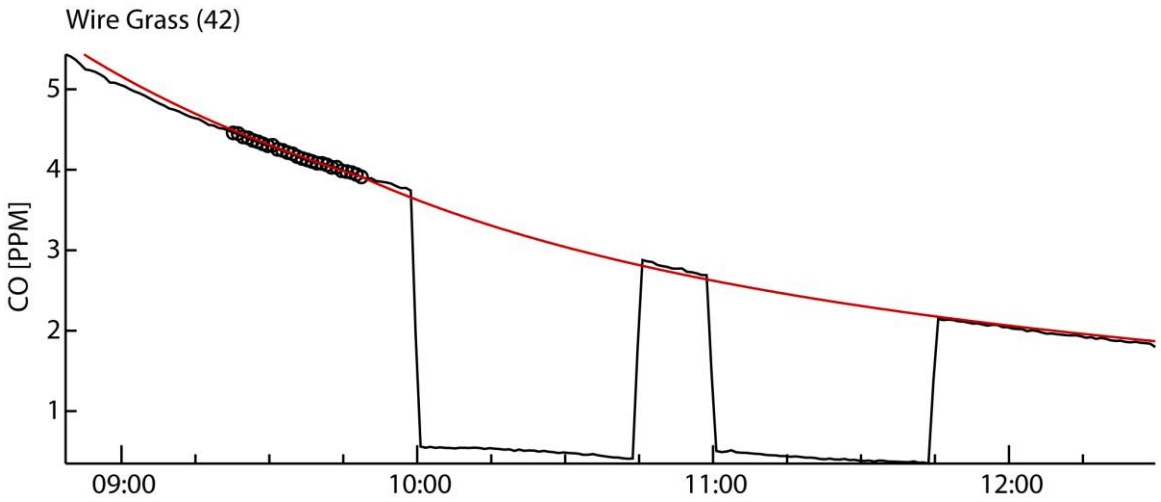

Figure 4.7 Measured (black), and calculated (red) CO concentrations during a wire grass burn.

After calculating the rate at which air was coming into the combustion lab during each burn, I used these values to model the decrease in SO_4^{2-} measured by the AMS, in the same way as CO above. Sulfate should also be non-volatile and conserved during dilution, like the gas species discussed above. However, it is a particle, not a gas, and thus changes in mass concentration will be due to deposition as well as dilution. Calculating SO_4^{2-} concentrations using Eq 4.8 requires some estimate of background concentrations outside the combustion lab, which were not measured. However, there are five IMPROVE sites within ~100 miles of Missoula (Figure 4.8) that report total $PM_{2.5}$ as well as SO_4^{2-} concentrations every three days [*Pitchford et al.*, 2007]. These sites are set up in remote locations and thus give an idea of regional conditions, but not any local urban emissions. There is also an EPA site in Missoula which measures total $PM_{2.5}$. I compared these local $PM_{2.5}$ values to the average $PM_{2.5}$ from the five IMPROVE sites during the FLAME 3 time period. The values were somewhat correlated (Figure 4.9), however, there was a constant offset of about 1.5 $\mu g\ m^{-3}$. This likely indicates that

Missoula is affected by the same regional sources as the IMPROVE sites, but with some impact from additional local emissions.

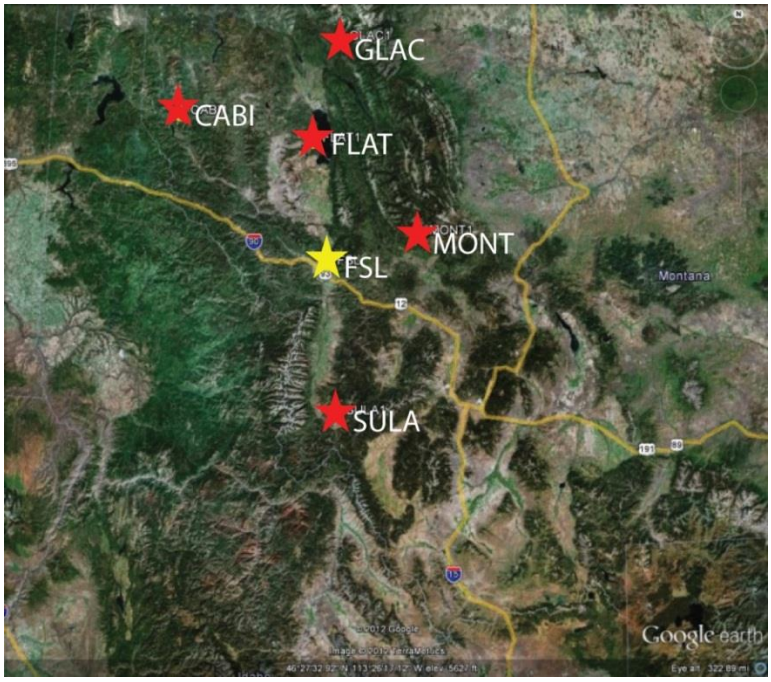

Figure 4.8 Locations and four letter abbreviations of the IMPROVE sites used to determine background SO_4^{2-} concentrations.

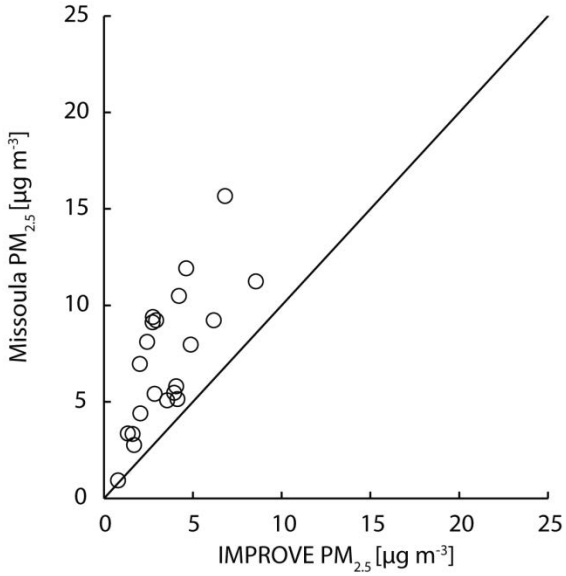

Figure 4.9 $PM_{2.5}$ measured in Missoula versus average $PM_{2.5}$ from five IMPROVE sites within 100 miles of Missoula (data from 01/09/2009 – 31/10/2009).

To account for local emissions of SO_4^{2-}, I increased the SO_4^{2-} values averaged over the five IMPROVE sites (circles in Figure 4.10) by the same percentage increase as total $PM_{2.5}$ in Missoula (gray line in Figure 4.10). This gave some estimate of SO_4^{2-} mass concentrations less than 2.5 μm outside the combustion lab during the FLAME 3 time period. However, as discussed in Appendix 1, the AMS measurements only represent ~$PM_{0.7}$ and thus will not measure some of the $PM_{2.5}$ mass. *Levin et al.* [2009] showed that in remote areas mass distributions are bimodal with roughly half of the mass falling below the AMS cutoff, ~700 nm. Fresh emission, however, should be much smaller. I thus assumed that the AMS could see half of the SO_4^{2-} mass measured by the IMPROVE network as well as all of the additional local SO_4^{2-} mass, that is the difference between the measured and adjusted values in Figure 4.10. The resulting best estimate of infiltrating SO_4^{2-} is shown by the red line in Figure 4.10. Because the IMPROVE and EPA data sets have only three day resolution I linearly interpolated between measurements.

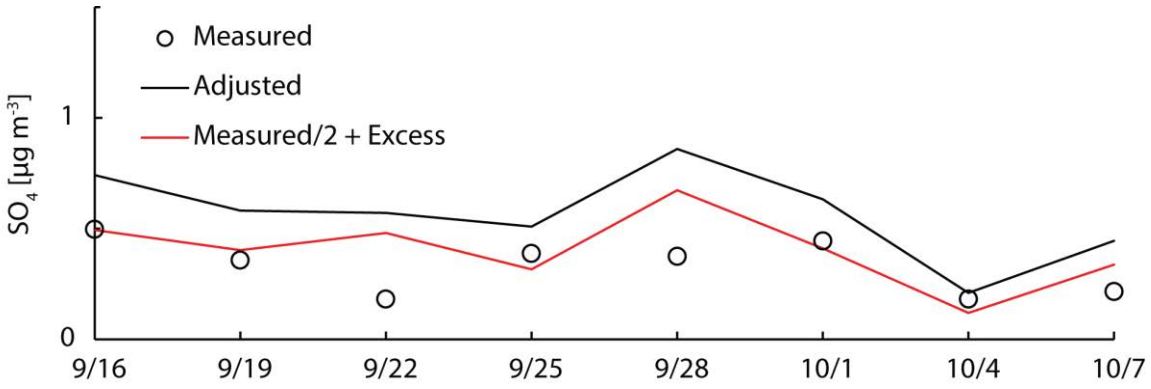

Figure 4.10 SO_4^{2-} concentrations averaged over the five IMPROVE sites within 100 miles of Missoula (circles). The grey line represents the SO_4^{2-} concentrations adjusted for local urban emissions and the red line shows the best estimate of SO_4^{2-} detectable by the AMS (see text for explanation or these calculations).

Using the above estimate for background SO_4^{2-} mass concentrations, I modeled SO_4^{2-} concentration decay using the infiltration rate calculated from CO concentrations. The resulting calculated SO_4^{2-} concentrations are plotted in Figure 4.11 along with those measured by the AMS. While measured and modeled SO_4^{2-} agree well at the beginning of the burn, by the end modeled SO_4^{2-} is higher. This is likely due to the fact that particulate matter will be lost to deposition as well as being diluted by outside air, and this is not accounted for in the modeled concentrations. Non-reactive gas species, however, should only decrease due to dilution. Thus, infiltration calculated from gas species should provide a lower limit for the decrease of aerosol species. However, it is likely that organic aerosol will behave more like sulfate, with some depositional loss. Black carbon (BC) is also a non-reactive particulate species and should behave similarly to SO_4^{2-}. Figure 4.12 shows the concentrations of BC and SO_4^{2-} aerosol species (normalized by the peak concentration) for burn 38 (BC data were not available for burn 42). As expected, both SO_4^{2-} and BC show a very similar pattern as concentrations decrease due to dilution and deposition. Organic carbon should undergo these same processes and, therefore, I used the changes in SO_4^{2-} (corrected for background SO_4^{2-}) to adjust dry mass burned to account for overall dilution in the combustion lab. Using this approach, the dilution ratio is simply calculated as

$$DR_{chamber}(t) = \frac{C_{so4\_0}}{C_{so4}(t)} \qquad \textbf{Eq. 4.9}$$

where the numerator is the initial sulfate concentration and the denominator is the concentration at each time step (minute). Using SO_4^{2-} to calculate the dilution experienced by the organic material requires two key assumptions. First, I am assuming that any deposited particulate organic will be removed from the system, and cannot interact with species in the air. This is not

true as surface components can continue to evaporate and condense to be in equilibrium with their environment. This would lead to an overestimation of dilution. The second assumption is that both gas and particle species are deposited at the same rate, that of SO_4^{2-}. Again, this is likely not true as gas phase deposition is typically much faster than particle [e.g. *Beem et al.,* 2010]. Further, deposited organic gases have been shown to stick to metal surfaces, thus leading to a net sink of organic material to the walls [*VanLoy et al.*, 1997]. Enhanced loss of organic vapors to the walls would lead to the organic material experiencing an increased effective dilution to that calculated from SO_4^{2-} loss.

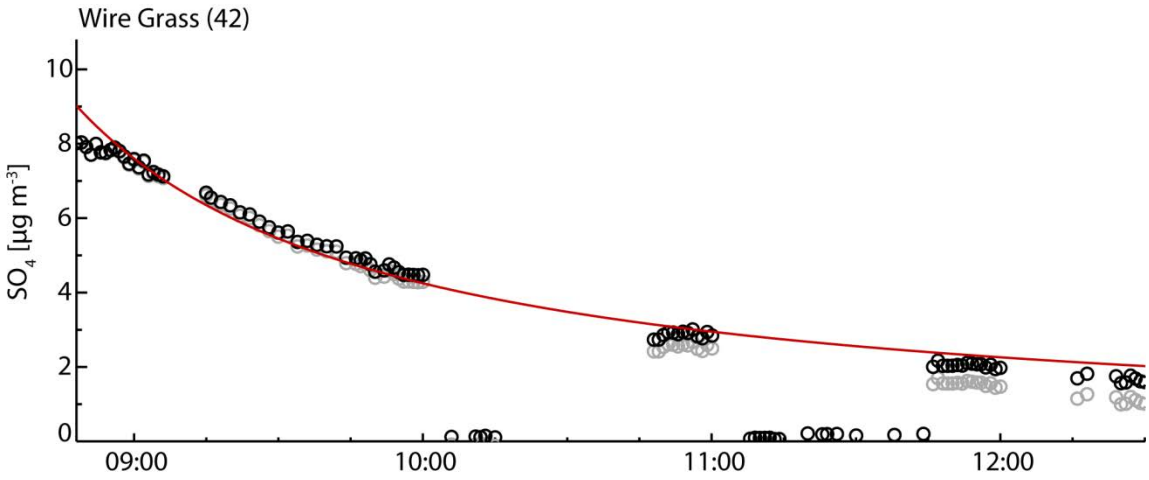

Figure 4.11 Measured (black), and calculated (red) SO_4^{2-} concentrations during a wire grass burn. Gray circles show the change in SO_4^{2-} when background concentrations are removed.

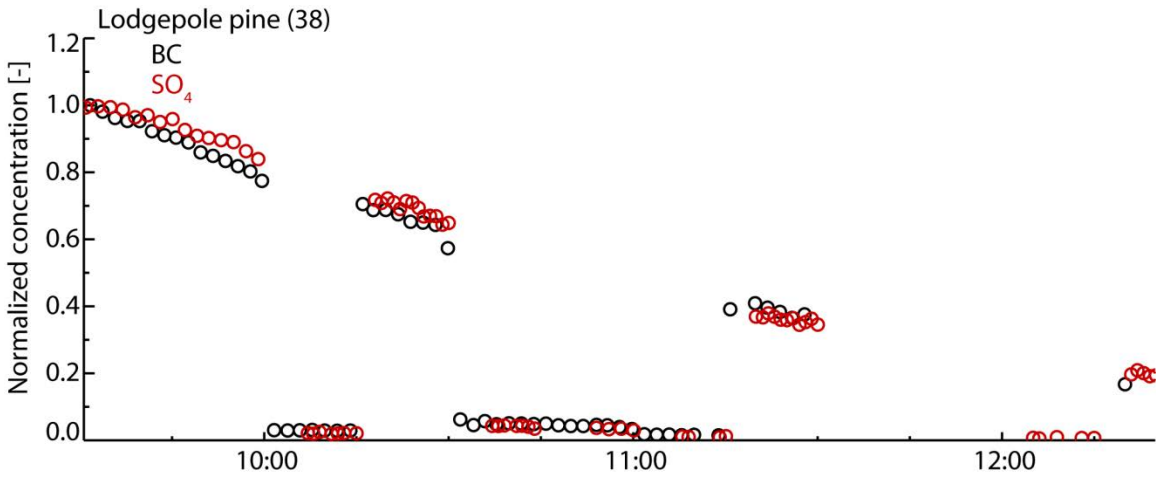

Figure 4.12 Normalized SO_4^{2-} and black carbon concentrations.

4.3.4. Dilution in the dilution barrels

The above discussion accounts for continuous, uncontrolled "dilution" of the emissions during each experiment that occurs via infiltration of outside air, and, in the case of particulate matter, via deposition to the chamber surfaces. The sample was also actively diluted using the two barrel system described above, and this additional dilution must also be computed. I calculated dilution ratios in the barrels from the measured flow rates of sample and clean air flow from the ratio of total air (sample + clean) to sample air entering the barrels. Because the sample flow coming into the high dilution barrel was drawn from the low dilution barrel, I multiplied the dilution in this barrel by that of the low dilution barrel to get the total dilution ratio. Although we tried to keep the flows through the two dilution barrels constant, there were some changes in flow rates when switching between sample and bypass flows. Thus, the dilution ratios in the barrels were not always constant. Also, pressure fluctuations in the barrels led to fluctuations in dilution as well, especially at the higher dilution ratios. Both of these effects can be seen in Figure 4.13 which shows the low (blue) and high (red) dilution ratios during burn 42. The

changes in sample flow through the barrels meant that concentrations in the barrels were not at steady state when sampling from the barrel began, and thus the first five minutes of each dilution barrel measurement period are not used.

I also calculated dilution in the barrels from the difference in SO_4^{2-} between the combustion lab and dilution barrels (circles in Figure 4.13). However, since the AMS sample line was switched between the combustion lab and dilution system I do not have any concurrent measurements in both locations. Therefore, I filled in the gaps in combustion lab SO_4^{2-} data by fitting an exponential decrease to the data points before and after each dilution barrel measurement. I then compared the change in SO_4^{2-} between this filled in combustion lab data and the barrel measurements to calculate dilution. To account for the time delay in the dilution system, I compared barrel measurements to combustion lab concentrations one residence time earlier (~1.3 min) for the low dilution barrel and two residence times earlier (~2.6 min) for the high dilution barrel.

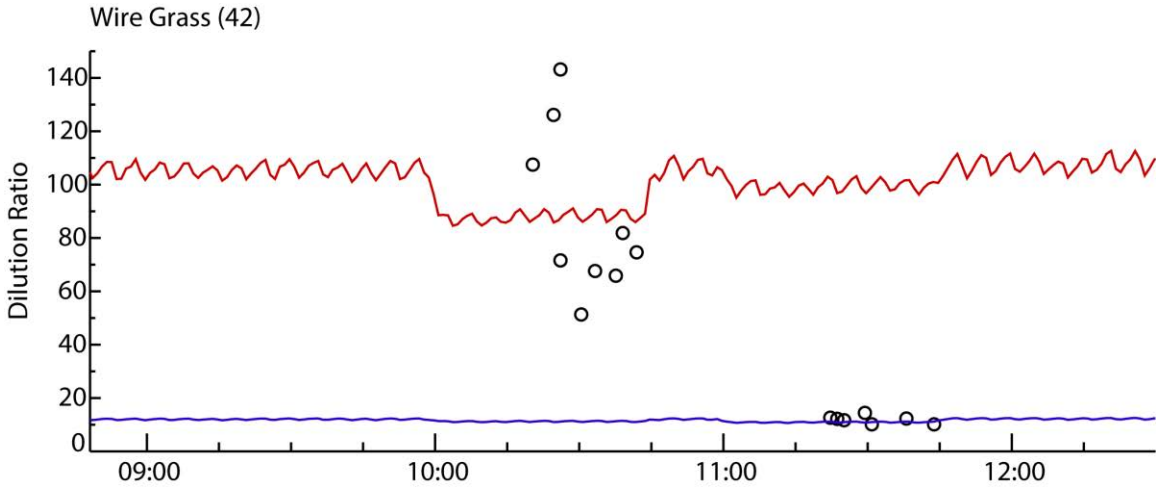

Figure 4.13 Dilution calculated from flows (lines) and SO_4 (circles) in the two barrel dilution system during burn 42.

Figure 4.14 shows dilution ratios calculated from measured flow rates plotted against those calculated from SO_4^{2-} measurements. While there is some scatter in dilution ratios calculated from the two methods, especially for the lower dilution ratios, all values agreed within ± 20 %. The data used for Figure 4.14 are averaged over each dilution time period, with the first 5 minutes of data removed to allow for barrel equilibration. As well, I removed any AMS data with SO_4^{2-} concentrations below 0.1 μg m^{-3}. For all further analysis I use these average data and report just one data point for each dilution barrel measurement time period (seen in Figure 4.15).

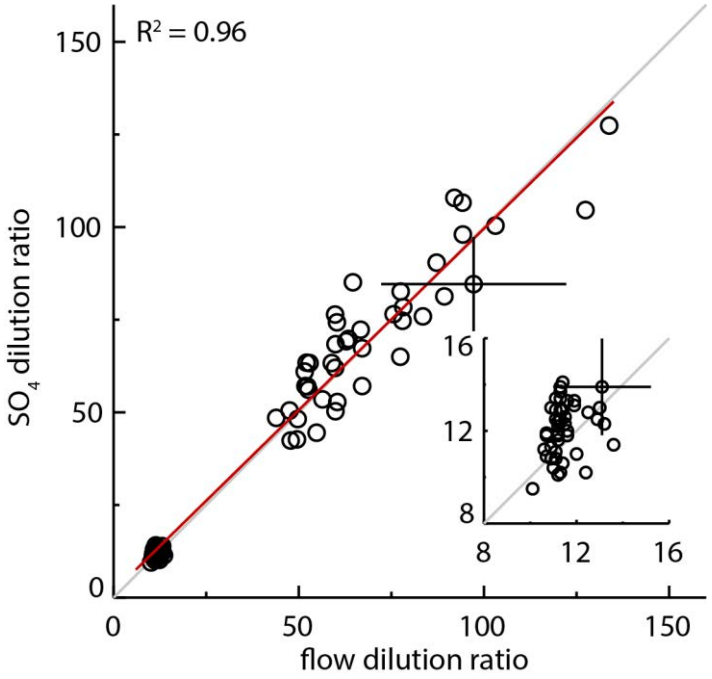

Figure 4.14 Comparison of dilution ratios calculated from changes in SO_4^{2-} concentrations to those calculated from flow rates. Inset plot show dilution in the low dilution barrel.

4.3.5. Calculating partitioning

I used the combined dilutions in the combustion chamber and the controlled, active dilution system to adjust the concentration of total consumed mass (calculated from total measured C emissions and fuel C content) over the course of each experiment. This quantity represents the maximum observable OA concentration at every time in the experiment, and was compared with the actual observed OA concentration in order to determine if volatilization was occurring. Figure 4.15 shows the timeline of this dilution adjusted consumed mass as well as the measured OA concentration for a single burn. If the organic aerosol were completely non-volatile, organic mass would decrease by dilution only and the ratio of organic mass to dilution adjusted consumed mass (the two data streams in Figure 4.15) would not change. If, however, there was a larger decrease in organic aerosol concentration greater than what could be attributed to dilution, this will be attributed to gas/particle phase repartitioning.

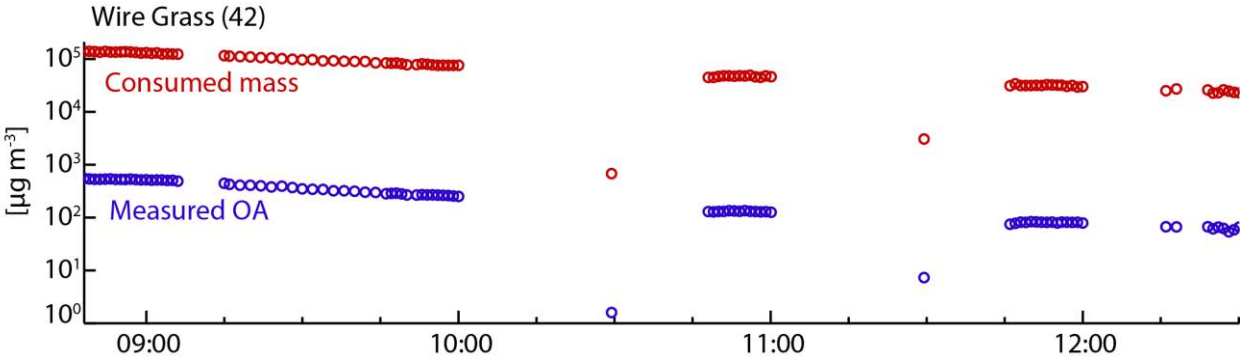

Figure 4.15 Timeline of organic aerosol mass concentration and dilution adjusted dry mass burned.

4.4. Results and discussion

4.4.1. Volatility of organic material

Figure 4.16 shows the ratio of organic aerosol (OA) to dilution adjusted consumed mass as a function of total OA concentration for two lodgepole pine burns. This ratio, expressed in units of kg OA / kg fuel, is an emission factor (EF). As expected [*Grieshop et al.*, 2009], the EFs decrease as the aerosol becomes more dilute, indicating a repartitioning of semi-volatile material as the system equilibrates with the new ambient conditions. In fact, the ratio of organic aerosol to total emissions decreases by about half over the course of both experiments. This finding indicates that by the time fire emissions are diluted to remote ambient concentrations, a 50% change in calculated EF might be realized, depending on the concentration at which the EF was initially calculated. Volatility below the lowest measured OA concentration cannot be constrained from these data, but volatility at lower saturation concentrations was probed by the CMU thermodenuder measurements. Error bars in Figure 4.16 represent measurement uncertainty propagated through the infiltration, dilution and emission factor calculations using standard error propagation. The largest contributor to this uncertainty is the ± 20% uncertainty in the AMS measurements [*Bahreini et al.*, 2009] as values from this instrument are used in both the numerator and denominator of the EF calculations.

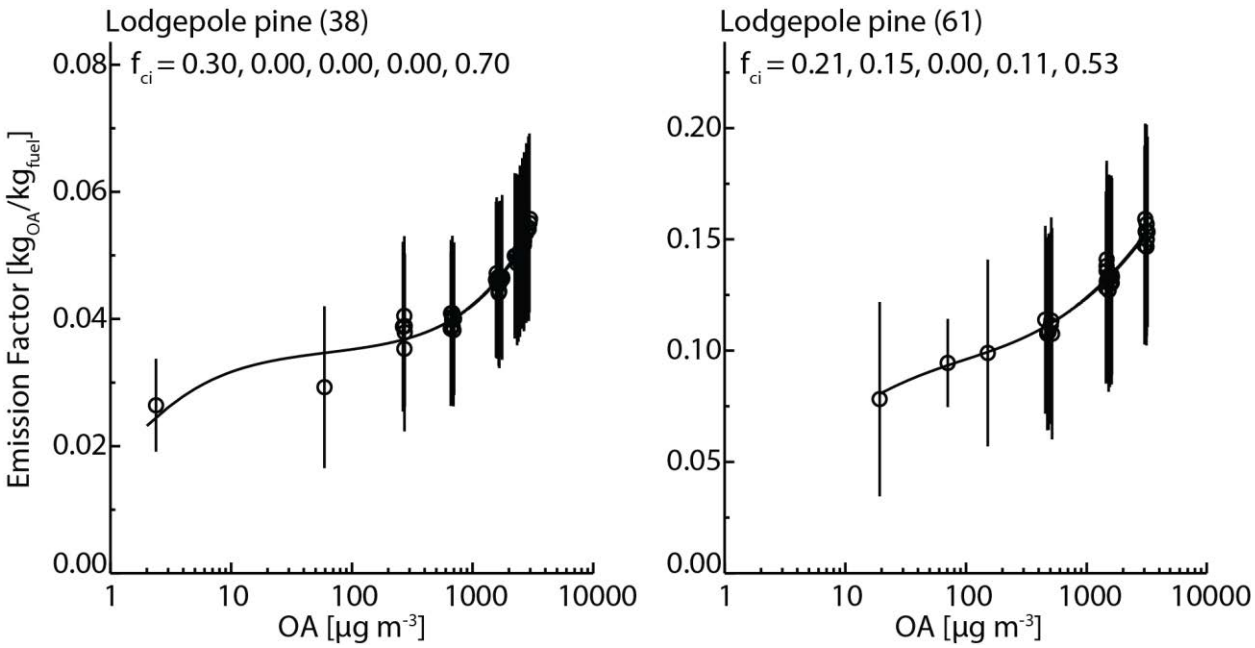

Figure 4.16 Changes in emission factor as a function of OA concentration for two lodgepole pine burns. Note differences in y-axis scales, indicative of different total C emissions for these two burns.

It is clear from Figure 4.16 that the organic emissions from these two burns contain species with a range of volatilities. That is, some aerosol mass is lost quickly upon dilution while some remains in the aerosol form even at low OA concentrations. I fit the dilution data shown in Figure 4.16 to the volatility basis set using Eq 4.1 by using the C_i values, the mass in each bin, as the fitting coefficients. I fit the curves using a least squares regression fit at five C^* bins between 1 and 10000 µg m^{-3} constraining the fitting coefficients to be greater than or equal to zero, since negative C_i values are physically meaningless. The best fit curves are shown in black in Figure 4.16. Note that the y-axis scales in the two lodgepole pine burns shown in the figure are quite different, indicating different combustion conditions resulting in differing emission of total organic C. In order to more directly compare burn-to-burn C_i values, I compared the fraction of emissions in a C_i bin to the total of all C_i values (f_{ci} values reported in

Figure 4.16). The f_{ci} values are analogous to the height of the bars in Figure 4.1, that is they represent the fraction of organic mass with volatility within the range of each VBS bin. For both burns shown in Figure 4.16, the lowest and highest C^* bins accounted for most, or all, of the organic mass. This finding indicates a nearly bimodal (two component) volatility distribution with a highly volatile component and very low volatility component of the organic species, as used in many prior estimates of OA yields [*Odum et al.*, 1996]. It must be noted, however, that the lower end of this volatility distribution is not well constrained. The mass attributed to the C^* = 1 μg m^{-3} could in fact be spread across any number of bins with lower saturation concentration.

The bi-modal volatility distributions indicated by these fits are somewhat different than those determined by *Grieshop et al.* [2009] for wood smoke. Using both dilution and thermodenuders they found a more continuous volatility distribution with significant contributions to total OA mass in all bins between C^* = 1 and 1000.

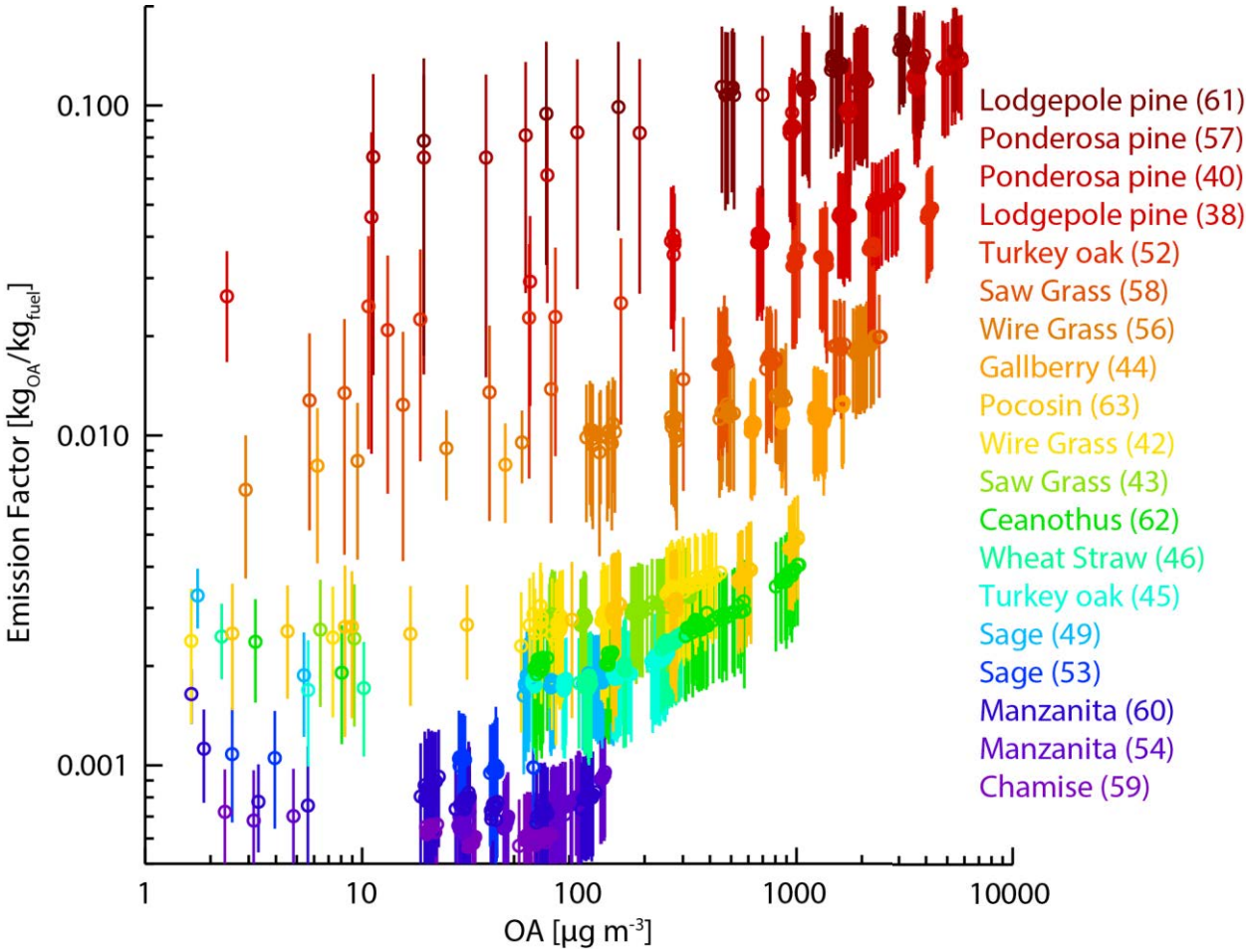

Figure 4.17 Changes in emission factor as a function of OA concentration.

Figure 4.17 shows EF versus OA concentration for all of the burns. Although somewhat subtle on the log/log axis shown in Figure 4.17, EF decreased with decreasing OA concentration for almost every burn. More obvious in Figure 4.17 is the large variability in initial EF. Emission factors are strongly related to fuel type, moisture content and combustion conditions as discussed by *McMeeking et al.* [2009]. Although EFs are ultimately needed by modelers, here I focus on the adjustment of EFs under dilution. Thus, Figure 4.18 shows the same data as Figure 4.17, but normalized at OA = 1000 µg m^{-3}. Only burns with initial OA concentrations greater than 1000 µg m^{-3} are included in Figure 4.18. Burns with lower OA concentrations tended to be

more flaming dominated and, thus, produced higher EC concentrations, with OC:EC ratios close to 1 [*Levin et al.*, 2009; *McMeeking et al.*, 2009]. Under these conditions adsorption may be as important as absorption, or may even be the dominant mechanism, in controlling gas/particle partitioning [*Shrivastava et al.*, 2006]. Normalization of the EF values changes the magnitude of the C_i coefficients from Eq 4.1 but does not alter the mass fraction attributable to each C^* bin. The solid black line in Figure 4.18 is the average VBS fit for all burns. The fitting coefficients for this line, as well as the individual fits for each burn, are shown in Table 4.2. I observed very similar organic aerosol partitioning behavior across all burns. For all burns shown in Figure 4.18 except for ceanothus, the average best fit VBS distribution fell within the measurement uncertainty. The ceanothus burn also had the lowest initial OA mass of the burns shown in Figure 4.18. Therefore, we may not be capturing the true volatility behavior for this case at higher concentrations.

Table 4.2 Fraction of total organic mass in each C^* bin for all burns with initial OA concentration greater than 1000 μg m^{-3}

	C* [μg m^{-3}]	1	10	100	1000	10000
61	**Lodgepole pine**	0.21	0.15	0.00	0.11	0.53
57	**Ponderosa pine**	0.34	0.00	0.06	0.16	0.44
40	**Ponderosa pine**	0.13	0.10	0.05	0.00	0.72
38	**Lodgepole pine**	0.30	0.00	0.02	0.00	0.70
52	**Turkey oak**	0.25	0.00	0.02	0.00	0.73
58	**Saw grass**	0.52	0.00	0.01	0.20	0.27
56	**Wire grass**	0.15	0.00	0.00	0.00	0.85
44	**Gallberry**	0.38	0.00	0.01	0.15	0.45
63	**Pocosin**	0.10	0.00	0.00	0.00	0.90
62	**Ceanothus**	0.08	0.00	0.00	0.00	0.92
	Average	0.25	0.02	0.02	0.06	0.65

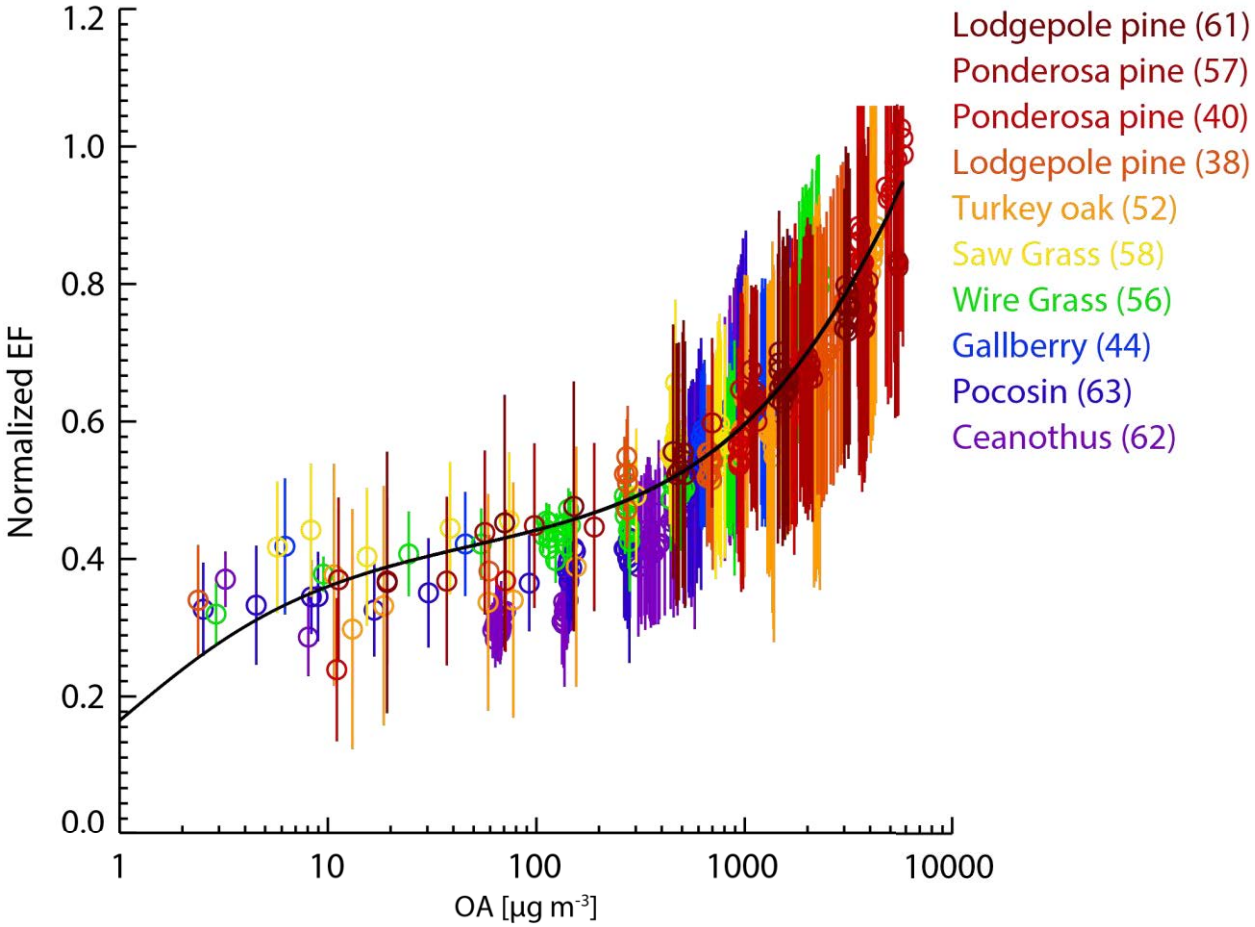

Figure 4.18 Normalized changes in emission factor as a function of OA concentration. Black line is the average best fit to the volatility basis set.

4.4.2. Sources of uncertainty in estimated OA volatility

As can be seen from the fitting coefficients in Table 4.2, and inspection of Figure 4.18, below about 100 µg m^{-3} there was very little change in EF with decreasing OA concentration. That is, there was no further volatilization of the aerosol and OA concentration simply decreased by dilution. This result could indicate that at these lower concentrations (typical of atmospherically relevant concentrations) organic aerosol from biomass burning can be treated as non-volatile in models. However, there are at least three potential experimental artifacts that could be biasing these low concentration measurements. These include: deposition to the barrel

walls; residence time limitations; and liquid-to-solid phase changes induced by rapid mixing and cooling. Further, the simplified calculations presented here ignore the distributions of residence times in the barrels, treating them as idealized, continuous-flow, well-mixed systems.

First, if organic aerosol particles are deposited to the walls of the dilution barrels during the course of an experiment, they can serve as a reservoir of semi-volatile organics and thus invalidate the assumption that the dilution air was devoid of any organic species. By increasing the concentration of gas phase semi-volatile species in the barrels above the level of dilution, some volatilization of incoming smoke particles could be inhibited, and the effect might change with time during each experiment. The barrels were flushed with clean air before each burn to attempt to volatilize any deposited organic aerosol and thus minimize contamination across experiments, but the efficacy of this treatment was not documented.

If some particles were deposited to the interior surfaces of the dilution drums, and subsequently evaporated, higher than expected concentrations of gas phase VOCs should be observed in the drums. As mentioned above, for a few burns I do have corresponding measurements of some gaseous VOCs in the combustion lab and dilution drums. I calculated dilution ratios from these measurements in the same way as I did using SO_4^{2-} (described above), and compared these values to those calculated from flow rates. As can be seen in Figure 4.19, dilution ratios calculated from VOC measurements are consistently lower than those calculated from flow rates or SO_4^{2-}. The reported uncertainty in the VOC measurements is ~50% [*Welsh-Bon*, personal communication]. Further, the measured VOCs account for only a small amount of total gas phase VOC mass. Therefore I cannot use these data as a quantitative measurement of VOC dilution ratios in the barrel. They do suggest, however, that our dilution ratios calculated from flow rates, or SO_4^{2-} concentrations, may be higher than the effective dilution ratio the

organic species are actually experiencing in the barrels. Decreasing the effective dilution ratio would result in higher dilution adjusted consumed mass (since this value is simply initial consumed mass decreased by dilution ratio). Lower calculated EFs, and thus a higher volatility estimate, would result.

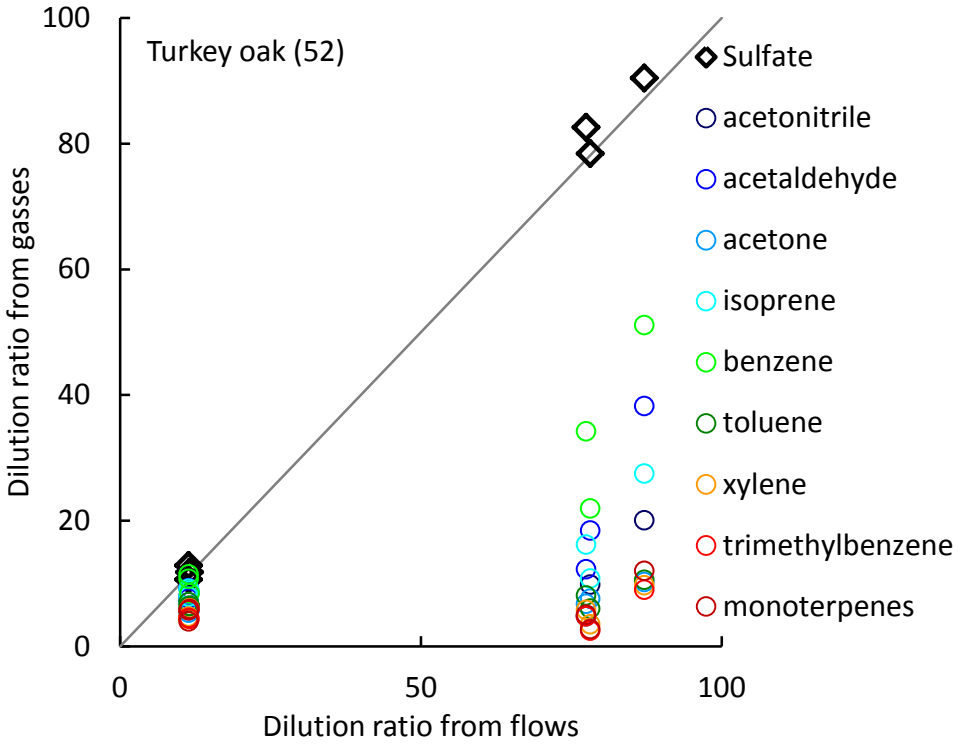

Figure 4.19 Dilution ratio calculated from SO_4^{2-} (diamonds) and a number of gaseous VOC's (circles) versus dilution ratios calculated from flow rates

A second potential problem with the dilution system is that the evaporating particles may not have sufficient time to achieve equilibrium with their evolved gases. If the residence time in the barrels was less than the time required to reach equilibrium (Eq. 4.5) less mass would be lost to evaporation than expected, leading to higher than expected EF. The residence time in each

dilution barrel was ~1.3 minutes; however, recent studies have indicated that equilibration times for organic species might be much longer than this. *Grieshop et al.* [2007] diluted SOA formed from α-pinene ozonolysis using a continuous flow dilution tunnel with a residence time of roughly 30 s. They also observed no partitioning for OA concentrations below ~600 μg m^{-3}. When they diluted the aerosol in the Teflon reaction chamber in which it was formed, however, they did observe slow particle evaporation down to theoretically predicted concentrations, but on the timescale of hours. They were surprised at this result as previous studies of this system indicated that the SOA particles should evaporate in less than 30 s. *Grieshop et al.* [2009] also performed isothermal dilution experiments with diesel exhaust and flash vaporized lubricating oil, both sources of organic aerosol. They filled a Teflon chamber with these emissions and then diluted the sample with filtered, scrubbed air for 45 minutes. They observed continuous evaporation of the aerosol for about 2.5 hours after dilution stopped. In their experiments, initial aerosol concentrations were around 1300 μg m^{-3}, and they observed about a 20% reduction in aerosol mass due to evaporation after wall loss correction (however, wall losses still lead to significant uncertainty in this estimate). They also observed a continuous decrease in EF with dilution down to ~20 μg m^{-3}, but they did not measure below this concentration.

Grieshop et al. [2009] modeled the time-dependent decrease in particle mass using the dynamic equation for particle evaporation presented by *Bilde and Pandis* [2001] and found that an effective uptake coefficient (α) two to three orders of magnitude below the commonly assumed value of 1 was needed to match the data. That is, there was much higher resistance to mass loss than commonly assumed for absorptive partitioning. *Lee at al.* [2011] used a thermodenuder at relatively low temperatures (T = 25 – 100 °C) to probe the volatility of various SOA compounds. They found that a variable α, dependent on temperature, gave the best model

fit to their data, suggesting that at higher temperatures the aerosol exhibits much lower resistance to mass change due, perhaps, to enhanced diffusivity or a phase change of the particle.

Absorptive partitioning theory assumes that the particles are liquid, allowing molecules to move freely though the particle. Recent studies, however, have shown that organic aerosols may exist in an amorphous or glassy state in the atmosphere [*Koop et al.*, 2011; *Mikhailov et al.*, 2009; *Virtanen et al.*, 2010; *Zobrist et al.*, 2008]. The higher viscosity of solid-like particles could severely limit the ability of molecules to move through the bulk of the particle to the surface and evaporate, thus increasing resistance to mass transfer. If "freezing" of the particles was occurring in the dilution barrels, the relatively short residence time would be insufficient for the particles to reach equilibrium and evaporate. Therefore, the aerosol would appear non-volatile. The high flow rates of the clean, dried dilution air relative to the sample flow might present conditions conducive to initial rapid volatilization and latent-heat-derived lowering of the surface temperature of the particles.

The above considerations indicate that aerosol volatility determined from dilution barrel data may be biased too low (that is, the aerosol is more volatile at low OA concentrations than indicated by the experimental data). A thorough investigation of these effects should be conducted via controlled experiments designed to isolate the various potential contributions to artifacts, as discussed in Future Work (Chapter 5). For this study, however, a check against the estimated volatility distributions can be conducted by comparing them with those obtained from thermodenuder data collected by the CMU group. The methods and analysis of the thermodenuder measurements from this experiment are the subject of a separate manuscript [*May et al.,* in preparation]. Here, I simply compare the volatility distributions determined from thermodenuder measurements with those from our dilution experiments. Table 4.3 shows the

volatility distribution for two VBS fits to the TD data for all combined experiments; the least squares regression best fit and another fit that fell within the TD experimental uncertainty, due to unknown ΔH_v and α parameters, and provided a better fit to the dilution data. The best fit volatility distributions determined from TD measurements is more continuous and less "bi-modal" than that from our dilution data, resembling that found by *Grieshop et al.* [2009]. That is, the distribution has more components with volatility in the intermediate bins, not just the high and low bins. Also, because the TD can be heated to temperatures much higher than ambient conditions, this method can probe the volatility distribution at much lower C^* bins than can be accessed from the dilution setup. The TD measurements indicate the aerosol continued to evaporate as OA concentrations were lowered, whereas the dilution data seem to suggest a flattening of volatility below ~100 μg m^{-3}. As discussed above, using TD data to determine volatility requires a number of assumptions, including assumptions about the ΔH_v and α parameters. Thus, there are a wide range of potential volatility distributions given the expected range in these variables. Due to this, the dilution data (from the combustion lab and CMU smog chamber, but not the dilution barrels) were used to constrain the number of TD fits by minimizing the χ^2 statistic, and the resulting alternate fit is also listed in Table 4.3. Although dilution data were used to constrain the alternate TD fit, this solution assigns more mass to the C^* = 100 and 1000 μg m^{-3} bins than that from dilution data alone.

Table 4.3 The best fit volatility distribution determined from thermal denuder (TD) data as well as an alternate fit to these data constrained by the dilution fit.

C^* [μg m^{-3}]	0.001	0.01	0.1	1	10	100	1000	10000
Dilution fit	-	-	-	0.25	0.02	0.02	0.06	0.65
TD best fit	0.025	0.15	0.025	0.075	0.15	0.2	0.125	0.25
TD alt fit	0.00	0.01	0.00	0.00	0.10	0.10	0.10	0.60

4.4.3. Organic aerosol composition

So far in this analysis I have been treating the AMS organics as a single lumped aerosol component, using the total organic mass measured by the AMS. The AMS organic signal, however, can be broken down into families of organic aerosol with similar oxygen content to more fully examine the makeup of the organic aerosol. These components have the general forms, $C_xH_y^+$, $C_xH_yO^+$ and $C_xH_yO_z^+$, that is the ions detected by the AMS contain zero, one or more than one oxygen**.** These individual families of organic aerosol can be treated in the same way as total OA above to determine their volatility distributions.

I calculated emission factors of each OA component, in the same way as discussed above, and plotted them as a function of total OA. Figure 4.20 shows these values for the same lodgepole pine burns discussed above. I also fit each of these curves to the VBS using Eq. 4.1 and five C^* bins from 1 to 10,000 μg m^{-3} (lines in Figure 4.20, fitting coefficients in Table 4.4). From Figure 4.20 it appears that for both burns, all the organic components displayed some volatile behavior; emission factors decrease with decreasing OA concentration in all cases.

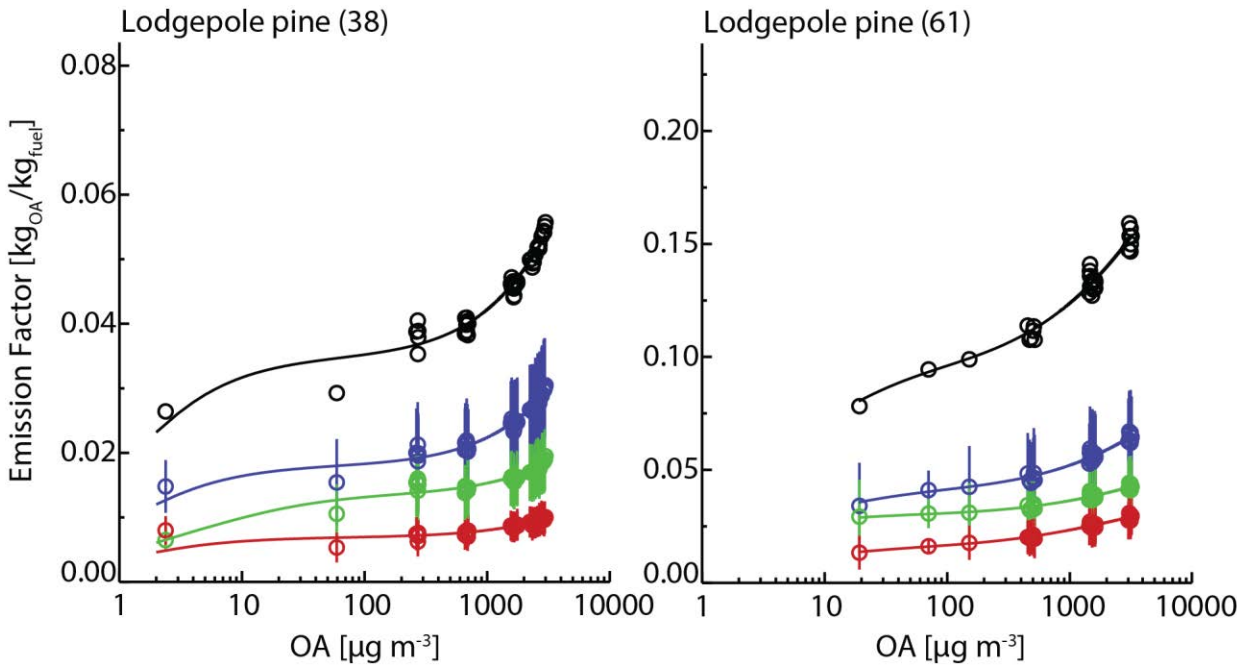

Figure 4.20 Changes in the emission factors of the three organic components as a function of OA concentration for two lodgepole pine burns.

The shape of the volatility distributions can be seen from the VBS fitting coefficients listed in Table 4.4. As with the total OA, discussed above, the volatility distributions for each organic component also appears to be bimodal. All of the components have a large, highly volatile fraction, with most of the remaining mass in the lowest volatility bin. Again, the mass represented in the $C^* = 1$ µg m^{-3} may in fact have saturation concentrations much lower than this, but this cannot be determined from these data.

Table 4.4 Fraction of total organic mass and organic family mass in each C^* bin.

	C^* [μg m^{-3}]	1	10	100	1000	10000
Burn 38	**All OA**	0.30	0.00	0.00	0.00	0.70
	C_xH_y	0.27	0.00	0.00	0.02	0.73
	C_xH_yO	0.23	0.17	0.00	0.00	0.60
	$C_xH_yO_z$	0.36	0.00	0.00	0.00	0.64
Burn 61	**All OA**	0.21	0.15	0.00	0.11	0.53
	C_xH_y	0.24	0.10	0.00	0.08	0.58
	C_xH_yO	0.45	0.00	0.00	0.11	0.44
	$C_xH_yO_z$	0.20	0.14	0.00	0.24	0.42

Figure 4.21 shows the fraction of the total organic aerosol in each organic family for the same lodgepole pine burns as in Table 4.4. As would be expected from two burns of the same fuel, the initial mass fractions of each organic family were very similar between the two burns with values falling within the AMS measurement uncertainty (represented by bars in Figure 4.21). Also, while diluting in the combustion lab, the aerosol from both burns behaved in the same way, with a decrease in the C_xH_y and increase in the C_xH_yO components. However, in the dilution barrels the C_xH_yO fraction actually decreased sharply during burn 38, while it continued to increase during burn 61. This discrepancy may be partly due to an unaccounted for uncertainty at lower concentrations, or may represent some unknown process occurring in the dilution barrel.

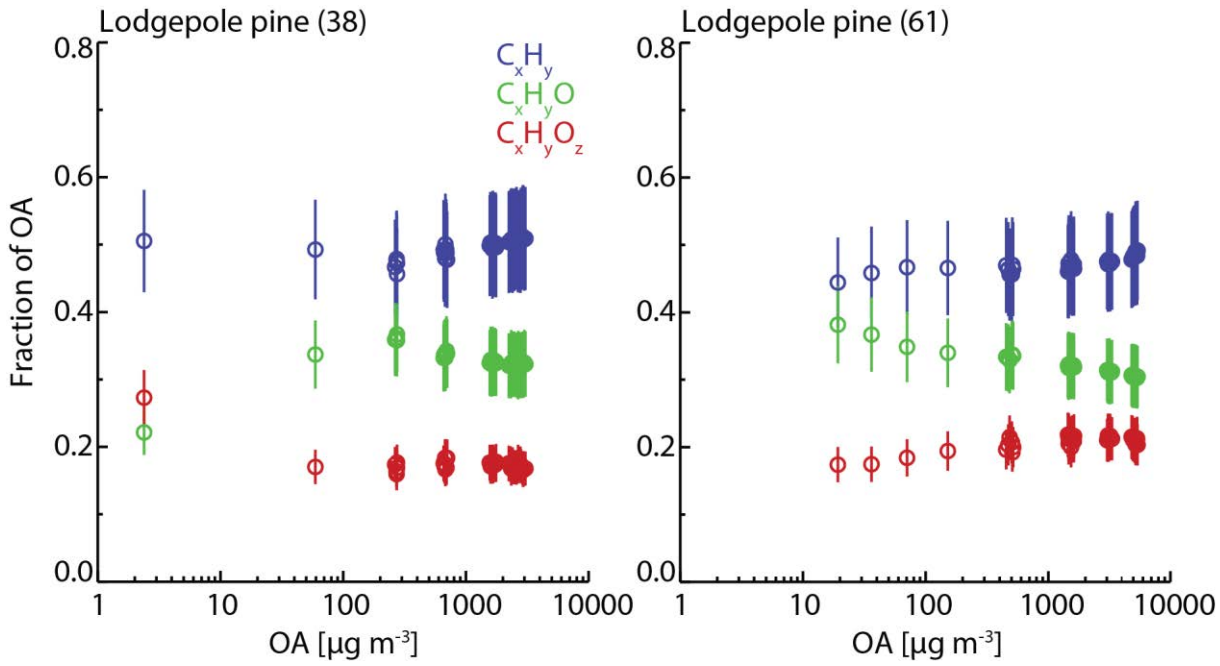

Figure 4.21 Changes in the fraction of each of the three organic components as a function of OA concentration for two lodgepole pine burns

On average, over all burns, the organic aerosol behaved more similar to burn 61, with small decreases in the fractions of C_xH_y and $C_xH_yO_z$, and a steady increase in the fraction of C_xH_yO. Figure 4.22 shows these fractions averaged over all burns. I averaged the data for each burn into bins centered around logarithmically spaced order of magnitude OA mass concentrations, and then averaged across all burns. The bars in Figure 4.22 indicate the standard deviation in the binned values across all burns, not measurement uncertainty as with previous plots. Standard deviations are much higher for the dilution barrel data. The fractional increase in C_xH_yO and decrease in the other two components could indicate some differences in volatility among these components, however, there could also be some unknown and uncharacterized chemical transformations occurring as the aerosol ages. Oxidation in the combustion lab is

probably fairly minimal, however, as the combustion lab has little light and the aerosol is only held in the room for a few hours.

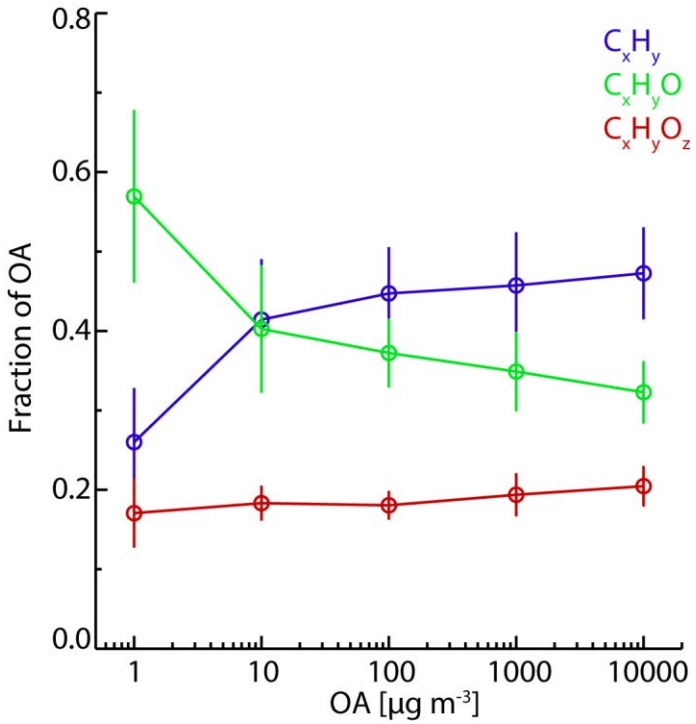

Figure 4.22 Changes in the fraction of each of the organic aerosol components as a function of OA concentration averaged over all burns

Our findings with respect to the relative volatility of the organic fractions are somewhat at odds with the relationships between C^* and O:C proposed by *Jimenez et al.* [2009]. In Figure 4 of their paper, the authors suggest that O:C in ambient aerosol increases with decreasing vapor pressure, especially for C^* lower than 1 µg m^{-3}, whereas the data from this study show only weak trends in volatility with O:C. However, the potential artifacts in our dilution system suggest that similar experiments, with better controls, are needed to assess whether there is a relationship

between O:C in biomass burning emissions, overall volatility, and the volatility of the individual OA components.

4.5. Summary and conclusions

Biomass burning is a major source of aerosol, particularly organic aerosol, to the atmosphere and is especially important in the western US. To understand the characteristics of the aerosol in this region we must know the contributions of biomass combustion to total aerosol mass as well as how these particles behave in the atmosphere. Many studies have examined gas and aerosol emissions from fires and determined emission factors for various fuels and combustion conditions. Several studies have also examined the potential for new particle formation in fire plumes as the gas phase species oxidize and condense. In this chapter I examined another important process, the loss of aerosol mass due to volatilization as the plume isothermally dilutes. The goal is to describe the fire emissions as a continuous distribution of organic species with varying volatilities which will partition between gas and condensed phases as ambient conditions change. Correctly representing this behavior in models is necessary to accurately predict organic aerosol concentrations.

One of the main goals of the third Fire Lab at Missoula Experiment was to quantify the volatility distribution of organic emissions from biomass combustion and fit this distribution to the Volatility Basis Set (VBS) proposed by *Donahue et al.* [2006], thus allowing models to realistically treat gas/particle partitioning of biomass burning emissions as atmospheric conditions change. To this end, fresh emissions from the combustion of a wide range of commonly burned fuels were diluted, using aerosol-, water-, and vapor-free air, to

atmospherically-relevant background conditions in a two stage dilution system. Emissions were also diluted by infiltrating background air as they were held in the combustion lab for several hours. By comparing the change in organic aerosol to the change in total fire emissions as these emissions were diluted, I was able to develop estimates of the volatilities of these emissions and fit these results to the VBS.

In every case, I observed partitioning to the gas phase as the emissions were diluted. That is, organic aerosol concentrations decreased faster than could be accounted for by dilution alone, indicating the presence of semi-volatile organic species. In fact, for all burns with initial OA concentrations above ~1000 μg m^{-3} I observed about a 50% loss in organic aerosol mass due to volatilization as the aerosol was diluted, which could potentially result in a factor of 2 difference in calculated emission factors. There was also considerable consistency in volatility behavior across most burns and, thus, one volatility distribution could be used to model the general behavior of these emissions.

During FLAME 3, volatility of the organic material was also measured using a thermodenuder system. To determine volatility from thermally forced evaporation, assumptions must be made about the enthalpy of vaporization as well as the uptake coefficient of the evaporating material. Given the range in these parameters a large number of volatility distributions could be fit to the measured reduction in aerosol mass with heating. Volatility distributions determined from the dilution measurements discussed in this work fell within the range of potential thermodenduer derived solutions, and can be used to help constrain some of the unknown variables needed for analysis of the thermodenduer results. By heating the sample to very high temperatures, ~200 º, the thermodenduer is also able to probe the behavior of low

volatility material. These measurements indicate that the aerosol continued to evaporate at saturation concentrations which could not be reached with the dilution system.

5. Summary, conclusions and future work

5.1. Summary and conclusions

In this dissertation I have presented measurements of aerosol concentration, size distribution, chemical composition and hygroscopicity from several field campaigns focused on assessing aerosol properties in the mountains of Colorado and Wyoming, as well as laboratory data showing the semi-volatile nature of organic emissions from biomass combustion. These data are useful for modeling studies wishing to determine the effects of aerosols on clouds, precipitation, climate and visibility in this region. However, while there was some consistency in the range of measured aerosol number and volume concentrations and size distribution parameters across all field studies, these values were all statistically different from one another. That is, the data presented in this work cannot be viewed as representative of some larger, cohesive regional aerosol. Instead, these data emphasize the inherent difficulty in correctly modeling aerosol properties due to their highly variable nature, both spatially and temporally. While the data and findings presented in this dissertation, and summarized below, are useful in filling in some unknowns in our understanding of aerosols concentrations, size distributions, composition, mixing state, hygroscopicity and volatility in the mountainous regions of the western US, they also highlight the need for continued measurements and investigation of these parameters in these and other locations.

In the following, I outline the key research findings addressing the three specific goals of this work that were stated in the Introduction.

Goal 1: *Present typical aerosol number and volume concentrations and size distributions as well as seasonal cycles and the factors that influence these properties.* Aerosol number and volume

concentrations and size distributions were measured during three periods over several years (2006 – 2010) as part of the Rocky Mountain Atmospheric Nitrogen Study (RoMANS) as well as during summer, 2011 as part of the Grand Tetons Reactive Nitrogen Deposition Study (GrandTReNDS). While the focus of our measurements during the Bio-hydro-atmosphere interactions of Energy, Aerosols, Carbon, H_2O, Organics & Nitrogen (BEACHON) project was on aerosol hygroscopicity, aerosol number concentrations and size distributions were also measured during this study over a smaller size range. All three study locations represent high altitude, remote and relatively clean regions of the western US, and are expected to have aerosol concentrations and characteristics distinct from the more populated and polluted regions of the country [*Malm et al.*, 2004]. The aerosol data presented here are therefore useful in determining typical concentrations and size distributions for aerosols in these regions.

As expected, aerosol concentrations measured during all three studies were generally low, with average number concentrations ranging between 1000 – 2000 cm^{-3} during the summer months. During the two year-long studies (RoMANS 2 and BEACHON) there was an observed seasonal cycle in aerosol number and volume concentrations with minimum values during the winter increasing to a maximum in summer or early fall. The seasonal cycle in aerosol fine volume concentrations measured during RoMANS 2 was similar to that of $PM_{2.5}$ organic and sulfate mass concentrations measured by the IMPROVE sampler collocated with the ROMANS site. Summertime increases in mass measured by the IMPROVE sampler were largely due to increased organic aerosol mass [*Malm et al.*, 2004]. During BEACHON, the seasonal cycle in aerosol number concentrations was observed to correlate well with the frequency of events typical of new particle formation. Aerosol measured during these events appeared to be dominated by organics and these events could be, at least partially, responsible for the increased

aerosol number and organic mass concentrations observed during the biologically active summer months.

Goal 2: Determine aerosol chemical composition and hygroscopicity and their importance to CCN concentrations.

While IMPROVE measurements in the Rocky Mountain region suggest that 25 – 50 % of fine mode aerosol mass is organic, assuming that $PM_{2.5}$ dust concentrations are all in the coarse mode, aerosol composition measurements made during BEACHON, RoMANS 2010 and GrandTReNDS indicate a much higher organic mass fraction for sub-micron particles, most important for determining CCN concentrations. Aerosol composition measured by an Aerosol Mass Spectrometer (AMS) and derived from aerosol hygroscopicity measurements indicated fine mode organic mass fractions of 70 – 90% during the summer months, with slightly lower values during the winter for particles greater than ~0.15 μm. High organic mass fractions led to low values of the hygroscopicity parameter, κ, measured during BEACHON and calculated from aerosol composition measurements during RoMANS 2010 and GrandTReNDS. Over the entire year-long BEACHON study, κ had an average value of 0.16 ± 0.08, similar to values determined in tropical and boreal forests, and lower than the commonly assumed value of $\kappa_{continental} = 0.3$. In order to correctly determine the potential concentrations of CCN in models, for a given supersaturation, hygroscopicity must be properly represented. As I showed in Chapter 3, correctly accounting for both aerosol hygroscopicity as well as the variation in hygroscopicity with size are needed to correctly predict CCN concentrations for a given supersaturation. However, for higher supersaturation values, ~0.3% and higher, most of the variability in CCN concentration is captured by changes in total number concentrations.

As well as the seasonal cycle in number and volume concentrations, there were also seasonal changes in aerosol hygroscopicity, and hence chemical composition. During the year-long BEACHON campaign the κ values of particles ~0.15 μm or larger decreased from 0.2 – 0.3 during the winter and spring months to ~0.15 during the summer. Smaller particles exhibited little or no such seasonal change and had continuously low κ values, ~0.15. The seasonal change in aerosol hygroscopicity for the larger particles was also correlated with the frequency of new particle formation events, decreasing as the frequency of these events increased. Also, during specific events the κ values of the largest measured particles was observed to decrease as the new particles grew to these sizes. If the particles associated with these events were predominantly organic, as is suspected, this would account for the observed decrease in aerosol hygroscopicity with increasing event frequency.

Goal 3: Determine the volatility distribution for organic material from biomass combustion.

While new particle formation and growth is likely a source of fine mode organic mass in remote area of the Rocky Mountains, the largest measured increase in organic fraction occurred during a smoke event during GrandTReNDS. Also, some of the highest measured aerosol number and fine mode volume concentrations during RoMANS 2, RoMANS 2010 and GrandTReNDS were associated with impacts from biomass burning smoke plumes. Aerosols emitted from biomass combustion are a significant contributor to local and regional aerosol loadings in the mountainous areas of the western US, resulting in clear deviations from the typically clean nature of these areas. Because of the importance of biomass burning aerosols in this, and many other, regions, it is important to correctly represent these emissions in models. The majority of biomass burning emissions, other than CO and CO_2, are organic compounds many of which can transition between gas and condensed phases based on ambient temperature

and aerosol concentrations. In order to model these emissions, therefore, and predict their impacts on aerosol loadings and size distributions, and subsequent effects on visibility reduction, CCN concentrations and cloud properties, the volatility of these emissions must be properly represented.

The purpose of the third Fire Lab at Missoula Experiment (FLAME 3) was to determine the volatility distribution of organic material emitted during biomass combustion. To do this, fire emissions from combustion of fuels typically burned in the western and southeastern US were diluted over time, leading to decreases in aerosol concentrations over several orders of magnitude. By comparing the change in organic aerosol mass concentrations to that of total fire emissions I was able to determine the volatility of organic material and fit this to a volatility distribution. Emissions from all burns with initial organic aerosol concentrations greater than 1000 μg m^{-3} had similar volatility distributions with an average of ~65% of the organic mass falling into the most volatile, highest saturation concentration, bin (C^* = 10000 μg m^{-3}) and much of the remaining mass falling into the lowest volatility bin (C^* = 1 μg m^{-3}). Thermodenuder measurements, able to discern volatility in lower C^* bins by heating the sample to very high temperatures, indicated that this least volatile fraction could in fact be spread across several bins of even lower saturation concentration. The volatility distributions presented in this work are helpful in determining the behavior of modeled organic emissions as the initial high concentrations are advected downwind and diluted. Representative volatility distributions can also be used to modify emission factors determined under varying initial aerosol concentrations, to determine how these emissions will change under varying atmospheric concentrations.

5.2. Future work

In this dissertation I have presented results from several extensive data sets measured during a number of campaigns. Data of this quantity and quality present numerous opportunities for discovery. Here I list three specific areas of potential future research.

1) I have repeatedly noted the spatial and temporal variability in aerosol concentrations, size distribution parameters and composition. Due to this variability, measurements from a single site are difficult to generalize to a larger region. It would be very useful if, at least some of, this variability could be explained and accounted for. One way to do this is through the use of back-trajectory models and multiple linear regression. To do this, measured variability in some property, such as aerosol number concentration, is modeled using a number of potentially predictive variables, such as trajectory origin, transport time, precipitation along trajectory path and other variables. This can determine which variables are most important in determining local variation in aerosol concentrations, and may be useful in understanding the local variability of measured aerosol properties.

2) During BEACHON-RoMBAS many groups measured a host of aerosol and gas species and parameters and a number of data sets are available for further analysis. Aerosol size distributions and composition were measured down to 4 nm, where new particle nucleation can be detected. I would like to use these data along with the size resolved CCN data to examine aerosol hygroscopicity during times of high new particle formation events to determine their effect on κ and CCN concentrations.

3) While the FLAME 3 study provided valuable information about the volatility of organic emissions from biomass combustion, there were a number of factors which may have biased our

measurements (listed in Chapter 4). Future measurement campaigns could be designed to avoid such issues, and better quantify volatility distributions. Specifically, unconstrained dilution in the combustion lab should be avoided in future studies. This could be done by sampling emissions into a Teflon smog chamber at the beginning of a burn, as was done by the CMU group during FLAME 3, and then diluting the sample in the chamber. Using this method, sample could be initially diluted and then measured for several hours, thus determining the time needed for evaporating particles to reach equilibrium. This would provide very useful information about the uptake coefficient of these organic emissions which could be further used to constrain volatility distributions calculated from thermodenuder data and give insight into particle phase. One potential difficulty with holding the smoke for an extended period of time in a smoke chamber is the increased time will lead to greater wall loses and potential interactions with deposited species. While wall loses can be accounted for through measurement and models, this would still add uncertainty to the derived volatility distributions [*e.g. Grieshop et al.,* 2009].

References

Abbs, D. J., and R. A. Pielke (1986), THERMALLY FORCED SURFACE FLOW AND CONVERGENCE PATTERNS OVER NORTHEAST COLORADO, *Monthly Weather Review*, *114*(12), 2281-2296, doi:10.1175/1520-0493(1986)114<2281:tfsfac>2.0.co;2.

Akagi, S. K., R. J. Yokelson, C. Wiedinmyer, M. J. Alvarado, J. S. Reid, T. Karl, J. D. Crounse, and P. O. Wennberg (2011), Emission factors for open and domestic biomass burning for use in atmospheric models, *Atmospheric Chemistry and Physics*, *11*(9), 4039-4072, doi:10.5194/acp-11-4039-2011.

Albrecht, B. A. (1989), Aerosols, cloud microphysics, and fractional cloudiness, *Science*, *245*, 1227-1230.

An, W. J., R. K. Pathak, B. H. Lee, and S. N. Pandis (2007), Aerosol volatility measurement using an improved thermodenuder: Application to secondary organic aerosol, *Journal of Aerosol Science*, *38*(3), 305-314, doi:10.1016/j.jaerosci.2006.12.002.

Andreae, M. O., et al. (2002), Biogeochemical cycling of carbon, water, energy, trace gases, and aerosols in Amazonia: The LBA-EUSTACH experiments, *Journal of Geophysical Research-Atmospheres*, *107*(D20), doi:8066 10.1029/2001jd000524.

Andreae, M. O., and P. Merlet (2001), Emission of trace gases and aerosols from biomass burning, *Global Biogeochemical Cycles*, *15*(4), 955-966, doi:10.1029/2000gb001382.

Andreae, M. O., and D. Rosenfeld (2008), Aerosol-cloud-precipitation interactions. Part 1. The nature and sources of cloud-active aerosols, *Earth-Science Reviews*, *89*(1-2), 13-41, doi:10.1016/j.earscirev.2008.03.001.

Andreae, M. O., D. Rosenfeld, P. Artaxo, A. A. Costa, G. P. Frank, K. M. Longo, and M. A. F. Silva-Dias (2004), Smoking rain clouds over the Amazon, *Science*, *303*(5662), 1337-1342, doi:10.1126/science.1092779.

Asa-Awuku, A., G. J. Engelhart, B. H. Lee, S. N. Pandis, and A. Nenes (2009), Relating CCN activity, volatility, and droplet growth kinetics of beta-caryophyllene secondary organic aerosol, *Atmospheric Chemistry and Physics*, *9*(3), 795-812.

Asa-Awuku, A., A. Nenes, S. Gao, R. C. Flagan, and J. H. Seinfeld (2010), Water-soluble SOA from Alkene ozonolysis: composition and droplet activation kinetics inferences from analysis of CCN activity, *Atmospheric Chemistry and Physics*, *10*(4), 1585-1597.

Ashley, W. S., T. L. Mote, P. G. Dixon, S. L. Trotter, E. J. Powell, J. D. Durkee, and A. J. Grundstein (2003), Distribution of mesoscale convective complex rainfall in the United States, *Monthly Weather Review*, *131*(12), 3003-3017, doi:10.1175/1520-0493(2003)131<3003:domccr>2.0.co;2.

Augustine, J. A., and F. Caracena (1994), LOWER-TROPOSPHERIC PRECURSORS TO NOCTURNAL MCS DEVELOPMENT OVER THE CENTRAL UNITED-STATES, *Weather and Forecasting*, *9*(1), 116-135, doi:10.1175/1520-0434(1994)009<0116:ltptnm>2.0.co;2.

Bahreini, R., et al. (2009), Organic aerosol formation in urban and industrial plumes near Houston and Dallas, Texas, *Journal of Geophysical Research-Atmospheres*, *114*, doi:10.1029/2008jd011493.

Bahreini, R., M. D. Keywood, N. L. Ng, V. Varutbangkul, S. Gao, R. C. Flagan, J. H. Seinfeld, D. R. Worsnop, and J. L. Jimenez (2005), Measurements of secondary organic aerosol from oxidation of cycloalkenes, terpenes, and m-xylene using an Aerodyne aerosol mass spectrometer, *Environmental Science & Technology*, *39*(15), 5674-5688, doi:10.1021/es048061a.

Baron, J. S., H. M. Rueth, A. M. Wolfe, K. R. Nydick, E. J. Allstott, J. T. Minear, and B. Moraska (2000), Ecosystem responses to nitrogen deposition in the Colorado Front Range, *Ecosystems*, *3*(4), 352-368.

Barth, M., et al. (2005), Coupling between land ecosystems and the atmospheric hydrologic cycle through biogenic aerosol pathways, *Bulletin of the American Meteorological Society*, *86*(12), 1738-1742, doi:10.1175/bams-86-12-1738.

Beem, K. B., et al. (2010), Deposition of reactive nitrogen during the Rocky Mountain Airborne Nitrogen and Sulfur (RoMANS) study, *Environmental Pollution*, *158*(3), 862-872, doi:10.1016/j.envpol.2009.09.023.

Bilde, M., and S. N. Pandis (2001), Evaporation rates and vapor pressures of individual aerosol species formed in the atmospheric oxidation of alpha- and beta-pinene, *Environmental Science & Technology*, *35*(16), 3344-3349, doi:10.1021/es001946b.

Bond, T. C., and R. W. Bergstrom (2006), Light absorption by carbonaceous particles: An investigative review, *Aerosol Science and Technology*, *40*(1), 27-67, doi:10.1080/02786820500421521.

Borys, R. D., D. H. Lowenthal, and D. L. Mitchell (2000), The relationships among cloud microphysics, chemistry, and precipitation rate in cold mountain clouds, *Atmospheric Environment*, *34*(16), 2593-2602, doi:10.1016/s1352-2310(99)00492-6.

Boy, M., et al. (2008), New particle formation in the front range of the colorado rocky mountains, *Atmospheric Chemistry and Physics*, *8*(6), 1577-1590.

Cabada, J. C., A. Khlystov, A. E. Wittig, C. Pilinis, and S. N. Pandis (2004), Light scattering by fine particles during the Pittsburgh Air Quality Study: measurements and modeling, *Journal of Geophysical Research-Atmospheres*, *109*(D16), 14, doi:D16s0310.1029/2003jd004155.

Canagaratna, M. R., et al. (2007), Chemical and microphysical characterization of ambient aerosols with the aerodyne aerosol mass spectrometer, *Mass Spectrometry Reviews*, *26*(2), 185-222, doi:10.1002/mas.20115.

Cappa, C. D., and J. L. Jimenez (2010), Quantitative estimates of the volatility of ambient organic aerosol, *Atmospheric Chemistry and Physics*, *10*(12), 5409-5424, doi:10.5194/acp-10-5409-2010.

Carrico, C. M., S. M. Kreidenweis, W. C. Malm, D. E. Day, T. Lee, J. Carrillo, G. R. McMeeking, and J. L. Collett (2005), Hygroscopic growth behavior of a carbon-dominated aerosol in Yosemite National Park, *Atmospheric Environment*, *39*(8), 1393-1404, doi:10.1016/j.atmosenv.2004.11.029.

Carrico, C. M., M. D. Petters, S. M. Kreidenweis, A. P. Sullivan, G. R. McMeeking, E. J. T. Levin, G. Engling, W. C. Malm, and J. L. Collett (2010), Water uptake and chemical composition of fresh aerosols generated in open burning of biomass, *Atmospheric Chemistry and Physics*, *10*(11), 5165-5178, doi:10.5194/acp-10-5165-2010.

Cerully, K. M., et al. (2011), Aerosol hygroscopicity and CCN activation kinetics in a boreal forest environment during the 2007 EUCAARI campaign, *Atmos. Chem. Phys. Discuss.*, *11*, 15029–15074.

Chang, R. Y. W., J. G. Slowik, N. C. Shantz, A. Vlasenko, J. Liggio, S. J. Sjostedt, W. R. Leaitch, and J. P. D. Abbatt (2010), The hygroscopicity parameter (kappa) of ambient organic aerosol at a field site subject to biogenic and anthropogenic influences: relationship to degree of aerosol oxidation, *Atmospheric Chemistry and Physics*, *10*(11), 5047-5064, doi:10.5194/acp-10-5047-2010.

Charlson, R. J., S. E. Schwartz, J. M. Hales, R. D. Cess, J. A. Coakley, J. E. Hansen, and D. J. Hofmann (1992), Climate forcing by anthropogenic aerosol, *Science*, *255*(5043), 423-430, doi:10.1126/science.255.5043.423.

Chen, L. W. A., P. Verburg, A. Shackelford, D. Zhu, R. Susfalk, J. C. Chow, and J. G. Watson (2010), Moisture effects on carbon and nitrogen emission from burning of wildland biomass, *Atmospheric Chemistry and Physics*, *10*(14), 6617-6625, doi:10.5194/acp-10-6617-2010.

Christensen, J. H. (1997), The Danish Eulerian hemispheric model - A three-dimensional air pollution model used for the Arctic, *Atmospheric Environment*, *31*(24), 4169-4191, doi:10.1016/s1352-2310(97)00264-1.

Clegg, S. L., P. Brimblecombe, and A. S. Wexler (1998), Thermodynamic model of the system H+-NH4+-SO42--NO3--H2O at tropospheric temperatures, *Journal of Physical Chemistry A*, *102*(12), 2137-2154.

Clement, A. C., R. Burgman, and J. R. Norris (2009), Observational and Model Evidence for Positive Low-Level Cloud Feedback, *Science*, *325*(5939), 460-464, doi:10.1126/science.1171255.

Colburn, K. A., and P. R. S. Johnson (2003), Air pollution concerns not changed by S-PLUS flaw, *Science*, *299*(5607), 665-666, doi:10.1126/science.1082105.

Cotton, W. R., Z. Levin, and SpringerLink (Online service) (2009), Aerosol pollution impact on precipitation a scientific review, edited, pp. xxi, 386 p. ill. (some col.), maps 324 cm., Springer,, Dordrecht ; London.

Cubison, M. J., B. Ervens, G. Feingold, K. S. Docherty, I. M. Ulbrich, L. Shields, K. Prather, S. Hering, and J. L. Jimenez (2008), The influence of chemical composition and mixing state of Los Angeles urban aerosol on CCN number and cloud properties, *Atmospheric Chemistry and Physics*, *8*(18), 5649-5667.

Cubison, M. J., et al. (2011), Effects of aging on organic aerosol from open biomass burning smoke in aircraft and laboratory studies, *Atmospheric Chemistry and Physics*, *11*(23), 12049-12064, doi:10.5194/acp-11-12049-2011.

Dahneke, N. M. (1983), Simple kinetic theory of Brownian diffusion in vapors and aerosols, in *Theory of dispersed multiphase flow*, edited by R. E. Meyer, pp. 97 - 133, Acedimic Press, New York.

DeCarlo, P. F., et al. (2006), Field-deployable, high-resolution, time-of-flight aerosol mass spectrometer, *Analytical Chemistry*, *78*(24), 8281-8289, doi:10.1021/ac061249n.

Donahue, N. M., J. H. Kroll, S. N. Pandis, and A. L. Robinson (2012), A two-dimensional volatility basis set - Part 2: Diagnostics of organic-aerosol evolution, *Atmospheric Chemistry and Physics*, *12*(2), 615-634, doi:10.5194/acp-12-615-2012.

Donahue, N. M., A. L. Robinson, and S. N. Pandis (2009), Atmospheric organic particulate matter: From smoke to secondary organic aerosol, *Atmospheric Environment*, *43*(1), 94-106, doi:10.1016/j.atmosenv.2008.09.055.

Donahue, N. M., A. L. Robinson, C. O. Stanier, and S. N. Pandis (2006), Coupled partitioning, dilution, and chemical aging of semivolatile organics, *Environmental Science & Technology*, *40*(8), 2635-2643, doi:10.1021/es052297c.

Douglas, M. W., R. A. Maddox, K. Howard, and S. Reyes (1993), THE MEXICAN MONSOON, *Journal of Climate*, *6*(8), 1665-1677, doi:10.1175/1520-0442(1993)006<1665:tmm>2.0.co;2.

Draxler, R. R. (1999), HYSPLIT4 user's guide*Rep.*, NOAA Air Resources Laboratory, Silver Spring, MD.

Draxler, R. R., and G. D. Hess (1997), Description of the HYSPLIT_4 modeling system*Rep.*, 24 pp, NOAA Air Resources Laboratory, Silver Spring, MD.

Draxler, R. R., and G. D. Hess (1998), An overview of the HYSPLIT_4 modeling system of trajectories, dispersion, and deposition, *Aust. Meteor. Mag.*, *47*, 295-308.

Drewnick, F., et al. (2005), A new time-of-flight aerosol mass spectrometer (TOF-AMS) - Instrument description and first field deployment, *Aerosol Science and Technology*, *39*(7), 637-658, doi:10.1080/02786820500182040.

Duhl, T. R., D. Helmig, and A. Guenther (2008), Sesquiterpene emissions from vegetation: a review, *Biogeosciences*, *5*(3), 761-777.

Duplissy, J., et al. (2008), Cloud forming potential of secondary organic aerosol under near atmospheric conditions, *Geophysical Research Letters*, *35*(3), doi:L03818 10.1029/2007gl031075.

Dusek, U., G. P. Frank, J. Curtius, F. Drewnick, J. Schneider, A. Kurten, D. Rose, M. O. Andreae, S. Borrmann, and U. Poschl (2010), Enhanced organic mass fraction and decreased hygroscopicity of cloud condensation nuclei (CCN) during new particle formation events, *Geophysical Research Letters*, *37*, doi:L03804 10.1029/2009gl040930.

Engelhart, G. J., R. H. Moore, A. Nenes, and S. N. Pandis (2011), Cloud condensation nuclei activity of isoprene secondary organic aerosol, *Journal of Geophysical Research-Atmospheres*, *116*, 11, doi:D02207 10.1029/2010jd014706.

Feingold, G., W. R. Cotton, S. M. Kreidenweis, and J. T. Davis (1999), The impact of giant cloud condensation nuclei on drizzle formation in stratocumulus: Implications for cloud radiative properties, *Journal of the Atmospheric Sciences*, *56*(24), 4100-4117, doi:10.1175/1520-0469(1999)056<4100:tiogcc>2.0.co;2.

Fenn, M. E., et al. (2003), Ecological effects of nitrogen deposition in the western United States, *Bioscience*, *53*(4), 404-420.

Ford, B., and C. L. Heald (2012), An A-train and model perspective on the vertical distribution of aerosols and CO in the Northern Hemisphere, *Journal of Geophysical Research-Atmospheres*, *117*, doi:10.1029/2011jd016977.

Fors, E. O., E. Swietlicki, B. Svenningsson, A. Kristensson, G. P. Frank, and M. Sporre (2011), Hygroscopic properties of the ambient aerosol in southern Sweden - a two year study, *Atmospheric Chemistry and Physics*, *11*(16), 8343-8361, doi:10.5194/acp-11-8343-2011.

Fountoukis, C., P. N. Racherla, H. van der Gon, P. Polymeneas, P. E. Charalampidis, C. Pilinis, A. Wiedensohler, M. Dall'Osto, C. O'Dowd, and S. N. Pandis (2011), Evaluation of a three-dimensional chemical transport model (PMCAMx) in the European domain during the EUCAARI May 2008 campaign, *Atmospheric Chemistry and Physics*, *11*(20), 10331-10347, doi:10.5194/acp-11-10331-2011.

Fritsch, J. M., R. J. Kane, and C. R. Chelius (1986), THE CONTRIBUTION OF MESOSCALE CONVECTIVE WEATHER SYSTEMS TO THE WARM-SEASON PRECIPITATION IN THE UNITED-STATES, *Journal of Climate and Applied Meteorology*, *25*(10), 1333-1345, doi:10.1175/1520-0450(1986)025<1333:tcomcw>2.0.co;2.

Fuzzi, S., et al. (2006), Critical assessment of the current state of scientific knowledge, terminology, and research needs concerning the role of organic aerosols in the atmosphere, climate, and global change, *Atmospheric Chemistry and Physics*, *6*, 2017-2038.

Gebhart, K. A., S. M. Kreidenweis, and W. C. Malm (2001), Back-trajectory analyses of fine particulate matter measured at Big Bend National Park in the historical database and the 1996 scoping study, *Science of the Total Environment*, *276*(1-3), 185-204, doi:10.1016/s0048-9697(01)00779-3.

Gebhart, K. A., B. A. Schichtel, M. G. Barna, and W. C. Malm (2006), Quantitative back-trajectory apportionment of sources of particulate sulfate at Big Bend National Park, TX, *Atmospheric Environment*, *40*(16), 2823-2834, doi:10.1016/j.atmosenv.2006.01.018.

Gebhart, K. A., B. A. Schichtel, W. C. Malm, M. G. Barna, M. A. Rodriguez, and J. L. Collett (2011), Back-trajectory-based source apportionment of airborne sulfur and nitrogen concentrations at Rocky Mountain National Park, Colorado, USA, *Atmospheric Environment*, *45*(3), 621-633, doi:10.1016/j.atmosenv.2010.10.035.

Ghan, S. J., X. Liu, R. C. Easter, R. Zaveri, P. J. Rasch, J. H. Yoon, and B. Eaton (2012), Toward a Minimal Representation of Aerosols in Climate Models: Comparative Decomposition of Aerosol Direct, Semidirect, and Indirect Radiative Forcing, *Journal of Climate*, *25*(19), 6461-6476, doi:10.1175/jcli-d-11-00650.1.

Grieshop, A. P., N. M. Donahue, and A. L. Robinson (2007), Is the gas-particle partitioning in alpha-pinene secondary organic aerosol reversible?, *Geophysical Research Letters*, *34*(14), doi:L1481010.1029/2007gl029987.

Grieshop, A. P., M. A. Miracolo, N. M. Donahue, and A. L. Robinson (2009), Constraining the Volatility Distribution and Gas-Particle Partitioning of Combustion Aerosols Using Isothermal Dilution and Thermodenuder Measurements, *Environmental Science & Technology*, *43*(13), 4750-4756, doi:10.1021/es8032378.

Gunthe, S. S., et al. (2009), Cloud condensation nuclei in pristine tropical rainforest air of Amazonia: size-resolved measurements and modeling of atmospheric aerosol composition and CCN activity, *Atmospheric Chemistry and Physics*, *9*(19), 7551-7575.

Hallar, A. G., D. H. Lowenthal, G. Chirokova, R. D. Borys, and C. Wiedinmyer (2011), Persistent daily new particle formation at a mountain-top location, *Atmospheric Environment*, *45*(24), 4111-4115, doi:10.1016/j.atmosenv.2011.04.044.

Hallquist, M., et al. (2009), The formation, properties and impact of secondary organic aerosol: current and emerging issues, *Atmospheric Chemistry and Physics*, *9*(14), 5155-5236.

Hand, J. L., D. E. Day, G. M. McMeeking, E. J. T. Levin, C. M. Carrico, S. M. Kreidenweis, W. C. Malm, A. Laskin, and Y. Desyaterik (2010), Measured and modeled humidification factors of fresh smoke particles from biomass burning: role of inorganic constituents, *Atmospheric Chemistry and Physics*, *10*(13), 6179-6194, doi:10.5194/acp-10-6179-2010.

Hand, J. L., and S. M. Kreidenweis (2002), A new method for retrieving particle refractive index and effective density from aerosol size distribution data, *Aerosol Science and Technology*, *36*(10), 1012-1026, doi:10.1080/02786820290092276.

Hand, J. L., S. M. Kreldenweis, D. E. Sherman, J. L. Collett, S. V. Hering, D. E. Day, and W. C. Malm (2002), Aerosol size distributions and visibility estimates during the Big Bend regional aerosol and visibility observational (BRAVO) study, *Atmospheric Environment*, *36*(32), 5043-5055.

Hand, J. L., and W. C. Malm (2007), Review of aerosol mass scattering efficiencies from ground-based measurements since 1990, *Journal of Geophysical Research-Atmospheres*, *112*(D18), 24, doi:D1620310.1029/2007jd008484.

Hansen, J., M. Sato, and R. Ruedy (1997), Radiative forcing and climate response, *Journal of Geophysical Research-Atmospheres*, *102*(D6), 6831-6864, doi:10.1029/96jd03436.

Heald, C. L., et al. (2011), Exploring the vertical profile of atmospheric organic aerosol: comparing 17 aircraft field campaigns with a global model, *Atmospheric Chemistry and Physics*, *11*(24), 12673-12696, doi:10.5194/acp-11-12673-2011.

Heald, C. L., et al. (2012), Atmospheric ammonia and particulate inorganic nitrogen over the United States, *Atmos. Chem. Phys.*, *12*, 10295–10312, doi:10.5194/acp-12-10295-2012.

Heald, C. L., D. J. Jacob, R. J. Park, L. M. Russell, B. J. Huebert, J. H. Seinfeld, H. Liao, and R. J. Weber (2005), A large organic aerosol source in the free troposphere missing from current models, *Geophysical Research Letters*, *32*(18), doi:10.1029/2005gl023831.

Hennigan, C. J., et al. (2011), Chemical and physical transformations of organic aerosol from the photo-oxidation of open biomass burning emissions in an environmental chamber, *Atmospheric Chemistry and Physics*, *11*(15), 7669-7686, doi:10.5194/acp-11-7669-2011.

Hildemann, L. M., G. R. Cass, and G. R. Markowski (1989), A dilution stack sampler for collection of organic aerosol emissions - design, characterization and field-tests, *Aerosol Science and Technology*, *10*(1), 193-204, doi:10.1080/02786828908959234.

Hossain, A., S. Park, J. S. Kim, and K. Park (2012), Volatility and mixing states of ultrafine particles from biomass burning, *Journal of Hazardous Materials*, *205*, 189-197, doi:10.1016/j.jhazmat.2011.12.061.

Janhall, S., M. O. Andreae, and U. Poschl (2010), Biomass burning aerosol emissions from vegetation fires: particle number and mass emission factors and size distributions, *Atmospheric Chemistry and Physics*, *10*(3), 1427-1439.

Jimenez, J. L., et al. (2009), Evolution of Organic Aerosols in the Atmosphere, *Science*, *326*(5959), 1525-1529, doi:10.1126/science.1180353.

Jirak, I. L., and W. R. Cotton (2006), Effect of air pollution on precipitation along the front range of the Rocky Mountains, *Journal of Applied Meteorology and Climatology*, *45*(1), 236-245, doi:10.1175/jam2328.1.

Jung, J. G., C. Fountoukis, P. J. Adams, and S. N. Pandis (2010), Simulation of in situ ultrafine particle formation in the eastern United States using PMCAMx-UF, *Journal of Geophysical Research-Atmospheres*, *115*, doi:10.1029/2009jd012313.

Kammermann, L., M. Gysel, E. Weingartner, and U. Baltensperger (2010), 13-month climatology of the aerosol hygroscopicity at the free tropospheric site Jungfraujoch (3580 m a.s.l.), *Atmospheric Chemistry and Physics*, *10*(22), 10717-10732, doi:10.5194/acp-10-10717-2010.

Kanakidou, M., et al. (2005), Organic aerosol and global climate modelling: a review, *Atmospheric Chemistry and Physics*, *5*, 1053-1123.

Khain, A., and B. Lynn (2009), Simulation of a supercell storm in clean and dirty atmosphere using weather research and forecast model with spectral bin microphysics, *Journal of Geophysical Research-Atmospheres*, *114*, doi:10.1029/2009jd011827.

Khain, A., D. Rosenfeld, and A. Pokrovsky (2005), Aerosol impact on the dynamics and microphysics of deep convective clouds, *Quarterly Journal of the Royal Meteorological Society*, *131*(611), 2639-2663, doi:10.1256/qj.04.62.

Kim, S., T. Karl, A. Guenther, G. Tyndall, J. Orlando, P. Harley, R. Rasmussen, and E. Apel (2010), Emissions and ambient distributions of Biogenic Volatile Organic Compounds (BVOC) in a ponderosa pine ecosystem: interpretation of PTR-MS mass spectra, *Atmospheric Chemistry and Physics*, *10*(4), 1759-1771.

King, S. M., T. Rosenoern, J. E. Shilling, Q. Chen, and S. T. Martin (2007), Cloud condensation nucleus activity of secondary organic aerosol particles mixed with sulfate, *Geophysical Research Letters*, *34*(24), 5, doi:L24806 10.1029/2007gl030390.

King, S. M., T. Rosenoern, J. E. Shilling, Q. Chen, Z. Wang, G. Biskos, K. A. McKinney, U. Poschl, and S. T. Martin (2010), Cloud droplet activation of mixed organic-sulfate particles produced by the photooxidation of isoprene, *Atmospheric Chemistry and Physics*, *10*(8), 3953-3964.

Kinne, S., et al. (2006), An AeroCom initial assessment - optical properties in aerosol component modules of global models, *Atmospheric Chemistry and Physics*, *6*, 1815-1834.

Koehler, K. A., P. J. DeMott, S. M. Kreidenweis, O. B. Popovicheva, M. D. Petters, C. M. Carrico, E. D. Kireeva, T. D. Khokhlova, and N. K. Shonija (2009), Cloud condensation nuclei and ice nucleation activity of hydrophobic and hydrophilic soot particles, *Physical Chemistry Chemical Physics*, *11*(36), 7906-7920, doi:10.1039/b905334b.

Kohler, H. (1936), The nucleus in and the growth of hygroscopic droplets, *Transactions of the Faraday Society*, *32*(2), 1152-1161, doi:10.1039/tf9363201152.

Koop, T., J. Bookhold, M. Shiraiwa, and U. Poschl (2011), Glass transition and phase state of organic compounds: dependency on molecular properties and implications for secondary organic

aerosols in the atmosphere, *Physical Chemistry Chemical Physics*, *13*(43), 19238-19255, doi:10.1039/c1cp22617g.

Kroll, J. H., and J. H. Seinfeld (2005), Representation of secondary organic aerosol laboratory chamber data for the interpretation of mechanisms of particle growth, *Environmental Science & Technology*, *39*(11), 4159-4165, doi:10.1021/es048292h.

Kulmala, M., et al. (2004a), A new feedback mechanism linking forests, aerosols, and climate, *Atmospheric Chemistry and Physics*, *4*, 557-562.

Kulmala, M., H. Vehkamaki, T. Petaja, M. Dal Maso, A. Lauri, V. M. Kerminen, W. Birmili, and P. H. McMurry (2004b), Formation and growth rates of ultrafine atmospheric particles: a review of observations, *Journal of Aerosol Science*, *35*(2), 143-176, doi:10.1016/j.jaerosci.2003.10.003.

Kunzli, N., et al. (2000), Public-health impact of outdoor and traffic-related air pollution: a European assessment, *Lancet*, *356*(9232), 795-801, doi:10.1016/s0140-6736(00)02653-2.

Lapina, K., et al. (2011), Investigating organic aerosol loading in the remote marine environment, *Atmospheric Chemistry and Physics*, *11*(17), 8847-8860, doi:10.5194/acp-11-8847-2011.

Lee, B. H., J. R. Pierce, G. J. Engelhart, and S. N. Pandis (2011), Volatility of secondary organic aerosol from the ozonolysis of monoterpenes, *Atmospheric Environment*, *45*(14), 2443-2452, doi:10.1016/j.atmosenv.2011.02.004.

Lee, S. S. (2012), Effect of Aerosol on Circulations and Precipitation in Deep Convective Clouds, *Journal of the Atmospheric Sciences*, *69*(6), 1957-1974, doi:10.1175/jas-d-11-0111.1.

Leibensperger, E. M., L. J. Mickley, D. J. Jacob, W. T. Chen, J. H. Seinfeld, A. Nenes, P. J. Adams, D. G. Streets, N. Kumar, and D. Rind (2012), Climatic effects of 1950-2050 changes in US anthropogenic aerosols - Part 1: Aerosol trends and radiative forcing, *Atmospheric Chemistry and Physics*, *12*(7), 3333-3348, doi:10.5194/acp-12-3333-2012.

Lerach, D. G., and W. R. Cotton (2012), Comparing Aerosol and Low-Level Moisture Influences on Supercell Tornadogenesis: Three-Dimensional Idealized Simulations, *Journal of the Atmospheric Sciences*, *69*(3), 969-987, doi:10.1175/jas-d-11-043.1.

Lerach, D. G., B. J. Gaudet, and W. R. Cotton (2008), Idealized simulations of aerosol influences on tornadogenesis, *Geophysical Research Letters*, *35*(23), doi:10.1029/2008gl035617.

Levin, E. J. T., S. M. Kreidenweis, G. R. McMeeking, C. M. Carrico, J. L. Collett, and W. C. Malm (2009), Aerosol physical, chemical and optical properties during the Rocky Mountain Airborne Nitrogen and Sulfur study, *Atmospheric Environment*, *43*(11), 1932-1939, doi:10.1016/j.atmosenv.2008.12.042.

Levin, E. J. T., et al. (2010), Biomass burning smoke aerosol properties measured during Fire Laboratory at Missoula Experiments (FLAME), *Journal of Geophysical Research-Atmospheres*, *115*, doi:D18210 10.1029/2009jd013601.

Levin, E. J. T., A. J. Prenni, M. D. Petters, S. M. Kreidenweis, R. C. Sullivan, S. A. Atwood, J. Ortega, P. J. DeMott, and J. N. Smith (2012), An annual cycle of size-resolved aerosol hygroscopicity at a forested site in Colorado, *Journal of Geophysical Research-Atmospheres*, *117*, doi:D0620110.1029/2011jd016854.

Lipsky, E. M., and A. L. Robinson (2005), Design and evaluation of a portable dilution sampling system for measuring fine particle emissions from combustion systems, *Aerosol Science and Technology*, *39*(6), 542-553, doi:10.1080/027868291004850.

Lipsky, E. M., and A. L. Robinson (2006), Effects of dilution on fine particle mass and partitioning of semivolatile organics in diesel exhaust and wood smoke, *Environmental Science & Technology*, *40*(1), 155-162, doi:10.1021/es050319p.

Litschert, S. E., T. C. Brown, and D. M. Theobald (2012), Historic and future extent of wildfires in the Southern Rockies Ecoregion, USA, *Forest Ecology and Management*, *269*, 124-133, doi:10.1016/j.foreco.2011.12.024.

Liu, X., et al. (2012), Toward a minimal representation of aerosols in climate models: description and evaluation in the Community Atmosphere Model CAM5, *Geoscientific Model Development*, *5*(3), 709-739, doi:10.5194/gmd-5-709-2012.

Luo, G., and F. Yu (2011), Simulation of particle formation and number concentration over the Eastern United States with the WRF-Chem plus APM model, *Atmospheric Chemistry and Physics*, *11*(22), 11521-11533, doi:10.5194/acp-11-11521-2011.

Mack, L. A., et al. (2010), Optical closure experiments for biomass smoke aerosols, *Atmospheric Chemistry and Physics*, *10*(18), 9017-9026, doi:10.5194/acp-10-9017-2010.

Maddox, R. A. (1980), MESOSCALE CONVECTIVE COMPLEXES, *Bulletin of the American Meteorological Society*, *61*(11), 1374-1387, doi:10.1175/1520-0477(1980)061<1374:mcc>2.0.co;2.

Malm, W. C., and D. E. Day (2000), Optical properties of aerosols at Grand Canyon National Park, *Atmospheric Environment*, *34*(20), 3373-3391.

Malm, W. C., and J. L. Hand (2007), An examination of the physical and optical properties of aerosols collected in the IMPROVE program, *Atmospheric Environment*, *41*(16), 3407-3427.

Malm, W. C., G. R. McMeeking, S. M. Kreidenweis, E. Levin, C. M. Carrico, D. E. Day, J. L. Collett, T. Lee, A. P. Sullivan, and S. Raja (2009), Using High Time Resolution Aerosol and Number Size Distribution Measurements to Estimate Atmospheric Extinction, *Journal of the Air & Waste Management Association*, *59*(9), 1049-1060, doi:10.3155/1047-3289.59.9.1049.

Malm, W. C., B. A. Schichtel, M. L. Pitchford, L. L. Ashbaugh, and R. A. Eldred (2004), Spatial and monthly trends in speciated fine particle concentration in the United States, *Journal of Geophysical Research-Atmospheres*, *109*(D3), doi:10.1029/2003jd003739|issn 0148-0227.

Malm, W. C., J. F. Sisler, D. Huffman, R. A. Eldred, and T. A. Cahill (1994), Spatial and seasonal trends in particle concentrations and optical extinction in the United-States, *Journal of Geophysical Research-Atmospheres*, *99*(D1), 1347-1370.

Markowski, G. R. (1987), Improving Twomey algorithm for inversion of aerosol measurement data, *Aerosol Science and Technology*, *7*(2), 127-141.

Marlon, J. R., et al. (2012), Long-term perspective on wildfires in the western USA, *Proceedings of the National Academy of Sciences of the United States of America*, *109*(9), E535-E543, doi:10.1073/pnas.1112839109.

Massoli, P., et al. (2010), Relationship between aerosol oxidation level and hygroscopic properties of laboratory generated secondary organic aerosol (SOA) particles, *Geophysical Research Letters*, *37*, 5, doi:L24801 10.1029/2010gl045258.

Mathur, R., et al. (2005), Multiscale air quality simulation platform (MAQSIP): Initial applications and performance for tropospheric ozone and particulate matter, *Journal of Geophysical Research-Atmospheres*, *110*(D13), doi:10.1018/2004jd004918.

McMeeking, G. R., et al. (2010), Black carbon measurements in the boundary layer over western and northern Europe, *Atmospheric Chemistry and Physics*, *10*(19), 9393-9414, doi:10.5194/acp-10-9393-2010.

McMeeking, G. R., et al. (2009), Emissions of trace gases and aerosols during the open combustion of biomass in the laboratory, *Journal of Geophysical Research-Atmospheres*, *114*, doi:D1921010.1029/2009jd011836.

McMeeking, G. R., S. M. Kreidenweis, C. M. Carrico, J. L. Collett, D. E. Day, and W. C. Malm (2005a), Observations of smoke-influenced aerosol during the Yosemite Aerosol Characterization Study: 2. Aerosol scattering and absorbing properties, *Journal of Geophysical Research-Atmospheres*, *110*(D18), doi:10.1029/2004jd005624.

McMeeking, G. R., S. M. Kreidenweis, C. M. Carrico, T. Lee, J. L. Collett, and W. C. Malm (2005b), Observations of smoke-influenced aerosol during the Yosemite Aerosol Characterization Study: Size distributions and chemical composition, *Journal of Geophysical Research-Atmospheres*, *110*(D9), doi:10.1029/2004jd005389.

McMeeking, G. R., et al. (2006), Smoke-impacted regional haze in California during the summer of 2002, *Agricultural and Forest Meteorology*, *137*(1-2), 25-42.

Mehta, A. J., et al. (2012), Occupational Exposure to Dusts, Gases, and Fumes and Incidence of Chronic Obstructive Pulmonary Disease in the Swiss Cohort Study on Air Pollution and Lung and Heart Diseases in Adults, *American Journal of Respiratory and Critical Care Medicine*, *185*(12), 1292-1300, doi:10.1164/rccm.201110-1917OC.

Mikhailov, E., S. Vlasenko, S. T. Martin, T. Koop, and U. Poschl (2009), Amorphous and crystalline aerosol particles interacting with water vapor: conceptual framework and experimental evidence for restructuring, phase transitions and kinetic limitations, *Atmospheric Chemistry and Physics*, *9*(24), 9491-9522.

Moore, R. H., K. Cerully, R. Bahreini, C. A. Brock, A. M. Middlebrook, and A. Nenes (2012), Hygroscopicity and composition of California CCN during summer 2010, *Journal of Geophysical Research-Atmospheres*, *117*, 14, doi:10.1029/2011jd017352.

Moteki, N., and Y. Kondo (2010), Dependence of Laser-Induced Incandescence on Physical Properties of Black Carbon Aerosols: Measurements and Theoretical Interpretation, *Aerosol Science and Technology*, *44*(8), 663-675, doi:10.1080/02786826.2010.484450.

Odum, J. R., T. Hoffmann, F. Bowman, D. Collins, R. C. Flagan, and J. H. Seinfeld (1996), Gas/particle partitioning and secondary organic aerosol yields, *Environmental Science & Technology*, *30*(8), 2580-2585, doi:10.1021/es950943+.

Pankow, J. F. (1987), REVIEW AND COMPARATIVE-ANALYSIS OF THE THEORIES ON PARTITIONING BETWEEN THE GAS AND AEROSOL PARTICULATE PHASES IN THE ATMOSPHERE, *Atmospheric Environment*, *21*(11), 2275-2283, doi:10.1016/0004-6981(87)90363-5.

Pankow, J. F. (1988), PARTITIONING OF ORGANIC-COMPOUNDS BETWEEN THE GAS AND ATMOSPHERIC PARTICULATE PHASES, *Abstracts of Papers of the American Chemical Society*, *195*, 157-AGRO.

Pankow, J. F. (1994), An absorption model of gas-particle partitioning of organic compounds in the atmosphere, *Atmospheric Environment*, *28*(2), 185-188, doi:10.1016/1352-2310(94)90093-0.

Park, R. J., D. J. Jacob, and J. A. Logan (2007), Fire and biofuel contributions to annual mean aerosol mass concentrations in the United States, *Atmospheric Environment*, *41*(35), 7389-7400.

Perez, L., R. Rapp, and N. Kunzli (2010), The Year of the Lung: outdoor air pollution and lung health, *Swiss Medical Weekly*, *140*, 6-10, doi:10.4414/smw.2010.13129.

Petters, M. D., C. M. Carrico, S. M. Kreidenweis, A. J. Prenni, P. J. DeMott, J. L. Collett, and H. Moosmuller (2009a), Cloud condensation nucleation activity of biomass burning aerosol, *Journal of Geophysical Research-Atmospheres*, *114*, 16, doi:D22205 10.1029/2009jd012353.

Petters, M. D., C. M. Carrico, S. M. Kreidenweis, A. J. Prenni, P. J. DeMott, J. L. Collett, and H. Moosmüller (2009b), Cloud condensation nucleation activity of biomass burning aerosol, *Journal of Geophysical Research-Atmospheres*, *114*, 16, doi:D22205 10.1029/2009jd012353.

Petters, M. D., and S. M. Kreidenweis (2007), A single parameter representation of hygroscopic growth and cloud condensation nucleus activity, *Atmospheric Chemistry and Physics*, *7*(8), 1961-1971.

Petters, M. D., S. M. Kreidenweis, A. J. Prenni, R. C. Sullivan, C. M. Carrico, K. A. Koehler, and P. J. Ziemann (2009c), Role of molecular size in cloud droplet activation, *Geophysical Research Letters*, *36*, doi:L22801 10.1029/2009gl040131.

Petters, M. D., et al. (2009d), Ice nuclei emissions from biomass burning, *Journal of Geophysical Research-Atmospheres*, *114*, doi:D07209 10.1029/2008jd011532.

Petters, M. D., A. J. Prenni, S. M. Kreidenweis, and P. J. DeMott (2007), On measuring the critical diameter of cloud condensation nuclei using mobility selected aerosol, *Aerosol Science and Technology*, *41*(10), 907-913, doi:10.1080/02786820701557214.

Pilinis, C., S. N. Pandis, and J. H. Seinfeld (1995), Sensitivity of direct climate forcing by atmospheric aerosols to aerosol-size and composition, *Journal of Geophysical Research-Atmospheres*, *100*(D9), 18739-18754.

Pitchford, M. L., W. Malm, B. Schichtel, N. Kumar, D. Lowenthal, and J. Hand (2007), Revised algorithm for estimating light extinction from IMPROVE particle speciation data, *Journal of the Air & Waste Management Association*, *57*(11), 1326-1336, doi:10.3155/1047-3289.57.11.1326.

Pitchford, M. L., B. A. Schichtel, K. A. Gebhart, M. G. Barna, W. C. Malm, I. H. Tombach, and E. M. Knipping (2005), Reconciliation and interpretation of the Big Bend National Park light extinction source apportionment: Results from the Big Bend Regional Aerosol and Visibility Observational study - Part II, *Journal of the Air & Waste Management Association*, *55*(11), 1726-1732.

Poschl, U., et al. (2010), Rainforest Aerosols as Biogenic Nuclei of Clouds and Precipitation in the Amazon, *Science*, *329*(5998), 1513-1516, doi:10.1126/science.1191056.

Poschl, U., D. Rose, and M. O. Andreae (2009), Part 2: Particle Hygroscopicity and Cloud Condensation Nucleus Activity, *Clouds in the Perturbed Climate System: Their Relationship to Energy Balance, Atmospheric Dynamics, and Precipitation*, 58-72.

Poulain, L., Z. Wu, M. D. Petters, H. Wex, E. Hallbauer, B. Wehner, A. Massling, S. M. Kreidenweis, and F. Stratmann (2010), Towards closing the gap between hygroscopic growth and CCN activation for secondary organic aerosols - Part 3: Influence of the chemical composition on the hygroscopic properties and volatile fractions of aerosols, *Atmospheric Chemistry and Physics*, *10*(8), 3775-3785.

Prenni, A. J., M. D. Petters, S. M. Kreidenweis, P. J. DeMott, and P. J. Ziemann (2007), Cloud droplet activation of secondary organic aerosol, *Journal of Geophysical Research-Atmospheres*, *112*(D10), doi:D10223 10.1029/2006jd007963.

Presto, A. A., and N. M. Donahue (2006), Investigation of alpha-pinene plus ozone secondary organic aerosol formation at low total aerosol mass, *Environmental Science & Technology*, *40*(11), 3536-3543, doi:10.1021/es052203z.

Pringle, K. J., H. Tost, A. Pozzer, U. Poschl, and J. Lelieveld (2010), Global distribution of the effective aerosol hygroscopicity parameter for CCN activation, *Atmospheric Chemistry and Physics*, *10*(12), 5241-5255, doi:10.5194/acp-10-5241-2010.

Ramanathan, V., P. J. Crutzen, J. T. Kiehl, and D. Rosenfeld (2001), Atmosphere - Aerosols, climate, and the hydrological cycle, *Science*, *294*(5549), 2119-2124.

Ranjan, M., A. A. Presto, A. A. May, and A. L. Robinson (2012), Temperature Dependence of Gas-Particle Partitioning of Primary Organic Aerosol Emissions from a Small Diesel Engine, *Aerosol Science and Technology*, *46*(1), 13-21, doi:10.1080/02786826.2011.602761.

Reid, J. S., T. F. Eck, S. A. Christopher, R. Koppmann, O. Dubovik, D. P. Eleuterio, B. N. Holben, E. A. Reid, and J. Zhang (2005a), A review of biomass burning emissions part III: intensive optical properties of biomass burning particles, *Atmospheric Chemistry and Physics*, *5*, 827-849.

Reid, J. S., R. Koppmann, T. F. Eck, and D. P. Eleuterio (2005b), A review of biomass burning emissions part II: intensive physical properties of biomass burning particles, *Atmospheric Chemistry and Physics*, *5*, 799-825.

Ridley, D. A., C. L. Heald, and B. Ford (2012), North African dust export and deposition: A satellite and model perspective, *Journal of Geophysical Research-Atmospheres*, *117*, doi:10.1029/2011jd016794.

Riipinen, I., J. R. Pierce, N. M. Donahue, and S. N. Pandis (2010), Equilibration time scales of organic aerosol inside thermodenuders: Evaporation kinetics versus thermodynamics, *Atmospheric Environment*, *44*(5), 597-607, doi:10.1016/j.atmosenv.2009.11.022.

Riipinen, I., et al. (2011), Organic condensation: a vital link connecting aerosol formation to cloud condensation nuclei (CCN) concentrations, *Atmospheric Chemistry and Physics*, *11*(8), 3865-3878, doi:10.5194/acp-11-3865-2011.

Roberts, G. C., and A. Nenes (2005), A continuous-flow streamwise thermal-gradient CCN chamber for atmospheric measurements, *Aerosol Science and Technology*, *39*(3), 206-221.

Robinson, A. L., N. M. Donahue, M. K. Shrivastava, E. A. Weitkamp, A. M. Sage, A. P. Grieshop, T. E. Lane, J. R. Pierce, and S. N. Pandis (2007), Rethinking organic aerosols: Semivolatile emissions and photochemical aging, *Science*, *315*(5816), 1259-1262, doi:10.1126/science.1133061.

Robinson, N. H., et al. (2011), Evidence for a significant proportion of Secondary Organic Aerosol from isoprene above a maritime tropical forest, *Atmospheric Chemistry and Physics*, *11*(3), 1039-1050, doi:10.5194/acp-11-1039-2011.

Roesler, E. L., and J. E. Penner (2010), Can global models ignore the chemical composition of aerosols?, *Geophysical Research Letters*, *37*, doi:10.1029/2010gl044282.

Romakkaniemi, S., A. Arola, H. Kokkola, W. Birmili, T. Tuch, V. M. Kerminen, P. Raisanen, J. N. Smith, H. Korhonen, and A. Laaksonen (2012), Effect of aerosol size distribution changes on AOD, CCN and cloud droplet concentration: Case studies from Erfurt and Melpitz, Germany, *Journal of Geophysical Research-Atmospheres*, *117*, doi:10.1029/2011jd017091.

Rose, D., S. S. Gunthe, E. Mikhailov, G. P. Frank, U. Dusek, M. O. Andreae, and U. Poschl (2008), Calibration and measurement uncertainties of a continuous-flow cloud condensation nuclei counter (DMT-CCNC): CCN activation of ammonium sulfate and sodium chloride aerosol particles in theory and experiment, *Atmospheric Chemistry and Physics*, *8*(5), 1153-1179.

Rosenfeld, D., U. Lohmann, G. B. Raga, C. D. O'Dowd, M. Kulmala, S. Fuzzi, A. Reissell, and M. O. Andreae (2008), Flood or drought: How do aerosols affect precipitation?, *Science*, *321*(5894), 1309-1313, doi:10.1126/science.1160606.

Saarikoski, S., H. Timonen, K. Saarnio, M. Aurela, L. Jarvi, P. Keronen, V. M. Kerminen, and R. Hillamo (2008), Sources of organic carbon in fine particulate matter in northern European urban air, *Atmospheric Chemistry and Physics*, *8*(20), 6281-6295.

Saide, P. E., et al. (2012), Evaluating WRF-Chem aerosol indirect effects in Southeast Pacific marine stratocumulus during VOCALS-REx, *Atmospheric Chemistry and Physics*, *12*(6), 3045-3064, doi:10.5194/acp-12-3045-2012.

Saleeby, S. M., and W. R. Cotton (2005), Aerosol influence on Winter orographic precipitation, *Bulletin of the American Meteorological Society*, *86*(4), 477-478.

Saleeby, S. M., W. R. Cotton, and J. D. Fuller (2011), The Cumulative Impact of Cloud Droplet Nucleating Aerosols on Orographic Snowfall in Colorado, *Journal of Applied Meteorology and Climatology*, *50*(3), 604-625, doi:10.1175/2010jamc2594.1.

Saleeby, S. M., W. R. Cotton, D. Lowenthal, R. D. Borys, and M. A. Wetzel (2009), Influence of Cloud Condensation Nuclei on Orographic Snowfall, *Journal of Applied Meteorology and Climatology*, *48*(5), 903-922, doi:10.1175/2008jamc1989.1.

Saleh, R., A. Khlystov, and A. Shihadeh (2012), Determination of Evaporation Coefficients of Ambient and Laboratory-Generated Semivolatile Organic Aerosols from Phase Equilibration Kinetics in a Thermodenuder, *Aerosol Science and Technology*, *46*(1), 22-30, doi:10.1080/02786826.2011.602762.

Schichtel, B. A., K. A. Gebhart, W. C. Malm, and M. G. Barna (2005), Reconciliation and interpretation of Big Bend National Park particulate sulfur source apportionment: Results from the Big Bend Regional Aerosol and Visibility Observational study - Part I, *Journal of the Air & Waste Management Association*, *55*(11), 1709-1725.

Schichtel, B. A., W. C. Malm, G. Bench, S. Fallon, C. E. McDade, J. C. Chow, and J. G. Watson (2008), Fossil and contemporary fine particulate carbon fractions at 12 rural and urban sites in the United States, *Journal of Geophysical Research-Atmospheres*, *113*(D2), doi:D0231110.1029/2007jd008605.

Schlesinger, M. E., and X. J. Jiang (1991), REVISED PROJECTION OF FUTURE GREENHOUSE WARMING, *Nature*, *350*(6315), 219-221.

Schneider, J., S. Weimer, F. Drewnick, S. Borrmann, G. Helas, P. Gwaze, O. Schmid, M. O. Andreae, and U. Kirchner (2006), Mass spectrometric analysis and aerodynamic properties of various types of combustion-related aerosol particles, *International Journal of Mass Spectrometry*, *258*(1-3), 37-49, doi:10.1016/j.ijms.2006.07.008.

Schwarz, J. P., et al. (2006), Single-particle measurements of midlatitude black carbon and light-scattering aerosols from the boundary layer to the lower stratosphere, *Journal of Geophysical Research-Atmospheres*, *111*(D16), doi:D1620710.1029/2006jd007076.

Seinfeld, J. H., and S. N. Pandis (2006), *Atmospheric chemistry and physics : from air pollution to climate change*, 2nd ed., xxviii, 1203 p. pp., Wiley, Hoboken, N.J.

Sharkey, T. D., A. E. Wiberley, and A. R. Donohue (2008), Isoprene emission from plants: Why and how, *Annals of Botany*, *101*(1), 5-18, doi:10.1093/aob/mcm240.

Shrivastava, M. K., E. M. Lipsky, C. O. Stanier, and A. L. Robinson (2006), Modeling semivolatile organic aerosol mass emissions from combustion systems, *Environmental Science & Technology*, *40*(8), 2671-2677, doi:10.1021/es0522231.

Sihto, S.-L., et al. (2010), Seasonal variation of CCN concentrations and aerosol activation properties in boreal forest, *Atmos. Chem. Phys. Discuss.*, *10*, 28231-28272.

Simoneit, B. R. T., J. J. Schauer, C. G. Nolte, D. R. Oros, V. O. Elias, M. P. Fraser, W. F. Rogge, and G. R. Cass (1999), Levoglucosan, a tracer for cellulose in biomass burning and atmospheric particles, *Atmospheric Environment*, *33*(2), 173-182, doi:10.1016/s1352-2310(98)00145-9.

Snider, J. R., and M. D. Petters (2008), Optical particle counter measurement of marine aerosol hygroscopic growth, *Atmospheric Chemistry and Physics*, *8*(7), 1949-1962.

Storer, R. L., S. C. van den Heever, and G. L. Stephens (2010), Modeling Aerosol Impacts on Convective Storms in Different Environments, *Journal of the Atmospheric Sciences*, *67*(12), 3904-3915, doi:10.1175/2010jas3363.1.

Tang, I. N. (1996), Chemical and size effects of hygroscopic aerosols on light scattering coefficients, *Journal of Geophysical Research-Atmospheres*, *101*(D14), 19245-19250.

Telford, P. J., et al. (2010), Effects of climate-induced changes in isoprene emissions after the eruption of Mount Pinatubo, *Atmospheric Chemistry and Physics*, *10*(15), 7117-7125, doi:10.5194/acp-10-7117-2010.

Textor, C., et al. (2006), Analysis and quantification of the diversities of aerosol life cycles within AeroCom, *Atmospheric Chemistry and Physics*, *6*, 1777-1813.

Trenberth, K. E., and J. T. Fasullo (2009), Global warming due to increasing absorbed solar radiation, *Geophysical Research Letters*, *36*, doi:10.1029/2009gl037527.

Trenberth, K. E., J. T. Fasullo, and J. Kiehl (2009), EARTH'S GLOBAL ENERGY BUDGET, *Bulletin of the American Meteorological Society*, *90*(3), 311-+, doi:10.1175/2008bams2634.1.

Tucker, D. F., and N. A. Crook (1999), The generation of a mesoscale convective system from mountain convection, *Monthly Weather Review*, *127*(6), 1259-1273, doi:10.1175/1520-0493(1999)127<1259:tgoamc>2.0.co;2.

Turpin, B. J., and H. J. Lim (2001), Species contributions to PM2.5 mass concentrations: Revisiting common assumptions for estimating organic mass, *Aerosol Science and Technology*, *35*(1), 602-610.

Twomey, S. (1974), Pollution and Planetary Albedo, *Atmos. Environ.*, *8*(12), 1251-1256.

Twomey, S. (1975), Comparison of constrained linear inversion and an iterative nonlinear algorithm applied to indirect estimation of particle-size distributions, *Journal of Computational Physics*, *18*(2), 188-200.

van den Heever, S. C., G. G. Carrio, W. R. Cotton, P. J. DeMott, and A. J. Prenni (2006), Impacts of nucleating aerosol on Florida storms. Part I: Mesoscale simulations, *Journal of the Atmospheric Sciences*, *63*(7), 1752-1775, doi:10.1175/jas3713.1.

Van Den Heever, S. C., and W. R. Cotton (2007), Urban aerosol impacts on downwind convective storms, *Journal of Applied Meteorology and Climatology*, *46*(6), 828-850, doi:10.1175/jam2492.1.

van den Heever, S. C., G. L. Stephens, and N. B. Wood (2011), Aerosol Indirect Effects on Tropical Convection Characteristics under Conditions of Radiative-Convective Equilibrium, *Journal of the Atmospheric Sciences*, *68*(4), 699-718, doi:10.1175/2010jas3603.1.

VanLoy, M. D., V. C. Lee, L. A. Gundel, J. M. Daisey, R. G. Sextro, and W. W. Nazaroff (1997), Dynamic behavior of semivolatile organic compounds in indoor air .1. Nicotine in a stainless steel chamber, *Environmental Science & Technology*, *31*(9), 2554-2561, doi:10.1021/es960988q.

Virtanen, A., et al. (2010), An amorphous solid state of biogenic secondary organic aerosol particles, *Nature*, *467*(7317), 824-827, doi:10.1038/nature09455.

Volkamer, R., J. L. Jimenez, F. San Martini, K. Dzepina, Q. Zhang, D. Salcedo, L. T. Molina, D. R. Worsnop, and M. J. Molina (2006), Secondary organic aerosol formation from anthropogenic air pollution: Rapid and higher than expected, *Geophysical Research Letters*, *33*(17), doi:10.1029/2006gl026899.

Ward, D. S., and W. Cotton (2011a), A Method for Forecasting Cloud Condensation Nuclei Using Predictions of Aerosol Physical and Chemical Properties from WRF/Chem, *Journal of Applied Meteorology and Climatology*, *50*(7), 1601-1615, doi:10.1175/2011jamc2644.1.

Ward, D. S., and W. R. Cotton (2011b), Cold and transition season cloud condensation nuclei measurements in western Colorado, *Atmospheric Chemistry and Physics*, *11*(9), 4303-4317, doi:10.5194/acp-11-4303-2011.

Ward, D. S., T. Eidhammer, W. R. Cotton, and S. M. Kreidenweis (2010), The role of the particle size distribution in assessing aerosol composition effects on simulated droplet activation, *Atmospheric Chemistry and Physics*, *10*(12), 5435-5447, doi:10.5194/acp-10-5435-2010.

Watson, J. G. (2002), Visibility: Science and regulation, *Journal of the Air & Waste Management Association*, *52*(6), 628-713.

Weber, R. J., J. J. Marti, P. H. McMurry, F. L. Eisele, D. J. Tanner, and A. Jefferson (1997), Measurements of new particle formation and ultrafine particle growth rates at a clean continental site, *Journal of Geophysical Research-Atmospheres*, *102*(D4), 4375-4385, doi:10.1029/96jd03656.

Weimer, S., M. R. Alfarra, D. Schreiber, M. Mohr, A. S. H. Prevot, and U. Baltensperger (2008), Organic aerosol mass spectral signatures from wood-burning emissions: Influence of burning conditions and wood type, *Journal of Geophysical Research-Atmospheres*, *113*(D10), doi:10.1029/2007jd009309.

Wexler, A. S., and J. H. Seinfeld (1992), Analysis of aerosol ammonium-nitrate - departures from equilibrium during SCAQS, *Atmospheric Environment Part a-General Topics*, *26*(4), 579-591, doi:10.1016/0960-1686(92)90171-g.

Winklmayr, W., H. C. Wang, and W. John (1990), Adaptation of the Twomey algorithm to the inversion of cascade impactor data, *Aerosol Science and Technology*, *13*(3), 322-331.

Witek, M. L., P. J. Flatau, P. K. Quinn, and D. L. Westphal (2007), Global sea-salt modeling: Results and validation against multicampaign shipboard measurements, *Journal of Geophysical Research-Atmospheres*, *112*(D8), doi:10.1029/2006jd007779.

Xie, X. N., and X. D. Liu (2011), Effects of spectral dispersion on clouds and precipitation in mesoscale convective systems, *Journal of Geophysical Research-Atmospheres*, *116*, doi:10.1029/2010jd014598.

Yamashita, K., M. Murakami, A. Hashimoto, and T. Tajiri (2011), CCN Ability of Asian Mineral Dust Particles and Their Effects on Cloud Droplet Formation, *Journal of the Meteorological Society of Japan*, *89*(5), 581-587, doi:10.2151/jmsj.2011-512.

Yokelson, R. J., T. J. Christian, T. G. Karl, and A. Guenther (2008), The tropical forest and fire emissions experiment: laboratory fire measurements and synthesis of campaign data, *Atmospheric Chemistry and Physics*, *8*(13), 3509-3527.

Yue, X., L. J. Mickley, J. A. Logan, and J. O. Kaplan (2012), Ensemble projections of wildfire activity and carbonaceous aerosol concentrations over the western United States in the mid-21st century *J. Geophys. Res., submitted*.

Zhang, Q., et al. (2007), Ubiquity and dominance of oxygenated species in organic aerosols in anthropogenically-influenced Northern Hemisphere midlatitudes, *Geophysical Research Letters*, *34*(13), doi:L13801 10.1029/2007gl029979.

Zhang, Y. (2008), Online-coupled meteorology and chemistry models: history, current status, and outlook, *Atmospheric Chemistry and Physics*, *8*(11), 2895-2932.

Zhang, Y., X. Y. Wen, and C. J. Jang (2010), Simulating chemistry-aerosol-cloud-radiation-climate feedbacks over the continental US using the online-coupled Weather Research Forecasting Model with chemistry (WRF/Chem), *Atmospheric Environment*, *44*(29), 3568-3582, doi:10.1016/j.atmosenv.2010.05.056.

Zhao, Z., M. S. Pritchard, and L. M. Russell (2012), Effects on precipitation, clouds, and temperature from long-range transport of idealized aerosol plumes in WRF-Chem simulations, *Journal of Geophysical Research-Atmospheres*, *117*, doi:10.1029/2011jd016744.

Zobrist, B., C. Marcolli, D. A. Pedernera, and T. Koop (2008), Do atmospheric aerosols form glasses?, *Atmospheric Chemistry and Physics*, *8*(17), 5221-5244.

Appendix 1. Instrumentation

This Appendix describes the instrumentation used during RoMANS, GrandTReNDS and FLAME 3.

A1.1 RoMANS and GrandTReNDS

During both RoMANS studies and the GrandTReNDS study, aerosol size distributions were measured with three different instruments: a differential mobility particle sizer (DMPS; TSI 3085, TSI Incorporated, Minneapolis, MN), an optical particle counter (OPC; LASAIR 1003, Particle Measuring Systems, Boulder, CO) and an aerodynamic particle sizer (APS; TSI 3021). The instruments measured over the diameter ranges 0.04 – 0.63 μm, 0.39 – 0.95 μm and 1.0 - 20 μm respectively and were operated with 15 minute temporal resolution. The sizing instruments were housed inside a temperature-controlled mobile lab during all three studies. A sample flow of 0.6 LPM was pulled through an inlet in the roof of the lab and then passed through a Perma Pure dryer (Perma Pure Inc., Toms River, NJ) with a dry sheath flow of 1 LPM which dried the sample to RH < 10%. The sample flow was then split into two 0.3 LPM flows which went to the OPC and DMPS. To avoid losses of larger particles, the APS sampled through a separate inlet, with no bends, at 5.0 LPM. The APS inlet was heated to ~ 35 ˚C, thus drying the sample to RH < 15%. The sample flow was exposed to this heated region for about 0.5 s. This short residence time limits the loss of volatile particles [*An et al.*, 2007] yet is still long enough for any water on the aerosol to react to the lower RH [*Snider and Petters*, 2008]. During a few time periods of heavy rain, however, the APS drying system was insufficient to dry the aerosol. These times were obviously detected due to the sharp increase in aerosol volume

concentrations in the upper APS size bins during some rain events and these data were discarded. The inlets for both the DMPS/OPC and APS were approximately 5 m above ground level.

The three instruments all use a different technique to determine aerosol size. The DMPS consisted of a differential mobility analyzer (DMA; TSI 3081) that utilizes the relationship between the motion of a charged particle in an electric field, the electrical mobility, and the particle's diameter to select particles of a specified diameter. These size selected particles were then counted by a condensation particle counter (CPC; TSI 3010) which condenses butanol onto the particles to grow them to a size easily detected optically. The DMA was operated with a sheath flow of 3.0 LPM and a sample flow of 0.3 LPM. Because the CPC requires a sample flow of 1.0 LPM, 0.7 LPM of dried and HEPA filtered air was added to the CPC sample line after the DMA. The DMA stepped through 25 voltage settings, corresponding to 25 diameter bins, between 0.04 - 0.87 μm every 15 minutes.

The OPC uses light scattered by a particle passing through a 632.8 nm wavelength laser beam to determine particle size. Larger, purely scattering particles will scatter more light than smaller particles with a similar refractive index, assuming spherical particles, and the instrument uses the detected intensity of scattered light to size the particle based on calibrations with particles of known refractive index. The LASAIR 1003 sizes particles into 8 bins with manufacturer calibrated lower bin limit diameters of 0.1, 0.2, 0.3, 0.4, 0.5, 0.7, 1.0 and 2.0 μm. Although the OPC can be operated at much higher time resolution, data from the OPC were averaged every 15 minutes to match the sampling time of the DMPS. To avoid coincidence errors, more than one particle entering the optical chamber at once, the OPC operates at a very low flow rate, 0.028 LPM.

The APS sizes particles based on their motion in an accelerating flow. Sample is drawn into the instrument at 1.0 LPM and then accelerated by a sheath flow. Smaller particles, with less inertial lag, will accelerate more quickly with the flow while larger particles, of the same density, take longer to accelerate and will thus have a lower velocity at the end of the inlet nozzle. The APS calculates particle velocity by determining the time required for a particle to pass through two laser beams separated by 100 μm. The instrument then uses this velocity to size the particle into one of 52 bins, between 0.5 and 20 μm with a base 10 logarithmic bin width of 0.03 μm. Because the APS utilizes the particles aerodynamic drag to determine size, it is actually measuring aerodynamic diameter (d_{ae}), which is dependent on particle shape and density as well as physical size. As with the OPC, I assumed the predominately aged particles measured during RoMANS and GrandTReNDS were spherical. An appropriate effective density that was used to convert the aerodynamic diameters into equivalent "true" diameters was derived by aligning the APS output with that of the other sizing instruments, as described below.

Because the three aerosol sizing instruments all measure over different size ranges and exploit different aerosol characteristics to determine particle size, the outputs from the instruments have to be reconciled to produce one continuous size distribution. This was done following the alignment method developed by *Hand and Kreidenweis* [2002]. Briefly, the data from the DMPS, OPC and APS were first interpolated to the same diameter grid using a Twomey fit [*Markowski*, 1987; *Twomey*, 1975; *Winklmayr et al.*, 1990]. The alignment method then minimized the difference between the DMA and OPC data in the overlap region between these two measurements by adjusting the assumed particle refractive index, the OPC response to particles of varying real refractive index having been previously determined by laboratory calibrations. After aligning the OPC to the DMA data the APS data were then fit to this adjusted

OPC data by changing assumed particle effective density, which might include the impacts of shape factor on the aerodynamic size. The final result of the alignment was a combined aerosol number distribution spanning particle diameter from 0.04 – 20 μm every 15 minutes, together with the best-fit refractive index and effective density. From these number distribution data I also calculated aerosol volume distributions with the volume in diameter bin *i* (V_i) calculated as

$$v_i = \frac{\pi}{6} D_i^3 \times N_i \qquad \textbf{Eq A1.1}$$

where N_i is the number of particles with diameter D_i. This again makes the assumption that the particles were all spherical.

The sizing instruments and alignment technique have been previously utilized during the Yosemite Aerosol Characterization Study (YACS) which occurred in 2002 [*McMeeking et al.*, 2005b], the 1999 Big Bend Regional Aerosol and Visibility Observational (BRAVO) study [*Hand et al.*, 2002] and the first RoMANS study (RoMANS 1) which occurred during two phases in the Spring and Summer of 2006 [*Levin et al.*, 2009].

Sizing for all three instruments is sensitive to sample flow rate. Therefore, flows were checked routinely, about twice weekly, during the RoMANS and GrandTReNDS studies using a Gilibrator flow meter (Sensidyne, St Petersburg, FL). The monodisperse flow exiting the DMA column (Q_{smaple}) was controlled by adjusting the amount of make-up air added between the DMA and CPC. Measured Q_{smaple} was always within ± 10% of its nominal 0.3 LPM value, but was adjusted at almost every flow check to be within ± 1%. The OPC and APS flows were adjusted twice each during RoMANS 2, the APS flows were adjusted once during GrandTReNDS and neither instrument required adjustement during RoMANS 2010. During all studies the OPC and APS sample flow rates were maintained within ± 1% and ± 5% of their nominal values,

respectively. Measured flows outside these ranges indicated either problems with the pumps or compressed air system or blocked inlets and these data were discarded. Aerosol sizing was checked using NIST traceable polystyrene latex spheres (PSL; Thermo Fisher Scientific Inc, Waltham, MA), at the beginning and end of each study and periodically during the year-long RoMANS 2 study. No drift in sizing was detected for any instrument, as long as flow rates were properly adjusted. Zero checks were also performed on all instruments during each study using a HEPA filter.

In addition to the particle sizing instrumentation, a host of complimentary instruments measured the concentration and speciation of many gasses and particles as well as meteorological variables during all three studies. I will describe only those instruments providing data that I used in my analyses.

During certain time periods of the ROMANS 2010 and GrandTReNDS campaigns, sub-micron aerosol composition was measured with a High Resolution Time of Flight Aerosol Mass Spectrometer (HR-ToF-AMS, hereafter referred to as AMS, Aerodyne Research Inc., Billerica, MA). This instrument has been previously described in detail [*Canagaratna et al.*, 2007; *DeCarlo et al.*, 2006; *Drewnick et al.*, 2005]. In brief, the instrument contains three main sections. In the first section the sample flow is focused down into a narrow beam by passing through an aerodynamic lens which allows particles ~35 – 700 nm to pass into the instrument. When operated in the Particle Time Of Flight (PTOF) mode, the aerosol beam is then intersected by a spinning disk, or chopper, with an open slot which allows evenly spaced packets of particles to pass into the second part of the instrument, the time of flight region. Particles are separated as a function of aerodynamic diameter (d_{ae}) as they traverse the time of flight region, where particles with lower aerodynamic drag, that is smaller d_{ae}, will accelerate faster and, thus,

traverse the region quicker. For spherical particles with similar densities, this translates to smaller physical diameter particles arriving at the detector first. The chopper can also be moved out of the particle path (MS mode), allowing total mass concentrations to be measured but sacrificing particle size information. At the end of the time of flight region, particles are impacted onto a thermal vaporizer heated to 600 °C which evaporates all nonrefractory material. Crustal material, or dust, and elemental carbon will not volatilize and thus cannot be detected using this method. However, the AMS can detect organic species, as well as inorganic ionic species such as ammonium, nitrate, sulfate and chloride. The evaporated fragments are ionized via electron ionization and then enter the time of flight mass spectrometer where they are separated based on mass (m) and charge (z) and then detected.

The AMS sizing was checked using several sizes of monodisperse PSL spheres spanning the diameter range 70 – 700 nm at the beginning of each study. Ionization efficiency (IE) was checked using 350 nm ammonium nitrate particles following *Canagaratna et al.* [2007]. The IE calibration aerosol was generated using a TSI 3076 constant output atomizer and then size selected using a DMA (TSI 3080). Ionization efficiency was checked weekly during RoMANS 2010 and GrandTReNDS to insure no instrument drift in IE during the course of each study. Study averaged IE was used to process all data. Data processing and analysis were performed with the standard AMS software, Squirrel and Pika, using Igor Pro (Wavemetrics, Lake Oswego, Oregon).

During all three studies a number of instruments measured gas phase species including CO and several gaseous reactive nitrogen species. NO_x and NH_3 wer measured with an API 201A (Teledyne, San Diego, CA). This instrument works by converting NH_3 and NO_2 to NO using a high temperature molybdenum converter and then determines NO concentrations by

detecting the light given off from the chemiluminescent reaction of NO with O_3. By alternating the sample line between two converters heated to 315, at which NO_2 is evolved, and 825 ˚C, for NH_3, as well as a sample line with no converter, the instrument can determine NH_3, NO_2 and NO concentrations. The instrument was calibrated at the beginning and end of each study using NO, NO_2 and NH_3 at 20 and 60 ppb. Calibration gasses were generated using a model 700 dynamic dilution calibrator (Teledyne) and a model 701 zero air generator (Teledyne). Daily calibration and zero checks were also performed with NO and zero air.

During GrandTReNDS, meteorological variables including wind speed, wind direction, RH, temperature, precipitation and surface pressure were measured using a AIO-210 weather station (Climatronics Corp. Bohemia, NY). Meteorology data for the RoMANS site were provided from a permanent 10 m met tower operated by the CASTnet program (data available from epa.gov/castnet).

There were several periods during the RoMANS studies when the measurement site was impacted by campfire smoke from the adjacent summer camp. These events were typically in the evening during the summer and were characterized by sharp increase in aerosol number concentrations and CO concentrations. During RoMANS 2010 data from the CSU AMS further indicated the presence of smoke during these time periods. Biomass burning organic aerosol (BBOA) can be identified from AMS data from fragments of levoglucosan ($C_6H_{10}O_5$), a cellulose combustion product [*Schneider et al.*, 2006; *Simoneit et al.*, 1999; *Weimer et al.*, 2008]. Because the focus of this work is on regional aerosol characteristics, time periods with clear impact from the local camp were removed.

A1.2 FLAME 3

During FLAME 3, submicron aerosol mass concentration and speciation were measured with the same AMS used during RoMANS 2010 and GrandTReNDS and described above. During FLAME 3, the AMS IE was checked every two days using 350 nm ammonium nitrate as described above. Sizing was checked using PSL at the beginning of the study.

Black carbon was measured with a Single Particle Soot Photometer (SP2; Droplet Measurement Technology). This instrument uses a 1064 nm Nd:YAG laser to heat light absorbing particles, primarily black carbon, to temperatures high enough for the particle to incandesce. The energy given off by this incandescence, proportional to the incandescing mass, is detected optically and this signal is converted to particle mass [*Schwarz et al.*, 2006]. The instrument was calibrated prior to the study using size selected graphitic carbon aerosol (Aquadag, Acheson Industries, Port Huron, MI) as described by *McMeeking et al.* [2010]. Changes in the effective density of Aquadag with size, needed to convert from DMA selected diameter to mass, were corrected for following *Moteki amd Kondo.* [2010].

Total aerosol concentrations were measured with an ultra-fine condensation particle counter (UCPC 3776; TSI Inc). This instrument passes the sample through a growth tube supersaturated with respect to butanol, causing particles to grown to sizes large enough to be easily detected and counted optically. The 3776 has a nominal lower detection limit of 2.5 nm (TSI 3776 spec sheet).

Measurements of CO, CO_2, NO and NO_2 were also made in the combustion lab and dilution barrels during FLAME 3. These instruments were operated by the FSL. Carbon dioxide was measured with a Li-Cor Model 6262 non-dispersive infrared gas analyzer (Li – Cor,

Lincoln, NE). The instrument has a maximum range of 1000 ppm and a precision of ±1 ppm at 350 ppm. Carbon monoxide was measured using a Thermo Environmental Model 48C variable-range gas filter correlation analyzer. This instrument's precision was ±1% of the full scale and it has a nominal lower detection limit of 40 ppb (Model 48C instrument manual). Both instruments were calibrated before each burn with standards of known concentration.

A chemilumunescence analyzer 42c (Thermo Environmental Instruments Inc., Franklin, MA) was used to measure NO and NO_2 concentrations. The instrument works by converting NO_2 to NO using a high temperature molybdenum converter and then determines NO concentrations by detecting the light given off from the chemiluminescent reaction of NO with O_3. By alternating the sample line between the converter and no converter, the instrument can determine both NO and NO_2 concentrations. All the FSL instruments shared a sample line with the AMS and thus measured from the combustion lab and dilution system on the same schedule.

Carbon dioxide and NO_x were also measured in the combustion lab only with a Li-Cor 6262 (CO_2) and a Thermo-Electron 42i NO_x analyzer (NO_x). These instruments were operated by Aerodyne, who provided quality-controlled 1-minute data to our database.

Total hydrocarbons (THC) were measured by a Thermo Environmental Model 51 analyzer using flame ionization detection. This instrument was calibrated daily using a known mixture of CH_4, C_2H_4 and C_3H_8.

Appendix 2. AMS charge balance

Calculation of κ from AMS data requires some assumptions about the form of sulfate in the aerosol. Fully neutralized ammonium sulfate has a lower hygroscopicity than acidic sulfate species, such as $(NH_4)_3H(SO_4)_2$ or $NH_4H(SO_4)$ [*Petters and Kreidenweis*, 2007]. For all the calculations in Chapter 3 I assumed a fully neutralized aerosol. To test this assumption I calculated the amount of NH_4^+ needed to fully neutralize the aerosol from the equation

$$NH_{4\,predicted}^{+} = \frac{36}{132} SO_4^{2-} + \frac{18}{80} NO_3^{-} \qquad \textbf{Eq A2.1}$$

This equation gives the amount of NH_4^+ needed to fully neutralize all of the measured SO_4^{2-} and NO_3^-. However, nitrate could be in the form of organic nitrate, as appeared to be the case during BEACHON-RoMBAS. Therefore, Eq A2.1 would provide an upper bound on the amount of NH_4^+ needed. If chloride is present some NH_4^+ could also be in the form of ammonium chloride and this would also have to be accounted for in Eq A2.1. However, chloride was below the detection limit during all the studies discussed here and is thus not included.

Figure A2.1 shows the results of Eq A2.1 plotted against measured NH_4^+ during RoMANS 2010 (green), GrandTReNDS (red) and BEACHON-RoMBAS (black). The dark gray line is the one-to-one line and the light gray lines represent the uncertainty in the AMS measurement [*Bahreini et al.*, 2005]. During BEACHON and GrandTReNDS the measured ammonia was always equal to or greater than the amount needed to fully neutralize the aerosol, even when including NO_3^- in Eq A2.1. During RoMANS 2010, most values fell below the one-to-one line but almost all were within the instrument uncertainty. Only during a few time periods of RoMANS 2010 was measured NH_4^+ inadequate to neutralize the measured SO_4^{2-} and NO_3^-.

These time periods were always associated with elevated nitrate and organic mass, and thus could be influenced by organic nitrate compounds.

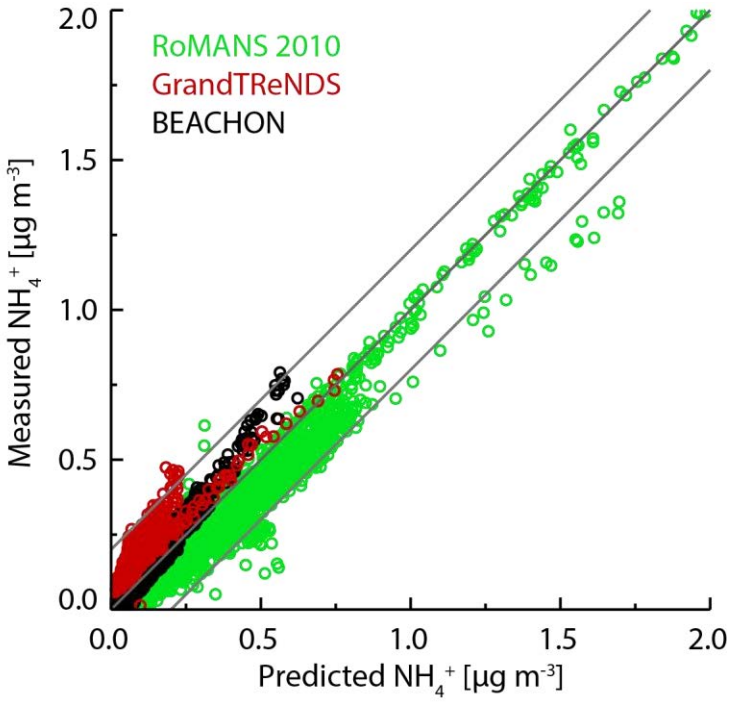

Figure A2.1 Measured NH_4^+ plotted against the amount needed to neutralize the aerosol. Gray lines indicated AMS measurement uncertainty.

Appendix 3. What effect does condensing organic material have on CCN concentrations?

One way in which biogenic volatile organic compounds (BVOC) impact cloud condensation nuclei (CCN) is by condensing onto existing particles. This process changes CCN properties by increasing mean aerosol diameter and, if the condensing material is chemically different than the existing particle, by changing hygroscopicity. Assume a particle with some initial volume (V_1) and hygroscopicity (κ_1) and condense some volume of a second compound (V_2; κ_2) onto it. How will this process affect the supersaturation required for CCN activation of this particle?

This question can be answered by solving Eq. 10 in *Petters and Kreidenweis* [2007] for critical supersaturation, the supersaturation at which a particle activates as a CCN, as a function of the particle's hygroscopicity, κ, and dry diameter, D_d:

$$s_c = \frac{c}{\sqrt{\kappa D_d^{\,3}}} \qquad \textbf{Eq. A3.1}$$

$$c = 16\sqrt{\frac{1}{27}\left(\frac{\sigma_{s/a} M_w}{RT\rho_w}\right)^3}$$

where $\sigma_{s/a}$ is surface tension of the air-water interface, assumed to be equal to the surface tension of pure water, $\sigma_w = 0.072$ J m^{-2}, R is the universal gas constant and M_w and ρ_w are the molecular weight and density of water.

From Eq. 7 in *Petters and Kreidenweis* [2007] κ of the two component system can then be calculated as:

$$\kappa = \frac{\kappa_1 V_1 + \kappa_2 V_2}{V_1 + V_2} \qquad \textbf{Eq.A3.2}$$

The dry diameter of the particle can be calculated from the respective volumes (assuming volume additivity) as:

$$D_d = 6^{1/3}\left(\frac{V_1 + V_2}{\pi}\right)^{1/3} \qquad \textbf{Eq. A3.3}$$

Substituting Eq. A3.2 and Eq. A3.3 into Eq. A3.1 and differentiating with respect to V_2 results in:

$$\frac{ds_c}{dV_2} = -\frac{1}{12}\frac{c\sqrt{6\pi}\kappa_2}{\left(\kappa_1 V_1 + \kappa_2 V_2\right)^{3/2}} \qquad \textbf{Eq. A3.4}$$

From Eq. A3.4 , it can be seen that if $\kappa_2 = 0$, the condensing compound is non-hygroscopic, then $ds_c/dV_2 = 0$. That is, there will be no change in critical supersaturation as organic material condenses onto the particle. The increase in diameter and decrease in hygroscopicity directly compensate and there will be no change in the CCN properties of the aerosol. Also, because of the negative sign in Eq. A3.4, if $\kappa_2 > 0$, then $ds_c/dV_2 < 0$. Thus, even if the overall hygroscopicity of the particle decreases as the organic vapors condense, the corresponding size increase will have the net effect of lowering the supersaturation necessary for the particle to activate as a CCN. Therefore, if condensational growth is due solely to the

condensation of organic compounds with low hygroscopicity onto a highly hygroscopic sulfate particle, the overall concentrations of particles active at a particle critical supersaturation will either remain the same or increase.

Appendix 4. Laminar flow element calibrations

Sample line flows into and out of the dilution barrels used during FLAME 3 were continuously monitored by measuring the pressure drop across laminar flow elements (LFE) as shown in Figure 4.3. The LFEs were calibrated twice during the study by measuring the volumetric flow rate through the LFE for a range of flows using a Gilibrator flow cell (Sensidyne, St Petersburg, FL). To convert from measured pressure drop to flow rate, a polynomial was fit to the calibration data. Figure A4.1 shows the calibration data and fits for the three LFEs. In Figure A4.1, the sample line between the combustion lab and the low dilution barrel is referred to as "smoke", the line between the low and high dilution barrels as "transfer" and the line to the instruments as "instrument". There was a shift in calibration for the smoke inlet and transfer line LFEs between the two calibrations. To account for this shift, a linear interpolation between the two calibration fits, based on the date, was used to process the flow rate measurements on days between the calibrations. There was no change in the instrument line LFE calibration and thus the same polynomial was applied for all study dates.

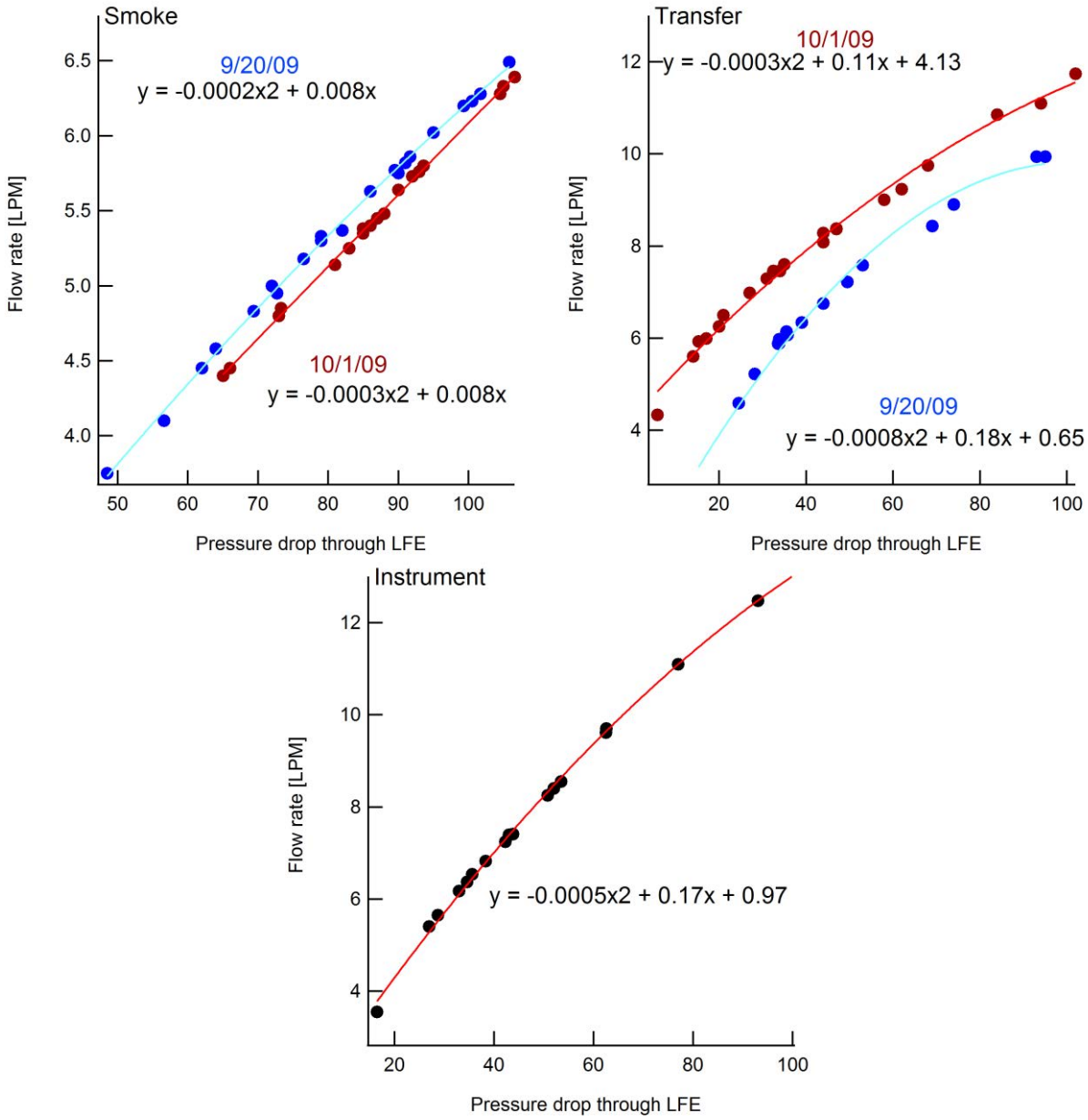

Figure A4.1 LFE calibration data. Blue points show data from the first calibration (9/20/09) and red from the second (10/1/09). The instrument LFE showed no change in calibration and all data points are shown in black.

Appendix 5. Infiltration rates from gas measurements

Table A5.1 Infiltration rates calculated from AERODYNE (AERO) and Fire Sciences Lab (FSL) gas measurements using Eq4.7. All values are in $m^3 min^{-1}$.

		CO_2		CO	NO		NO_2	
Burn #	**Fuel**	**AERO**	**FSL**	**FSL**	**AERO**	**FSL**	**AERO**	**FSL**
38	Lodgepole pine	28.86	16.41	20.93	32.71	33.47	49.8	32.34
40	Ponderosa pine	21.72	12.6	16.11	12.41	14.82	51.64	14.35
42	Wire Grass	16.51	14.39	15.81	17.17	15.18	36.31	37.77
43	Saw Grass	20.19	14.14	13.73	11.4	11.56	44.5	26.89
44	Gallberry	6.31	3.94	4.89	5.95	6.16	40.64	22.07
45	Turkey oak	16.11	14.15	19.3	18.25	11.25	61.58	21.53
46	Wheat Straw	3.43	4.27	4.86	4.37	5.47	64.39	19.96
49	Sage	3.2	2.44	13.2	12.73	11.71	-	16.22
52	Turkey oak	23.14	16.02	19.93	13.07	20.7	83.01	-
53	Sage	18.63	17.77	17.81	15.17	17.31	-	30.97
54	Manzanita	24.12	22	22.12	19.93	21.85	244.36	29.68
56	Wire grass	16.27	15.25	16.97	16.26	29.33	155.95	26.65
57	Ponderosa pine	19.07	-	18.96	-	8.59	-	-
58	Saw grass	21.24	16.22	24.13	25.22	19.23	66.22	7.13
59	Chamise	20.83	17.89	19.54	24.01	18.96	-	33.64
60	Manzanita	21.14	17.62	20.69	7.92	22.57	-	-
61	Lodgepole pine	20.62	3.78	21.26	4.35	30.31	-	-
62	Ceanothus	28.61	28.67	29.35	36.25	32.72	-	29.98
63	Pocosin	13.72	12.82	15.96	18.93	7.92	66.42	32.66
	Average	**18.09**	**13.91**	**17.66**	**16.45**	**17.85**	**80.40**	**25.46**
	Std. dev.	**7.24**	**6.75**	**5.85**	**8.93**	**8.86**	**60.44**	**8.42**

Table A5.2 Background gas measurements used to calculate infiltration rates. The negative value for Burn 38 CO indicates a calibration issue.

Burn #	Fuel	CO_2 [PPM]	CO [PPM]	NO_2 [PPB]	NO [PPB]
38	Lodgepole pine	417.5	-1.05	11.28	0.10
40	Ponderosa pine	414.9	0.11	15.69	0.83
42	Wire Grass	421.3	0.25	6.67	1.38
43	Saw Grass	442.2	0.20	10.55	0.00
44	Gallberry	420.6	0.15	9.44	0.38
45	Turkey oak	439.0	0.20	7.87	3.03
46	Wheat Straw	429.0	0.10	9.70	0.20
49	Sage	419.1	0.08	5.25	0.00
52	Turkey oak	411.6	0.07	5.95	0.00
53	Sage	429.0	0.05	4.90	0.00
54	Manzanita	413.1	0.02	5.55	0.00
56	Wire grass	408.1	0.01	5.75	0.00
57	Ponderosa pine	403.7	0.10	2.66	0.00
58	Saw grass	463.3	0.00	3.43	0.00
59	Chamise	409.9	0.10	2.24	0.12
60	Manzanita	409.7	0.10	4.45	0.04
61	Lodgepole pine	400.1	0.10	1.81	0.05
62	Ceanothus	418.7	0.30	2.86	0.10
63	Pocosin	365.2	0.10	6.48	0.54